From the Institute of Biomedical Optics
of the University of Lübeck
Director: Prof. Dr. rer. nat. Alfred Vogel

Linking biological effects of laser irradiated gold nanoparticles with temperature increase and formation of vapor bubbles

Dissertation
for Fulfillment of
Requirements
for the Doctoral Degree
of the University of Lübeck

from the Department of Natural Sciences

Submitted by

Florian Rudnitzki
from Bad Oldesloe
Lübeck 2018

First referee: Prof. Dr. rer. nat. Gereon Hüttmann

Second referee: Prof. Dr. rer. nat. Christian Hübner

Date of oral examination: 03. May 2019

Approved for printing. Lübeck, 09. May 2019

Abstract

The interaction of short pulsed laser radiation with strongly light-absorbing nanoparticles leads to nanoscale thermophysical effects in and around the nanoparticles. The physical mechanisms involved and the action radius vary with the particle size and the pulse duration. Irradiation of spherical gold nanoparticles with short laser pulses at wavelengths around 520 nm leads to heating and formation of microbubbles, or photochemical reactions. These effects can be used for selective cell elimination, when binding gold nanoparticles to specific biological target structures on the cell membrane. Therefore, spherical AuNP with 30 nm diameter were directly conjugated to IgG monoclonal antibodies targeting the CD30 membrane protein of human KARPAS-299 cells. For irradiation with laser pulses of 4 ns duration at a wavelength of 532 nm maximum elimination efficiency of 99 % was achieved for these cells growing in suspension. For adherent growing OVCAR-3 cells, maximum elimination was around 70 %.

Besides cell elimination the molecular release from the nanoparticle surface as principle mechanism to manipulate cells was studied in this thesis. Coumarin dye labeled siRNA covalently bound to nanoparticles was released when irradiated with 4 ns pulses at 532 nm. The release was determined by measuring changes in absorption spectra as well as fluorescence spectra of the coumarin molecule.

In both studies, bubble formation around nanosecond pulsed irradiated AuNP is assumed to be the main cause of cell elimination and molecular release. These measurements were conducted on solutions of randomly distributed nanoparticles, which prohibits direct correlation of the bubble wall velocity, expansion radius and the corresponding bubble energy with biological effects. In order to investigate individual nanoparticles, a microscope setup for single particle imaging and bubble detection by means of scattered light detection was developed.

In this thesis backscattered light detection is used to follow bubble formation around gold nanoparticles. The dark field microscopy set up allows the detection and pulsed irradiation of single gold nanoparticles. The oscillating cavitation bubble was detected with a continuous laser confocal coupled into the microscope with the irradiation laser beam. Backscattered light detection gives a direct measure of the bubble wall motion and radius during the bubble oscillation generated by a single laser pulse.

Experimental results showed, that irradiation at the theoretical bubble formation limit of bubbles around 30 nm gold nanoparticles, was not sufficient for cell elimination. While optical methods have not yet approached the required sensitivity to detect bubbles at the formation threshold, our experiment and calculation suggest, the reaching of the critical point of water is the starting point of the generation of nanobubbles. Biological effects like cell elimination or molecular release need considerably higher temperatures to drive bubbles with sufficient maximum diameters.

Modeling of bubble formation and expansion as well as the calculation of the spatio-temporal temperature increase demonstrate the involvement of more complex mechanisms as could be included in the analytical calculation.

The developed setup can generate experimental data for verification of more detailed modeling of bubble formation around AuNP. In future bubble formation around nanoparticles immobilized on cell membranes can be studied to understand the biological effect of nanocavitation.

Kurzfassung

Die Wechselwirkung von kurz gepulster Laserstrahlung mit stark lichtabsorbierenden Nanopartikeln führt zu nanoskaligen thermophysikalischen Effekten. Die beteiligten physikalischen Mechanismen und ihre Reichweite variieren mit der Partikelgröße und der Pulsdauer. Die Bestrahlung sphärischer Goldnanopartikel mit kurzen Laserpulsen bei einer Wellenlänge um 520 nm führt zur Erwärmung und Bildung von Mikrokavitationsblasen oder photochemischen Reaktionen. Wenn die Goldnanopartikel spezifisch an Zellmembranen gebunden sind, können diese Effekte zur selektiven Zelleliminierung verwendet werden. Dazu wurden sphärische AuNP mit 30 nm Durchmesser direkt mit monoklonalen IgG-Antikörpern konjugiert, die selektiv an das CD30-Membranprotein von KARPAS-299-Zellen binden. Bei definierter Bestrahlung mit Laserpulsen von 4 ns Dauer mit einer Wellenlänge von 532 nm wurde für diese in Suspension wachsenden Zellen eine maximale Eliminationseffizienz von 99% erreicht. Für adhärent wachsende OVCAR-3-Zellen betrug die maximale Elimination etwa 70%.

Neben der Zelleliminierung wurde in dieser Arbeit auch die molekulare Freisetzung von der Nanopartikeloberfläche als prinzipieller Mechanismus zur Manipulation von Zellen untersucht. Mit Cumarin markierte siRNA, die kovalent an Nanopartikel gebunden war, wurde bei Bestrahlung mit Laserpulsen von 4 ns Dauer und einer Wellenlänge von 532 nm freigesetzt. Ergebnisse der gemessenen Änderungen von Absorptionsspektren sowie von Fluoreszenzspektren des Cumarinmoleküls wiesen eine Freisetzung nach.

In beiden Studien wird eine durch gepulste Laserbestrahlung induzierte Blasenbildung um die AuNP als Hauptmechanismus für die Zelleliminierung bzw. molekulare Freisetzung betrachtet. Diese Annahme basiert auf Messungen an Lösungen mit statistisch verteilten Nanopartikeln. Einblick in die Geschwindigkeit der Blasenwand, den Expansionsradius und die entsprechende Blasenenergie einer einzelnen Blasenbildung gaben diese Experimente nicht. Um diese Größe an einzelnen Nanopartikeln bestimmen zu können, wurde ein Mikroskopaufbau zur Einzelpartikel- und Blasendetektion mittels Streulichtmessung entwickelt.

Im Rahmen dieser Arbeit wurden interferometrische Messungen an Kavitationsblasen um einzelne immobilisierte Goldnanopartikel durchgeführt. Dazu wurde eine Dunkelfeldmikroskopie aufgebaut, welche die Detektion und kurze gepulste Bestrahlung einzelner Goldnanopartikel ermöglicht. Die oszillierende Kavitationsblase wurde mit einem CW Laser detektiert, welcher konfokal mit einem gepulsten Laser zur bestrahlung von Partikeln in das Mikroskop eingekoppelt wurde. Das detektierte Rückstreulicht liefert ein direktes Maß für die Bewegung und den Radius der Blasenwand während der durch einen einzelnen Laserpuls erzeugten Blasenschwingung.

Die durchgeführten Versuche zeigten, dass die Bestrahlung an der theoretischen Schwelle von Blasenbildung um 30 nm Goldnanopartikel keine Zelleliminierung bewirkt. Während optische Methoden die erforderliche Empfindlichkeit zur Detektion der Blasenbildungsschwelle noch nicht erreicht haben, legen unsere Ergebnisse nahe, dass das Erreichen des kritischen Punktes von Wasser die Voraussetzung zur Entstehung von Blasen ist. Für biologische Anwendungen wie Zelleliminierung oder molekulare Freisetzung sind wesentlich höhere Temperaturen notwendig, um ausreichende Blasengrößen zu erhalten.

Modellierung der Blasenbildung und Expansion sowie die Berechnung der räumlich zeitlichen Temperaturerhöhung, zeigen die Beteiligung komplexerer Mechanismen auf, die nicht in die analytische Berechnung einbezogen werden konnten.

Der Dunkelfeldmikroskop-Aufbau dieser Arbeit kann in Zukunft experimentelle Daten für die Entwicklung und Verifikation detaillierterer Modellierung der Blasenbildung um AuNP liefern. Die entwickelten Techniken liefern die Grundlage für weitere Untersuchungen zur Wirkung von Nanoblasen auf Zellmembranen.

Contents

1 Introduction

Laser procedures provide high precision in the manipulation and destruction of microscopic structures. Two different approaches exist: Focusing laser radiation to regions with dimensions smaller than the applied wavelength leads to high temperatures in the irradiated volumes. Alternatively damage can be induced on small structures, which exhibit a much stronger absorption than their surroundings. Ablation [1] and selective thermolysis [2, 3] of tissue are only two examples of the second approach with a broad range of medical or biological applications. However, the range of destruction is often larger than the size of the absorbing volume due to plasma formation, explosive evaporation and thermal diffusion to the peripheral structures. In order to reduce the collateral thermal damage the laser pulse width can be adjusted to the thermal relaxation of the heated volume. Provided the absorption of the target structure is higher than the surrounding and heat diffusion is prevented, a selective destruction of tissue is then possible. This principle of selective photothermolysis can be applied for therapeutic treatment of single cells and tissue [4, 5]. Here, the spatial precision is not achieved by "aiming" at the target, but by selective absorption of the target, e. g. the micron sized melanin particles [6, 7], and the choice of adequate irradiation parameters.

In order to affect nanometer regions or those, that exhibit only weak absorption contrast other techniques are required. The unique optical properties of noble metal nanoparticles link optical technologies, which are restricted by their diffraction limited resolution to the micrometer range, with the nanoscaled world of cell biology. The method of nanoparticle assisted laser inactivation (NALI) provides an opportunity to confine the destruction to subcellular dimensions on the lower nanometer scale [3, 4]. NALI takes advantage of the large optical absorption cross section of particles, which are coupled to the target structure. Short pulsed laser irradiation ranging from femto- to nanoseconds can heat particles to very high temperatures and allow selective modification or destruction of cells and proteins specifically without harming their environment. Therefore, this method is also referred to as laser activated nanoparticle directed cell elimination and manipulation (LAND-CEM).

In result of an interaction with laser radiation physical effects occur in and around the strongly light-absorbing nanoparticles, which allow a variety of interesting applications ranging from functional analysis of proteins to the treatment of diseases [4, 8, 6, 9, 10] and further to increase in contrast for imaging and sensing modalities in diagnostic applications [11, 12, 13]. Depending on the pulse duration and particle properties, the physical mechanism of the effects can vary together with the action radius, which can range from nano- to microscale. Possible applications include a selective destruction of cells can be achieved by binding gold nanoparticles to specific biological target structures. Irradiation of spherical gold nanoparticles with short laser pulses at wavelengths around 520 nm leads to heating and formation of microbubbles, or photochemical reactions [8, 5, 7, 14]. The applicability of spherical gold nanoparticles irradiated with nanosecond pulses for cell (permeabilization and) elimination was successfully demonstrated in vitro [8, 15, 10, 16, 17, 18].

Knowledge of functionality, structure and interactions of cells or cell organelles, as the smallest structural and functional units of an organism, is the basis for the understanding of physiological and pathological processes. Optical technologies for the detection, isolation and characterization of individual cell types contribute continually to a better understanding of common diseases such as infections or cancer. Methods for purification and manipulation of cellular functions constitute a basis of various diagnostic and therapeutic procedures. However, current methods have limitations caused by high technical complexity for labeling and detection of the desired cells, or prerequisite preparation of the cell material.

Laser induced nanoparticle mediated processes can be utilized in purification processes of cell cultures [19]. The combination of laser irradiation of nanoparticles with flow cytometry [20, 21] or microscopic setups [9, 19, 22] are novel optical method that permits a gentle isolation and preparation of cells or cultures.

1.1 Cellular effects of laser irradiated gold nanoparticles

Cell elimination

Gold nanoparticles (AuNP) exhibit large optical absorption cross section and photostability compared to conventional organic chromophores used for example in photodynamic therapy (PDT). Depending on the applied radiant exposure and the pulse duration gold nanoparticles can be heated very efficiently by pulsed laser irradiation, which leads to thermal or mechanical processes arising in the nano- or microscale surrounding of the nanoparticle. When bound to cells, these effects allow high precision cell manipulation, which was demonstrated by nanosecond laser pulsed irradiated gold nanoparticles [3, 23, 4, 8, 5]. Cavitation bubbles have been identified as an effective mechanism for the elimination of cells and also for the denaturation of proteins [24, 25, 14].

Besides the optical properties of the particles ways of coupling to the respective target structure play a crucial role. AuNP are biocompatible [26, 27] and can be functionalized by surface modification with antibodies, aptamers or other proteins [28, 29]. A functionalization with selectively binding molecules is the basis of specific targeting for cell elimination [8] or transfection [30, 10, 31, 32, 33]. Once the particles are bound to the target structures cell elimination, also referred to as cell depletion or cell culture purification respectively, can be achieved with high spatial and temporal precision. Highly efficient elimination of lymphocytes labeled with gold nanoparticles was demonstrated under nanosecond pulsed irradiation, while unlabeled cells remained unaffected [19, 18]. Figure 1.1 illustrates the principle of the cell elimination by laser irradiated gold nanoparticles, which targeted a specific cell membrane protein.

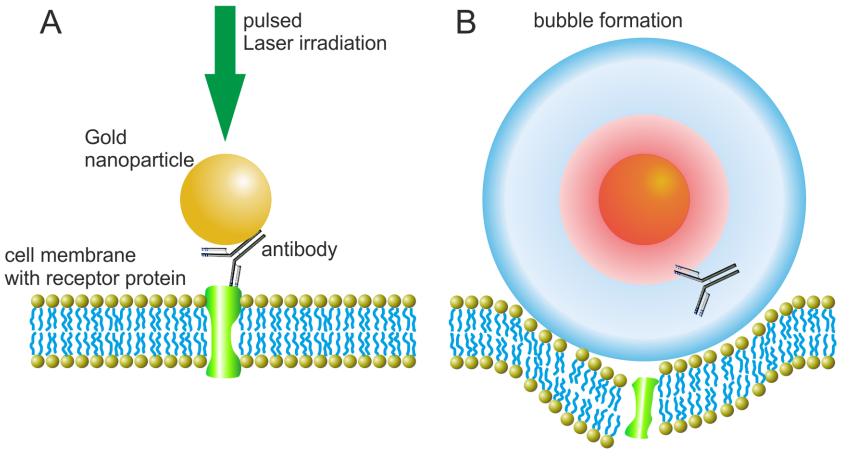

Figure 1.1: Principle of cell elimination by pulsed laser irradiation of an antibody functionalized gold nanoparticle targeting a receptor protein in the cell membrane (A). Bubble formation follows on sufficient radiant exposure and can destroy the cell membrane (B).

Molecular release from nanoparticles for cell manipulation

The introduction of gene-regulating drugs is already widely used to intervene specifically in functions of selected cells. Current methods are based on the transfection of individual cells by microinjection [34, 35] and on the non-directed transfection of a large number of cells by (bio-)chemical methods [36, 37], electroporation [38, 39] and viral-mediated [40, 41, 42] transfection. Microinjection is not suitable for high throughput processing of cells and non-directed methods show limited cell specificity in mixed cultures. Transfection using viral vectors are comparably complex and requires appropriate certifications to biosafety guidelines. Gold nanoparticles exhibit specific absorption properties [43, 44, 45] and can be functionalized with different molecules [28]. Thus, AuNP can be utilized as optically addressable, non-viral carriers of biologically active substances for the spatio-temporal triggering of cellular modification in different cell cultures [27]. Furthermore, this targeted optical release from nanostructures can combine the advantages of a targeted approach with high throughput. The manipulation process is

intended to be gentler and more specific than previous methods. An important aspect is, that the release is independent from physiological conditions within the cell, while being controlled externally via optical stimulation.

Optically addressable release of molecules provides temporally and spatially controllable modulation of individual cells in different cell culture systems. Gold nanoparticles were investigated either as pure carrier of drugs [46], DNA [47, 48] or siRNA [49, 50, 51] or as optically addressable unit in multi-functional nanoparticles [52]. In particular, manipulation of cells with siRNA offers interesting applications based on the down regulation of a specific target gene expression [53]. Despite initial encouraging results, optically induced release of DNA from gold nanoparticles and the required combination of irradiation and nanoparticle parameters [54] are still the subject of ongoing research.

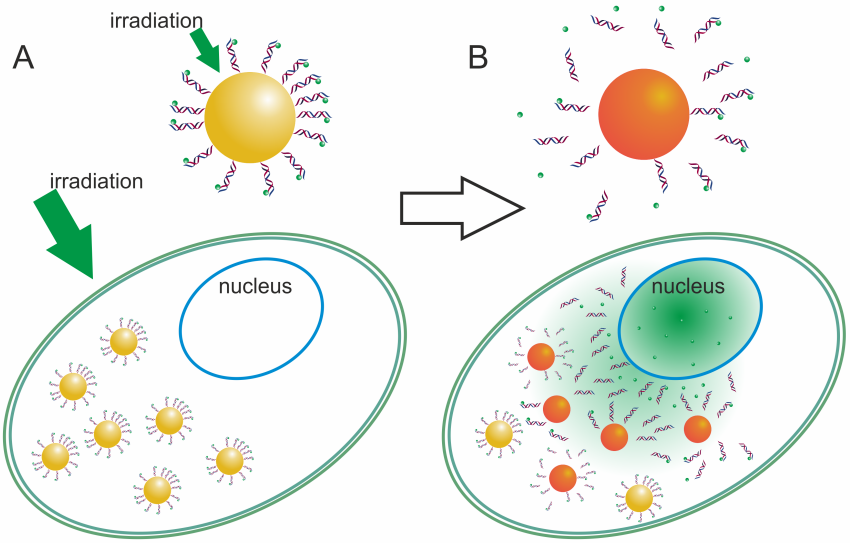

Figure 1.2: Principle of the light induced molecular release inside a cell. Irradiation of cells loaded with RNA labeled gold nanoparticles (A) causes increasing nanoparticle temperature and the release of the siRNA (B).

1.2 Motivation - Main objectives of the thesis

This thesis covers the interdisciplinary work on biological effects of short laser pulsed irradiated gold nanoparticles and links to the temperature increase and bubble formation around the particles. The capability of spherical and rod-shaped nanoparticles to eliminate or manipulate cells was demonstrated in different experimental settings. For several applications, optimal particle and irradiation parameters such as size, functionalization, wavelength and pulse durations respectively were identified. However, this optimization was based in most cases on empirical data, while the underlying mechanisms and accompanying effects are still not fully known and understood.

Lin and Kelly investigated the cavitation and acoustic emission around microparticles under picosecond pulsed laser irradiation [55]. They discussed the resulting microcavitation as a mechanism for cellular damage in biologic tissue containing pigment particles . Radt et al. demonstrated cell killing by picosecond pulsed irradiation of AuNPs, which were specifically bound to cells. Further, Radt et al. and Bever et. al. were able to inactivate proteins under similar irradiation conditions [8, 14].Wijaya et al. were able to optically triggered release of DNA oligonucleotides from the surface of nanorods with the help of femtosecond pulsed radiation [52]. By utilizing nanorods of different aspect rations, they showed a specific release depending on the irradiation wavelength, which matched the particle size related absorption peak. However, for pulse durations on the low picosecond range melting and fragmenting of the nanoparticles can be expected above certain radiant exposure and was demonstrated in experiments [56, 57, 58, 14] and predicted by theoretical considerations [59].

In contrast to picosecond pulses, nanosecond pulsed irradiation is not expected to cause fragmentation of the nanoparticles. It is further assumed that heating leads to cavitation bubbles on the particle surface with nanoscale expansion and effects on the targeted cells will be of mechanical or thermal nature.

Basic research on laser irradiated gold nanoparticles aims for a description of the involved thermodynamic processes. In order to study the nanoparticle-mediated effects Lapotko et al. successfully utilized thermal microscopy, which combines in a pump-probe experiment pulsed irradiation of the particles with phase contrast microscopy [60, 61]. This approach holds the disadvantage of not providing quantitative data on the size of submicrometer cavitation bubbles or their dynamics.

Recent experiments with nanoparticles ensembles support the hypothesis that upon pulsed irradiation of nanoparticles at their absorption peak wavelength primarily the generation of cavitation bubbles is responsible for cell elimination or destruction of adjacent structures [62, 18]. These experiments on ensembles of particles and cells do not allow for a specific detection of the effects, since deducing physical or chemical mechanisms from correlation to the laser parameters or particle properties with the biological effects is very unspecific and prone to errors.

This thesis spans over biological experiments for cell elimination and siRNA release by means of pulsed irradiated gold nanoparticles as well as basic physical experiments on single particles. In the first part laser induced nanoparticle directed cell elimination and molecular release are investigated (Chapter 3 and Chapter 4). An increase in cell elimination and molecular release with higher radiant exposures was observed. Further, the cell elimination depends on the nanoparticle concentration used to incubate with cells. Extraordinary high temperatures of the gold nanoparticles and the surrounding water were calculated for the radiant exposures at which biological effects were observed. Thus, the question arises, which are the underlying mechanisms of action. Before describing a new experimental approach for single nanoparticle experiments (Chapter 5) the state of the science in this field is reviewed (Chapter 5.2). So far, these experimental investigations clarify only a part of the involved thermodynamic mechanisms of bubble formation and expansion.

The second part of this thesis deals with basic physical experiments on single particles. A novel experimental setup was built combining darkfield contrast and imaging spectroscopy as well as backscattered light detection on single gold nanoparticles during pulsed laser irradiation (cf. Chapter 5). Measurement of the scattered light spectrum provides information of the particle size and the backscattered light provides a measure of the bubble formation.

Comparable techniques for the detection of nanoparticles were utilized by several groups in order to detect changes of the plasmon resonance absorption in the scope of sensor applications [13, 63, 64]. Other groups utilized darkfield contrast in order to detect the nanoparticles utilized to generate thermomechanical effects, however, without spectral identification of each single nanoparticle [60, 16]. Usually the particle properties were determined by measurements of multi-particle samples and not on single particle basis. In this work, the optical properties of an AuNP were determined for each irradiation experiment individually. By means of interferometric detection of scattered light a few hundred nanometer sized cavitation bubble and the bubble wall motion over time were measured.

Three issues regarding the formation and dynamics of vapor bubbles formed around pulsed laser irradiated gold nanoparticles will be discussed:

- Temperature increase within the nanoparticle and its nearest surrounding.
  An estimation of the physical and chemical processes within and around the particles requires knowledge of the temporal and spatial temperature distribution. Depending on the radiant exposure purely thermal effects due to heat diffusion as well as mechanical effects due to explosive vaporization of the medium and subsequent bubble expansion are caused by the laser irradiation.

- Bubble formation, bubble wall velocity and maximum expansion radius depending on the applied pulse duration and radiant exposure.
  A bubble, which is formed in the aqueous surrounding of a particle due to explosive evaporation, has strong impact on the cell membrane or a cell compartment at which the irradiated particle is attached to. Knowing the radius and extend of damage as a function

of the irradiation parameters is important for cell depletion and manipulation in cultures. A control of bubble size by the laser parameters used, could allow to tailor damage radii.

- Reproducibility of the laser induced bubble dynamics around the nanoparticles.
  Systematic investigations of the dependency of biological effects on laser parameters require reproducible measurements. Though, in literature there are several measurements of bubble sizes generated nanoparticles [60, 65, 16], systematic measurements were only done by Plech and co-workers [66, 67, 68]. The direct measurements of the bubble wall dynamics after pulsed irradiation, is described in this work for the first time.

In the last section, Chapter 6, the experimental results of cell elimination and siRNA release are discussed and linked to results from the single particle measurements. With detailed knowledge of the involved mechanisms, in future parameters for the laser irradiation could be defined to obtain the desired effects without collateral damages as for ablation occurs.

2 Electro- and thermodynamics of gold nanoparticles

The phenomena occurring due to the short pulsed laser irradiation of gold nanoparticles in an aqueous environment are explained by physical principles related to the optical properties (Chapter 2.1) and the thermodynamic behavior (Chapter 2.2) of the heated gold nanoparticles and the surrounding water. Strong heating of water can be followed by a liquid-vapor phase transition and lead to bubble formation (Chapter 2.3 and Chapter 2.4), which can be utilized for selective elimination of cells and for the optically triggered release of molecules from the particle surface.

2.1 Optical properties of gold nanoparticles

Gold nanoparticles absorb optical radiation very efficiently. An incident electromagnetic field interacts with electrons confined in the particle and stimulates resonant oscillation modes. The resulting plasmons, multipole density oscillations of quasi free electrons relative to the atomic cores in a metal crystal lattice, induce an additional electromagnetic field. The frequency and intensity of the plasmon excitation band are highly sensitive to the boundary conditions such as size and shape of the observed particles and of its material as well as the surrounding environment properties.

2.1.1 Dielectric properties of gold

A simple explanation to the optical properties of free electrons in metal such as gold is given by the Drude-Sommerfeld model [69]. Gold has a completely filled valence band and a partly filled conduction band with a Fermi energy of approximately $E_F = 5.5\,\mathrm{eV}$. Gold atoms form a bulk lattice with a free electron density of $n_f = 5.85 \cdot 10^{22} cm^3$. These conduction band electrons, each of mass m_e, are assumed to move freely between collisions with lattice ions, lattice defects, phonons and other electrons forming a quasi free (ideal) gas. For nonmagnetic metals the permeability μ can be assumed to be unity for frequencies in the visible spectral range. The electric field of an incident plane electromagnetic wave $E\left(\overrightarrow{r},t\right) = E_0 \exp\left(\imath \cdot \overrightarrow{k} \cdot \overrightarrow{r} - \imath \cdot \omega \cdot t\right)$, leads acceleration of each electron inducing a dipole moment $\overrightarrow{p} = e \cdot \overrightarrow{r}$. The resulting polarization of the metal is $\overrightarrow{P} = n_f \cdot \overrightarrow{p} = \varepsilon_0 \chi(\omega) \overrightarrow{E}$, whereas ε_0 and $\chi(\omega) = \varepsilon\left(\omega\right) - 1$ are vaccum permittivity and the electric susceptibility respectively. Further, the ratio of the induced dipole moment to the electric field is termed polarizability α, which detrermines the dynamical response of the metal electronic system to the external field by $n_f \alpha = \varepsilon_0 \left(\varepsilon\left(\omega\right) - 1\right)$. In general, the linear response of metals to an electric field with frequency ω is described by the complex dielectric function $\varepsilon\left(\omega\right) = \varepsilon'\left(\omega\right) + \imath\,\varepsilon''\left(\omega\right)$, which is governed by electron transitions in the conduction band and a contribution of interband transitions. The real part of the dielectric function $\varepsilon'\left(\omega\right)$ is related to the stored energy within the medium and is determined by the electric susceptibility $\chi(\omega)$. The imaginary part $\varepsilon''\left(\omega\right)$ is related to the energy dissipation within the medium, which causes a phase shift of the polarization relative to the external electric field. Scattering of electrons results in energy dissipation and contributes to the imaginary part.

The Drude-Sommerfeld model calculates the complex dielectric function from the response of free conduction electrons to the electric field of an incident electromagnetic wave $E\left(\overrightarrow{r},t\right)$. Under the condition of independent electrons the macroscopic response is determined by multiplying the single electron response function with the number of electrons present in the metal. The dielectric function of a metal at given angular frequency ω is then

$$\varepsilon\left(\omega\right) = \varepsilon_\infty\left(\omega\right) - \frac{\omega_p^2}{\omega\left(\omega + \imath\gamma_0\right)} \tag{2.1}$$

with the Drude plasma frequency or Eigenfrequency $\omega_p = \sqrt{n_f\, e^2 / \left(\varepsilon_0\, m^*\right)}$. m^* denotes the effective electron mass and $\gamma_0 = 1/\tau$ is the collision rate with τ being the electron relaxation time. Bound electrons, which contribute to polarizability due to interband transitions, are considered by the additional term $\varepsilon_\infty\left(\omega\right)$.

For wavelengths longer than 680 nm the Drude-Sommerfeld model describes the dielectric properties of gold quite accurate , while at shorter wavelengths an additional contribution of electrons excited from lower energy bands into the conduction band to $\varepsilon''\left(\omega\right)$ is observed.

For calculation of absorption for AuNPs an experimentally determined dielectric function of gold was used. Johnson and Christy obtained values for the refractive index n and the extinction coefficient k of the complex index of refraction, which is related to complex dielectric function by $N(\omega) = n(\omega) + \imath k(\omega) = \sqrt{\varepsilon(\omega)}$ [70]. Figure 2.1 shows the real part and the imaginary part of the dielectric function calculated with the quasi-free-electron or Drude model as well as the experimental data by Johnson and Christy. For all calculations that require the dielectricfunction of gold an interpolation function of the Johnson and Christy data was used throughout this thesis, if not stated differently.

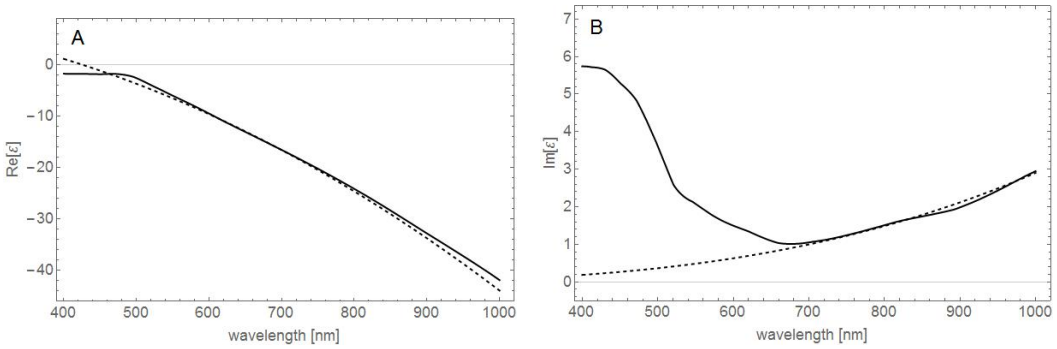

Figure 2.1: Real part (A) and imaginary part (B) of the dielectric function. The experimental data from Johnson and Christy (solid lines) compared to the calculated values using the Drude-model ($\omega_p = 9.1eV/\hbar$, $\gamma_0 = 67meV/\hbar$, $\varepsilon_\infty = 9.84$). Below 660 nm an additional contribution due to the excitation of electrons from the valence band to the conduction band is observed for the absorption of gold.

Based on the permittivity the skin depth δ, which describes the penetration depth of an electromagnetic wave into matter, can be calculated. For a plane wave propagating in direction of z through matter with given complex refractive index the wave vector can be written as $\overrightarrow{k_z} = \overrightarrow{r_z} \cdot |\overrightarrow{k_z}| = \overrightarrow{r}\,(\omega/c)\,(n + \imath k)$ leading to

$$E(\overrightarrow{r}, t) = E_0(\overrightarrow{r_z}, t)\,\exp[\imath \cdot \omega \cdot (n/c \cdot r_z - t)]\,\exp[-r_z/\delta] \tag{2.2}$$

whereas $\delta = c/(\omega \cdot k) = \lambda/(2\pi k)$ is the skin depth. Due to dependency on k, which is the imaginary part of the refractive index or the extinction coefficient respectively, δ depends on the absorption of the metal. The corresponding penetration depth of the light intensity $I \propto |E|^2$ is determined by $\delta_I = c/(2\omega k) = \lambda/(4\pi k)$.

For gold nanoparticles surrounded by water and incident light of the visible and near infrared wavelength range, the penetration depth ranges from 16 to 29 nm (cf. Figure 2.2).

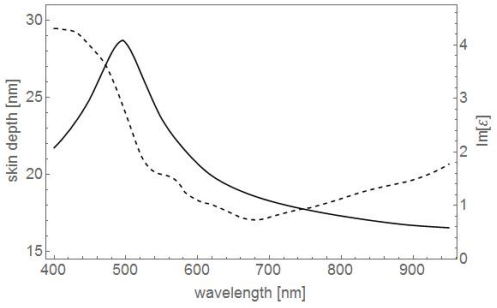

Figure 2.2: Skin depth of a gold nanoparticle surrounded by water and imaginary part of the dielectric function of gold (Johnson and Christy data, dashed line) relative to the refractive index of water. At the onset of interband transitions the penetration depth increases and reaches a maximum of 29 nm for light with a wavelength of 495 nm.

2.1.2 The particle plasmon

An incident electromagnetic wave interacts with a gold nanoparticle by elastic scattering and absorption processes. If the particles are sufficiently small, retardation of the electromagnetic field can be neglected. Absorption and scattering can then be calculated in a simple way by an electrostatic approximation of Maxwell's equations from to the polarizability of the particle.

The conduction band electrons of the nanoparticle response to an incident electric field with a collective displacement relative to the atomic cores of the nanoparticle lattice leading to polarization charges on the surface. Due to Coulomb forces a harmonic oscillation spatially confined to the nanoparticle occurs, which is termed particle plasmon. Figure 2.3 depicts the formation of the particle plasmon schematically.

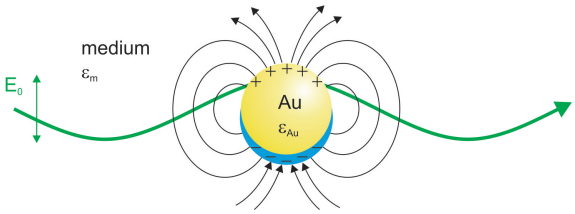

Figure 2.3: Principle model of the formation of a particle plasmon. An incident electric field excites a harmonic oscillation of the quasi-free conduction band electrons of the nanoparticle.

For particles much smaller than the wavelength of irradiation ($R_p \ll \lambda$) the electromagnetic field can be assumed homogeneous over the particle dimensions. Therefore the plasmon acts like an oscillating dipole, which emits comparable to the Hertz dipole an electric field. The polarizability α_{sph} of the sphere, which relates the induced dipole moment to the electric field by $p(\omega) = \varepsilon_m(\omega) \cdot \alpha \cdot E_0$, can be found with help of the Clausius-Mossotti relation

$$\alpha_{sph}(\omega) = 4\pi R_p^3 \varepsilon_0 \frac{\varepsilon_{np}(\omega) - \varepsilon_m(\omega)}{\varepsilon_{np}(\omega) + 2\varepsilon_m(\omega)} \tag{2.3}$$

Thus, the external field is the superposition of the incident field and the field of a dipol centered at the particle. The dipole moment induced by the external field is defined by

$$p = \varepsilon_m 4\pi R_p^3 \varepsilon_0 \frac{\varepsilon_{np}(\omega) - \varepsilon_m(\omega)}{\varepsilon_{np}(\omega) + 2\varepsilon_m(\omega)} E_0, \tag{2.4}$$

whereas $\varepsilon_{np}(\omega)$ and $\varepsilon_m(\omega)$ are the dielectric functions of the nanoparticle and the embedding medium respectively [71, 72, 69].

The amount of energy that is absorbed or scattered from incident irradiation is given by the optical cross-sections σ_{sca} and σ_{abs} respectively. These can than be calculated from the polarizability by [72]

$$\sigma_{sca} = \frac{k^4}{6\pi\varepsilon_0^2} |\alpha|^2 \tag{2.5}$$

$$\sigma_{abs} = \frac{k}{\varepsilon_0} \Im\{\alpha\} \tag{2.6}$$

$$\sigma_{ext} = \sigma_{scat} + \sigma_{abs} \tag{2.7}$$

with $k = 2\pi/\lambda_m$, which is calculated from the irradiation wavelength in vacuum λ_0 by $\lambda_m = \lambda_0/\sqrt{\varepsilon_m/\varepsilon_0}$ for a wave propagating in the host medium with the dielectric function ε_m. The polarizability $\alpha_{sph}(\omega)$ and therefore the scattering and absorption exhibit resonant behavior under the quasistatistic condition, that $|\varepsilon_{np}(\omega) + 2\varepsilon_m(\omega)|$ approaches zero. The small size of the particles is the physical cause of these resonances. The free electrons and positive lattice atoms form an oscillator system. The small size of the particles is the physical cause of these resonances. The free electrons and the positive lattice atoms form an oscillator system in which

the restoring force is given by the polarizability of the particle and the surrounding medium. Nanoparticle diameter and the polarizability influence the spectral position of the resonance band. As seen in the dielectric function (Equation 2.1), scattering of the electrons dampens the oscillation and influences amplitude and spectral width of the resonance band.

2.1.3 The Mie Theory

A general solutions of the interaction of a plane electromagnetic wave with a spherical particle of arbitrary material was published by Gustav Mie [44]. A comprehensive description of the Mie theory can be found in the monographs of van de Hulst (p. 114 - 129) [73], Bohren and Huffman (p. 82 - 123) [72] as well as Kreibig & Vollmer (p. 26 ff) [69]. Following Bohren and Huffman a brief description of the results will be given here.

In order to calculate the extinction of a metal colloid Mie solved the Maxwell equations for a planar electromagnetic wave incident to a spherical particle surface. The scattered wave results from partial waves, which originate from the multipole oscillation within the particle. Internal and the external electromagnetic fields of a spherical particle with radius R_p and complex refractive index n_1 can be expressed by spherical harmonic functions. This multipole expansion of a plane wave to spherical harmonics with the multipole order l contains the scattering coefficients a_l, b_l for the external fields and coefficients c_l, d_l for the inner fields. Under the condition magnetic permeability μ of the particle and the surrounding medium are assumed to be unity the scattering coeffeicients are

$$a_l = \frac{m\Psi_l(mx)\,\Psi_l'(x) - \Psi_l(x)\,\Psi_l'(mx)}{m\Psi_l(mx)\,\xi_l'(x) - \xi_l(x)\,\Psi_l'(mx)} \tag{2.8}$$

$$b_l = \frac{\Psi(mx)\,\Psi_l'(x) - m\Psi_l(x)\,\Psi_l'(mx)}{\Psi(mx)\,\xi_l'(x) - m\xi_l(x)\,\Psi_l'(mx)} \tag{2.9}$$

with the l^{th} order Ricatti-Bessel functions Ψ_l and ξ_l and the derivatives Ψ_l' and ξ_l' to the arguments x and mx respectively. The size parameter $x = 2\pi R_p/\lambda_m$ relates the particle circumference to the incident wavelength and may be also written as product of wave number (propagation constant) k and particle radius R_p so that $x = k \cdot R_p$. m is the relative refractive index, which relates the particle refractive index n_1 to the surrounding medium refractive index n_m so that $m = n_1/n_m = \sqrt{\varepsilon_1/\varepsilon_m}$. The scattering and extinction cross sections result from the energy scattering rate W_{sca} and energy extinction rate W_{ext} referred to incident irradiance I_{in} by

$$\sigma_{sca} = \frac{W_{sca}}{I_{in}} = \frac{2\pi}{|k|^2}\sum_{l=1}^{\infty}(2l+1)\left(a_l^2 + b_l^2\right) \tag{2.10}$$

and

$$\sigma_{ext} = \frac{W_{ext}}{I_{in}} = \frac{2\pi}{|k|^2}\sum_{l=1}^{\infty}(2l+1)\,\Re\left\{a_l + b_l\right\}. \tag{2.11}$$

Under the condition of a non-absorbing medium surrounding the particle its absorption cross section is related to scattering and extinction cross section by

$$\sigma_{ext} = \sigma_{sca} + \sigma_{abs} \tag{2.12}$$

Depending on the particle size either scattering or absorption dominates extinction. According to Equation 2.6 and Equation 2.5 the absorption cross section increases with particle volume while the scattering cross section increases with the square of the volume. For sufficiently small particles ($R_p < 30\,nm$) the absorption contributes predominantly to extinction [74]. Only a dipole oscillation is excited and the Mie theory approaches the electrostatic approximation. Hence, the electrostatic approximation serves as a first estimation, which holds for sufficiently small nanoparticles. With increasing particle size higher oscillation modes are formed, while the scattering amplitude increases. Figure 2.4 illustrates absorption and scattering spectra of spherical particles with different diameters calculated with help of the Mie theory and the dipole approximation respectively.

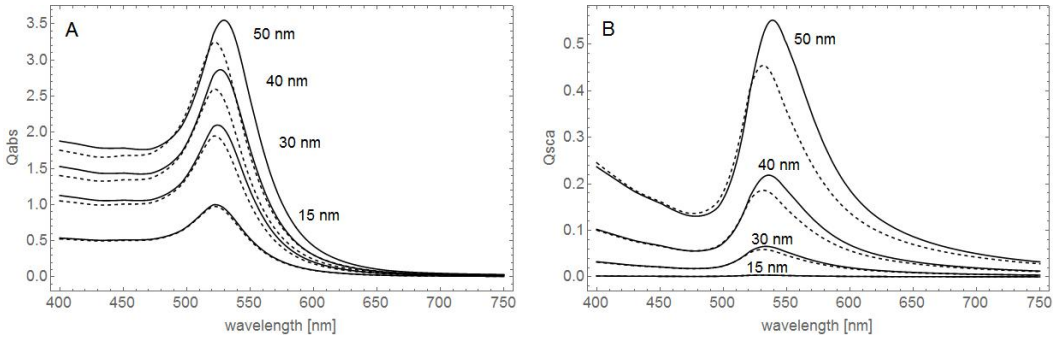

Figure 2.4: Absorption (A) and scattering (B) spectra of gold nanoparticles in water with diameters of 15 nm, 30 nm, 40 nm and 50 nm, calculated by Mie equations (solid lines) and by dipole approximation (dashed lines). The dielectric function of gold measured by Johnson and Christy [70].

Further, efficiency factors Q can be defined by relating the extinction, scattering and absorption cross sections to the particle cross-sectional area πR_p^2:

$$Q = \frac{\sigma}{\pi R_p^2} \tag{2.13}$$

Within the geometrical optics, the efficiency factors of any particle to absorb and deflect an incident beam could not be greater than unity. However, geometrical optics is not a good approximation, if particle dimensions are not considerably larger than the wavelength. Mie theory shows that nanoparticles with dimensions below the wavelength of an incident beam can scatter and absorb much more light than is geometrically incident upon them.

2.1.4 Extension of the Mie theory to core-shell systems

Mie theory can be extended to concentric core-shell structures with arbitrary numbers of shells of arbitrary material [75, 76]. Sinzig et al. developed a recursive formalism, which allows iterative calculation of the scattering coefficients for a multilayered sphere. Following Bohren and Huffmann the absorption and scattering of a gold nanoparticle surrounded by a vapor bubble in aqueous environment can be calculated with help of the scattering coefficients:

$$a_l = \frac{\Psi_l(y)\left[\Psi_l'(m_2 y) - A_l\chi_l'(m_2 y)\right] - m_2\Psi_l'(y)\left[\Psi_l(m_2 y) - A_l\chi_l(m_2 y)\right]}{\xi_l(y)\left[\Psi_l'(m_2 y) - A_l\chi_l'(m_2 y)\right] - m_2\xi_l'(y)\left[\Psi_l(m_2 y) - A_l\chi_l(m_2 y)\right]} \tag{2.14}$$

$$b_l = \frac{m_2\Psi_l(y)\left[\Psi_l'(m_2 y) - B_l\chi_l'(m_2 y)\right] - \Psi'(y)\left[\Psi_l(m_2 y) - B_l\chi_l(m_2 y)\right]}{m_2\xi_l(y)\left[\Psi_l'(m_2 y) - B_l\chi_l'(m_2 y)\right] - \xi_l'(y)\left[\Psi_l(m_2 y) - B_l\chi_l(m_2 y)\right]} \tag{2.15}$$

$$A_l = \frac{m_2\Psi_l(m_2 x)\,\Psi_l'(m_1 x) - m_1\Psi_l'(m_2 x)\,\Psi_l(m_1 x)}{m_2\chi_l(m_2 x)\,\Psi_l'(m_1 x) - m_1\chi_l'(m_2 x)\,\Psi_l(m_1 x)} \tag{2.16}$$

$$B_l = \frac{m_2\Psi_l(m_1 x)\,\Psi_n'(m_2 x) - m_1\Psi_l(m_2 x)\,\Psi_l'(m_1 x)}{m_2\chi_l'(m_2 x)\,\Psi_n(m_1 x) - m_1\chi_l(m_2 x)\,\Psi_l'(m_1 x)} \tag{2.17}$$

$y = 2\pi R_s/\lambda_m$ is the size parameter with regards to the radius R_s of the shell with refractive index $n_2 = \sqrt{\varepsilon_2}$. m_1 and m_2 are refractive indices of the particle and the shell respectively related to the refractive index of the surrounding medium.

2.1.5 Angular distribution of scattering, amplitude function

In addition to the scattering cross section the angle dependent scattering amplitude and further the scattering intensities in the far field for $k \cdot r \ll R_p^2$ can be determined with the help of the Mie coefficients. The scattering plane is defined by the propagation direction of the incident and the scattered wave enclosing the scattering angle θ. The incident electric field E_i encloses a

polarization angle ϕ with respect to the scattering plane. Both, incident and scattered electric field obtain components parallel $\parallel$ and perpendicular $\perp$ referred to this plane. With respect to the components of the incident field $E_{i\parallel} = E_0 \cdot \cos(\phi)$ and $E_{i\perp} = E_0 \cdot \sin(\phi)$, the scattered far field components are

$$E_{s\parallel} = E_{i\parallel} \frac{\exp(\imath(kr - \omega t))}{-\imath kr} \cdot S_2(\cos(\theta)) \tag{2.18}$$

$$E_{s\perp} = - E_{i\perp} \frac{\exp(\imath(kr - \omega t))}{-\imath kr} \cdot S_1(\cos(\theta)) \tag{2.19}$$

with the scattering amplitude functions

$$S_1(\cos(\theta)) = \sum_{l=1}^{\infty} \frac{2l+1}{l(l+1)} \{a_l \pi_l(\cos(\theta)) + b_l \tau_l(\cos(\theta))\} \tag{2.20}$$

$$S_2(\cos(\theta)) = \sum_{l=1}^{\infty} \frac{2l+1}{l(l+1)} \{b_l \pi_l(\cos(\theta)) + a_l \tau_l(\cos(\theta))\} \tag{2.21}$$

Here, the functions $\pi_l(\cos(\theta))$ and $\tau_l(\cos(\theta))$, associated with the Legendre functions $P_l^1(\cos(\theta))$ of the first kind of order 1 and degree n, describe the angular scattering patterns of the spherical harmonics.

$$\pi_l(\cos(\theta)) = \frac{1}{\sin(\theta)} P_l^1(\cos(\theta)) \tag{2.22}$$

$$\tau_l(\cos(\theta)) = \frac{d}{d\theta} P_l^1(\cos(\theta)) \tag{2.23}$$

It follows for scattering in forward direction ($\theta = 0°$) that

$$S_1(0°) = S_2(0°) = \frac{1}{2} \sum_l (2l+1)(a_l + b_l) \tag{2.24}$$

yields in the scattering cross section given by eq. 2.10.
The intensity of a wave is proportional to the square of the electric field amplitude $I = E \bullet E* = |E|^2$, so that for perpendicular and parallel polarization as well as for non-polarized beams the scattered intensity can be obtained by

$$I_{s\parallel} = \frac{|S_2(\cos(\theta))|^2}{k^2 r^2} I_i \tag{2.25}$$

$$I_{s\perp} = \frac{|S_1(\cos(\theta))|^2}{k^2 r^2} I_i \tag{2.26}$$

$$I_s = \frac{I_{s\parallel} + I_{s\perp}}{2} \tag{2.27}$$

2.1.6 Electrostatic approximation for rodshaped nanoparticles

The electrostatic theory for scattering and absorption of spherical particles with diameters much smaller than the incident wavelength has a simple extension to ellipsoidal particles. Ellipsoids with $a > b = c$ are prolate and with $a = b > c$ oblate. Gold nanorods discussed within the the thesis are best approximated by prolate ellipsoids. The major axes of $2 \cdot a$ is referred to as length and the minor axes of $2 \cdot b = 2 \cdot c$ as width. The polarizability of an elliptical shaped particle needs to be extended by a geometrical factor L, which characterizes the depolarization. As a result of the two additional axes of an elliptical particle, two further dipole oscillations can develop. The polarizability of small ellipsoids α_e as well as coated ellipsoids $\alpha_{e,coated}$ are given by [73, 72]:

$$\alpha_e = V \frac{\varepsilon_1 - \varepsilon_2}{\varepsilon_1 + L_L(\varepsilon_1 - \varepsilon_2)} \tag{2.28}$$

$$\alpha_{e,coated} = V_2 \frac{(\varepsilon_2 - \varepsilon_m)(\varepsilon_2 + (\varepsilon_1 - \varepsilon_2)(L_{L,1} - \nu L_{L,2})) + \nu\varepsilon_2(\varepsilon_1 - \varepsilon_2)}{(\varepsilon_2 + (\varepsilon_1 - \varepsilon_2)(L_{L,1} - \nu L_{L,2}))(\varepsilon_m + L_{L,2}(\varepsilon_2 - \varepsilon_m)) + \nu L_{L,2}\varepsilon_2(\varepsilon_1 - \varepsilon_2)} \tag{2.29}$$

with the longitudinal (long axes) depolarization factor L_L for a prolate ellipsoid of eccentricity $e = \sqrt{1-\beta^{-2}}$ calculated from the ellipse aspect ratio β of the length and width ($\beta = a/b$). $\nu = V_1/V_2$ is the ratio of volumes. Parameters with the subscript 1 belongs to the particle core and subscript 2 to the coating material.

$$L_L = \frac{1-e^2}{e^2}\left(\frac{1}{2e}\ln\left(\frac{1-e}{1+e}\right) - 1\right) \tag{2.30}$$

The sum over the three possible depolarization factors L is 1, so that the transversal (short axes) depolarization is $L_T = (1 - L_L)/2$. Oriented ellipsoids possess strongly polarization dependent absorption. The longitudinal and transverse surface plasmon resonance - abbreviated LSPR and TSPR respectively - of the ellipsoids are basically independent and can be excited separately by irradiating with the electric field oscillating parallel to the respective axis. Considering the orientation of a single particle the absorption coefficient is [77]:

$$\sigma_{abs} = k\,\Im\left\{\alpha_L \cos^2(\theta) + \alpha_T\left(1 - \cos^2(\theta)\right)\right\}, \tag{2.31}$$

whereas θ describes the angle between long particle axis and the electric field vector of the incident light. In order to obtain the efficiency factors Q for the ellipsoidal particles the absorption cross section is normalized to the area cross section of an spherical particle with the volume of the ellipsoid. The effective radius of its cross section is $r_{eff} = \left(a \cdot b^2\right)^{1/3}$ [78, 79].

Figure 2.5 illustrates the shift of the absorption maximum to longer wavelengths with increasing aspect ratio of the ellipsoid axes. In the calculations for ellipsoids multipole oscillations were neglected. If the particle exceeds a certain size, also a red shift in the longitudinal resonance peak wavelength is observed additionally to the increase of the absorption and FWHM of the LSPR band. Applying the quasi static approximation only the increase in absorption efficiency can be described. Higher orders retardation effects become also more important for larger aspect ratios. These effects are not considered by the depolarization factor L, which is introduced to extend the polarizability.

The effect of different polarization angles is depicted in Figure 2.6. The absolute value of the longitudinal absorption band reaches a maximum for parallel polarization with the long axes at $\theta = 0°$. For polarization along the short axis ($\theta = 90°$) the longitudinal absorption vanishes. The peak wavelength of the longitudinal absorption does not change with the polarization.

Considering randomly oriented ellipsoids the polarizability is equal to the average over the three principle polarizabilities given by $\langle\alpha\rangle = \frac{1}{3}\alpha_L + \frac{2}{3}\alpha_T$ [72, page 152].

An exact calculation and for arbitrarily shaped particles numerical and finite element methods have been developed:

- T-Matrix method
- Extended Boundary Condition Method
- Finite-Difference-Time Domain (FDTD)
- Multiple Multipole Approximation (MMA)
- Discrete Dipole Approximation (DDA)

A review of these methods can be found in [80].

Kooij and Poelsema have investigated the influence of size and geometrical shape on the optical properties of randomly oriented metallic nanorods with the help of the DDA [79]. They considered ellipsoidal as well as cylindrical geometries. Absorption spectra calculated for prolate

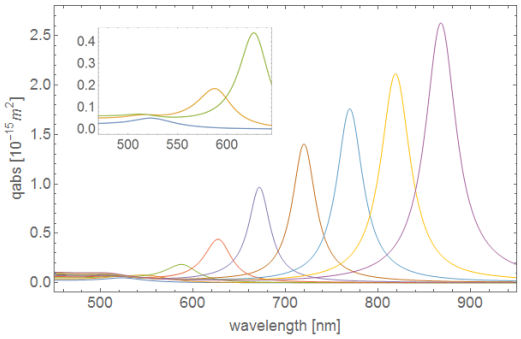

Figure 2.5: Absorption spectra of randomly oriented prolate ellipsoids with the aspect ratios between $\beta = 1$ and $\beta = 5$. With increasing aspect ratio the LSPR shifts to longer wavelength. As a result of the increasing particle volume, the absorption increases. The inset shows the absorption spectra for nanorods with aspect rations $\beta = 1$, $\beta = 2$ and $\beta = 2.5$, whereas the absorption spectrum for $\beta = 1$ is equal to the absorption of a spherical particle.

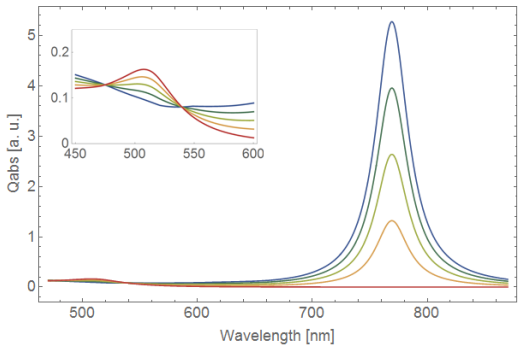

Figure 2.6: Absorption spectra of a prolate ellipsoids with the small radius of 5 nm and $\beta = 4$ depending on the angle between the incident electric field vector and the major axes. From $\theta = 0°$ (blue) to $\theta = 90°$ (red).

ellipsoids with the quasistatic approximation differ from the DDA calculations and the deviation increases with the aspect ratio: the DDA calculated LSPR peak shifts to longer wavelength and the band becomes lower and broader. The LSPR peak of cylinders shifts even further to the red ($\Delta\lambda \approxeq 50 - 75\,nm$) and the extinction efficiency increases as compared to the peak position shift calculated for ellipsoids. A cylinder has, in comparison to an ellipsoid of same length and width, more matter at the ends, which leads to a larger "effective" aspect ratio. DDA calculations exhibit additional red shift and broadening of the LSPR peak with increasing size at constant aspect ratio. These observations are in agreement with the conclusion that higher order multipoles contribute to the optical characteristics for larger nanorods. Nevertheless, Kooij and his co-workers found, that the experimentally determined LSPR peak was located in between that of the calculated absorption spectra for ellipsoids and cylinders. In order to correct the LSPR peak shift and band broadening, which were calculated for cylindrical nanoparticles by the dipol approximation, Prescott and Mulvaney have determined factors, which can be found in [81].

2.1.7 Influence of the refractive index of medium and a supporting substrate

Spectral position and shape of a particle plasmon resonance band depend on both, the local dielectric function of the nanoparticles material and the hosting medium. Equation 2.3 shows the influence of the medium on the polarizability of the particle. For a constant value of the surrounding dielectric function and thus a constant refractive index $\varepsilon_m = n_m^2$ the dielectric function of the nanoparticle material determines the spectral shape and position of the resonance peak. Considering for a gold nanoparticle an increase in the refractive index of the medium leads to a shift to longer wavelengths. In addition, a strong increase of the scattering cross

section occurs due to decreasing plasmon damping related to the imaginary part of the gold dielectric function.

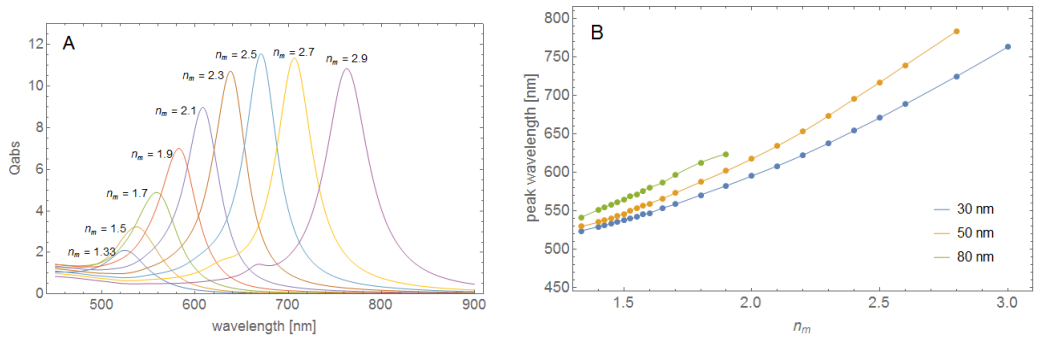

Figure 2.7: (A) Absorption spectra of gold nanoparticles with 30 nm diameter for different refractive index of the hosting media. (B) The absorption peak shifts to longer wavelengths with increasing refractive index of the surrounding medium (blue 30 nm AuNP, yellow - 50 nm AuNP and green - 80nm AuNP).

Nanoparticles experience inhomogeneous refractive index in their surrounding due to the interface. For calculating absorption and scattering the definition of an effective refractive index n_{eff} by

$$n_{eff} = g \cdot n_m + (1 - g)\, n_{sub} \tag{2.32}$$

was successfully used. g is an appropriate weighting factor. First attempt to account for a supporting substrate was described by Kreibig and Vollmer [69]. Curry et al. experimentally observed for silver particles bound to a silanated glass substrate changes in the plasmon resonance due to induced variations in the local refractive index [82]. They analyzed the shift in the plasmon resonance and applied the simple weighting of the contributions from the substrate and the environment in Equation 2.32.

2.2 Laser induced heating of gold nanoparticles

2.2.1 Thermalization of a gold nanoparticle

The temperature increase in gold nanoparticles by pulsed laser irradiation depends on its optical properties and heat diffusion. The short laser pulse couples to the conduction band electrons of a metal nanoparticle and excites a particle plasmon. This excitation process involves only a fraction of the electrons. Within 10 fs the plasmon decays radiatively [83] and mostly non-radiatively [84], whereas only the non-radiative decay contributes to particle heating [85, 74]. Due to inter- and intraband processes, which involve electron-electron scattering in the particle, the excited electrons thermalize within 500 fs [86] to 1 ps [87]. For particle diameters below 10 nm electron-surface scattering contributes to thermalization as well. The thermalized electrons heat the particle lattice by electron-phonon coupling. Within a time span of 10 ps the nanoparticle lattice reaches thermal equilibrium.

Heat transfer from the nanoparticle to the surrounding medium takes place on a scale of hundred picoseconds to nanoseconds. Depending on the pulse duration the heat transfer will begin after irradiation is completed or while irradiation still takes place. Also, the thermal coupling of the nanoparticle to the surrounding across a boundary layer affects the heat transfer to environment. Increased temperature may cause phase changes of the surrounding water and lead to cavitation bubbles. Figure 2.8 depicts schematically the thermalization of the nanoparticle and the heat diffusion to the environment that may lead to formation of a vapor bubble.

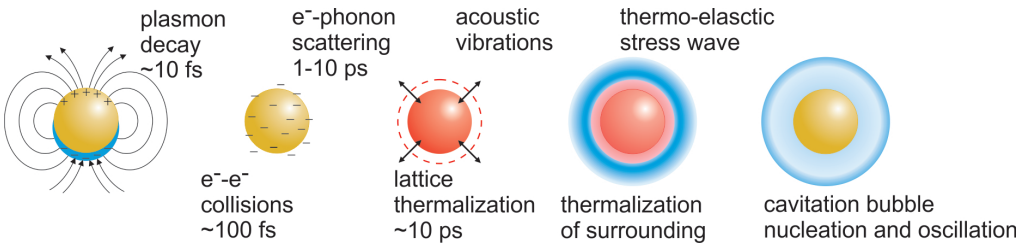

Figure 2.8: Processes in and around a gold nanoparticle upon pulsed laser excitation.

2.2.2 Heat conduction on the nanoscale

A homogeneous temperature distribution within the nanoparticle lattice will be reached after the thermalization time $\tau_{T,p}$ approximated by

$$\tau_{T,p} = R_p^2/4\alpha_p. \tag{2.33}$$

Here, α_p denotes the thermal diffusivity of the nanoparticle material [24]. The thermal diffusivity α relates the thermal conductivity κ of a substance to its specific heat capacity c and density ρ. Comparable to the duration of thermal relaxation within the nanoparticle the thermalization time $\tau_{T,l}$ is defined as the time constant for the thermal balancing processes of the particle with its surroundings. Also referred to as thermal confinement, it can be approximated by

$$\tau_{T,l} = R_p^2/4\alpha_m. \tag{2.34}$$

Here, α_m denotes the thermal diffusivity of the surrounding medium [24]. However, a layer surrounding the spherical nanoparticle with the thickness of thermal diffusion length $l_d = \sqrt{\alpha_m \tau_d}$ causes cooling of the nanoparticle. Considering ideal thermal coupling between the nanoparticle and the surrounding a diffusive heat transfer to the medium can be assumed and allows for estimation of the cooling time τ_d by equating the heat capacity of the particle with the heat capacity of the layer with thickness l_d, $\frac{4}{3}\pi R_p^3 c_p \rho_p = 4\pi R_p^2 l_d c_l \rho_l$ [88]. This leads to

$$\tau_d = \frac{R_p^2}{3^2} \frac{(\rho_p c_p)^2}{\rho_l c_l} \frac{1}{\kappa_l} \tag{2.35}$$

with the specific heat capacities c, densities ρ and thermal conductivities κ for the liquid (l) and the particle (p). According to Equation 2.35 an irradiation with nanosecond pulse duration ($\tau_L > 500\,\mathrm{ps}$) exceeds thermal confinement of a nanoparticle with 10 nm diameter.

However, due to phonon scattering at material borders such as the particle-medium interface a finite temperature discontinuity occurs. The impedance, also known as Kapitza impedance occurs especially, if the mean free path of the phonons is larger than the particle dimensions and at large heat flows across the interface. In case, that heat diffusion in the surrounding medium is faster than the diffusion across the interface, the cooling time is controlled by the interface thermal conductance. With the help of the equation $V\, c_p \rho_p = S \cdot G \cdot t_{d,g}$ [88], which relates the heat conductivity of the nanoparticle to the total conductance of the particle-medium interface, the cooling time is approximated by

$$\tau_{d,G} = \frac{R_p \rho_p c_p}{3G}. \tag{2.36}$$

V is the particle volume, S the particle surface area and G the thermal conductance of the interface layer of infinitesimal thickness. At an interface conductance of $105\,\mathrm{MW\,m^{-2}\,K^{-1}}$, which was determined for gold nanoparticles, [89] the cooling time for a 10 nm sphere increases from 10 ps to approximately 80 ps. Nevertheless, considering the irradiation pulse durations τ_L>500 ps used for the experimental investigations in this thesis the thermalization of the particle can be assumed instantaneous and homogeneous, which is the initial condition for the analytical description of the heat transfer.

Equating τ_d and $\tau_{d,G}$ allows to define a critical value of the interface conductance G of equal contributions of diffusive heat distribution and interface conductance controlled heat diffusion:

$$G_c = 3\kappa_l \frac{(\rho_l\, c_l)^2}{\rho_p\, c_p} \cdot \frac{1}{R_p}$$

For gold nanoparticles with radii in the range between 5 and 50 nm the critical interface conductivity ranges between 60 and 600 $\mathrm{MW\,m^{-2}\,K^{-1}}$.

2.2.3 Temperature increase by energy deposition with pulsed laser irradiation

The transfer of the laser pulse energy to the particle occurs below 10 ps and transfer to the surrounding in the range of 100 ps. Due to high thermal conductivity of the free electrons heat transport within the particle is significantly faster than heat transfer into the environment via phonon-phonon coupling. Thus, for the calculation of the spatio-temporal temperature increase the temperature inside the nanoparticle can be assumed homogeneously.

In order to describe the temperature increase inside and around the particle, two coupled differential equations are introduced. The first one is a continuity equation, which expresses the continuous change of thermal energy due to the flow across the boundary layer (Equation 2.37). As described by the Fourier law the flux is proportional to the particle surface, the difference of temperature across this area and the thermal conductivity G of the boundary layer. The second equation describes the Newtons law of heat transfer as flux in the medium as a result of the spatial derivation of the temperature (Equation 2.38).

When the particles are spherical, the differential equations can be transformed to a one dimensional problem. In the following equations the previously introduced nomenclature for the material properties is used and completed by introducing the particle mass m_p. The derivation of the analytical description of heat dissipation follows [90].

$$m_p c_p \frac{d}{dt} T_p(t) + 4\pi R^2 G \left(T_p(t) - T_l(r = R_P, t)\right) = 0 \tag{2.37}$$

$$\left[\frac{\partial}{\partial t} T_l(r,t)\right]_{r=R} + \frac{G}{K}\left(T_p(t) - T_l(r = R_P, t)\right) = 0 \tag{2.38}$$

with the heat diffusion coefficient of the surrounding medium $K = \kappa_l \cdot \rho_l \cdot c_l$. The particle temperature $T_p(t)$ is independent from location within the nanoparticle, because a homogeneous temperature distribution is assumed. $T_l(r,t)$ denotes the temperature of the surrounding medium. Temperature dependencies of the thermal parameters K, G, κ, ρ and c are neglected.

The boundary condition proposes a linear heat transfer across the surface. In case of a vanishing interface conductance G ($G \to 0$), the nanoparticle is thermally isolated. In the opposite case, when the surface is no barrier for the heat transfer($G \to \infty$), surface temperature inside and outside the particle are the same ($T_p(t) = T_l(r = R_P, t)$). Carslaw and Jaeger propose the solution of the differential equations by Laplace transformation, which leads to the following expressions :

$$m_p c_p \left(s\tilde{T}_p(s) - T_p^*\right) + 4\pi R^2 G \left(\tilde{T}_p(s) - \tilde{T}_l(r = R, s)\right) = 0 \tag{2.39}$$

$$\left[\frac{\partial}{\partial s} \tilde{T}_l(r,s)\right]_{r=R} + \frac{G}{K}\left(\tilde{T}_p(s) - \tilde{T}_l(r = R, s)\right) = 0 \tag{2.40}$$

This is possible considering energy deposition within the nanoparticle with laser pulse duration that meet the thermal confinement conditions. s denotes the time-conjugated variable in the Laplace domain. The temperature increase after a Dirac pulse deposition yields to the initial condition $T_p^* = T_p(t = 0)$. All calculated temperatures are increases with respect to an initial temperature T_0. The solution of these two equations with the unknown particle and surrounding medium temperature as functions of place and time is also given in Carslaw's and Jaeger's work by:

$$\tilde{T}_l(r > R, s) = \frac{A}{r} \cdot \exp\left(\sqrt{\frac{s}{\kappa}} \cdot (r - R)\right) \tag{2.41}$$

The amplitude A of the exponential function is determined by applying this approach to Equation 2.40 in the Laplace domain and is proportional to T_p^*. Appropriate substitution with $u = T \cdot r$, which results from the reduction of radial to a one-dimensional problem, and inverse Laplace transform leads to an exponential function of particle temperature within an integral. The variable of integration results from the substitution within the region from zero to infinity:

$$T_p\left(r < R_p, t\right) = \frac{2kR^2g^2T_p^*}{\pi} \cdot \int_0^\infty \frac{u^2 \exp\left(-\frac{\kappa \cdot u^2 \cdot t}{R^2}\right)}{\left(u^2\left(1 + R \cdot g\right) - k \cdot R \cdot g\right)^2 + \left(u^3 - k \cdot R \cdot g \cdot u\right)^2} du \tag{2.42}$$

$$\text{with}\, k = \frac{4\pi R^3 \rho_l c_l}{m_p c_p}\,,\; g = \frac{G}{K}$$

The dimensionless constant k and g, which reflects the ratio of the heat conductivity G of the interface and K of the surrounding medium, are introduced for compactness of the formulas. Equation 2.42 represents the solution to the Equations 2.39 and 2.40, which allows for calculation the nanoparticle temperature over time. This solution also serves as initial condition for the solution of the differential equations, which allows for calculation of the surrounding medium temperature at $\mathrm{r = R_p}$ over time:

$$\begin{aligned} T_l\left(r = R, t\right) = {} & \frac{2\,k\,R^2g^2T_p^*}{\pi} \cdot \int_0^\infty \frac{u^2 \exp\left(-\frac{\kappa \cdot u^2 \cdot t}{R^2}\right)}{\left(u^2\left(1 + R \cdot g\right) - k \cdot R \cdot g\right)^2 + \left(u^3 - k \cdot R \cdot g \cdot u\right)^2} du \\ & - \frac{m_p c_p k\, g^2 T_p^*}{2\pi^2 R^2 G} \cdot \int_0^\infty \frac{\frac{\kappa \cdot u^4}{R^2} \exp\left(-\frac{\kappa \cdot u^2 \cdot t}{R^2}\right)}{\left(u^2\left(1 + R \cdot g\right) - k \cdot R \cdot g\right)^2 + \left(u^3 - k \cdot R \cdot g \cdot u\right)^2} du \end{aligned} \tag{2.43}$$

The particle is considered an instantaneous point source of heat, which produces a temperature distribution with an exponential decay. The second term is the decay, which is caused by the thermal impedance of the boundary layer defined on the particle surface for distance $r = R_p$.

The temperature distribution in the medium $r > R_p$ is described by the error function. Substitution with the integration variable μ leads furthermore to a change in integration boarders:

$$T_l\left(r > R, t\right) = \frac{2R}{r\sqrt{\pi}} \int_{(r-R)/2\sqrt{\kappa t}}^\infty T_l\left(r = R, t - \frac{\left(r - R\right)^2}{4\kappa\mu^2}\right) \cdot \exp\left(-\mu^2\right) d\mu \tag{2.44}$$

This analytical description of heat conduction is only valid for homogeneous media.

Irradiation of a particle with the absorption cross section σ_{abs} and volume V_p with radiant exposure H results in the Dirac pulse shaped temperature increase by T_p^*.

$$T_p^* \quad = \quad \frac{\sigma_{abs} \cdot H}{\rho_p \cdot V_p \cdot c_p} \tag{2.45}$$

2.2.4 Temperature increase by energy deposition with quasi continuous laser irradiation

In case the laser pulse duration exceeds the thermal confinement, heat transfer takes place while irradiation is not completed. Following temperature increase at continuous irradiation (cw mode) is calculated within the irradiation at a steady state of energy absorption and heat flow to the surrounding of the particle will be established. At initial time point $t = 0$ the particle and surrounding have equal temperature, for $t > 0$ a constant heating energy is supplied.

$$m_p \cdot c_p \cdot \frac{d}{dt} T_p\left(t\right) + 4 \cdot \pi \cdot R^2 \cdot G\left(T_p\left(t\right) - T_l\left(r = R, t\right)\right) = Q \tag{2.46}$$

$$\left[\frac{\partial}{\partial t} T_f\left(r, t\right)\right]_{r=R} + \frac{G}{K} \cdot \left(T_p\left(t\right) - T_l\left(r = R, t\right)\right) = 0 \tag{2.47}$$

The first differential equation (Equation 2.39) is expanded by the term Q, which characterizes the delivered heat energy. The second differential equation remains unmodified compared to the Dirac pulse excitation since it describes the heat flow from a view point outside the particle. The equations are also solved in the Laplace domain for the particle temperature and the distribution in the surrounding fluid:

$$T_p(t) = \frac{Q(1+Rg)}{4\pi R^2 K g} - \frac{Q R k^2 g^2}{2\pi^2 K} \cdot \int_0^\infty \frac{\exp\left(-\frac{\kappa \cdot u^2 \cdot t}{R^2}\right)}{\left(u^2(1+R\cdot g) - k\cdot R\cdot g\right)^2 + \left(u^3 - k\cdot R\cdot g\cdot u\right)^2} du \quad (2.48)$$

$$T_l(r=R,t) = \frac{m_p c_p}{4\pi R^2 G}\frac{d}{dt}T_p(t) + T_p(t) - \frac{Q}{4\pi R^2 G} \quad (2.49)$$

$$T_l(r>R,t) = \frac{2R}{r\sqrt{\pi}} \int_{(r-R)/2\sqrt{\kappa t}}^\infty T_l\left(r=R, t-\frac{(r-R)^2}{4\kappa\mu^2}\right)\cdot \exp\left(-\mu^2\right) d\mu \quad (2.50)$$

Under stationary conditions, which establish at a certain time after the begin of irradiation, the heat flow into the medium equals the optically absorbed irradiation. Thus, the temperature increase is primarily determined by the particle absorption.

2.2.5 The use of the convolution theorem

The solution of the differential equations 2.37 and 2.38 describes the temperature response to an incident Dirac pulse. In order to calculate the temperature for an arbitrary shaped pulses the temperature response to a Dirac pulse is convolved with the time function of the incoming pulse. For this mathematical treatment of the heat conduction it is prerequisite, that the thermal behavior of the nanoparticle is linear and time-invariant. These conditions are met for a system with linear differential equations with time independent parameters.

As a result of convolving the normalized laser pulse function $f(t)$ with the solution of heat distribution $T(r,t)$ according to Equations 2.42 to 2.44 the temperature response $T_{pulse}(r,t)$ to a finite and arbitrarily shaped laser pulse is determinable by

$$T_{pulse}(r,t) = T(r,t) \otimes f(t) \quad (2.51)$$

with

$$\int_0^\infty f(t)\,dt = 1\frac{mJ}{cm^2} \quad (2.52)$$

This convolution results in the temperature increase ΔT with respect to the normalized fluence of 1 mJ/cm^2, while the radiant exposure is considered in the calculation of T_p^* used to calculate the temperature response $T(r,t)$. The heat distribution at a location with distance r from the particle center can be calculated as a function of time. Figure 2.9 shows the temperature increase in an AuNPs with 50 nm diameter and the surrounding liquid at $r = R_p$ for a 532 nm Gaussian shaped irradiation with pulse durations of 800 ps and 4 ns. Absorption was calculated with the help of the Mie coefficients and an interface conductance of $G = 105\,MW\,m^{-2}\,K^{-1}$ was assumed. These conditions will be applied in all the further calculations and specified explicitly if different conditions apply.

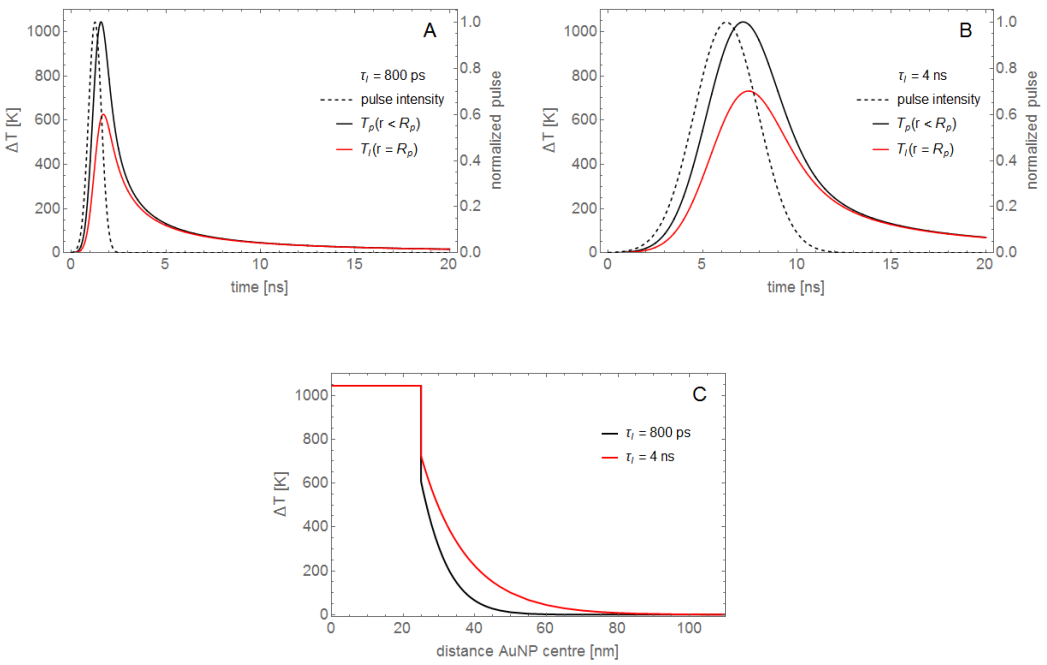

Figure 2.9: Temperature increase within (black) and around (red) pulsed laser irradiated gold nanoparticles. AuNP with 50 nm diameter under pulsed irradiation with (A) 800 ps, 6.83 mJ cm^{-2} and (B) 4 ns, 15.81 mJ cm^{-2} at a wavelength of 532 nm. The assumed pulse shape is shown as a dotted line. For both irradiations, a temperature increase of 1043 K with respect to room temperature at 293 K was calculated for the AuNP. (C) Spatial distribution of the temperature increase at specific time of maximum particle temperature for irradiation pulse duration of 800 ps (black) and 4 ns (red).

2.2.6 Thermoelastic pressure wave

The thermodynamic state of a body is described by its pressure, volume and temperature. A change in volume of a body with a constant number of atoms can be caused by variations of temperature or pressure. The relative volume change can be described as a linear combination of volume changes due to changes in pressure and temperature [91, 92].

$$\frac{dV}{V} = \frac{1}{V}\left(\frac{\partial V}{\partial p}\right)_T \cdot dp + \frac{1}{V}\left(\frac{\partial V}{\partial T}\right)_p \cdot dT$$

The first term describes the (isothermal) compressibility and the second term the (isobar) thermal expansion.

As a consequence of a rapid temperature increase the gold nanoparticle volume increases and generates thermoelastic pressure waves in the surrounding medium. The acoustic confinement time and the laser pulse duration determine the amplitude and frequency range of the wave. The acoustic confinement is determined by the transit time of a wave through the nanoparticle given by

$$\tau_{ac,p} = \frac{2R_p}{\nu_f}. \tag{2.53}$$

ν_f denotes the sound velocity within the given medium. For an AuNP with radius between 5 nm and 50 nm the acoustic confinement ranges from 3 ps to 30 ps. For irradiation with pulse duration above acoustic confinement time, a pressure wave is emitted during the incident irradiation pulse. Kahn and Diebold described thermoelastic waves generated by a Q-switched laser excited single particle [93]. They showed that the temporal profile of the emitted pressure wave is also determined by the geometry of the particle and its acoustic properties, the density and speed of sound relative to those of the surrounding fluid. Heat diffusion and viscosity of

the surrounding medium can damp the thermo-elasic pressure wave [94]. Excitation with a Gaussian shaped laser pulse

$$I(t) = \frac{H}{\Theta\sqrt{\pi}} \exp\left[-\left(\frac{t}{\Theta}\right)^2\right]$$

with irradiation H and a pulse duration $\Theta_{laser} = \tau_L/\sqrt{4Ln\,(2)}$ (full width at half maximum) above the acoustic confinement ($\tau_L \gg \tau_{ac}$) leads to a pressure wave amplitude of [24]

$$p_{TE}(r \geq R_p, t) = \mu_{abs} \cdot H \cdot \Gamma \cdot \frac{2}{3\sqrt{\pi}} \cdot \frac{\rho_f}{\rho_p} \cdot \left(\frac{\tau_{ac}}{2\Theta_{laser}}\right)^3 \cdot \left(\frac{\nu_{p,l}}{\nu_{f,l}} - \nu_{p,l} \cdot \frac{t}{r}\right) \cdot \exp\left[-\left(\frac{t - \frac{r}{\nu_{f,l}}}{\Theta_{laser}}\right)^2\right] \tag{2.54}$$

with he Grüneisen parameter Γ

$$\Gamma = V\left(\frac{dP}{dE}\right)_V = \frac{\beta_p \nu_{p,l}^2}{c_p}.$$

$r \geq R_p$ is the distance from the nanoparticle center, μ_{abs} denotes the effective volumetric absorption coefficient of the gold nanoparticle and the Grüneisen parameter Γ summarizes the dependency of the pressure wave on the volume expansion β_p, the longitudinal sound velocity $\nu_{p,l}$ and the specific heat capacity c_p of the nanoparticle. The indices p and f denote properties of the nanoparticle and the surrounding fluid respectively. Equation 2.54 neglects shear waves, which cannot propagate in liquids. The absorption coefficient for a gold nanoparticle is approximated by

$$\mu_{abs} = \frac{\sigma_{abs}}{V_p} = \frac{3Q_{abs}}{4R_p}.$$

The thermoelastic pressure wave travels in radial symmetry from the nanoparticle and follows the derivation with time of irradiation pulse, while the peak amplitude increases linearly with radiant exposure as shown in Figure 2.10.

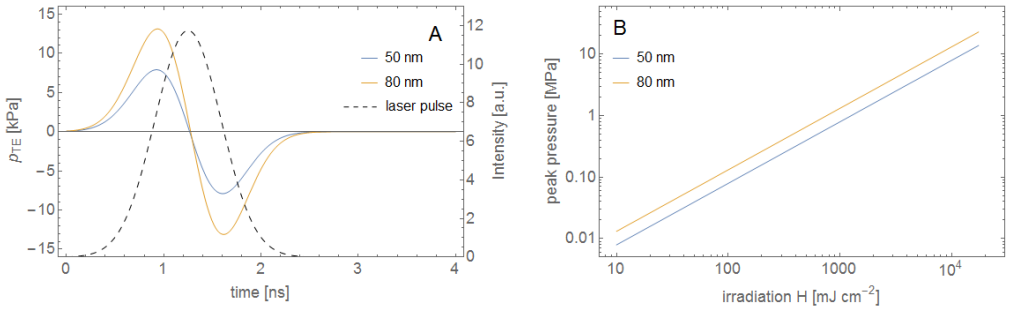

Figure 2.10: (A) The amplitude of a thermoelastic pressure wave (solid line) follows approximately the derivation of the irradiation pulse (dashed line) with respect to time. (B) The peak ampliude increases linearly with irradiation. Pressure wave were calculated for AuNPs with 50 nm and 80 nm diameter under 800 ps pulsed irradiation at a wavelength of 532 nm.

2.2.7 Phase transition, spinodal decomposition, bubble formation and cavitation

Besides the emission of thermoelastic pressure waves the temperature increase of a laser irradiated gold nanoparticle can lead to abrupt vaporization of the surrounding liquid. Depending on the heating rate, which relates temperature increase to duration of the thermal energy supply, different processes can cause phase transition of the water. If water is heated under normal conditions ($p_{norm} = 0.1$ MPa, $T_{norm} = 273$ K) to its evaporation temperature ($T_{vap} = 373$ K),

spontaneous liquid-vapor transition may occur forming vapor bubbles within the liquid, also referred to as boiling.

At higher heating rate, which is established under short pulsed irradiation of a nanoparticle (cf. Chapter 2.2.3), water can be heated under normal conditions to temperatures above the evaporation temperature where it forms a metastable state. The temperature at the critical point of water is the upper limit of the metastable state. In experiments with heating rates around $10^7\,\mathrm{K\,s^{-1}}$ [95] and $10^{11}\,\mathrm{K\,s^{-1}}$ [6] a rapid liquid-vapor transition, also termed as explosive evaporation or phase explosion [96], was observed for a water temperature in the ranging between 80 % and 90 % of the critical point of water.

In the case of a gold nanoparticle under short pulsed irradiation heating is confined to a volume with few nanometer radius around the nanoparticle. The phase transition within the layer of liquid around the nanoparticle involves spinodal decomposition and leads for sufficient irradiation to bubble formation and expansion to the microscale.

The liquid-vapor phase transition

The thermodynamic state of a system can be described by the thermodynamic potentials internal energy U, Helmholtz free energy F, enthalpy H and Gibbs free energy G. Each one provides the complete description of a thermodynamic system [97]. Properties such as heat capacities as well as transport variables such as transferred heat Q and work W can be obtained by partial derivations of the potentials with respect to state variables entropy S, pressure p, volume V or temperature T.

Helmholtz energy and the Gibbs free energy are measures of a thermodynamic system based on the state variables T, V and p:

$$F(T) = U - T \cdot S$$
$$G(p, V, T) = U + p \cdot V - T \cdot S$$

The Gibbs free energy, also referred to as free enthalpy, exhibits local minima and maxima for stable and instable equilibria respectively (cf. Figure 2.11). At the saturation temperature the free enthalpy forms two minima of equal magnitude located at specific volumes corresponding to the liquid and the gaseous phase [98]. Thus, both phases can coexist equally separated by a local maximum of Gibbs free energy. This barrier is exceeded by a first-order phase transition from one stable state to the other requiring enthalpy of vaporization, which is also referred to as latent heat of vaporization. In a first-order phase transition, the first derivative of the Gibbs free energy is discontinuous across the phase boundary, which can be observed in a discontinuous change in volume and entropy.

For increasing temperature the local minimum of the liquid phase vanishes and the change from liquid to vapor happens instantaneously. This phase transition exhibits a continuous change in volume and entropy and is also referred to as a second-order phase transition.

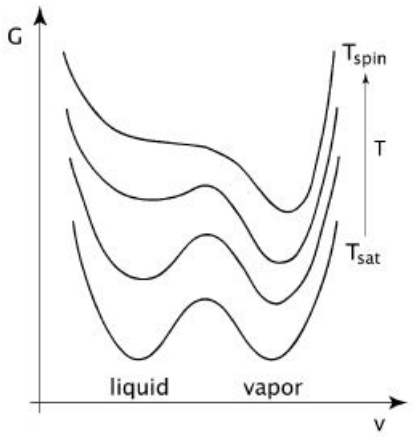

Figure 2.11: Gibbs free energy vs. specific volume. Reproduced from [1], with the permission of ACS Publishing.

In the p-T-projection of the phase diagram (cf.2.12) the system normally moves with increasing temperature along the liquid-vapor equilibrium curve, the binodale or saturated liquid/vapor line. But the liquid can exceed this saturation temperature and transcend to a metastable state. The thermodynamic stability boundary of the metastable state is determined by the second derivatives of the Gibbs thermodynamical potential by$(\partial p/\partial V)_T = 0$ and $(\partial T/\partial S)_p = 0$, which is known as spinodal [96]. A liquid-vapor phase transition across the liquid spinodal, which results from isotropic tensile stresses under isothermal conditions, is also known as cavitation [99].

Both, the superheated liquid as well as the subcooled vapor phase become unstable at the spinodale. Since for bubble formation around heated gold nanoparticles the liquid vapor transition alone is relevant the solid phase of water and the condensation processes related spinodal of saturated vapor will be omitted in further descriptions. The upper temperature and pressure limit of distinct phases is determined by the critical point, which is at the same time the upper limit of the spinodals of saturated liquid and saturated vapor as well as the binodale.

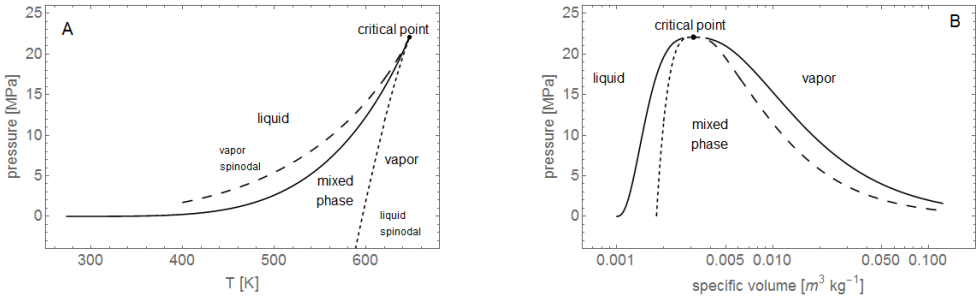

Figure 2.12: Projections of the phase diagram of water (A) the p-T-diagram and (B) the p-v-diagram. The binodale (solid), the liquid spinodal (dashed) and the vapor spinodal (long dashed).

Spinodal decomposition and bubble nucleation

Close to the spinodal already small pressure or temperature fluctuations can result in large density variation and vice versa, small density fluctuation can lead to large pressure variations as well. In particular, when reaching spinodal temperature the Gibbs free energy minimum corresponding to the liquid phase becomes small as such that a spontaneous fluctuation causes transition to the vapor phase. This phase separation can form a vapor cavity in the liquid accompanied by a strong pressure increase in the vapor phase, i. e. $p = 9.2\,\mathrm{MPa}$ for water at

atmospheric pressure [1]. Driven by the pressure the vapor expands explosively, hence the term phase explosion.

A phase transition at the spinodal causing formation of a vapor cavity in the superheated liquid can occur on a time scale ranging between 15 ps and 300 ps, which was experimentally found by Miotello et al. [100]. The lifetime of the metastable state decreases with temperature. Thus, superheat temperature and the extend of the incursion in the metastable region strongly determine the probability of its instantaneous collapse or the cavity growth respectively. In order to describe the phase transformation process as the water approaches the spinodal limit in more detail, homogeneous nucleation needs to be considered. Since classical nucleation theory has been developed extensively in numerous works a brief description of a one component system shall be sufficient.

The spontaneous formation of vapor cavities within superheated liquid caused solely by a small variation of the thermodynamic potential $\Delta G = \Delta\left(U - T_l S - p_l V\right)$ and is therefore referred to as homogeneous nucleation. Assuming transition at constant temperature the work to form a nucleus with volume V_v and a vapor-liquid interface with a surface area A_v against the water tension σ_l can be calculated from the difference between Gibbs free energy of the liquid phase (G_l) and the vapor phase (G_v) by

$$\Delta G = G_v\left(p_v\right) - G_l\left(p_0\right) - \left(p_v - p_0\right) V_v + A_v \sigma_l$$

with the liquid under total hydrostatic pressure p_0 and the vapor pressure p_v inside the nucleus. The vapor inside the spontaneously formed nucleus is in thermodynamic equilibrium with the surrounding metastable liquid ($G_v\left(p_v\right) = G_l\left(p_0\right)$). Thus, the chemical potential of the vapor and the liquid molecules are equal and the nucleus is formed under isothermal conditions. For isotropic σ_l the Gibbs free energy or work respectively required to form a nucleus of radius R_b, while the total hydrostatic pressure remains at p_0 and the vapor pressure p_v inside the cavity leading to $\Delta p = p_0 - p_v$, is given by [97]

$$\Delta G = \frac{4}{3}\pi R_b^3 \Delta p + 4\pi R_b^2 \sigma_l \tag{2.55}$$

Because the pressure difference scales with the volume of the nucleus and the contribution of surface tension scales by the vapor-liquid surface area, the free Gibbs energy will increase with radius of the vapor nucleus. For the condition $d\Delta G/dR = 0$ a maximum energy E_b representing the barrier impeding vapor bubble growth can be found for a radius termed critical radius R_c as determined by

$$E_b = \frac{16\pi}{3}\frac{\sigma_l^3}{\Delta p^2} \tag{2.56}$$

$$R_c = 2\sigma_l/\Delta p \tag{2.57}$$

For R_c the surface energy of the nucleus will be outbalanced by the gained volume energy. Driven by the difference between hydrostatic pressure of the liquid and the vapor pressure nuclei with a radius smaller than R_c decay spontaneously and nuclei with radii above R_c will spontaneously grow. Therefore, a metastable phase can remain until the finite energy barrier E_b is overcome and nucleation occurs. Figure 2.13 (A) shows the Gibbs free energy dependence on radius of the vapor nucleus as determined by Equation 2.55 for various superheat temperatures $dT = (T - T_{sat})$ above the saturation temperature $T_{sat} = 373\,\mathrm{K}$ under atmospheric pressure $p_0 = 0.1\,\mathrm{MPa}$. The maximum in each curve represents the energy barrier E_b at the corresponding critical radius. Figure 2.13 (B) shows the variation of the critical radius of a vapor nucleus with superheat temperature for water as determined by Equation 2.57. With increasing temperature above 100 °C a nucleus required to form a stable vapor bubble decreases in radius. For pure water at an increase of 145.8 K above atmospheric saturation temperature the energy barrier will be surpassed by nuclei above 15 nm radius. Because the Gibbs free energy remains finite until it vanishes at the critical temperature even at an increase by 205 K to spinodal temperature a nucleus with finite radius 2.5 nm is required (not plotted). Thus, for pure water nucleation remains an activated process with a finite free energy barrier [1].

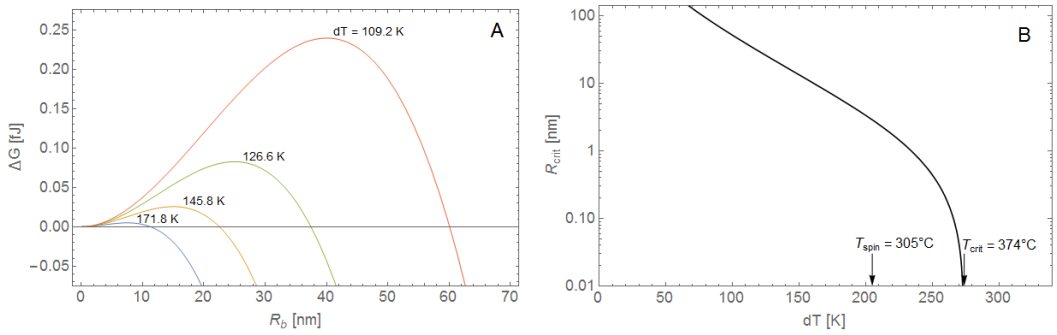

Figure 2.13: With increasing temperature above 100 °C the energy barrier and the radius of the nucleus required to form a stable vapor bubble decrease. At a temperature close to spinodal, the critical radius ranges in the dimensions of the gold nanoparticles. (A) Variation of the Gibbs free energy with radius R_b of the vapor nucleus in coexistence with a superheated liquid phase for various superheat temperatures $dT = (T - T_{sat})$, as determined by Equation 2.55. (B) variation of the critical radius with superheat temperature as determined by Equation 2.57.

Due to small fluctuation such as a density variation, metastable water will sooner or later undergo phase transition to a stable state such as a vapor nucleus within the previously homogeneous liquid phase. In order to form a stable phase a certain minimum size of the vapor nucleus is required, which is determined by the critical radius. The formation of such nuclei in a metastable phase is based on a stochastic process. The number N of formed nuclei is related exponentially to the minimum required energy E_b and can be estimated with help of a Gibbs-Boltzmann distribution [101]

$$N = N_0 \cdot \exp\left[-\frac{E_b}{k_b T}\right], \tag{2.58}$$

with N_0 the number density. According to Blander and Katz the volumetric nucleation rate J is obtained by

$$J\left(T,p\right) = N\sqrt{\frac{3\sigma_l}{\pi\, m_M}}\exp\left[-\frac{16\pi\sigma_l^3}{3k_b T\left(p_v - p_0\right)^2}\right] \tag{2.59}$$

Since the vapor pressure inside the nucleus strongly depends on the superheat temperature also the energy barrier is temperature dependent. Thus, for increasing superheat temperature not only E_b and R_{crit} decrease, but also the nucleation rate strongly rises. In order to account for the duration of a vapor nucleus to grow to a critical nucleus, equation 2.59 can be modified by the nucleation time τ [96]

$$J\left(T,p\right) = N\sqrt{\frac{3\sigma_l}{\pi\, m_M}}\exp\left[-\frac{16\pi\sigma_l^3}{3k_b T\left(\eta\cdot p_{sat}\left(T\right) - p\right)^2}\right]\exp\left[-\frac{\tau}{t}\right] \tag{2.60}$$

$$\eta\left(T\right) = \exp\left[\frac{p_0 - p_{sat}\left(T\right)}{\rho\left(T\right) R_x T}\right] \tag{2.61}$$

$$\tau\left(T\right) = \sqrt{\frac{2\pi\, M}{R_x\, T}}\frac{4\pi\sigma p_s}{\left(p_{sat}\left(T\right) - p_0\right)^2} \tag{2.62}$$

whereas the time period of temperature heated above 100 °C is denoted by t, the number density N, the molecular weight m_M, the molar mass M and the molar gas constant R_x. The life time of a metastable liquid ranges around $18\,ps$ [102], $15 - 300\,ps$ [Kelly], $1 - 100\,ns$ [96]. Life time of the metastable state decreases significantly around $0.9\,T_{crit}$ [101].

The spinodal is the upper limit of the metastable state of a liquid and can therefore considered the upper limit of the stability for a thermodynamic system. Note, that in reality often heterogeneous nuclei are present prior to laser irradiation or if dealing with surfaces, the boundary

between solid and liquid itself exhibit a type of weakness of the liquid phase. Nucleation at surfaces is therefore termed heterogeneous. A gold nanoparticle constitutes a heterogeneity, which possibly reduces the free energy barrier for the phase transition. Heterogeneous nucleation at nanoparticles with diameters in the range of thermodynamic fluctuations around sites of spinodal decomposition [99, 103] is difficult to distinguish from homogeneous nucleation [99]. Thus, the described nucleation probability and rate determined for a homogeneous process represent a limit, since in case of a heated nanoparticle nucleation probability and rate can increase due to a locally decreased Gibbs free energy barrier at the gold-water interface.

2.3 Bubble dynamics in free medium

Once a critical vapor bubble nucleates a rapid expansion and a collapse of the bubble will follow. The bubble expansion is driven by the vapor pressure, which rapidly increases due to a phase change within the metastable liquid. During expansion the pressure decreases, while surface tension, hydrostatic pressure and heat conduction limit the bubble growth. With increasing radius the bubble wall motion slows down until the bubble reaches maximum expansion, and collapses. During the collapse the internal pressure increases again, leading to rebound of the bubble wall. Depending on the remaining energy after expansion and collapse of a bubble a multiple oscillation may occur. Also, generation of shock waves is associated with the final phase of a collapsing cavitation bubbles as well as plasma formation and sonuluminescence .

The first analysis of bubble dynamics in a liquid was carried out by Lord Rayleigh 1917 and numerous publications followed including theoretical and experimental studies by Plesset and Prosperetti [104], Lauterborn [105], Lauterborn and Vogel [106], Vogel [107, 108] and many more. Experimental studies of bubble formation and growth around rapidly heated nanoparticles were carried out for example by Plech et al. [66, 68], Neumann [15, 7, 109], Lapotko [60], Kitz [16], Lombard [110, 111, 112] and Meunier et al. [113, 114]. Purely numerical analysis was conducted by Pustovalov [78, 59], Egerev [115], Brujan [116, 117] and the results were compared to published experimental results. The oscillation dynamics of bubbles formed around gold nanoparticles follow the basic principles of bubble oscillations described first by Rayleigh and extended later by Plesset.

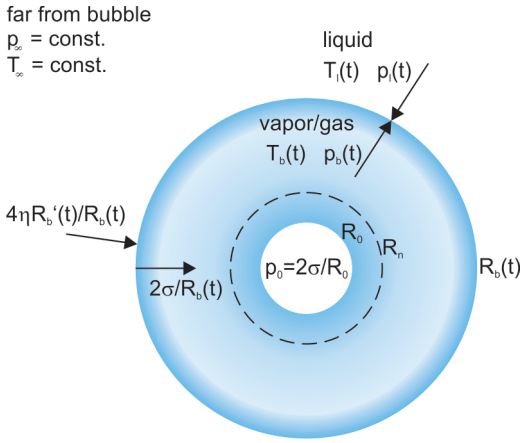

Figure 2.14: Spherical bubble formed within a liquid a round a nanoparticle

The Rayleigh-Plesset equation is used for calculation of the time dependence of the bubble growth rate and size of the bubble. Under the assumption of negligible heat conduction from the bubble to the surrounding liquid and constant vapor content within the bubble, the bubble wall motion is described in good approximation by the following differential equation [104, 99]:

$$\rho_l \left(R_b(t) \frac{d^2 R_b}{dt^2} + \frac{3}{2} \left(\frac{dR_b}{dt} \right)^2 \right) = p_b - p_\infty - \frac{2\sigma}{R_b(t)} - \frac{4\eta}{R_b(t)} \frac{dR_b}{dt} \tag{2.63}$$

$R_b(t)$ denotes the bubble radius, which varies in time, R_0 the initial bubble radius, ρ_l and p_∞ the density and constant pressure of the surrounding medium, σ the surface tension and η the viscosity. The equation is valid for incompressible liquids and provided that the phase transition has polytropic behavior given by $(p_b \cdot V_b)^\kappa = \text{constant}$ with a homogeneous vapor pressure p_b inside of a bubble with volume V_b. The vapor pressure p_0 is reached by the bubble at equilibrium radius, which is determined by the surface tension at the interface vapor water.

$$R_0 = \frac{2\sigma}{p_0 - p_\infty}. \tag{2.64}$$

Thus, the vapor pressure within the cavity is determined by

$$p_b(t) = p_0 \left(\frac{R_0}{R_b(t)} \right)^{3\kappa} \tag{2.65}$$

where κ denotes the polytropic exponent during expansion and collapse of the bubble. For the case of isothermal expansion and collapse phase κ equals unity, while adiabatic expansion yield in $\kappa \leq 1.67$.

The influence of heat and mass diffusion across the liquid-vapor phase transition at the bubble surface on bubble growth is neglected by the Rayleigh-Plesset equation. Both can be only approximated considering two limiting cases, the inertially controlled growth and the limited heat diffusion [104].

Upon nucleation, the temperature can be assumed constant over the superheated liquid as well as the cavity ($T_v = T_\infty$) with the ambient temperature $T_l(r \to \infty) = T_\infty$ spatially far from bubble). leading to an internal bubble pressure determined by $p_v = p_{sat}(T_\infty)$, which, at first, remains constant over time. The thermal energy of the cavity in equilibrium with the surrounding liquid is $Q_b = 4/3\pi R_b^3 h_v \rho_v$, whereas h_v denotes the latent heat of vaporization and ρ_v the equilibrium vapor density at water temperature [104]. The isobar conditions $\Delta p = p_\infty - p_v = const.$ are provided by compensation of the pressure decrease, which is related to increasing volume, by vaporization at the bubble interface. The heat energy $Q_l = 4\pi R_b^2 l_d \rho c_l \triangle T$ is supplied by the surrounding layer with thermal diffusion length $l_d = \sqrt{\alpha_l \, t_d}$ (cf. 2.2.2). Thus, the bubble growth is controlled by inertia.

As the bubble reaches maximum expansion the kinetic energy was transferred to potential energy, which can be approximated by calculating the performed work on volume increase neglecting the surface tension and viscosity of the surrounding water as determined by [118]

$$E_b = V_{b,max} \Delta p = \frac{4}{3} \pi R_{b,max}^3 (p_\infty - p_v) \tag{2.66}$$

Upon reaching the maximum radius the kinetic energy will be consumed and the expanded bubble collapses because of the pressure difference between the hydrostatic and the internal vapor pressure. The collapse phase may be treated in a first approximation by considering inertia and thermal diffusion under conditions such as during the expansion phase. During the initial compression of the bubble vapor condensates at the bubble interface, whereas transport of the resulting heat is controlled by thermal diffusion of the liquid. With further decrease of the bubble radius the vapor pressure increases. Similar to the expansion phase mass transport by condensation of the vapor at the interface limits the increasing pressure difference. Assuming again isobar conditions and provided that the bubble contains a negligible amount of gas and surface energy it follows, that the time for a bubble to collapse from its maximum extend $R_{b,max}$ to $R_b = 0$ can be determined by [119, 104]

$$\tau_{col} = 0.915 \sqrt{\frac{\rho_l}{\Delta p}} \cdot R_{b,max} \tag{2.67}$$

The Rayleigh-Plesset equation was extended to account for not full condensation of the water vapor inside the cavitation bubble [120, 121]. Due to the strong compression during collapse, the water vapor inside the bubble will exhibit very high values of the pressure and temperature. With decreasing vapor-liquid interface area the condensation rate becomes insufficient, whereas the vapor inside behaves like a non-condensable gas [120]. Thus, the isobar conditions of will be violated during the late stages of collapse. Furthermore, if the bubble wall velocity and

molecular velocity within the vapor reach sound velocity, compressibility of the liquid becomes relevant. To account for the incompressible volume of (inert) gas inside the bubble a van der Waals hard core law has been introduced by Löfsedt et al. [121]. For the gas content of the bubble obeying van der Waals law the pressure inside the bubble is determined by

$$p_b(t) = \left(p_0 + \frac{2\sigma_l}{R_0}\right)\left(\frac{R_0^3 - h^3}{R_b^3(t) - h^3}\right)^{\kappa} \tag{2.68}$$

with h the (collective) van der Waals hard-core radius [122, 123, 124, 125].

2.4 Bubble formation around laser heated gold nanoparticles

Selective nanophotothermolysis with gold nanoparticles

Pustovalov et al. studied the photothermal effects in and around gold nanoparticles under short pulsed laser irradiation in the scope of selective nanophotothermolysis. They theoretically examined accompanied phenomena such as the thermal protein denaturation, explosive liquid vaporization, melting and evaporation of nanoparticle, optical breakdown initiated by nanoparticles and accompanied to shock waves and explosion (fragmentation) of gold nanoparticles. However, their analysis was based on a theoretical model, while thy did not publish own experimental data that can verify their modeling results.

Their analysis was based on a differential equation, which describes the thermal energy deposition within the particle volume by laser irradiation. They accounted also for an energy loss from the nanoparticle by heat conduction, by evaporation and by radiation [59]. Irradiation pulse with duration τ_L and the intensity $I(t)$ constant over $0 \leq t \leq \tau_L$ were defined. For different pulses with durations ranging from thermalization time of the nanoparticle lattice $\tau_{T,p}$ (Equation 2.33) to thermalization time of the surrounding liquid layer $\tau_{T,l}$ (Equation 2.34) analytical solutions of the differential equation of temperature evolution $T(r,t)$ were calculated. For short pulses, with pulse duration shorter than particle thermalization time, heat transfer to the surrounding was assumed negligible, while for pulse durations longer than the thermalization time of the surrounding medium Pustovalov et al assumed, that a quasi-stationary heat flux from the particle to the surrounding occurs [78].

The temperature distribution was calculated for a gold nanoparticle with 30 nm diameter under irradiation with laser pulse durations of 1 ps, 1 ns and 1 µs and different absorbed intensities $I\,Q_{abs}$. To estimate possible effect on proteins they calculated the degree of thermal denaturation with a kinetic equation of exponential nature, which considers dependency on (the local) temperature. They suppose the layer thickness of denaturation can be controlled by varying laser pulse duration and nanoparticle size, while retaining spatial selectivity (precision).

Pustovalov et al. supposed, that an initial vapor layer forms by explosive evaporation and merging of critical nuclei once the nanoparticle surface has reached the spinodal point of water $T(r = R_p) \geq 590\,\mathrm{K}$. Calculations on the vapor blanket formation and dynamics were based on a model of Nigmaulin et al., who described the bubble dynamics in inhomogeneous heated liquids [126, 127]. The model is restricted to a rectangular laser pulse with a duration above acoustic confinement and shorter than thermal confinement. In simulations with their model a threshold of vapor formation around a gold nanoparticle with 30 nm radius was found for an absorbed energy rate of $I\,Q_{abs} = 10^7\,\mathrm{W\,cm^{-2}}$. Above threshold for an absorbed intensity $I\,Q_{abs} = 1.4{\cdot}10^7\,\mathrm{W\,cm^{-2}}$ their model predicted at the time point of 10 ns after laser pulse onset the formation of an initial vapor layer with outer radius $r_b = 37.2\,\mathrm{nm}$ at a temperature of $T_b = 578\,\mathrm{K}$ and a pressure of $p_b = 9.18\,\mathrm{MPa}$. According to Pustovalov et al. the vapor layer caused a temperature gradient from $T_p \sim 740\,\mathrm{K}$ (inside the nanoparticle) to $T_b = 578\,\mathrm{K}$ (inside the vapor layer). Based on these conditions they solved the Rayleigh-Lamb equation [127] and calculated a maximum bubble expansion of $R_{b,max} = 47.2\,\mathrm{nm}$, while the maximum expansion and collapse rate were $dR_B/dt = 50\,\mathrm{m\,s^{-1}}$ and $30\,\mathrm{m\,s^{-1}}$, respectively [59]. At this point it should be noted that the astonishingly precise information on bubble radii is probably due to the mathematical consideration of bubble formation without any consideration of experimental data.

In addition to vapor bubble formation Pustovalov et al. derived from the differential equation of nanoparticle heating a melting time Δt_M of nanoparticles, provided the pulsed laser irradi-

ation generates an increase to melting temperature of T_M [59]. Evaporation of the nanoparticle material was considered negligible during the melting process. For a gold nanoparticle of 20 nm radius at room temperature a metling time of $\Delta t_M = 0.32$ ns due to irradiation with $I_0 = 4\,\mathrm{MW\,c}m^{-2}$ (pulse length was not given) at a wavelength of 532 nm. Pustovalov et al. estimated the required energy of $Q_M = \rho_p V_p H_{melt} = 5.2{\cdot}10^3\, r_0^3$ for gold, for a nanoparticle $Q_M\,(R_p = 30\,\mathrm{nm}) = 1.4{\cdot}10^{-13}$J. Further, during heating and melting process the material properties substantially change. Due to a phase transition from solid to liquid gold a decrease of the density from $19.3\,\mathrm{g\,c}m^{-3}$ to $17.36\,\mathrm{g\,c}m^{-3}$ occurs. Assuming constant mass the variation in density corresponds to an volume increase of around 14 %, while the particle radius increases by 4 % (from 30 nm to 31.2 nm)[59]. Already below nucleation temperature this volume increase can be generate the thermomechanical (photoacoustic) effect of pressure wave emission.

Moreover melting at higher irradiation at the plasmon resonance wavelength may lead to evaporation of the nanoparticle material or even fragmentation. Both may be accompanied by optical breakdown.

In summary, the analysis by Pustovalov et al. is restricted to laser pulse durations that comply with thermal confinement. Subsequent processes base on the steady-state equations of energy conservation. Thus, heat deposition within the particle and conductive heat flux into the surrounding liquid are in equilibrium. This allowed to perform a numerical analysis in two steps. At first, for a nanoparticle spatially homogeneously heated by a rectangular laser pulse the conductive heat flux into the liquid water surrounding was determined. Second, spinodal decomposition follows within a liquid layer around the particle for temperature above the spinodal. The obtained vapor volume, temperature and pressure serve as initial condition for calculation of the bubble dynamics with the model by Nigmatulin et al. [126].

Modeling of the bubble formation around gold nanoparticles

Egerev et al. developed a physical model for bubble formation, which includes also the conversion of optical energy to acoustic energy [115]. They assume that the absorbed laser energy is used completely for heating of the AuNP and surrounding medium by homogeneous heat transfer as described by the differential equations

$$c_p \rho_p \frac{\partial T_p\,(r,t)}{\partial t} = k_p \triangle T_p\,(r,t) + \frac{\dot{E}\,(t)}{V_p},\; r \leq R_p \tag{2.69}$$

$$c_w \rho_w \frac{\partial T_w\,(r,t)}{\partial t} = k_w \triangle T_w\,(r,t)\,, \qquad r \leq R_p \tag{2.70}$$

where c, ρ and k are the specific heat capacity, density and thermal conductivity of the AuNP (subscript p) and the water (subscript w), respectively. However, they assume, that for sufficiently long irradiation, boiling of the water on the nanoparticle surface occurs prior to the end of the irradiation pulse. Egerev et al. assumed a threshold temperature is required for vapor bubble formation, which depends on laser fluence and pulse duration. In order to determine this threshold an increase to boiling temperature T_b was calculated accounting for heat diffusion during the irradiation pulse by simplifying the differential Equation 2.69 to

$$c_p \rho_p V_p \frac{dT_p\,(r,t)}{dt} = \dot{E}\,(t) - S_p q_{th} \tag{2.71}$$

$$q_{th} = -k_w \frac{\partial T_w\,(r,t)}{\partial r}\,|_{r=R_p} \tag{2.72}$$

with the nanoparticle surface S and the heat flux q_{th} across the AuNP-water interface. Note, that these differential Equations 2.69 to 2.72 essentially correspond to an approximation of the differential heat diffusion equations given in Chapter 2.2.3. However, in these equations finite interface conductivity is not considered. The energy required for heating the particle to the boiling temperature was defined the critical energy $E_c = \sigma_{abs} F_c$, where F_c denotes the corresponding critical laser fluence. Further, they assumed, that absorbed optical energy in excess of the critical energy E_c dissipates completely into the liquid-vapor phase transition, as the critical point of water is reached. This process was termed boiling at the critical point.

In order to determine the generated acoustic pressure, Egerev et al assumed an adiabatic bubble expansion following after the vapor formation. They solved the Rayleigh-Plesset equation as given by equation 2.63 for the bubble radius $R_b(t)$ and pressure $p_b(t)$.

Considering irradiation with rectangular pulses with a duration that satisfy thermal confinement by $\alpha_l \tau_L \ll R_p^2$, F_c was obtained analytically by

$$F_c = \frac{c_p \rho_p V_p}{\sigma_{abs}} T_b \tag{2.73}$$

while for longer irradiation pulses that satisfy thermal equilibrated diffusion into surrounding by $\alpha_l \tau_L \gg R_p^2$, the critical fluence was obtained by

$$F_c = \frac{4\pi R_p \, c_l \, \rho_l \, \alpha_l \, \tau_L}{\sigma_{abs}} T_b \tag{2.74}$$

The temperature increase in the nanoparticles continues after reaching the boiling temperature. With the help of F_c the evaporated mass m_b of the surrounding water initially evaporated to form the initial bubble radius R_0

$$m_b = \frac{4\pi(R_0^3 - R_p^3)\rho_{c,l}}{3} = \frac{(F - F_c)\,\sigma_{abs}}{E_{c,l}} \tag{2.75}$$

$$R_0 = \sqrt[3]{\frac{3}{4\pi\rho_{c,l}} \left(\frac{(F - F_c)\,\sigma_{abs}}{E_{c,l}} \right) + R_p^3} \tag{2.76}$$

with the internal energy as well as the density at the critical point of the liquid $E_{c,l}$ and $\rho_{c,l}$ respectively. Equation 2.76 is only valid for observation of irradiation above F_c. For irradiation below threshold the equation delivers an initial radius below nanoparticle radius leading to nonphysically results for the solution to the differential equation of the bubble wall motion.

After the initiation of boiling, the Rayleigh-Plesset Equation 2.63 was used to describe the bubble dynamics. In order to solve the differential equation Egerev et al. assumed for boundary conditions the initial temperature and pressure inside the nucleus to be those at the critical point of water.

Based on Landau and Lifshitz [97] Egerev et al. further derived equations that relate the acoustic pressure radiating from the expanding and oscillating bubble to the applied laser pulse energy. These calculations reveal a linear relationship of the maximum pressure caused by the laser irradiated nanoparticle with the incident laser fluence. This linear relationship was verified experimentally.

Modeling dynamics of cavitation nanobubbles

Brujan et al. published two numerical studies of transient cavitation bubbles generated around gold nanoparticles by pulsed irradiation based exactly on the model developed by Egerev et al. [116, 117]. They followed Egerev et al. assuming that excess light energy absorbed by the particle during the laser pulse is spent in boiling at the critical point of the surrounding water in order to obtain the conditions for calculation for the bubble motion. Brujan et al. utilized an extended Rayleigh-Plesset equation in their second study [117] the nanoparticle within the bubble was additionally considered to behave like a van der Waals hardcore.

They calculated initial and maximum bubble radii as well as the maximum vapor pressure inside bubbles formed around gold nanoparticles with particle radii ranging between $R_p = 5\,\text{nm}$ and 40 nm irradiated with short pulse durations, which comply with $\alpha_l \tau_L \ll R_p^2$, and with pulse duration of 10 ns, that are longer than the thermal relaxation time.

Based on their calculations, Brujan et al. concluded that maximum bubble radius and pressure inside the bubble increase with nanoparticle radius, pulse duration and applied fluence. The model predicted bubbles with maximum radius below 600 nm for application of short and long pulses with fluence up to $F = 10\,F_c$, with the critical fluence F_c as determined by Egerev et al. [115]. For long pulses and $F > 100\,F_c$, micrometer sized bubbles can form around a nanoparticle

of 10 nm diameter, while for short pulses a particle diameter above 40 nm would be required to generate bubbles in the micrometer range.

Further, they found that maximum bubble radius is related to the applied fluence by $R_{max} \propto \sqrt{F}$. Only for long pulses at fluence close to the presumed threshold of bubble formation the energy dependence of R_{max} is stronger. Brujan et al. calculated with this model, that the oscillation time predicted by the Rayleigh equation underestimates R_{max} for a nanoscale bubble generated by a gold nanoparticle. This is reasoned by the Rayleigh equation being inaccurate for bubble expansions below 1 µm, because surface tension and the viscosity of the medium surrounding the bubble are neglected. An underestimation of the actual R_{max} by a factor up to ≈ 2 for very small bubbles calculated by the Rayleigh equation was already found for bubbles generated by optical breakdown with the help of nanosecond laser pulses in pure water [103].

In order to verify his analytical results Brujan et al. used experimental results published by Kotaidis et al. [67]. However, these calculations were based on particles with a *radius* of 39 nm, in contrast to the experimental data, which were obtained for nanoparticles of 39 nm *diameter*.

Thermodynamic analysis of nanobubbles around gold nanoparticles

Lombard and Merabia et al. investigated heat transfer from gold nanoparticles into their surrounding and analyzed the thermodynamics of nanobubble generation [110, 111]. In order to describe the thermodynamics in the fluid around a nanoparticle as well as the bubble dynamics, Lombard et al. utilized a hydrodynamic model based on a free energy density to model interfacial heat transport and boiling at the nanoscale as described by Onuki et al. [128]. The temperature inside the gold nanoparticle was assumed to be spatially uniform. The temporal evolution of the nanoparticle temperature increase caused by short pulsed laser irradiation was determined with help of a differential equation[110]:

$$V_p c_p \frac{d}{dt} T_p(t) = F\,\sigma_{abs} \frac{\Pi(t/\tau_l)}{\tau_l} - S_p \phi \tag{2.77}$$

where S_p and V_p are the nanoparticle surface and volume respectively, c_p the nanoparticle specific heat and $\sigma_{abs} \cdot F$ the absorbed radiant exposure. The laser pulse function was defined by a gate function $\Pi(t/\tau_p) = 1$ for $0 < t < t_p$, and 0 otherwise. The equation relates to the change of the thermal energy within the particles due to decrease of the deposited energy by heat diffusion across the particle surface. In order to determine nanoparticle temperature T_p the laser pulse duration was set to $t_p = 7\,ps$, which corresponds to electron-phonon coupling time. $S \cdot \phi$ is the heat flux across the AuNP-fluid interface into the medium, while a finite interface conductivity of $G = 140\,MW\,m^{-2}K^{-1}$ was assumed.

Upon irradiation the nanoparticle temperature increased and a strong temperature gradient in the surrounding liquid due to conductive heat transfer was calculated. While the interface conductivity and the heat diffusion in the fluid controls the cooling kinetics of the AuNP in their simulations Lombard et al. predict bubble formation, when laser fluence exceeded a nanoparticle size depending threshold. They assumed spinodal decomposition drives the liquid-vapor phase transition within a thin layer with strong temperature gradient around the nanoparticle. The vaporization occurs with a time delay after the laser pulse onset, also referred to as vaporization time, which depends on the radiant exposure. The vaporization time exhibits a maximum at the bubble formation threshold and strongly decreases with the increasing radiant exposure. Subsequent vapor layer growth to a thickness above dimensions of the mean free diffusion path length of a vapor molecule leads to thermal insulation of the nanoparticle. The energy transfer to the surrounding fluid as well as to the vapor of the forming bubbledecreases strongly, whereas the nanoparticle cooling drops significantly. These assumptions were already described by Rudnitzki et al. when calculating the energy absorbed by a rod-shaped gold nanoparticle after bubble formation [18].

Lombard et al. found in their simulations that above nucleation threshold the fluid density in the vicinity of the particle decreases below the critical fluid density. The bubble nucleation coincides with spinodal crossing in the fluid at a distance of $r_{spin} \backsimeq 2$ nm from the nanoparticle surface, where the local temperature increased to $0.9 \cdot T_c \approx 550$ K [110]. For a gold nanoparticle with $R_p = 10$ nm a radiant exposure just above threshold of 9.2 mJ cm^{-2} led to a transient vapor

shell at a vaporization time of around 115 ps. This time is several times larger than typical heat diffusion time $\tau_{diff} = x^2 \rho_l \, c_v / \kappa_l$ over a distance of $x = 2\,\text{nm}$. Higher radiant exposures resulted in larger bubble sizes and oscillation life times, while the vaporization time further decreased. However, experimentally observed bubble threshold with comparable values were not published so far.

Besides bubble formation caused by spinodal decomposition within a layer of certain thickness, Lombard et al. described the effect of the thermal interface conductivity between the metal and the liquid, also referred to as reciprocal Kapitza resistance. A finite thermal interface conductivity delays the energy transfer from the nanoparticle to the surrounding, which significantly influences efficiency of vaporization defined by the ratio of energy stored in a 2 nm liquid layer over the energy supplied by the femtosecond laser pulse $\Gamma = E_{2\,nm} / E_{laser}$. According to their numerical simulation for different diameters ranging from 2 nm to 50 nm, a maximum efficiency Γ_{max} was found close to the individual size dependent threshold fluence. For increasing fluence the ratio Γ was found to decrease and further Γ_{max} was found to decrease with increasing particle size. Depending on the size either the time constant of heat diffusion in the surrounding liquid τ_{diff} or across the Kapitza resistance $\tau_{d,G}$ (cf. equation 2.36) dominate cooling kinetics of the nanoparticle. Due to comparable relaxation times τ_{diff} and $\tau_{d,G}$ a small nanoparticle can transfer energy to the liquid before a nanobubble appears, while for larger particles $\tau_{diff} \gg \tau_{d,G}$ vaporization leads to thermal insulation and thus to a lower efficiency in energy transfer. Further, due to the fluence dependency of vaporization time the conductive heat flux is interrupted earlier for higher irradiation, which leads to a drop in bubble formation efficiency as well. For irradiation close to the threshold, time for bubble formation is longest and therefore a significant part of the energy is transferred to the liquid phase by conductive heat flux.

Lombard et al. further found, that the initial formation of a thin vapor layer is accompanied by a radially emitted pressure wave. It is generated due to the sudden dilation of the liquid before the bubble forms and propagates with a velocity close to the speed of sound in the non-heated liquid. Close to the nanoparticle surface, the temperature related pressure in the liquid was found to exceed the critical pressure. It is presumably reasonable, that a layer of certain thickness surrounding the nanoparticle participates in the nucleation for substantial bubble expansion. Therefore, the Laplace pressure $2\sigma / R_p$ needs to be overcome.

Their further analysis demonstrated that the temporal increase of the nanobubble radius is well described by the Rayleigh-Plesset Equation 2.63, with growth assuming adiabatic evolution, while collapse was assumed isothermal referring to classic bubble formation theory [110, 111]. The vapor pressure inside the bubble is determined by

$$p_b(t) = p_{i,max} \left(\frac{R_{b,max}^3 - R_p^3}{R_b^3(t) - R_p^3} \right)^{\kappa} \tag{2.78}$$

whereas the nanoparticle within the bubble center was accounted for such as for a non-compressible volume. In a comparable way the Equation 2.68 accounts for the van der Waals hard core of incompressible inert gas. However, here $p_{i,max}$ is the pressure inside the bubble at maximum extend $R_{b,max}$. The initially strong pressure increase during nucleation and phase transition relaxes with expansion of the vapor bubble due to viscous forces of the liquid until reaching Laplace pressure at maximum radius determined by $p_{i,max} = 2\sigma / R_{b,max}$.

Based on a phase-field hydrodynamics model Lombard et al. analyzed vapor bubbles generated around gold nanoparticle under laser irradiation with rectangular pulse shape. In contrast to the experimental work of this thesis, thermal and acoustic confinement conditions were satisfied. Under nanosecond pulsed irradiation the finite interface conductivity can effect vaporization time and bubble formation presumably much stronger than for femtosecond pulses. Due to the interface conductivity, kinetics of vapor generation were found to be slow in comparison to the laser pulse duration. This explains the existence of a maximum of the energy efficiency of the vaporization process. Further, Lombard et al. described that the vaporization is also accompanied by melting of the nanoparticle.

3 Cell elimination by laser irradiated gold nanoparticles

Specific targeting of cell membranes by gold nanoparticles and irradiation with short pulsed laser can be used for efficient and selective cell elimination [8, 4, 5, 19]. For this method also referred to as nanoparticle mediated laser induced cell elimination (NALI) the accompanying physical phenomena are confined to a specific volume around the AuNP providing targeting selectivity. Thus, a precise control and tightly focusing of a laser become unnecessary and allow for instance, purification of cell cultures with high throughput.

In this study, an optical setup containing a nanosecond pulsed laser, an optical parametric oscillator and a platform with position controlled stage was used to treat cells growing in suspension and adherent growing cells. Colloidal AuNP with 30 nm diameter were directly conjugated to IgG monoclonal antibodies BerH2, which target the CD30 membrane protein of the human cells KARPAS-299. Depletion with an efficiency of over 99 % was achieved by nanosecond pulsed irradiation. The selectivity of cell depletion was shown with CD30-negative KARPAS-422 cells, which were not affected when irradiated in co-culture with KARPAS-299 cells.

NALI is not limited to cells in suspension, like other cell-selection methods such as FACS and MACS, which are commonly used for cell purification in biomedical research. The method can also be applied to adherent growing cells. Here, also the efficiency to eliminate adherent growing OVCAR-3 cells by targeting the epidermal growth factor receptor on the membrane was studied.

3.1 Introduction

In many areas of cell biology purification of live cells is essential to precisely characterize cell phenotype and associated functions. Cell sorting by using flow cytometry usually referred to as fluorescence activated cell sorting (FACS) [129] is of high importance in biological research. Alternative techniques for the bulk isolation of cells take advantage of paramagnetic particles and the separation of labeled cells in a magnetic field gradient [130]. Several million cells can be purified in a single flow through approach for positive selection or depletion. However, both methods, are limited by the need for non-adherent or detached cells in suspension. The use of micro fluidic system also limits the size of cells and particles that can be purified [131]. Moreover the problem that for certain fragile adherent cells such as primary or neuronal cells and hybridomas the process of detaching, sorting and return into culture may significantly reduces cellular physiology and cell yield is common to the FACS and MACS technologies.

Systems for the purification of adherent growing cells often utilize selection via a microscope. Laser microdissection and pressure catapulting have already proven to be able to dissect living cells from a cell culture, to catapult them into collection devices and recultivate them [132, 133, 134, 135]. However, a high throughput purification of adherent cells under microscopic guidance requires a sophisticated image analysis to identify the target cells and a complex system of laser optics for the elimination of the cells [136].

In this study, two different human cell-lines, the Lymphoma T-cells KARPAS-299 and the ovarial cancer cells OVCAR-3, were targeted by cell specific 30 nm AuNP conjugates in cell suspension and adherent cell culture. Selectivity was also tested with 30 nm AuNP functionalized with BerH2 antibodies for targeting the CD30 membrane protein on KARPAS-299 cells in co-culture of CD30-negative KARPAS-422. After incubation with AuNP conjugates the cells were irradiated with 4 ns laser pulses at the wavelength of 532 nm. CD30-negative KARPAS-422 cells, which were mixed with the CD30+ KARPAS-299 cells should show the selectivity of NALI.

Further, the effectiveness of rod-shaped gold nanoparticles (AuNR) for cell elimination was investigated. AuNR appear to be especially attractive for applications in biological tissue. Their plasmon resonance splits into the transversal surface plasmon resonance (TSPR), which remains around 520 nm, while the longitudinal surface plasmon resonance (LSPR) is shifted to longer wavelengths (cf. Chapter 2.1.6). Depending on the particle aspect ratio the LSPR may be located in the optical window of tissue between 700 nm and 1100 nm, while exhibiting a manifold stronger absorption than a sphere of equal volume. Thus, an increased efficiency of cell

elimination can be expected with laser pulses tuned to the near infrared absorption peak of the nanorods, while irradiation with 532 nm should exhibit much lower cell elimination efficiency.

3.2 Laser nanoparticle interaction and temperature increase

The strong optical absorption by the gold nanoparticle allows efficient cell elimination [15, 137, 138]. Scattering of radiation is not relevant for cell targeting, but may be used for visualizing of the particles or for a molecular detection [139, 13, 140, 141]. The absorption properties of gold nanoparticles (Chapter 2.1.3) and further the thermal diffusion across the nanoparticle surface are responsible for generating locally high temperatures, when irradiated by short laser pulses.

In gold nanoparticles, the electric field of incident light efficiently couples to quasi-free electrons inducing a charge separation, which collectively oscillates with the external electric field. This plasmon generates an additional electromagnetic field localized on the AuNP. Its resonance frequency depends on size, complex dielectric functions of the particle and the surrounding medium. The plasmon causes a high absorption and scattering of the incident electromagnetic field. For a spherical AuNP the absorption was calculated by the Mie theory (Chapter 2.1.3), utilizing the dielectric function of gold measured by Johnson and Christy [70].

Absorbed energy of the pulsed laser irradiation causes a temperature increase in AuNPs, which is influenced by heat conduction. The calculation of the spatial and temporal temperature distribution inside and around spherical symmetric AuNP with radius R_p is based on the two coupled differential Equations 2.37 and 2.38 [90, 89, 142]. From the solution for a Dirac-shaped irradiation (Green´s function), spatial and temporal temperature profiles were calculated by integrating over the temporal shape of the laser pulse (cf. Equations 2.42 to 2.51). Thermal properties of the involved materials were assumed to be constants.

Figure 3.1 A shows the temporal temperature increase inside a 15 nm sized AuNP. For comparison, the temporal temperature increase inside a 30 nm sized AuNP is shown in Figure 3.2 A. The spatial temperature increase is shown in Figure 3.1 B for both, a 15 nm and a 30 nm sized AuNP.

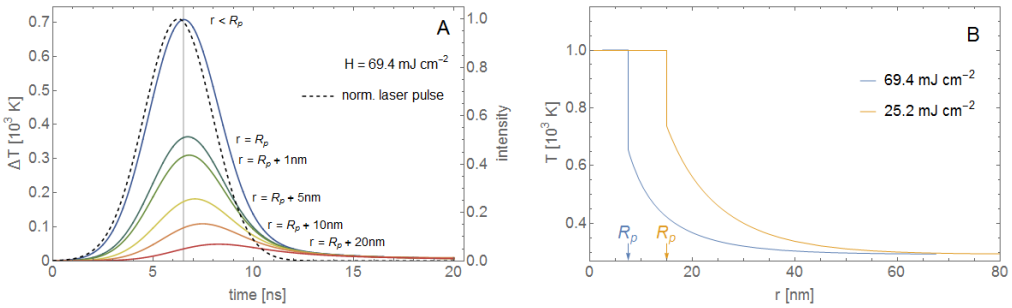

Figure 3.1: (A) Temperature increase calculated for a 15 nm AuNP (blue line) and at different distances (blue to red lines) in the surrounding medium after irradiation with a Gaussian shaped laser pulse of 4 ns FWHM duration. An irradiation wavelength of 532 nm was used. Radiant exposure of 69.4 mJ cm^{-2} and 25.2 mJ cm^{-2} lead to a maximum temperature increase of around 700 K within 15 nm and 30 nm AuNPs, respectively . (B) Temperature increase calculated as a function of the radial distance to the nanoparticle center at the time point of maximum temperature increase inside a 15 nm (vertical line A) and a 30 nm AuNP. A finite thermal conductivity across the AuNP-water interface causes a temperature drop of 35 % (15 nm) and 25 % (30 nm) for the water on the AuNP surfaces.

Under ns-pulsed irradiation extreme temperatures of the electrons, which can occur under fs-pulsed irradiation, are avoided. Thermalization of the electronic system and subsequently of the atomic lattice take place on the picosecond scale [85] and thus, the temperature of AuNP with diameter up to 30 nm closely follows the temporarily shape of the nanosecond laser pulse. However, thermal inertia causes increasing temporal delay between irradiance and particle temperature, which depends on the particle size. For instance, after maximal irradiance the

maximum temperature is reached at a time delay of 285 ps for 15 nm AuNPs and 585 ps for 30 nm AuNPs. After reaching maximum temperature the heat conduction of the surrounding liquid will outbalance the energy absorbed from the remaining incident laser pulse and the nanoparticle will cool down to nearly room temperature in less than 100 ns. Thus, irradiation with a pulse sequence at a repetition rate of a few tens of a Hertz can be considered as single pulsed irradiation.

Figure 3.2 A shows the temporal temperature increase of a 30 nm sized AuNP and of the surrounding medium at specified locations with distance r from the nanoparticle center for a Gaussian laser pulse with 4 ns duration at full width half maximum (FWHM). Figure 3.2 B shows the resulting temperature increase at the time point of peak particle temperature at 6.8 ns as well as at 9 ns. Over the AuNP volume a homogeneous temperature increase was assumed due to the high thermal diffusivity of gold. In the surrounding water temperature decreases nearly exponentially with distance to the AuNP surface. The finite thermal interface conductivity of $G = 105\,MW\,m^{-2}\,K^{-1}$[89] between the gold nanoparticle and the aqueous surrounding causes a temperature discontinuity across the nanoparticle surface located at $r = R_p$. After reaching maximum temperature the discontinuity decreases significantly (Figure 3.2 B). For instance, 9 ns after irradiation onset the discontinuity is around 95 K, which was around 260 K at the time point of 6.8 ns.

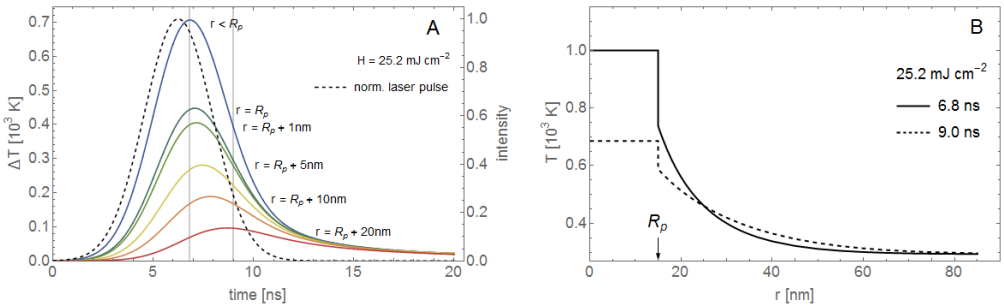

Figure 3.2: (A) Temperature increase over time calculated for a 30 nm AuNP (solid line, blue) at different locations r in the surrounding medium (solid lines, blue to red). Irradiation with a Gaussian shaped laser pulse of 4 ns FWHM duration (dashed line) with a wavelength of 532nm was assumed. An irradiation wavelength of 532 nm was taken into account. A radiant exposure of 69.4 mJ cm^{-2} leads to a maximum temperature increase of around 700 K inside the AuNP. (B) Calculated temperature increase for a 30 nm AuNP as a function of the radial distance r to the nanoparticle center at the time point of maximum temperature increase inside the AuNP (solid vertical line and dashed vertical line (A)). The finite thermal interface conductivity across the AuNP-water interface causes a discontinuity with a temperature drop of 25 % occurs. At 9 ns after irradiation onset (dashed vertical line in (A)) the temperature drop is decreased to 14%

In general, the nanoparticle size, the pulse duration as well as the radiant exposure determine the maximum temperature increase within an irradiated AuNP and in the surrounding water. In the thermal model (cf. Chapter 2.2.3), the temperature of the AuNP and in the surrounding water scales linearly with the radiant exposure. This holds approximately until a cavitation bubble forms around the particle, which changes optical absorption and heat conduction or until the particle starts to melt [18]. Outside this linear regime of constant optical and thermal properties mathematical modeling of the temperature evolution inside the nanoparticle and the surrounding medium becomes very difficult and was not done in this thesis.

When a cavitation bubble is formed the absorption of the nanoparticle decreases. Calculations (cf. Chapter 2.1.3 and 2.1.4) show for instance, at a wavelength of 532 nm the absorption cross sectionis of a 30 nm AuNP reduces from $\sigma_{abs} = 1.4 \cdot 10^{-15} m^2$ down to a lower limit of $\sigma_{abs,v} = 0.3 \cdot 10^{-15} m^2$. A refractive index of 1.0 was assumed for the surrounding of the AuNP, when a bubble formed. For AuNR the strong LSPR related absorption is decreased even stronger. For instance an AuNR with a width of 10 nm and a length of 40 nm the peak absorption located at a wavelength of 770 nm is decreased from $\sigma_{abs} = 5.3 \cdot 10^{-15} m^2$ down to a lower limit of $\sigma_{abs,v} = 0.05 \cdot 10^{-15} m^2$.

Also the heat conduction from the particle to the surrounding water breaks during the formation of the vapor bubble. In contrast to the calculation of temperature increase according to Equations 2.42 to 2.44, the calculation of the deposited energy $\triangle E_p$ also allows to consider reduced heat diffusion into the surrounding of the particle. Assuming adiabatic conditions due to the isolation by the vapor bubble the energy deposition within the gold nanoparticle can be calculated from the integral over the irradiance H of the laser pulse starting with expansion of the bubble at t_v [18]:

$$\triangle E_p\left(t\right) = \int_{t_v}^{t} \sigma_{abs,v} \cdot H\left(t'\right) dt'. \tag{3.1}$$

Under nanosecond pulsed irradiation a nanoparticle passes different heating phases. Figure 3.3 shows the calculated temperature and energy density of a 30 nm AuNP irradiated with 25.2 mJ cm^{-2} at a wavelength of 532 nm. The initial phase is governed by thermal diffusion and high absorption in the presence of water around the particle, which causes a rapid temperature increase of the whole nanoparticle. During the second phase vapor formation leads to thermal isolation of the AuNP and decrease in absorption due to changes in local index of refraction at the surface of the particle. This absorption loss is caused by surrounding vapor and remains transient, while for gold nanorods also melting and subsequent reshaping of the nanoparticle causes permanent absorption loss [18]. For a spherical AuNP only changes in the size as well as the refractive index of the metal and the surrounding effect the absorption, while for AuNR reshaping to a sphere leads to permanent loss of LSPR related absorption. During third phase low energy deposition and still a temperature increase can be expected despite the strongly decreased absorption. In case the vaporization enthalpy of gold is provided a loss of nanoparticle material will occur.

The initial phase can be clearly distinguished from the subsequent phases by the sudden bubble formation. In the time course of increasing energy density of the nanoparticle, the event of bubble formation is clearly marked by a discontinuity and the temperature increase could not be determined with the temperature model (Chapter 2.2.3).

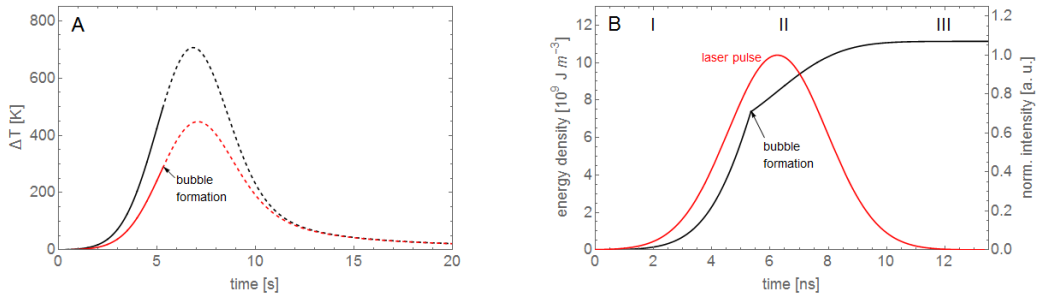

Figure 3.3: A) Calculated temperature increase inside a 30 nm AuNP (black line) and in the water on the particle surface (red line), when irradiated with 25.2 mJ cm^{-2} at a wavelength of 532 nm. Assumed pulse width was 4 ns. Without change of optical and thermal conditions after bubble formation temperature would follow the dashed lines. b) Energy density within the 30 nm AuNP calculated with Equation 3.1. Three heating phases (I – III) can be distinguished. I) initial phase of heating the AuNP until spinodal temperature is reached in the water. The spinodal temperature is assumed to be the minimum temperature for bubble formation. We assumed that water evaporates in 100 nm layer. Energy providing the latent heat of evaporation is comparably small and not visible on this scale. II) Energy density grows during AuNP temperature increase to 1336 K, while bubble formation causes thermal isolation and decreases absorption. The particle melts at constant particle temperature. III) Energy deposition in a liquid gold particle.

3.3 Experimental methods

3.3.1 Cells and cell culture

In order to determine the efficiency of NALI for purification of cell cultures the cell elimination efficiency was quantified in experiments with human lymphoma cells KARPAS-299 and KARPAS-422 (German Collection of Microorganisms and Cell Cultures , Braunschweig, Germany) as well as with cancer cells of type OVCAR-3. The membrane protein CD30 on the surface of KARPAS-299 cells was targeted with BerH2 antibody functionalized gold nanoparticles with a diameter of 30 nm. KARPAS-422 exhibit only minor expression of this membrane protein. Targeting of CD30 in cell cultures containing both, KARPAS-299 and KARPAS-422, should demonstrate the specificity of the cell elimination by AuNP. The adherent OVCAR-3 cells expressed epidermal growth factor receptors on their membranes, which was targeted with the Cetuximab antibody (EGFR).

The suspended cells were grown in 25 cm^2 culture flasks at 37°C and 5% CO_2 in a humidified incubator. KARPAS-299 were cultured in RPMI 1640 (Sigma Aldrich, USA) supplemented with 10 % fetal calf serum (FCS; PAA, Austria), 1% penicillin/streptomycin (PAA Laboratories, Pasching, Austria). For KARPAS-422 the medium was supplemented with 20 % FCS.

The adherent growing OVCAR-3 cells were cultured in 75 cm^2 flasks in RPMI 1640 supplemented with 20% FCS, 1% penicillin/streptomycin and 1% L-glutamine (PAA Laboratories, Pasching, Austria). Cells were harvested twice a week at a confluence of 80-90% by treatment with 0.05% Trypsin - 0.02% EDTA (Sigma Aldrich, USA) and subsequently seeded in new medium.

3.3.2 Preparation of gold nanoparticles

Colloidal gold solutions of 30 nm diameter (BBI Solutions, British Biocell International, United Kingdom) and rod-shaped nanoparticles with a small axis diameter of 10 nm and an aspect ratio of $\beta \approx 4$ (Nanopartz, USA) were utilized for the elimination of cells.

The functionalization of spherical gold nanoparticles with antibodies was based on electrostatic interaction with the nanoparticle surface. For the preparation of conjugates the AuNP solution was adjusted to the antibodies isoelectric point. The concentration of antibody providing a complete coating of the AuNP was determined by a titration series [14, 8]. After incubation of the particle solution with antibodies for 20 min at room temperature (RT) NaCl solution was added to each sample of the titration series in order to test the conjugate stability. Aggregation of the particle conjugates due to insufficient or excessive protein densities showed by a color change of the sample solution from red to dark violett. For application in cell elimination experiments the conjugates were produced then in larger amount by using the antibody concentration, which showed no color change in the titration series. After incubation the 30 nm AuNP conjugates solution was centrifuged at $22 \cdot 10^3$ g for 30 min to remove aggregates of gold and free antibodies. After centrifugation the fluffy pellet at the bottom, containing the AuNP-conjugates, was collected, while the solid pellet with gold aggregates and the supernatant with free antibodies were discarded. In order to verify the stability of the conjugates UV-Vis spectra were measured. The AuNP-conjugates concentration was calculated with help of the measured optical density (OD) at the wavelength of 532 nm.

3.3.3 Incubation of cell cultures with gold nanoaparticle conjugates

A predefined cell concentration was prepared in a volume of 50 µL and incubated with different concentrations of AuNP conjugates at 37°C and 5% CO_2. After incubation excess AuNP conjugates were removed by centrifugation with 400 g for 20 minutes at 20 °C (Heraeus Fresco 21 Centrifuge, Thermo Scientific, USA) and the suspension cells were resuspended in fresh medium. For irradiation, the cells were again taken up in medium and distributed in a 384 well plate, each sample contained $5 \cdot 10^4$ cells per well in 20 µl of medium.

For incubation and irradiation of adherent cells, $2 \cdot 10^4$ cells were plated in a 96 well plate with 200 µl medium. After growth for 20 h the medium was discarted and incubation was done in 50 µl solution with AuNP conjugates for 20 minutes. Following the incubation, the conjugate

solution was removed by pipetting and each sample was rinsed with PBS before being supplied with 200 µl of fresh medium.

3.3.4 Laser irradiation of the cells

Samples were irradiated with a frequency-doubled, Q-switched Nd:YAG Laser (Surelite I-20, Continuum, Santa Clara, CA, USA), which generates pulses of a duration of 4 ns at full width half maximum (FWHM) with at a wavelength of 532 nm (Figure 3.4). An optical parametric oscillator (OPO, Continuum, USA) allowed tuning of the laser wavelength in a range between 650 nm and 950 nm for irradiation experiments on cells targeted by gold nanorods. Pulse energy was adjusted by combination of a broadband $\lambda/2$ plate and a polarizing beam splitter. The diameter of the irradiation spot in the sample plane was adjusted by a lens to allow for an irradiation of the whole sample. Samples of suspended cells were placed in a custom made 384-well plates (Quartz well plate, well diameter 3.4 mm), adherent growing cells were placed in 96-well plates (Quartz well plate, well diameter 9 mm). In order to determine the single pulse radiant exposure, the beam radius, at which intensity falls to $1/e$ of the peak intensity in the beam center, was determined with the help of the knife edge method and the pulse energy was measured with a pyroelectric detector (PE25-C, Ophir).

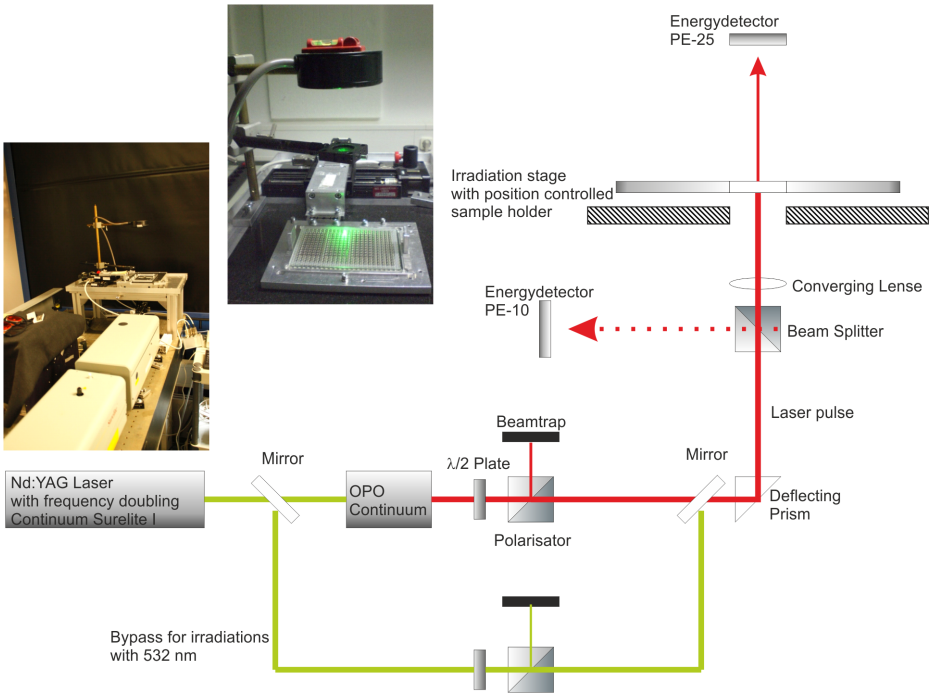

Figure 3.4: Experimental setup with Nd:YAG laser and OPO. The irradiation beam is directed with help of a deflecting prism into vertical direction. Irradiation of the cell samples placed in a multiwell plate with transparent bottom, hold by a position controlled stage.

3.3.5 Quantification of cell elimination by FACS analysis

Viability tests of the cells were carried out with the fluorescent dyes Calcein AM and Propidium Iodide (Sigma Aldrich, Live/Dead double staining kit no. 04511) in a flow cytometer (FACScan, Becton Dickinson, Franklin Lakes, NJ, USA). The acquired data were analyzed with help of the program "Flowing Software 2" (Version 2.5.1, Perttu Terho, Turku Centre for Biotechnology, University of Turku, Finland). Each cell sample was incubated in 40 nM calcein solution for 15 to 30 min at 37°C. Before measuring, cells were incubated in 40 nM propidium iodide solution. In general, vital cells exhibit strong calcein related signals. The calcein-AM dye stains living cells, because the membrane-permeable non-fluorescent substance is converted by enzymatic action into a membrane-impermeable but fluorescent dye. Only when the cell membrane integrity is destroyed, the propidium iodide can stain the DNA in cell nuclei, indicating dead and necrotic cells.

Flow cytometric analysis of cells stained with calcein-AM and propidium iodide are shown Figures 3.5 to 3.7, examplary. Cell vitality was quantified by gating the calcein positive cells and the elimination efficiency was quantified by gating propidium iodide positive cells in the fluorescence histogram of the respective channel. Untreated cells showed less than 15% dead cells, while after NALI treatment more than 95% of targeted cells were eliminated, i.e. less than 5% of the treated cells retained their membrane integrity. Insignificant effect on viability was found for non-irradiated cells incubated with conjugates and for non-incubated cells, which were irradiated with radiant exposure up to 1000 mJ cm^{-2}.

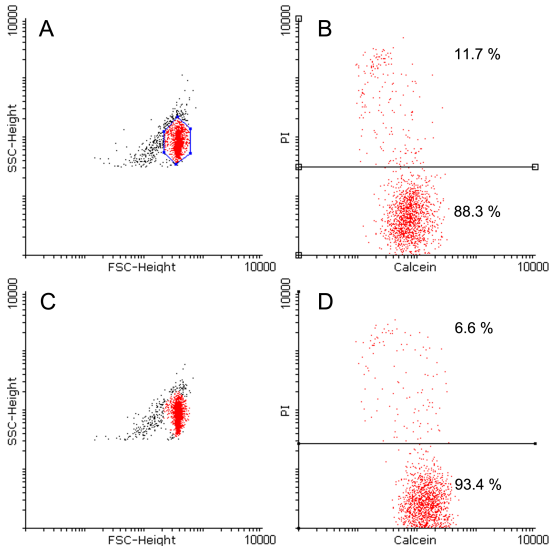

Figure 3.5: FACS analysis of KARPAS-299 cells, not incubated with AuNP (control). Cells to be analyzed for vitality by detecting the calcein and propidium iodid related fluorescence were selected in the forward scatter (FSC) vs. sideward scatter (SSC) dot plot (A, blue outlined area). Signal intensity of propidium iodine fluorescence plotted vs. calcein fluorescence (B) shows 11.7 % dead cells in the non-irradiated sample and 6.6 % dead cells for the cell sample irradiated with 875 mJ cm^{-2} (C, D).

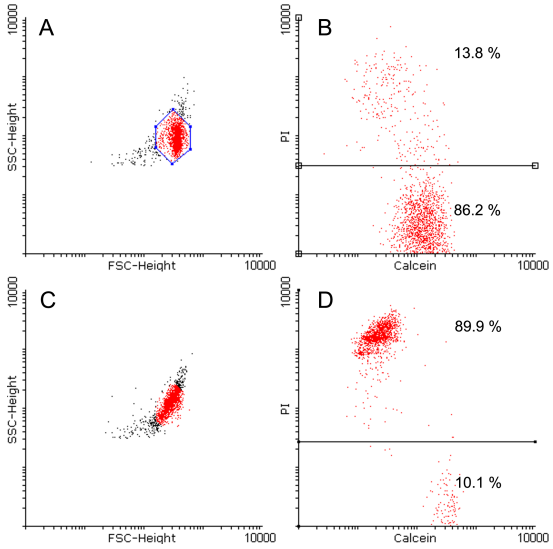

Figure 3.6: FACS analysis of KARPAS-299 cells, incubated with $4{\cdot}10^4$ AuNP conjugates per cell. Cells to be analyzed were selected in the FSC vs. SSC dot plot for non-irradiated cells (A, blue outlined area). The same selection was applied to the FSC vs. SSC dot plot for cells irradiated with 875 mJ cm^{-2} (C, outline not shown). Signal intensity of Propidium Iodine fluorescence plotted vs. Calcein fluorescence for the non-irradiated cells (B) shows 13.8 % dead cells and significant cell elimination of 89.9 % for the sample irradiated with 875 mJ cm^{-2} (D).

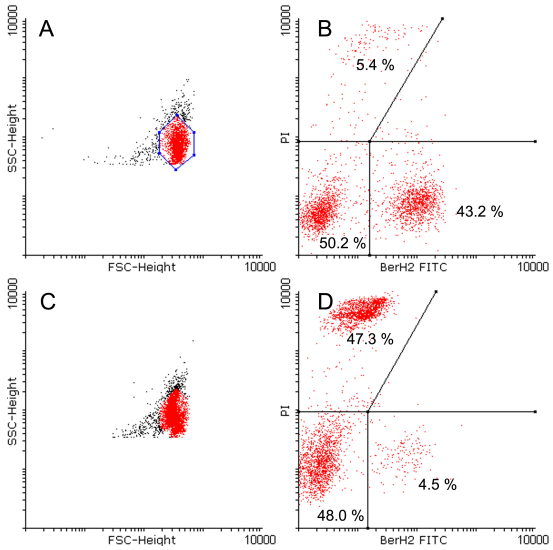

Figure 3.7: FACS analysis of a mixed cell culture containing 2/3 KARPAS-299 and 1/3 KARPAS-422 cells, incubated with $4{\cdot}10^4$ AuNP conjugates per cell. For the analysis non-irradiated cells were selected in the FSC vs. SSC dot plot (A, blue outlined area). The same selection was applied to the FSC vs. SSC dot plot for cells irradiated with 875 mJ cm^{-2} (C, outline not shown). In order to detect the CD30+ cells FITC labeled BerH2 antibodies were used. Signal intensity of Propidium Iodid fluorescence plotted vs. FITC fluorescence shows insignificant cell death for the non-irradiated sample (B) and 98% dead KARPAS-299 cells for the sample irradiated with 875 mJ cm^{-2} (D).

3.4 Results

3.4.1 Effective elimination of suspension cells directed by spherical gold nanoparticles

The cell vitality analysis after irradiation of KARPAS-299 cells incubated with 30 nm AuNP conjugates with 5 single pulses demonstrated effective and specific elimination of suspension cells. An exponential decrease of cell vitality was observed for both, the increase in AuNP conjugate concentration used for incubation and the increase of radiant exposure. Incubation with a concentration above 10^4, $2{\cdot}10^4$, $4{\cdot}10^4$ and $6{\cdot}10^4$ AuNP conjugates per cell and an irradiation with 5 pulses of radiant exposure with 875 mJ cm^{-2} caused elimination of around 72 %, 86 %, 97 % and 99 % of the CD30+ cells, respectively. Figure 3.8 shows the FACS result for KARPAS-299 cell vitality depending on the radiant exposures. In co-culture with KARPAS-422 cells a selective elimination was demonstrated. The fraction of vital KARPAS-299 cells (A) and of the KARPAS-422 cells (B) in the mixed cell culture depending on the irradiation is shown for incubation with different conjugate concentrations in Figure 3.9. Only an incubation with $6{\cdot}10^4$ AuNP conjugates per cell caused an unspecific elimination of the CD30- KARPAS-422 cells, while for lower incubation concentration .

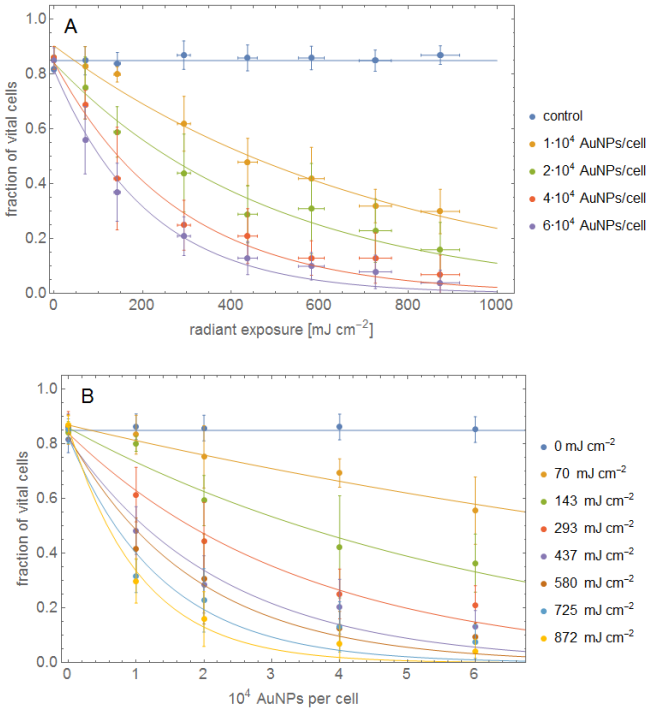

Figure 3.8: The fraction of vital cells in samples containing only KARPAS-299 cells after irradiation with different radiant exposure, for each 5 subsequent pulses were applied. The CD30+ KARPAS-299 cells were incubated with AuNP-BerH2 conjugates. Prominent cell elimination occurs for increasing irradiation, while non-incubated cells were unaffected (A). Increase in AuNP conjugate concentration used for incubation shows an exponential behavior (B).

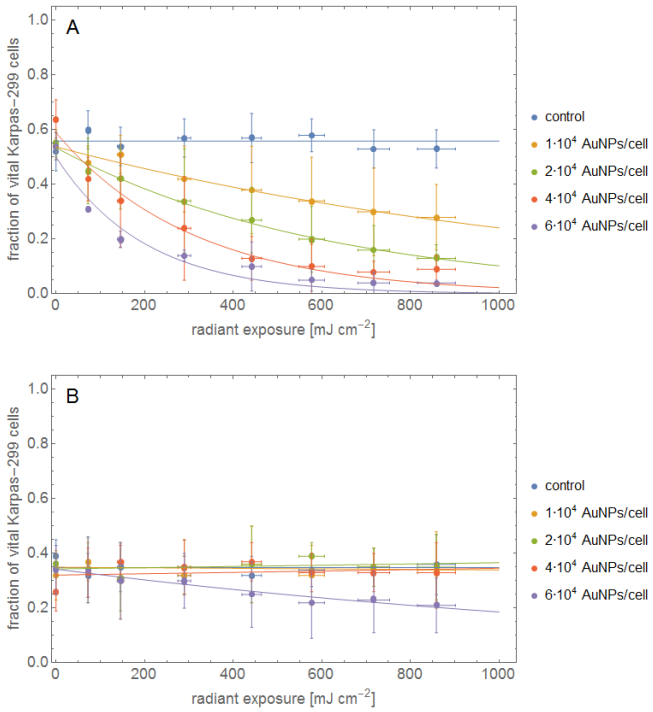

Figure 3.9: The fraction of vital KARPAS-299 cells (A) and KARPAS-422 cells (B) in samples of mixed cell cultures after irradiation with different radiant exposure. The cells were incubated with AuNP-BerH2 conjugates. The loss of vital KARPAS-299 cells increased with radiant exposure and with the concentration of AuNP conjugates used for incubation (A). The fraction of vital KARPAS-422 was constant over the range of applied irradiation, only for a larger incubation concentration of AuNP conjugates an unspecific loss of cell vitality occurs for irradiation above 400 mJ cm^{-2} (B).

3.4.2 Decreased elimination effectivity for adherent growing cells

In order to provide irradiation of the adherent cell grown on an area of 0.64 cm^2 (96 well plate, well diameter 9 mm) with up to 1 J cm^{-2} the beam was scanned over the sample at a scanning speed of 5 mm s^{-1}. The cell culture plate was moved through the beam in meander shape, while the laser was emitting with a repetition rate of 10 Hz. This pattern provided approximately 5 to 7 pulses per cell as it was applied on the suspension cells. In order to perform FACS analysis for quantification of the elimination efficiency the adherent growing cells were detached with trypsin.

For experiments with the OVCAR-3 cells a decreasing cell vitality was found for increasing irradiation and nanoparticle concentration as well (Figure 3.10). However, despite higher conjugate concentration applied for incubation the depletion of the OVCAR-3 cells was far less effective as the elimination rate of KARPAS-299 cells under comparable irradiation conditions. In contrast to the suspension cells the adherent cells incubated with $4{\cdot}10^4$, $6{\cdot}10^4$ and 10^5 AuNP conjugates per cell exhibited still a vitality of 55 %, 38 % and 27 % respectively upon irradiation with 275 mJ cm^{-2}, which remained nearly constant at that level for increasing radiant exposure.

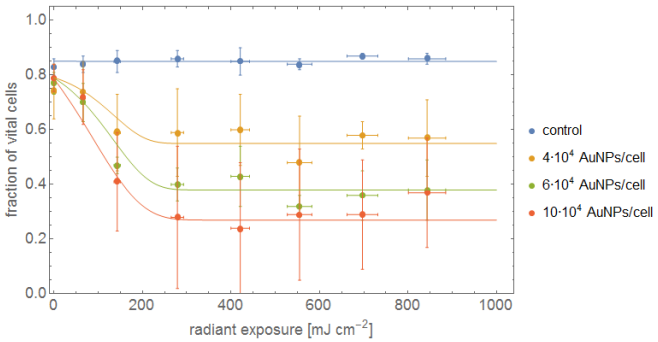

Figure 3.10: The fraction of vital OVCAR-3 cells after irradiation with different radiant exposure, for each 5 subsequent pulses were applied. The cells were incubated with AuNP-Erbitux conjugates. The loss of cell vitality significantly depends on the AuNP conjugate concentration used for incubation and shows saturation with the radiant exposure (solid lines). Non-incubated cells (control) were not effected by irradiation.

3.4.3 Cell elimination by laser irradiated gold nanorods

Besides spherical gold nanoparticles also rod-shaped nanoparticles were investigated for their capability to efficient cell elimination. Therefore, KARPAS-299 cells were incubated with AuNR conjugates and irradiated at a wavelength in the range between 770 nm and 810 nm of the peak absorption. For further comparison, nanorod incubated KARPAS-299 were also irradiated at 532 nm .

After incubation with AuNR conjugates and pulsed laser irradiation the fraction of vital cells exponentially decreased with increasing radiant exposure. At maximum applied radiant exposure, up to 90% of the nanorods-loaded KARPAS-299 cells were damaged, while the 85 % to 95 % of the KARPAS-299 cells without gold nanorods, remained vital independently of the radiant exposure (Figure 3.11). The values of cell elimination found for the control cells are typical for pipette-handled cell cultures.

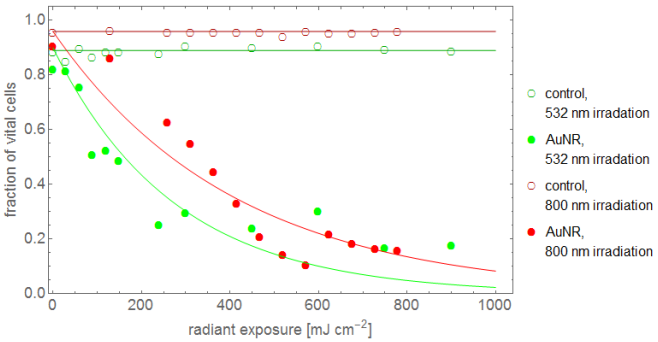

Figure 3.11: The fraction of KARPAS-299 cells showed prominent cell death after incubation with AuNR conjugates and irradiation with different radiant exposure. The loss of vital cells increased with radiant exposure showing exponential behavior, while cells without AuNR conjugates showed insignificant effect (solid lines).

3.5 Discussion

The study shows, that nanoparticle mediated laser induced cell elimination utilizing nanosecond pulsed laser irradiation is applicable on both, cells in suspensions and adherent growing cells. The specific functionalization of the AuNPs and short pulsed irradiation provide potentially high purity, selectivity and speed in a simple optical set up for the purification of cell cultures.

High cell elimination efficiency of spherical and rodshaped AuNP

An efficient cell elimination requires incubation with a sufficiently high concentration of conjugates. However, during incubation only a fraction of the conjugates binds to the target site. The quantification of the bound conjugates per cell is complex and involves analysis of the amount of receptors on the cell membrane as well as determining the number of conjugates, which can participate in the specific binding. Also estimating the AuNP conjugate concentration by measurements of the absorption spectra is imprecise. Thus, AuNP conjugate concentration was varied for elimination experiments with samples containing KARPAS-299 exclusively and with samples of KARPAS-299 cell that contained KARPAS-422 in co-culture. This showed, that a concentration of $4{\cdot}10^4$ AuNP conjugates per targeted cell provided efficient cell elimination of 99 %, while non-specific elimination was measured for incubation with $6{\cdot}10^4$ AuNP conjugates per cell. The unspecific cell elimination can be caused by accumulation of the AuNP also on CD30- cells due to cellular uptake related to the high nanoparticle load. Also unspecific binding of the AuNP-BerH2 conjugates to membrane proteins could affect the CD30- cells. According to the exponential relation between cell vitality and the conjugate concentration used for incubation a elimination efficiency of 99 % is expected for a radiant exposure with 875 mJ cm^{-2} after incubation with around $5{\cdot}10^4$ AuNP-BerH2 conjugates per CD30+ cell.

The application of NALI to eliminate adherent cells shows a lower efficiency than for the cells in suspension. An exact cause could not be identified on the basis of the irradiation experiments. To improve cell elimination for adherent cells increasing the amount of AuNP conjugates for incubation may not lead to desired results. A high AuNP conjugate concentration can also lead to an unspecific elimination of non-targeted cell types. Thus, to clarify, whether the cell size, accessible cell surface and the target proteins effect the elimination efficiency, further experiments should be conducted.

Utilizing rod-shaped nanoparticles for the application of NALI to eliminate cells in suspension contrary results were found for the nanosecond pulsed irradiation at two different wavelengths. Figure 3.12 depicts the fraction of vital KARPAS-299 cells dependent on the mean absorbed energy per AuNR and AuNP respectively. In contrast to the higher absorption at their LSPR peak wavelength, gold nanorods irradiated with a wavelength of around 800 nm (red circles) showed a reduced efficacy of cell killing per absorbed energy as compared to the effective cell elimination of AuNP with a diameter of 30 nm (blue circles). For reaching 50% cell death an approximately 5-fold radiant exposure when irradiating AuNR with 800 nm was required, which converts to 5-fold increased mean absorbed energy in comparison to 532 nm irradiation of AuNP. Cell elimination was also more effective - based on absorbed energy - when nanorods were irradiated with a wavelength of 532 nm (green circles), which is located in the less absorbing TSPR band with a peak at around 520 nm. In comparison to a 532 nm irradiation for reaching 50% cell death also a five-fold radiant exposure was needed with near infrared irradiation at 770 nm, which converts even to a 15-fold increased energy deposition in the nanoparticles.

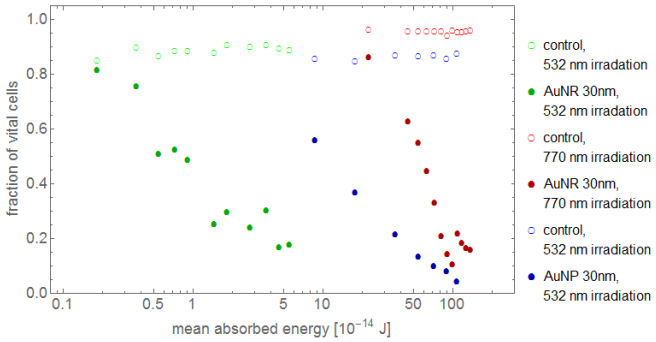

Figure 3.12: Vitality of KARPAS-299 cells after incubation with AuNR and AuNP conjugates plotted against absorbed energy per particle. The vitality decreased for increasing mean absorbed energy. Irradiation wavelength of 532 nm and 770 nm.

Bleaching of plasmon resonance absorption reduced cell elimination efficiency

The low cell elimination efficacy of gold nanorods under near-infrared irradiation at 800 nm may be caused by large individual variation of the particle absorption or by loss of absorption during the irradiation. The utilized gold nanorod preparations contain a polydisperse distribution of particle sizes, which origins from the synthesis processes, leading to an inhomogeneous broadening of the absorption band. Further, the orientation of the rodshaped particles towards the polarized laser beam introduces a significant variation of energy deposition inside the particles. Besides orientation the refractive index of the surrounding medium affects the spectral position of the LSPR band strongly. A vapor layer formation due to temperature increase above the spinodal point causes a change in the refractive index and subsequently results in LSPR band shifting to shorter wavelengths with increasing bubble expansion [18]. For the case that the particle temperature increase remained below the melting temperature, loss of absorption at the irradiation wavelength can be considered transient. A loss of the rod-like shape follows on a temperature increase that leads to partial or complete melting, whereby the LSPR band shifts into the visible range. In that case a absorption loss at the irradiation wavelength is permanent [18]. Figure 3.13 schematically illustrates five phases of increasing heat involved in the transient and permanent absorption bleaching. During irradiation time at sufficient radiant exposure the heat stored in a thin layer around the AuNR increases from room temperature (1) to the spinodal point (2), where bubble formation occurs while the melting and deformation process of the AuNR begins (3). The surrounding vapor combined with the deformation cause reduced absorption ability of the AuNR. At sufficient radiant exposure the particle temperature further increases causing complete melting and reshaping to a spherical AuNP (4) which finally cools down to room temperature after the irradiation (5).

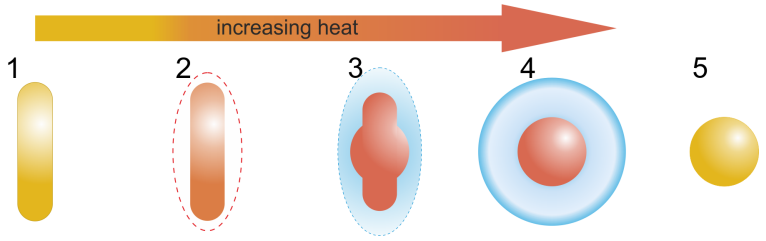

Figure 3.13: Different phases of increasing heat involved in the transient and permanent absorption bleaching during the incident laser pulse. Heat stored in a thin layer around the AuNR increases from room temperature (1) to the spinodal point (2). Bubble formation can occur while the melting and deformation process of the AuNR begins (3). At reduced absorption the energy deposition leads to further temperature increase, complete melting forming a spherical AuNP (4) cooling down to room temperature after the irradiation (5). Figure adapted from Figure 17 in [18].

Time-resolved absorption measurements with nanosecond time resolution verified the extreme sensitivity of the LSPR peak position due to formation of vapor bubbles around the particles [18]. Figure 3.14 shows two exemplary cases of polarization dependent energy absorption and subsequent temperature increase within a gold nanorod and in the water near its surface. For the calculation, a nanorod 40 nm in length and 10 nm in diameter on the small axis, which exhibits peak absorption at the wavelength of 770 nm, was considered. The temperature increase during the irradiation pulse is calculated for the material parameters $\rho_p = 19300\,\mathrm{kg\,m^{-3}}$, $c_p = 130\,\mathrm{m^2\,K^{-1}\,s^{-2}}$, $\rho_l = 1000\,\mathrm{kg\,m^{-3}}$, $c_l = 4190\,\mathrm{m^2\,K^{-1}\,s^{-2}}$, $\varkappa_l = 1.38425{\cdot}10^{-7}\,\mathrm{m^2\,s^{-1}}$ and $G = 105\,\mathrm{MW\,m^{-2}\,K^{-1}}$. For light polarized parallel and under an angel of 45 degree to the long particle axis absorption the cross sections at 770 nm are $\sigma_{abs} = 5.276{\cdot}10^{-15}\,\mathrm{m^2}$ and $\sigma_{abs} = 1.317{\cdot}10^{-15}\,\mathrm{m^2}$, respectively. Since the temperature calculation cannot consider parameter variation with temperature increase over time, constant values for room temperature are used. The resulting error in calculated temperature (Figure 3.14, solid lines) is considered negligible until the spinodal point of water is reached . Calculation of temperature above the spinodal point with the same constant parameters (Figure 3.14, dashed lines) is incorrect due to strong changes for instance in absorption and heat flow caused by the bubble formation. Here, peak absorption is decreased to a lower limit of $\sigma_{abs,v} = 0.03{\cdot}10^{-15}\,\mathrm{m^2}$. From the time

point of bubble formation, the energy deposited in the particle can be calculated considering the reduced absorption cross section. Based on this energy density allows estimating, whether partial or complete melting of the particles follows the bubble formation.

The transient and permanent bleaching of the near-infrared absorption band that occurs during an irradiation pulse strongly limit the thermal and mechanical destruction radius around the irradiated nanorod. This explains the insufficient cell elimination with nanosecond pulsed irradiated nanorods, which was previously assigned solely to photothermal reshaping [143].

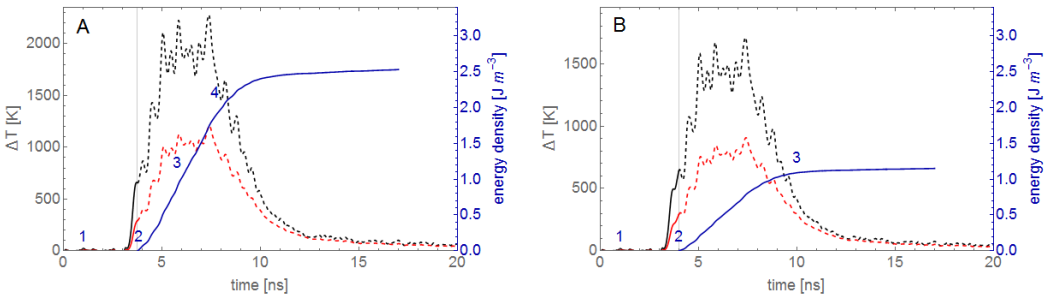

Figure 3.14: Temperature increase of a gold nanorod (black) and in the surrounding water at the particle surface (red) during a measured irradiation pulse with radiant exposure of 7.5 mJ cm^{-2} at the LSPR absorption peak. The incident laser pulse exhibited linear polarized light (A) parallel and (B) at an angle of 30 to the long nanorod axes. The temperature increases from room temperature (1) to the spinodal point (2) (solid lines). Here, bubble formation is assumed and significant change in optical parameters is expected. In the equations for temperature calculation the parameter variation, that occurs during bubble expansion, could not be considered. Dashed lines show temperature increase for unchanged parameters. After bubble formation the deposited energy density (blue line) was calculated for the changed conditions. Increased energy density leads to partial melting (3) and complete melting (4) of the nanorod.

3.6 Conclusion

The specific functionalization of the AuNPs and short pulsed irradiation provide potentially high purity and selectivity. Calculation of the temperature increase showed, that an efficient cell elimination required radiant exposure which inevitably leads to bubble formation around the irradiated spherical and rod-shaped gold nanoparticles. This bubble formation is also the cause of significant differences in the cell elimination efficiency observed in cell experiments with the different particles, in particular with the utilized nanorods. Contrary to the assumption that irradiation with a wavelength at the highest absorption achieves the greatest possible elimination effect, nanorods exhibit even the lowest cell elimination under irradiation with a wavelength at their absorption peak in the LSPR band. Even though, the spherical particles with 30 nm diameter exhibit much stronger absorption than the AuNR on the irradiation wavelength of 532 nm cell elimination efficiency of the spherical particles is lower than the elimination efficiency of AuNR irradiated at the much lower absorbing TSPR.

The low efficiency when utilizing the LSPR absorption of nanorods is reasoned in the strong sensitivity of this absorption band to changes in the optical properties of the surrounding medium., which exhibits transient and permanent absorption loss due to bubble formation. Both, the TSPR band of the AuNR and also the absorption band of the spherical AuNP, which are less affected by the bubble formation.

Nevertheless, bubble formation around nanosecond pulsed irradiated AuNP is assumed the main cause of cell elimination since thermal damage can be ruled out for two reasons. First, the nanoparticle mediated effects on cells required surprisingly high radiant exposures of up to 1000 mJ cm^{-2} for elimination of the targeted cells. To a large extent, the induced temperature increase calculated for a thin water layer on the surface of the spherical and rod-shaped gold nanoparticles exceeded the spinodal point. This temperature is considered the minimum

condition for bubble formation. However, only insignificant cell elimination was measured under the corresponding radiant exposure. Second, the volume around a nanoparticle is heated to temperatures above 40 °C for less than 10 ns. This time is not sufficient to effect protein or membrane integrity by denaturation processes. Hüttman et al. observed that decreasing heating time from micro- to nanoseconds leads to change in damage mechanism from thermal denaturation to mechanical damage [3]. Radt also concluded from his protein inactivation experiments on nanosecond pulsed irradiated gold nanoparticles that thermal denaturation is impossible [8]. It is plausible to deduce that thermal denaturation hardly contributes to cell elimination.

However, experiments, which revealed processes involved in cell elimination were conducted on solutions of randomly distributed nanorods. The measured signals represented an integral over different nanobubble formations, whereas the distinct energy dependency of bubble formation onset and expansion can not be determined. Thus, for investigations on the cell elimination mechanism and for optimizing this technique for different applications, knowledge of the cause of this discrepancy is required. For this purpose, it is necessary to carry out measurements on individual particles, which, in addition to the measurement of bubble size, also enables measuring influencing parameters such as the individual particle size. The detection of bubbles around particles located on artificial or biological membranes could provide insight into important mechanisms of effects of nanoparticles on cells.

4 Laser induced release of siRNA from gold nanoparticles

Controlled release of DNA, siRNA or bio-active molecules such as drugs at specific sites is of fundamental interest for selective therapies or basic studies in cell biology. Therefore, light-controlled release provides the advantage of high temporal selectivity of biological effects, while AuNP provide high spatial selectivity. Irradiation with short laser pulses can release for instance nucleic acids from gold nanoparticles.

The AuNP can easily be modified by binding biologically active molecules via a thiol-bond to the nanoparticle surface. Experiments with 15 nm and 30 nm AuNP demonstrated in this thesis the release of coumarin labeled siRNA induced by nanosecond pulsed laser irradiation. The coumarin labeling was used to detect siRNA released into the medium. After irradiation fluorescence in the medium increased, when siRNA was released by breaking the AuNP-thiol bond. The experiments showed, that the molecular release by nanosecond pulsed irradiation is based on a different mechanism than that of continuous or femtosecond irradiation. Local temperatures are considerably higher and bubble formation plays a crucial role in siRNA release and also in unwanted damage to the siRNA as well as to the surrounding cellular structures.

4.1 Introduction

Gold nanoparticles allow effective transfer the optical energy to heat. Locally high temperature confined to the AuNP and its close surrounding is generated by pulsed laser irradiation [3, 4, 18] potentially leading thermal denaturation, disruption, or photochemical modifications of nearby biological structures [5]. In principle, all these physical mechanisms can contribute to dissociation of the thiol bond between the AuNP and DNA or siRNA.

Release of DNA strands, which were either linked directly or by a complementary DNA strand to the AuNP, was demonstrated for femtosecond (fs) [144, 145], nanosecond (ns) [48] and continuous wave (cw) [145] laser irradiation. Mainly two different mechanisms for release were found for fs and cw pulses. Under fs pulsed irradiation energy is supplied within the charge carrier relaxation time [144, 145] and chemical bond breakage occurs due to the temperature increase of the free valence band electrons by 3 to 4 times hotter than the lattice [85], which can further lead to thiol-AuNP bond dissociation. Under cw irradiation, when the particle is in thermal equilibrium with the surrounding medium, melting of the double strand occurs at temperatures below 60°C [145]. Long time exposure to temperatures of 80°C can also destroy covalent thiol bonds [146].

In the regime of nanosecond laser pulses the electrons and lattice atoms of the particle exhibit the same temperature. However, a strong temperature gradient develops around an irradiated particle, where the elevated temperature decreases to the bulk temperature within a distance of several nanometers from the particle surface [18]. In this irradiation regime both, thiol-AuNP bond dissociation and dehybridization were observed simultaneously [48]. However, the effects were neither correlated with the local temperature increase nor impact on the siRNA and on the surrounding of the nanoparticle were discussed.

Because of the locally confined heating nanosecond pulsed irradiation of the gold particles appears especially attractive for potential applications. Under cw irradiation heat diffusion causes non-local increase of the bulk temperature, which may have unwanted detrimental effects on cell vitality. Related to their high peak powers fs-pulses may produce unwanted effects such as the near-field ablation from the AuNP [147] and fragmentation due to coulomb explosion [148] in the sample.

Thus, in order to estimate at which temperature increase the thiol-AuNP bond dissociates, conjugates with AuNP of two different sizes, to which the fluorescence labeled double-stranded siRNA was bound, were utilized. The fluorescence dye was attached to the strand coupled to the AuNP surface, which allowed for association of the detected release with a thiol-AuNP bond dissociation only. Sequences of 600 pulses over a time period of 60 seconds at increasing radiant exposure were applied to the whole sample. Release was quantified by changes of the nanoparticle absorption spectra and the increase of unbound fluorescing molecules in the solution. The temperature increase was calculated using an analytical thermal model, which accounts for plasmonic absorption, temporal shape of the laser pulses and thermal conduction from the particles via the surface into the surrounding water (cf. Chapter 2.2.2). Temperatures

at which release occurs shall pin down the physical processes cavitation bubble formation and particle melting which contribute to the molecular release and potential side effects that can limit the intracellular application.

4.2 Experimental Methods

4.2.1 Functionalization of gold nanoparticles with siRNA

In order to ensure RNase-free conditions all involved chemical solutions were treated with 0.1 % DEPC. The 15 nm AuNPs with a concentration of $1.4 \cdot 10^{12}$ particles ml^{-1} and 30 nm AuNPs with a concetration of $2.0 \cdot 10^{11}$ particles ml^{-1}, both citrate-modified (BBI, Cardiff, UK), were incubated with a freshly reduced fluorescent GAPDH-siRNA (GAPDH: Glyceraldehyde 3-phosphate dehydrogenase; BioSpring GmbH, Gerrmany) solution in water (14µl of an 18 µM or 14µl of a 27 µM solution respectively). Within 1 h, a 50 mM phosphate buffer with pH 7.5 was slowly added to the colloidal solution, followed by ultrasound treatment for 10 s. After incubation at room temperature (RT) for 12 h under the exclusion of light, AuNPs were purified by two successive centrifugations- ($22 \cdot 10^3$ g, 30 min, 4 °C) and resuspension-cycles in 800 µl of a 5 mM phosphate buffer with pH 7.5. To probe the breakage of the thiol-AuNP bond exclusively, the coumarin molecule was conjugated to the sense strand as illustrated in Figure 4.1. Dynamic light scattering (DLS) measurements showed no aggregation of the conjugates after synthesis (cf. Figure 4.2).

Figure 4.1: Schematic illustration of the AuNP-siRNA conjugate used to demonstrate the targeted release by pulsed laser irradiation.

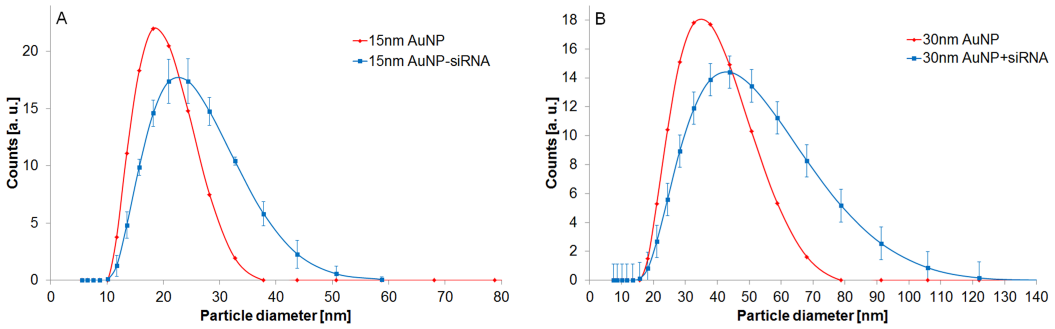

Figure 4.2: DLS measurements of (A) 15 nm and (B) 30 nm AuNP (red lines) and corresponding AuNP-siRNA conjugates (blue lines).

Conjugates were imaged by TEM (Type JEM-1011, Jeol, Peabody, MA, USA) before and after irradiation. 3 µl of each sample were placed on TEM grids (copper mesh with Formvar film no. SF162-3, Plano GmbH, Germany) and imaged after drying process. The manufacturer information (BBI, Cardiff, UK) regarding the particle size was verified by manual analysis of hundred particles in TEM images for non-irradiated samples. According to the technical data provided by the manufacturer, the gold nanoparticles had a mean diameter of 14.4 nm (Product Code EM.GC15, Batch 15673) and 30.6 nm (Product Code EM.GC30, Batch 16645). The coefficient of variation was $< 8\%$. Evaluation of TEM images for the size distribution of the 30 nm AuNP showed a mean particle diameter of 29.9 nm and a size variation coefficient of around 9.5 %, which was slightly higher than given by the manufacturer data sheet.

4.2.2 Irradiation of samples with AuNP-siRNA conjugates

The irradiation of samples of the AuNP-siRNA conjugates was carried out with help of the laser setup, which was used for the cell elimination experiments (cf. Chapter 3.3.4, Figure 3.4). For irradiation of the whole sample, which was placed in 384-well plates (Quartz well plate, well diameter 3.4 mm), the irradiation spot diameter in the sample plane was adjusted by means of a converging lens. In order to determine the single pulse radiant exposure, the beam radius, where intensity falls to 1/e of the peak intensity in the beam center, was determined with the help of the knife edge method and the pulse energy was measured with a pyroelectric detector (PE25-C, Ophir). All particles of a sample were irradiated simultaneously with 600 pulses at a repetition rate of 10 Hz for 60 s. The samples were not stirred, whereas non-local effects may occur only due to Brownian motion of the conjugates. Pulses with different radiant exposure up to 250 mJ cm^{-2} were applied.

4.2.3 Detection of released siRNA

To link the theoretical temperature calculations with the siRNA release, absorption of the AuNPs and fluorescence of the released dye were measured after irradiation of the samples with different radiant exposures. Particle extinction was measured before and after irradiation with a UV-Vis spectrometer (U-2900, Hitachi) in order to detect changes of the local index of refraction, when siRNA is released, or due to size changes and aggregation of the particles.

Measuring release by refractive index change is unsuitable to quantify the molecular release, since shift of the absorption peak is expected to be not sensitive enough. Thus, the he amount of siRNA released by pulsed laser irradiation was determined by the increase of fluorescence in the supernatant measured with a spectral fluorometer (Fluoromax, Horiba formerly Spex) after centrifugation of the sample ($21 \cdot 10^3$ g, 20 min at 4 °C, Heraeus Fresco 21, Thermo Fisher Scientific). The fluorescence of the coumarin dye molecule utilized for labeling allows for a simple optical detection of the siRNA. The optically detection is fast, however, an information in terms of siRNA integrity and functionality is not provided.

To verify the optically induced release, the remaining siRNA on the AuNPs was determined in a complementary measurement. The remaining pellet was redispersed in a solution of Dithiothreitol (DTT, Sigma-Aldrich, USA) for 20 h, which releases the remaining siRNA. The fluorescence in the supernatant was measured again after further centrifugation. Figure 4.3 illustrates schematically the controls and proof of release.

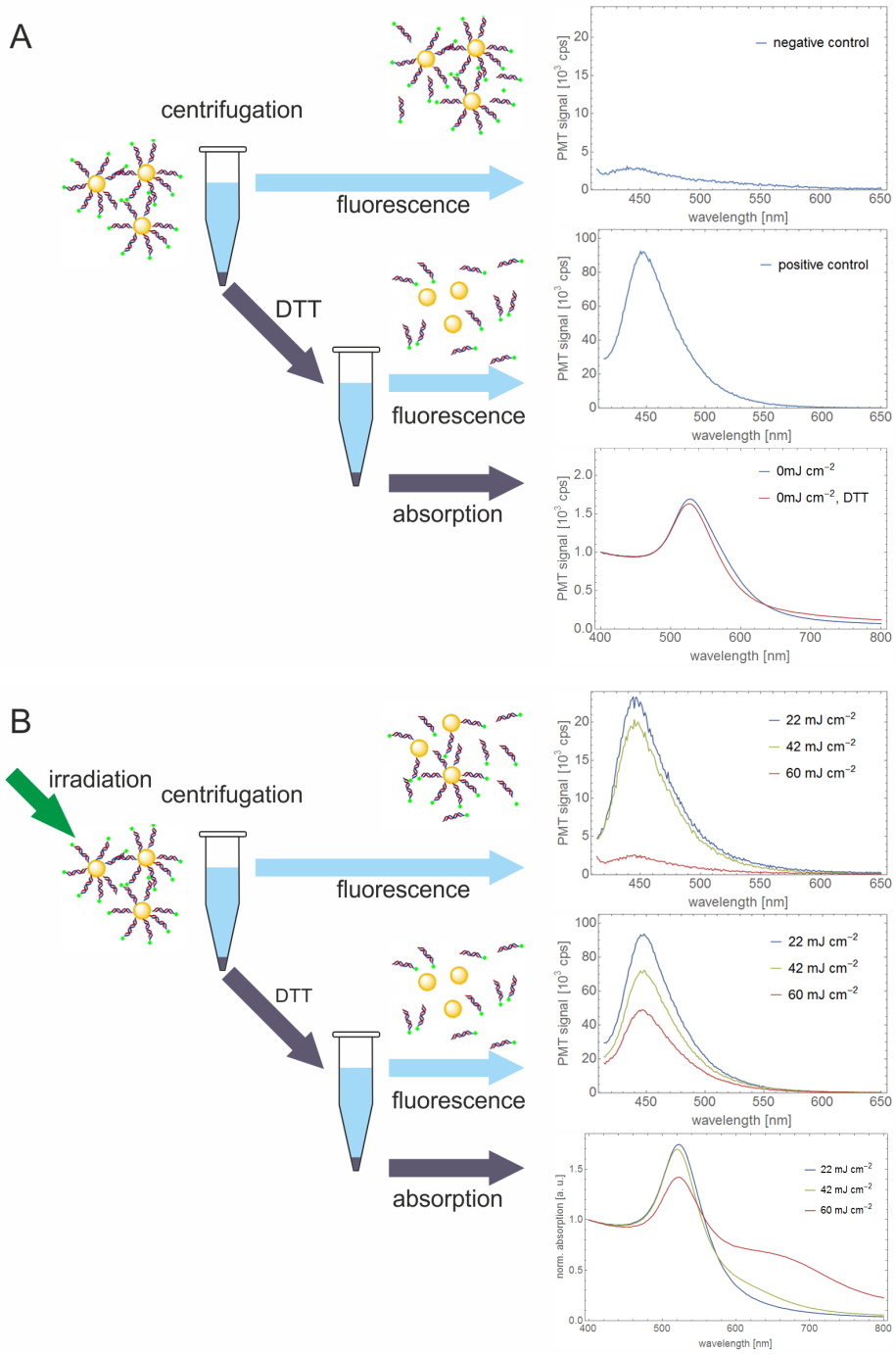

Figure 4.3: Detection of siRNA release by fluorescence measurements of the supernatant after centrifugation. Absorption measured for the resuspended pellets for detection of particle size changes and aggregation. (A) Non-irradiated conjugates exhibit low concentration of fluorescence dye labeled siRNA in the supernatant after centrifugation and served as negative control. Addition of DTT releases the siRNA and was used as positive control and reference fluorescence for full release, to which fluorescence of samples irradiated at different radiant exposure were related. The Absorption spectrum of the non-irradiated sample shows after DTT a small blue-shift. (B) Fluorescence and absorption measurements of irradiated samples after different centrifugation steps following the same protocol as in (A).

Non-irradiated conjugates served as negative control. For quantification of the fluorescence after full releases and as a positive control non-irradiated samples were incubated in DTT for 20 h. To analyze the dependency of siRNA release on radiant exposure a value of relative fluorescence was calculated from the integral of the measured fluorescence over the wavelength

range between 420 nm and 600 nm divided by the integral of the fluorescence measured for the positive control as described by

$$f_{rel} = \frac{\int I_{fluo,s}(\lambda)\, d\lambda}{\int I_{fluo,ctrl}(\lambda)\, d\lambda}. \tag{4.1}$$

Assuming that the dye molecule is not separated from the siRNA or destroyed by the irradiation, the relative fluorescence intensity should be proportional with the amount of released siRNA.

As an example, Figure 4.4 shows coumarin fluorescence spectra of the supernatant measured after laser irradiation of conjugates with 30 nm AuNP and coumarin labeled siRNA and the complementary measurement of fluorescence after redispersing the samples in DTT solution. The corresponding relative fluorescence f_{rel} (Equation 4.1) is shown in Figure 4.5.

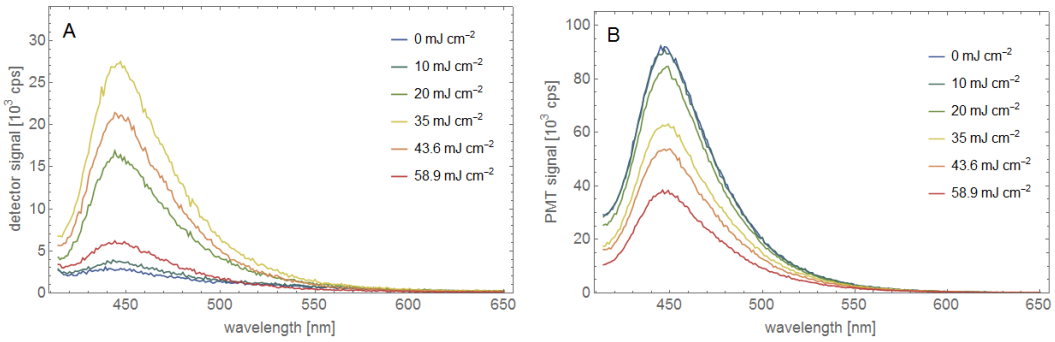

Figure 4.4: A) Fluorescence spectra in the supernatant after irradiation with different radiant exposure. Increase of fluorescence is caused by increasing release of the coumarin labeled siRNA. B) Fluorescence spectra in the supernatant after irradiation and the DTT treatment after irradiation. Particle diameter was 30 nm.

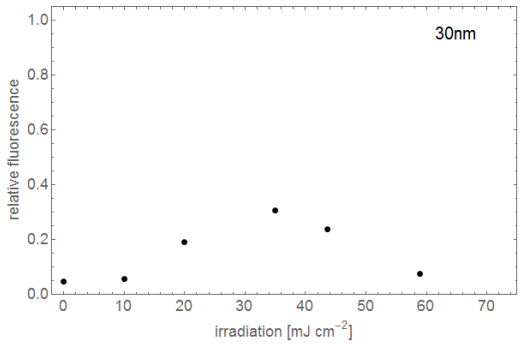

Figure 4.5: Relative fluorescence f_{rel} calculated for the fluorescence spectra detected in the supernatant of conjugates with 30 nm AuNP after irradiation with different radiant exposures. The relative fluorescence increased to a maximum of 30 % for irradiation with 35 mJ cm^{-2}, above a loss of fluorescence was detected.

4.3 Results and discussion

4.3.1 Change of the nanoparticle absorption

To study the molecular release of siRNA extinction spectra were measured after irradiation at different radiant exposure (Figure4.6). At both particle sizes a blue shift, which increased with the irradiation by a maximum of 4 nm was observed. For the conjugates with 30 nm AuNPs the extinction spectrum started to change when irradiated with radiant exposure above 10 mJ cm^{-2}, while the 15 nm conjugate required irradiation above 50 mJ cm^{-2} to cause a visible peak shift (Figure 4.7 A). Relating the extinction changes to the calculated increase of particle temperature, which would occur under the single pulse radiant exposure, the behavior becomes similar for both particle sizes (Figure 4.7 B). Most of absorption shift occurs at particle temperatures

below 1300 K. At higher temperature a significant increase of absorption in the wavelength range above 600 nm was observed, which can be attributed to increasing effective particle size (Figure 4.8). This was observed previously under ns-pulsed laser irradiation of AuNP nucleic acid conjugates[48, 145] and was related to aggregation, which causes delocalizing of the electron cloud over all adjacent AuNPs with a multitude of plasmon modes resulting in a broadening and damping of the SPR. Aggregation is probably caused by a loss of the surface stabilization . Therefore, in can be concluded, that the calculated particle temperatures of 1300 K most of the siRNA is released from the AuNP surface.

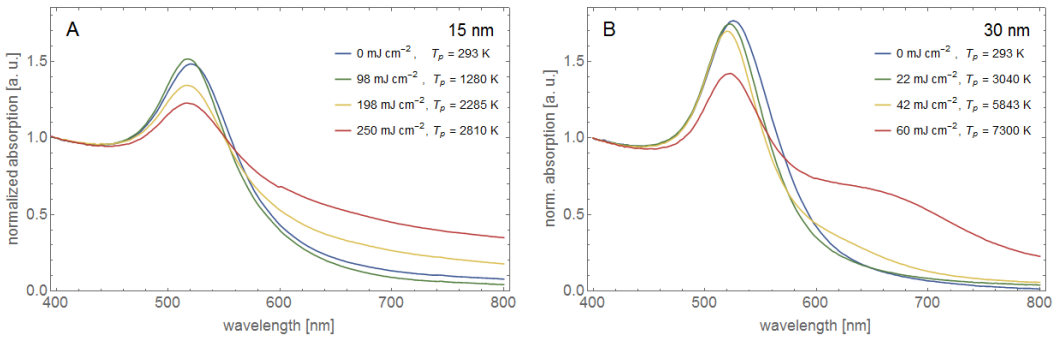

Figure 4.6: Absorption spectra of 15 nm and 30 nm AuNP-siRNA conjugates after irradiation at different radiant exposure. Spectra were normalized to their absorption at 400 nm. With increasing irradiation the absorption band peak exhibits a shift to shorter wavelengths. At higher radiant exposure absorption at 520 nm decreases and in the range above 600 nm absorption increases indicating aggregation.

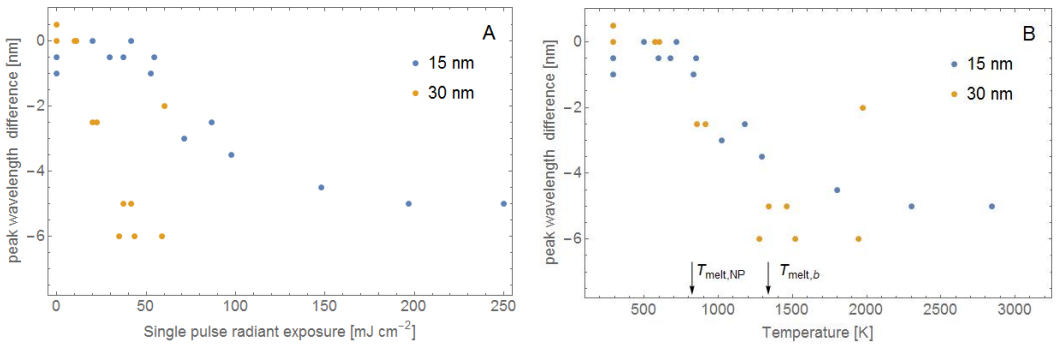

Figure 4.7: Blue shift of the peak extinction wavelength occurs for of both particle sizes at different radiant exposure (A), but at similar calculated particle temperatures (B).

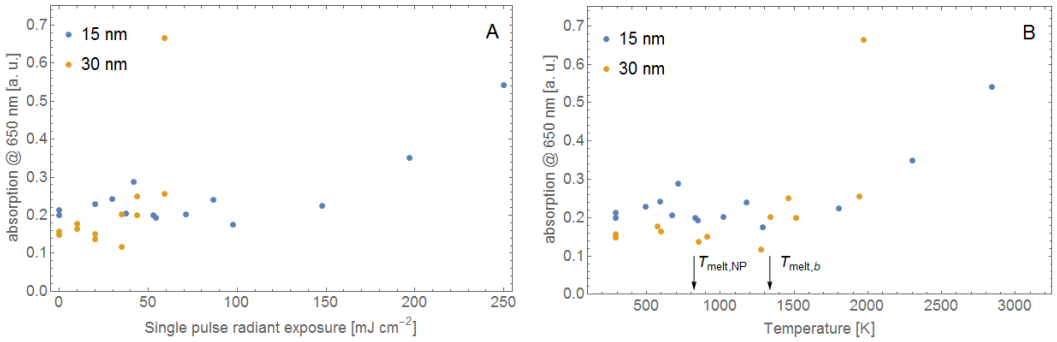

Figure 4.8: (A) Increase of particle extinction at 650 nm after irradiation with different radiant exposure. (B) Increase of absorption is observed in both particles at calculated temperature increase of above 1300 K.

Relating absorption peak shift and absorption increase in the range above 600 nm to calculated

particle temperatures corrects for differences in thermal conduction due to particle size and for the different absorption cross sections, $0.16 \times 10^{-15} m^2$ for 15 nm diameter and $1.40 \times 10^{-15} m^2$ for 30 nm (Equations 2.10 to 2.12). The good correspondence for the two different particle sizes suggests that particle temperature has large impact on the release of siRNA. However, changing absorption and heat conduction make the calculated temperatures after phase changes of water and gold completely unrealistic. Therefore, temperatures given here are only extrapolations from a regime, were all optical and thermal parameters remain constant. Calculation of the deposited energy $\triangle E_p$ (Equation 3.1) allows to account for both, the changed absorption and the changed heat diffusion. Nevertheless, temperature calculation should be valid until the spinodal point, which is assumed the minimum temperature of bubble formation.

Furthermore, the size distribution of the conjugates can influence the amount of released siRNA. Absorption and thus the temperature increase after irradiation with a given pulse duration and radiant exposure depend on the particle size. For particles with diameters up to around 70 nm this dependence is in an adverse manner: absorption increases with AuNP size, while the achieved temperature increase becomes smaller due to the larger heat capacity. Thus, larger particles will reach the spinodal temperature at which formation of a cavitation bubble is assumed at an earlier time point after irradiation onset. This reduces further energy deposition in the particle. Figure 4.9 shows the calculated time course of energy deposition (Equation 3.1) in 27 nm, 30 nm and 33 nm AuNP irradiated with a 4 ns pulse and radiant exposure of 25.2 mJ cm^{-2}.

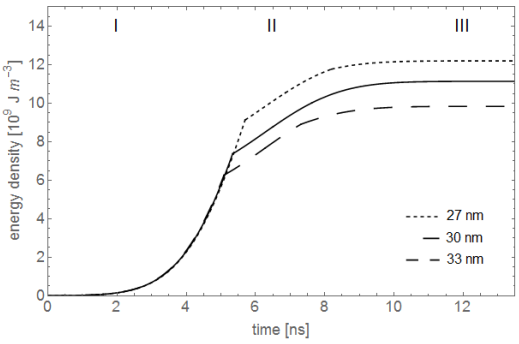

Figure 4.9: Calculated energy density in particles with 27 nm (short dashed), 30 nm (solid) and 33 nm (long dashed) irradiated with a Gaussian shaped 4 ns pulse duration and radiant exposure of 25.2 mJ cm^{-2}. Three heating phases (I – III) can be distinguished. I) initial phase of heating the AuNP until spinodal temperature is reached in the water. II) Energy density grows during AuNP temperature increase to 1336 K, while bubble formation causes thermal isolation and decreased absorption. The particle melts at constant particle temperature. III) Energy deposition in a liquid gold particle. The discontinuity at the beginning of phase II indicates bubble formation.

Calculations with help of Equation 3.1 showed that during the bubble formation around particles with diameters in the range of 27 nm to 33 nm a sufficient amount of energy was deposited to provide latent heat of melting (Figure 4.9). Resulting changes of the particle shape after irradiation indicate that melting temperatures were reached . These findings were verified by TEM images shown in Figures 4.10 and 4.11. For irradiation with radiant exposure around 10 mJ cm^{-2} surface melting of the AuNP was found, since loss of the facets of the 30 nm AuNP was observed. Radiant exposure of 23 mJ cm^{-2} led to significant reshaping of 30 nm particles, while for irradiation above 50 mJ cm^{-2} fragmentation was found. However, it was impossible to analyze siRNA loss as a function of the irradiation based on visualization of the nanoparticle siRNA coverage by means of TE microscopy. Because siRNA has the molecular size of only 19 to 20 base pairs, a possible inter particle distance could not be resolved. The molecule corona around the particle was not visible under TE microscopy.

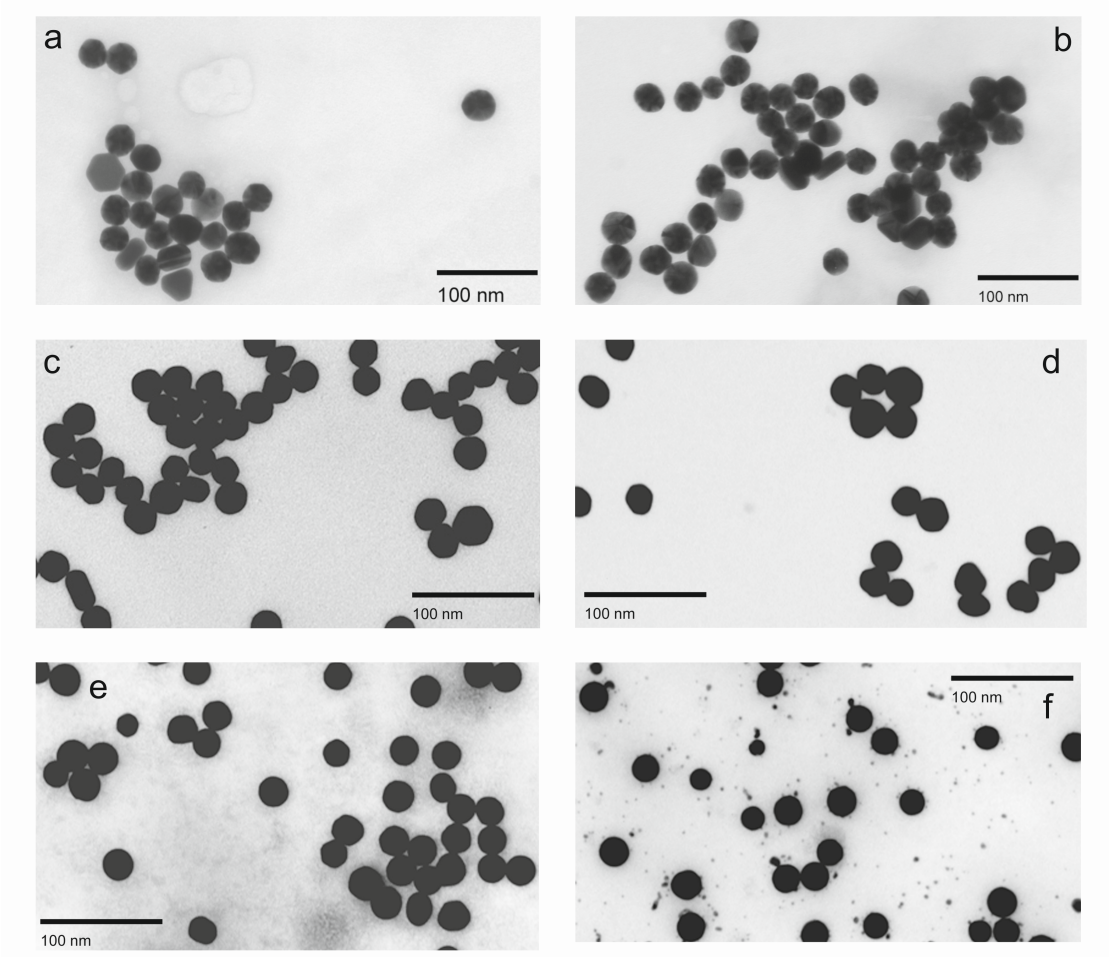

Figure 4.10: TEM images of 30 nm AuNP without siRNA coverage before irradiation (A) and after radiant exposure of 5.8 mJ cm^{-2} (B), 10.1 mJ cm^{-2} (C), 24.5 mJ cm^{-2} (D), 50.0 mJ cm^{-2} (E), 100 mJ cm^{-2} (F)

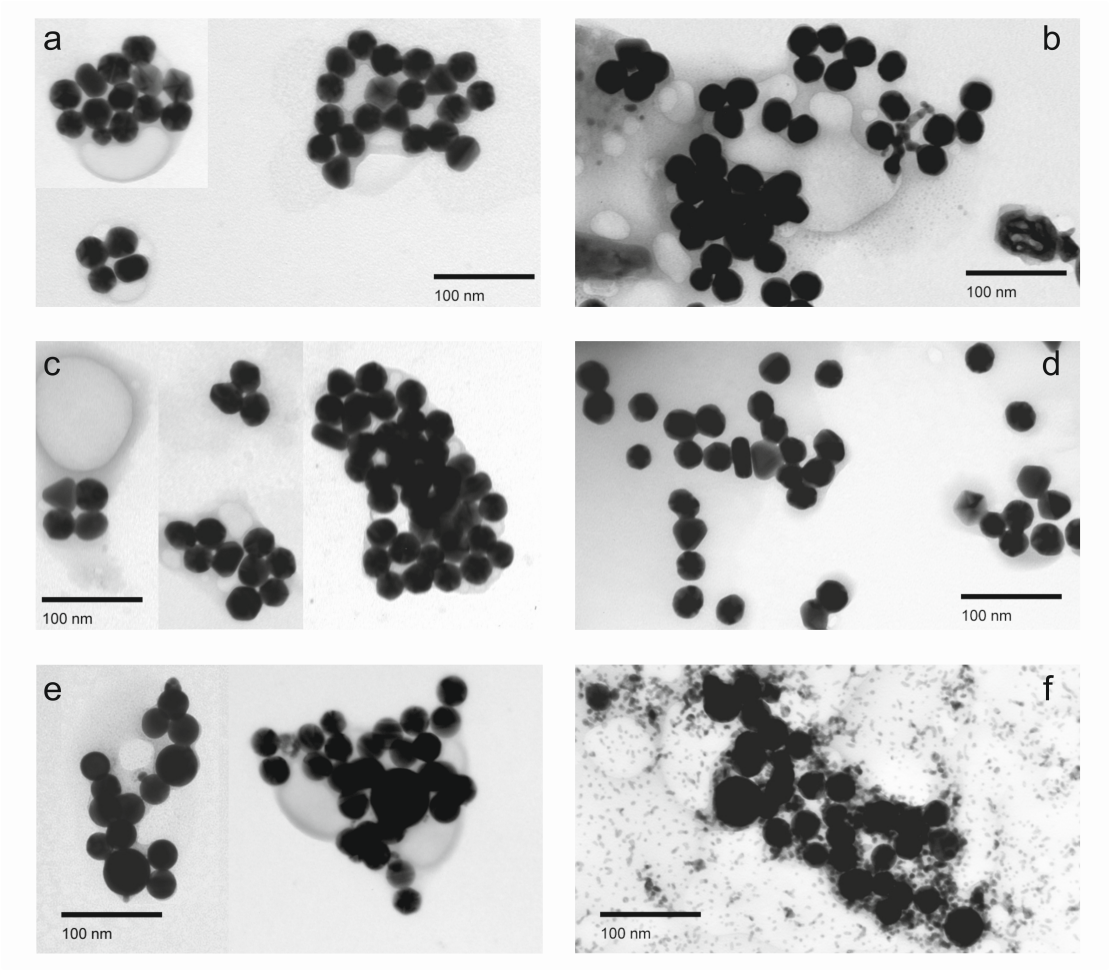

Figure 4.11: TEM images of 30 nm AuNP siRNA conjugates before irradiation (A) and after irradiation with radiant exposure of 5.0 mJ cm^{-2} (B), 10.0 mJ cm^{-2} (C), 23.0 mJ cm^{-2} (D), 50.0 mJ cm^{-2} (E), and 100 mJ cm^{-2} (F).

Absorption measurements of non-functionalized 30 nm AuNP showed increasing blue shift of the peak wavelength (Figure 4.12), due to surface melting and reshaping of the AuNP. The shift is not as prominent as the one for siRNA release; however, it cannot be clearly differentiated from the absorption shift due to reshaping of the particles. Also the change in absorption spectra showed, that melting temperatures are reached that can lead to cavitation bubble formation, at the light doses, at which siRNA release was observed.

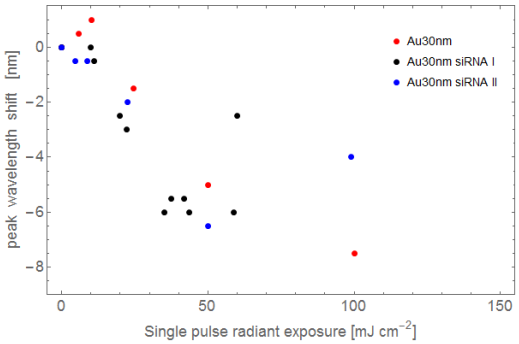

Figure 4.12: The absorption peak of 30 nm AuNP (blue dots) and of 30 nm AuNP with siRNA functionalization (black and red dots) shifts to shorter wavelength. The absolute shift of the absorption peak to shorter wavelength increased with the radiant exposure of the irradiation. Data represented by blue dots correspond to the TEM images shown in Figure 4.11. Irradiation of non-functionalized 30 nm AuNP (red dots) leads also to a shift of the peak wavelength. Corresponding TEM images of 30 nm AuNP without siRNA functionalization are shown in Figure 4.10.

Concluding from calculations of absorbed energy particle size affects the cavitation threshold (cf. Figure 4.9). With increasing particle size the bubble formation occurs at an earlier time point after laser pulse onset. Further, siRNA load should increase with the particle size and the amount of siRNA released from larger particles should equal the amount of released siRNA from a smaller AuNP with lower load, since cavitation should occur around smaller particles at a later time point. In this case, it is expected that the particle size dependence of the siRNA load could compensate the different time points of bubble formation.

4.3.2 Increase of coumarin fluorescence

After irradiating the conjugates of 15 nm and 30 nm AuNP with coumarin labeled siRNA fluorescence in the supernatant increased (Figure 4.13). In correspondence to the blue shift of the nanoparticle extinction, the conjugates with 15 nm AuNP exhibit maximum relative fluorescence f_{rel} of 0.2 after irradiation with 80 mJ cm^{-2} (Figure 4.13 A). A slightly higher increase to 30 % compared to the positive control was achieved for conjugates with 30 nm AuNP at radiant exposure of around 40 mJ cm^{-2} (Figure 4.13 B). This corresponds to the irradiation parameter, at which the blue shift of the extinction reached almost maximum. Nearly simultaneous with this maximum of fluorescence measured in the supernatant, in complementary measurements of the bound siRNA the detected fluorescence decreased as expected. Above 80 mJ cm^{-2} respectively 32 mJ cm^{-2} fluorescence in the supernatant decreased while also the amount of bound siRNA further decreased. Obviously, during irradiation the coumarin molecules are destroyed, which can be related to the temperature increase of the AuNPs and their surrounding. Photobleaching by absorption of the nanosecond pulses can be excluded as a reason for the loss of total coumarin fluorescence. When irradiating coumarin labeled siRNA in aqueous solution the fluorescence remained stable under radiant exposure with up to 100 mJ cm^{-2} (Figure 4.14 A). In contrast, Cy5-siRNA, which served as a positive control for photobleaching, loses its ability to emit fluorescence in a linear dose dependent manner. The photochemical destruction can be explained by the residual absorption of Cy5 at the irradiation wavelength, which is not present for coumarin (Figure 4.14B). The plasmon resonance absorption of an AuNP is spectrally located in a wavelength range above from the emitted peak fluorescence of coumarin.

The reduction of total coumarin fluorescence can be related to the calculated maximum temperature increase above 1300 K within the AuNP and 1000 K in a surrounding water layer on the AuNP surface.

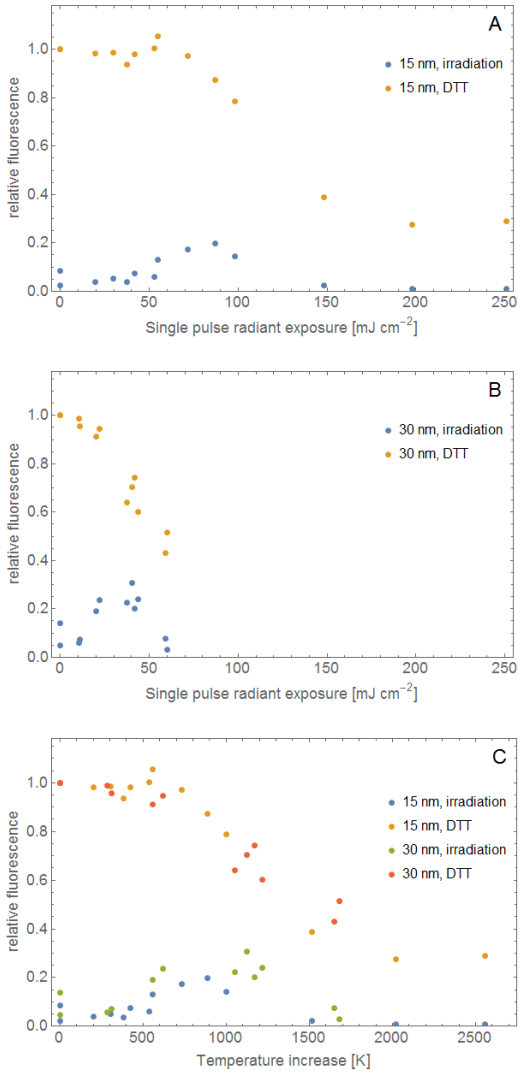

Figure 4.13: Fluorescence in the supernatant of conjugates with 15 nm and 30 nm and show a release. (A) For conjugates with 15 nm AuNP the measured fluorescence of released siRNA increased to a maximum of 20 % after irradiation with 80 mJ cm^{-2} (blue). Up to this radiant exposure, the fluorescence of bound siRNA behaves complementary (yellow). For higher radiant exposures, fluorescence of both fractions decreases. (B) Relative fluorescence (Equation 4.1) of released (blue) and bound (yellow) siRNA for irradiated conjugates with 30 nm AuNP. A maximum of around 30 % is reached after irradiation with 32 mJ cm^{-2}. Above this value, fluorescence of both siRNA fractions decreases as for 15 nm particles. (C) Plotted against the calculated temperature, the same behavior is observed for both particle sizes.

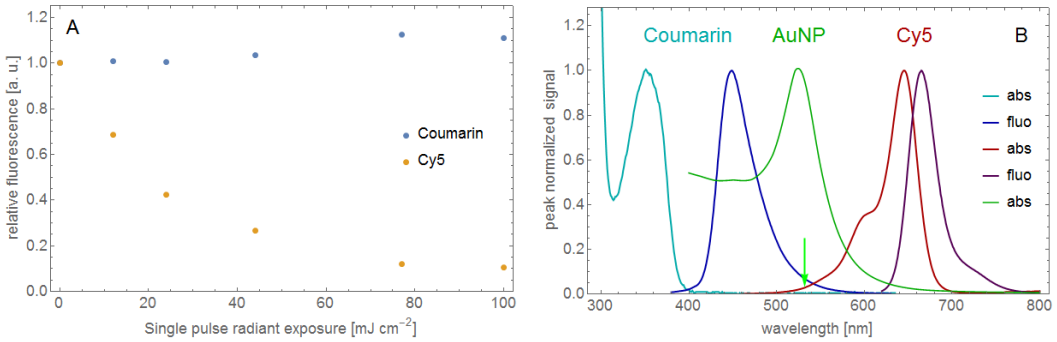

Figure 4.14: (A) Fluorescence signal of siRNA-coumarin and siRNA-Cy5 measured after 4 ns pulsed irradiation for 60 s at a repetition rate of 10 Hz. With increasing irradiation Cy5 fluorescence is bleached in linear dose-dependent manner, while fluorescence of the coumarin molecule remains stable. (B) Absorption and fluorescence spectra (peak normalized) of coumarin, Cy5 and 30 nm AuNP. The green arrow indicates the irradiation wavelength.

4.3.3 Mechanisms of siRNA release

Three mechanisms may be responsible for the molecular release of covalently linked siRNA from the nanoparticle surface: 1. A cleavage of the thiol-bonding by hot electrons, 2. thermal dissociation [146] and 3. the effect of the bubble formation. Dehybridization of the double stranded siRNA [149], which leads to release of the unlabeled strand does not contribute to the measured fluorescence and will therefore remain unperceived.

Jain and Goodman proposed that femtosecond pulsed laser excitation causes a hot-electron transfer from the plasmon decay, which leads to breaking of the AuNP-thiol bond with negligible local heating [144, 145]. However, the temperature calculations for the irradiation that lead to change in absorption and free coumarin fluorescence of conjugates with 15 nm and 30 nm AuNPs show, that cold bond breakage is obliviously not possible under nanosecond pulsed laser irradiation. siRNA release occurs at particle temperatures of more than 500°C, which are just above the expected bubble formation threshold and melting of gold. During an incident nanosecond laser pulse the electrons and the gold lattice thermally equilibrate, because thermalization of the electronic system and subsequently of the atomic lattice take place on the picosecond scale [85]. This is in contrast to fs-pulsed irradiation, which induces directly after irradiation an approximately five-fold stronger temperature increase of the electronic system than of the particle and its surroundings, which exhibit a larger heat capacity than the electrons.

Li et al. studied the thermal stability of DNA functionalized 20 nm AuNP by measuring the fluorescence of a dye molecule they used to label the DNA [146]. They showed that the fluorescence was quenched when bound to the AuNP, while after heating to above 60 °C a significant fluorescence was detectable. Further, within hours they observed cleavage of the AuNP-thiol bonding at temperatures of up to 85 °C.

In contrast to these experiments with homogeneous heating of the whole solution, nanosecond pulsed laser irradiation induce considerably higher temperatures in the AuNP and in its surrounding for a significantly shorter time. The possibility of a thermally activated bond breaking within the few nanoseconds of increased temperature can be estimated by the Arrhenius relation of temperature and reaction rate. When extrapolating the data given by Li et al. [146] a reaction rate of 11.5 s^{-1} is found for a nanoparticle temperature of 500 °C. Even at a nanoparticle temperature of 2,000 °C the rate will increase only to $2.5 \cdot 10^4$ s^{-1}. Assuming increased temperature for a duration of 5 ns in 600 pulses gives a total thermal exposure of 3 µs, which is too short to release at this rate significant amounts of covalently bound siRNA from the particles. Given the validity of the Arrhenius extrapolation, siRNA release must be caused by a non-thermal effect .

Onset of siRNA release occurred for 15 nm AuNP conjugates at 55 mJ cm^{-2} and for 30 nm AuNP conjugates at 16 mJ cm^{-2}. Here, the temperatures in the 15 nm and the 30 nm AuNP increase to a maximum of 580 °C and 469 °C, respectively. The particles heat a water shell near their surface to approximately 305 °C, which is near of the spinodale point water. At the

irradiation that leads to maximal fluorescence of the supernatant (80 mJ cm^{-2} and 32 mJ cm^{-2}, respectively) temperature in the liquid near the particle of 437°C (15 nm) and 584 °C (30 nm) were calculated, which exceeds the critical temperature of water. As a result of the strong AuNP temperature increase and the heat diffusion into the surrounding on the picosecond time scale a thin liquid layer on the AuNP surface overheats. Phase transition and rapid expansion of the vapor will follow [1, 110, 111]. Kotaides et al. showed, that the surrounding liquid around gold nanoparticles with 36 nm and 100 nm diameter vaporizes explosively at nucleation temperatures of 302 °C and 452 °C, respectively, when irradiated with femtosecond laser pulses [67].

Hence both, increased temperature and bubble formation may be responsible for the releases of the siRNA as schematically illustrated in Figure 4.15.

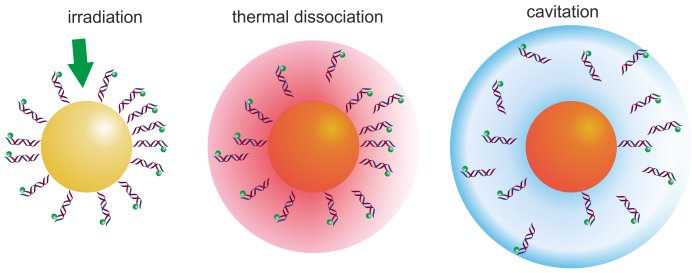

Figure 4.15: Schematic illustration of temperature increase and bubble formation involved in the release of molecules from the nanoparticle surface. Irradiation of the AuNP functionalized by dye labeled siRNA leads to a strong temperature increase inside and in the surrounding medium. Due to dissociation of the AuNP-thiol bondings the double stranded siRNA detaches from the AuNP. Further, upon sufficient temperature increase a vapor bubble can form and expand, which carries the molecules further into the surrounding.

So far, the contribution of shear and tensile forces at the vapor-liquid interface of an expanding cavitation bubble to dissociation of the Au-thiol bond or to the dehybridization of the double stranded siRNA is unclear and difficult to predict. The effort to release higher amounts of siRNA by increased single pulse radiant exposure caused coumarin and possibly the siRNA as well to lose its integrity. Besides, for targeted gene silencing the cavitation may cause undesired effects, such as increased cell elimination. Denaturation of proteins coupled to nanoparticles at even larger distances from the particle than the siRNA was demonstrated for ps-pulsed laser irradiation [150, 8, 14] and related to cavitation, but not to thermal denaturation.

Data of experiments with femtosecond laser pulsed irradiation of particle conjugates published by Goodman et al allow the same interpretation of bleaching fluorescence. They showed that a decrease in the detected DNA release occurs when a certain pulse energy was exceeded [145]. Further, a color change of the irradiated sample of gold nanoparticles and a loss of nanoshell integrity were observed, which could also be attributed to cavitation.

Thus, it is conceivable that cavitation limits the application of short pulsed laser irradiation for induced molecular release from gold nanoparticles in principle, at least when it is performed after cell uptake or very close to the cell membrane.

4.4 Conclusion

As siRNA release from gold particles after irradiation with nanosecond laser pulses was shown as result from AuNP-thiol bond breakage. Different radiant exposures were needed, when 15 nm or 30 nm particles were used. Maximum fluorescence of released siRNA was observed at 80 mJ cm^{-2} for 15 nm particles and at 32 mJ cm^{-2} for 30 nm particles. With these distinct radiant exposures for release, in principle it should be possible to address different molecules from different sized particles independently from each other within the same biological sample. However, the detection of the release by measuring the fluorescence of the dye used to label the siRNA, revealed a destruction of the dye molecule itself.

The corresponding temperature calculations show, that for 15 nm and 30 nm AuNPs the temperature increase is sufficient to cause cavitation. It is conceivable, that besides high temperatures

the predicted bubble formation is responsible for denaturation of the dye molecules.

Thus, nanosecond pulsed laser irradiation is not optimal for drug release from gold nanoparticles. If effective at all, tight control of irradiation parameters is required in order to avoid non-targeted effects such as elimination through intracellular induced cavitation. When targeting extracellular matrix and immune response in the vicinity of cells, vapor bubble formation may be utilized for transient permeabilization of the targeted cell.

5 Laser induced vapor bubbles around single gold nanoparticles

When irradiated with nanosecond laser pulses, gold nanoparticles can be used for efficient cell elimination (Chapter 3) and, to a lesser extent, for the release of molecules (Chapter 4). Both studies showed that the mechanism of the bubble formation around the AuNP and the impact on the surrounding are not fully understood. The underlying mechanism was investigated in experiments on particle solutions. However, responsible effects of bubble formation around the irradiated nanoparticles were only partly clarified, because all effects were only visible on ensembles of particles with varying properties.

Thus, single nanoparticle measurements should clarify the mechanism of bubble formation under nanosecond pulsed irradiation that leads to cell elimination or molecular release respectively. Therefore, the involved processes such as the temperature increase, the onset of bubble formation and maximum expansion should be clarified. The measured maximum bubble diameter for irradiation with different radiant exposure should deliver the mechanical energy available for the cell elimination or the molecular release. In particular the influence of the particle size and the pulse duration on the bubble formation should be investigated. These experiments should also aim for more detailed information on the conversion from laser pulse energy to thermal energy on the nanoscale and the further conversion to mechanical energy with impact on the microscale.

5.1 Introduction

A novel method to measure the dynamic oscillation of cavitation bubbles was developed by Vogel and co-workers [151, 152]. Their method is based on the measurement of backscattered light of a cavitation bubble that is generated by a focused laser beam. Due to interference the recorded photodetector signal exhibits a modulation, which is related to the velocity of the vapor-liquid interface varying during the bubble expansion and collapse. For the investigation of cavitation around gold nanoparticles the technique was adopted here for the bubble detection in combination with a darkfield microscopy and scattered light spectroscopy.

The darkfield contrast allowed for a precise detection of nanoparticles with sizes below optical resolution of conventional light microscopy. Because bubble nucleation and the dynamics depend on particle shape and size, these were determined before each experiment. For this purpose, the spectrum of scattered light from the nanoparticle detected under darkfield was measured.

Comparable experiments of single-shot vapor bubble generation and measurement around single nanoparticles by pulsed laser irradiation, that allow for the analysis of the bubble interface velocity, were not published so far. The method of bubble interferometry and typical signals will be demonstrated first with the help of plasma induced cavitation in free water and at a rigid surface, a glass substrate. The correlations of physical quantities with the characteristic signals recorded during the formation of bubbles will be explained at the free bubbles. From the signals detected for the bubble formation on nanoparticles, threshold radiant exposure, maximum bubble radius and the time varying bubble wall velocity and radius are determined. Based on these measured quantities and temperature calculation the mechnism of bubble formation around gold nanoparticles is discussed.

5.2 Pulsed laser irradiation of gold nanoparticles - state of the science

Both, the efficient and highly specific cell elimination as well as the molecular release from gold nanoparticles with nanosecond pulsed laser irradiation were demonstrated in this work. In combination with the temperature calculation, the experimental results lead to the conclusion that bubble formation leads to cell elimination and at leastr occurs as a side effect during molecular release from gold nanoparticles. Cavitation was also identified to be one main mechanism of cell elimination by other groups, who have investigated physical effects around gold nanoparticles by pulsed laser irradiation [3, 4, 5, 66, 153, 15, 154, 137, 16]. Analytical models, which include the temperature increase induced within the gold nanoparticle, the conductive heat flux into the nanoparticle surrounding as well as the formation of a vapor bubble were

reported [6, 155, 115, 116, 113, 156, 110]. In addition to cell elimination, the release of DNA [52, 51, 145] and siRNA [157, 48, 54] was shown in cell free solution as proof-of-principle as well as in living cells [51]. However, most published investigation was carried out on continuous or on femtosecond pulsed irradiation.

The results on cell killing by irradiated nanoparticles (cf. Chapter 3) and the molecular release study (cf. Chapter 4) left the question open what the mechanism of action is. For efficient cell elimination under nanosecond pulsed laser irradiation the temperature calculations showed, that an irradiated nanoparticle would undergo a high temperature increase ranging up to the boiling of the gold nanoparticle. The time point of the nucleation during the applied laser pulse is decisive for the deposited energy and subsequently developing temperature. Because of vapor formation around the particle the optical absorption and the thermal diffusion to the surrounding are changed drastically.

In the following chapters the work which contributes to the understanding of the physical processes around laser irradiated gold nanoparticles will be reviewed. Following the hypothesis of cavitation bubble formation is the main mechanism of cell elimination and molecular release, three principle effects will be addressed: first, the laser induced temperature increase of single gold nanoparticles (cf. Chapter 2.2.3), second, the bubble formation on the particle surface (cf. Chapter 2.4) and third, the measurement of the bubble expansion. The following section summarizes the experimental techniques and motivate the new approach of this thesis to clarify more details of the nanosecond pulsed laser induced bubble formation on gold nanoparticles.

5.2.1 Laser induced temperature increase of gold nanoparticles

Modeling the laser induced temperature increase in and around gold nanorods

Rudnitzki et al. analyzed the effects that are involved in pulsed laser irradiation of spherical and rod shaped gold nanoparticles [62, 18]. The optical properties of nanorods were calculated by electrostatic approximation assuming an elliptical shape (Equations 2.5 to and Equations 2.28 to 2.6), whereas dependency of the absorption cross sections on size and orientation distribution were considered .

Depending on the shape of the AuNP the temperature increase extends in a spherical or an elongated symmetry into the surrounding media with the nanoparticle in the center. This temperature increase causes bubble formation when exceeding threshold for explosive evaporation. For analysis of the thermal behavior calculated spatio-temporal temperature increase for rod-shaped AuNP in water was compared to time resolved absorption measurements during a nanosecond pulsed irradiation on different samples. Since this pulse duration exceeds the thermal confinement conditions, thermal conduction and heat diffusion determine the temperatures and subsequent phase changes of water and gold.

Rudnitzki et al. confirmed by three experiments the results of temperature modeling (Equations 2.33 to 2.45) and calculation of optical properties: (1) Measurement of the transmitted energy for different radiant exposures, (2) transient absorption measurements at the LSPR peak wavelength of 785 nm and (3) transient absorption measurement at the TSPR band around 520 nm. For the transient absorption measurement on the LSPR peak wavelength the irradiation laser pulse served as pump and probe pulse at the same time (cf. Figure 5.1).

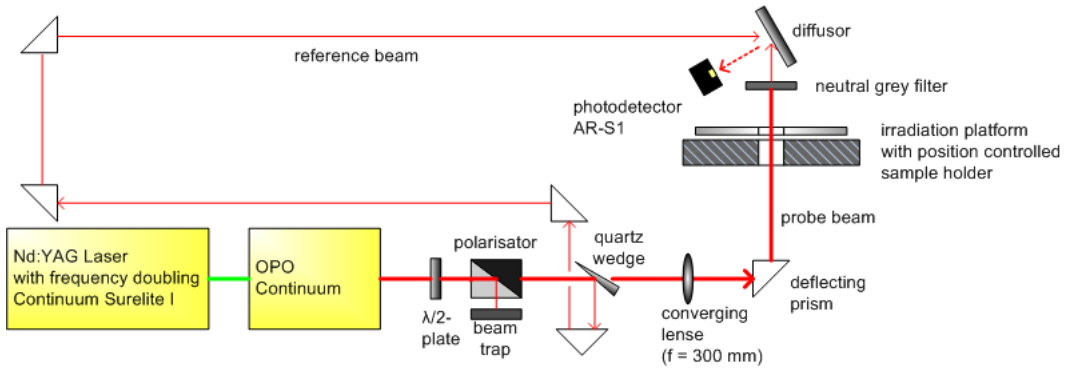

Figure 5.1: Optical arrangement for the transient absorption measurements at the LSPR peak wavelength of AuNR. For the transient absorption measurement on the TSPR peak wavelength additionally a cw laser emitting at 532 nm was arranged perpendicular to the pump laser within the sample (not shown). Reproduced from [18], with the permission of SPIE.

Three energy ranges were determined from the experiments, which were governed by the effects of transient and permanent loss of the LSPR absorption band located in the NIR wavelength range. The transient absorption loss, also referred to as transient bleaching is related to a reversible shift of the absorption band to shorter wavelengths due to the bubble formation around the irradiated AuNR. The permanent bleaching refers to absorption loss by irreversible shift of the LSPR band resulting from melting of the AuNR.

For the lowest range of $H \leq 5\,mJ\,cm^{-2}$ heat induced particle melting was not observed. Only transient bleaching of the LSPR band occurred: irradiation above $1.5\,mJ\,cm^{-2}$ can induce temperatures on the particle surfaces leading to evaporation of the surrounding medium. Consequently, the decrease in refractive index causes a LSPR band shift into the visible wavelength range.

In the medium range of $6.5\,mJ\,cm^{-2} \leq H \leq 13\,mJ\,cm^{-2}$ the bleaching of the LSPR band was resolved during single pulses. Correspondent temperature calculations predicted an increase of 600 K in the particle lattice, while an increase by 300 K was reached in the interface layer during a time range below 0.5 ns after the laser pulse onset for particles parallel aligned with the electric field vector of the incident light. At this point, transient LSPR peak bleaching reduced absorption to less than 2 % of the original efficiency. The fraction of particles, in which these temperatures can be induced, depends on their orientation. Single particles with optimal shape and orientation reach melting temperature. This was verified by TEM images and UV-VIS spectra. Thus, the transient absorption signal in the medium irradiation range revealed two effects: absorption loss by (a) LSPR band shift due to a vapor shield around the particle caused lower absorption at 0.5 ns (after pulse initiation) and (b) permanent bleaching of the LSPR band due to melting.

In the highest range of single pulse radiant exposure with $H > 13\,mJ\,cm^{-2}$, the time resolved measurement showed in a short range after pulse onset an absorption loss, which indicated the transient LSPR shift. At an irradiation above $13\,mJ\,cm^{-2}$ particle melting was observed in the transient absorption signal, which appeared in an absorbance decrease after each subsequent pulse. The lattice temperature of the particles increased by 600 K short after the onset of the irradiation pulse, at which the water evaporates from the surface. The immediately decreasing absorption at irradiation wavelength can lead to energy densities sufficient for partial or complete particle melting.

With increasing radiant exposure the measured absorption decrease at smaller time constants and the total loss with respect to original absorption increases. Further a saturation of maximal absorbance loss was found above $78\,mJ\,cm^{-2}$. According to calculations of the temperature and deposited energy density the lattice temperature reaches the melting point as soon as the particle is shielded by vapor. Nevertheless, the orientation limits the nanorod fractions, which undergo the complete rod to sphere transition. TEM images show an increased number of spherical particles, while still rod shaped particles can be found.

5.2.2 Bubble nucleation on single nanoparticles

Nucleation dynamics around single microabsorbers

Neumann et al. studied the nucleation dynamics around single microabsorbers in water when heated by pulsed laser irradiation [6, 15, 7, 109]. Aided by a microscopy setup with a standard 40X / 0.65 objective observation as well as excitation of particles within aqueous surrounding was established (Figure 5.2). Particles were excited by pulses of i) a frequency doubled, Q-switched Nd:YAG laser with 12 ns duration and ii) a frequency doubled, Q-switched Nd:YLF laser with 240 ns and 1.8 µs duration. In order to detect the oscillating vapor bubbles a HeNe laser was coupled coaxially with the pump laser through the microscope objective, while the probe light scattered at the forming bubble was detected in transmission. The setup was completed by a N_2-laser pumped dye laser tuned to an emission wavelength of 490 nm with 3 ns pulse duration, which served as illumination for fast flash photography with adjustable trigger delay related to the irradiation pulse.

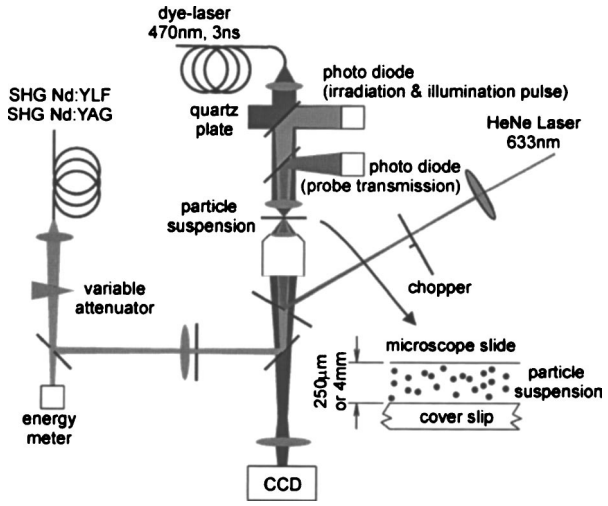

Figure 5.2: Experimental setup utilized by Neumann et al. Reproduced from [6], with the permission of SPIE.

Neumann et al. used the solution to the heat equation given by Goldenberg and Tranter [158] in order to determine temperature increase within and around irradiated spherical particles. However, this solution is explicitly valid for spatially and temporally homogeneous heat deposition. Neumann et al. [6] extended the model to arbitrary pulse shapes with help of the Green's function, which describes the temperature response to a dirac shaped laser pulse ($\Delta t \to 0$) at given r approximated by

$$T_{Green}\left(r,t\right) \approx T\left(r,t\right) - T\left(r,t-\Delta t\right) \tag{5.1}$$

The temporal temperature course at a given r was calculated by convolution (Equation 5.2) of the Green's function with the time-dependent power density of the absorbed light (Equation 5.3) from applied laser intensity $I\left(t\right)$ as given by

$$T\left(r,t\right) = T_{Green}\left(r,t\right) \otimes A\left(t\right) \tag{5.2}$$

$$A\left(t\right) = I\left(t\right) \frac{\sigma_{abs}}{\left(4/3\right)\pi R_p^3} \tag{5.3}$$

Neumann et al. determined the nucleation threshold fluence experimentally and calculated the related temperature increase of AuNP and the surrounding liquid layer. They considered spontaneously formed bubbles, which were entrapped on the nanoparticle surface [159] and caused inhomogeneous nucleation [160].

For gold nanoparticles with a radius of 250 nm a nucleation temperature of $T_{nuc} = (327 \pm 12)$ °C was obtained by fitting the semi-analytic thermal model to the experimentally measured fluence threshold, which increased with the pulse durations 12 ns, 240 ns and 1.8 µs from (106 ± 31) mJ cm^{-2} to (216 ± 84) mJ cm^{-2} and further to (651 ± 168) mJ cm^{-2}, respectively. They found a good agreement of experimentally and numerically determined bubble formation thresholds.

For bubble oscillation times between 50 ns and 300 ns flash photography images showed that maximum bubble size ranged between 0.5 µm and 3.5 µm slightly smaller than estimated by Equation 2.67 [24].

Photothermal bubble generation around gold nanoparticles

Lapotko et al. utilized optical scattering to investigate bubble generation around gold nanoparticles after short pulsed laser irradiation. In agreement with other groups they assume laser induced heating of the nanoparticle and the conductive heat diffusion into the surrounding medium. At sufficient irradiation, evaporation of a thin overheated water layer on the nanoparticle surface follows. The formed bubble expands provided that the initially deposited energy was sufficient to overcome the surface tension and the inner friction of the surrounding water. To account for the thermal generation due to a heated nanoparticle they used the term photothermal bubble (PTB) as well as plasmonic nanobubbles (PNB) [60, 65, 161].

For their studies Lapotko et al. coupled two pumping lasers (Nd-Yag LS2132, Lotis TII, Minsk and STA-01 SH, Standa Ltd, Vilnius) both emitting at a wavelength of 532 nm confocally into the illumination path of an inverted optical microscope. Optically scattering of bubble formation was detected by a charge coupled device (CCD) when illuminated by a pulsed probe laser at a wavelength of 690 nm. Further, PTB lifetime measurement was established by continuous probing with a cw laser at a wavelength of 633 nm confocal with the pump lasers and a photodetector (PDA 10A, Thorlabs), which detected the probe laser intensity transmitted by the sample.

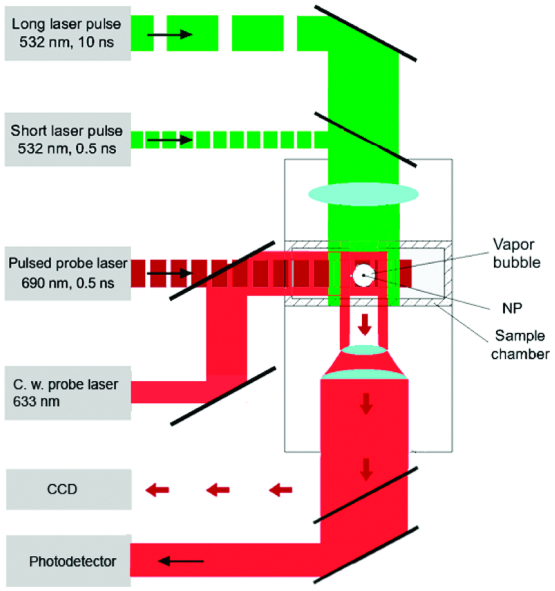

Figure 5.3: Pump-probe Laser setup utilized by Lapotko et al. Reproduced from [65], with the permission of ACS Publishing.

In their experiments bubble formation threshold fluence E_{PNB} and lifetime T_{PNB} were determined as well as the influence of different parameters such as the pulse duration and nanoparticle geometry on these parameters. Lifetime of the PTB generated around a nanoparticle was considered proportional to the maximum bubble diameter [60] and further "nearly proportional" to the incident fluence [65]. Lukianova-Hleb and Lapotko et al. reported on irradiation of nanoparticles with diameters ranging between 10 nm and 250 nm with pulse durations of 500 ps at a wavelength of 532 nm PTB formation thresholds ranging between 100 mJ cm^{-2} and 1800 mJ cm^{-2}.

In order to clarify the nature of bubble formation around AuNP Lukianova-Hleb and Lapotko et al. increased sensitivity of the experimental setup by tight focusing the probe laser beam onto the particle. Pulse radiant exposure was increased and from changes of the forward scattering signals they concluded, that below bubble formation threshold the irradiated AuNP has solely thermal impact on the environment. Heating of the water around the particle causes the thermal lens effect, which gradually disappeared on bubble formation at higher irradiation. Thus, they concluded for small bubbles with lifetimes between 9 and 13 ns that heat transfer to the surrounding medium is not prevented by a thin vapor layer. For higher radiant exposure generating larger bubbles with lifetimes above 13 ns mechanical impact on the environment dominated.

Further, their study on the pulse duration dependence of bubble formation revealed an increase of the PTB formation threshold with pulse duration, when increasing from 0.5 ns to 10 ns [60, 161].

In order to calculate the fluence threshold of bubble formation Lukianova-Hleb et al. used a model based on the hydrodynamic equation and the stiffened gas equation of state using parameters for water [65]. Thereby, a fluence they termed threshold of explosive boiling, which was required to increase the liquid temperature on the AuNP surface to the critical point of 647 K, was much lower than the experimentally determined PTB threshold. For a gold nanoparticle with 60 nm diameter an explosive boiling threshold around 2.5 mJ cm^{-2} was determined, while first bubble formation was measured for radiant exposure around 120 mJ cm^{-2}. They concluded from these results, that bubble generation does not coincide with the vapor formation on a transiently heated nanoparticle. Bubble formation requires an energy exceeding the explosive boiling threshold. Certainly, the generated vapor pressure needs to overcome the surface tension related Laplace pressure (cf. Equation 2.64), which is significantly increased for a bubble nucleation radius in the range of the nanoparticles.

5.2.3 Bubble dynamics around gold nanoparticles

Cavitation dynamics induced by ultrashort pulsed laser irradiation of gold nanoparticles

Plech et al. observed cavitation dynamics around gold nanoparticles with the help of laser pump-probe experiments (Figure 5.4 A and B) and small angle X-ray scattering (SAXS) measurements (Figure 5.4 C) [66]. They measured nanoscale vapor bubble formation around gold nanoparticles with a diameter of 9 nm, which were irradiated with laser pulses of 100 fs duration at a wavelength of 400 nm.

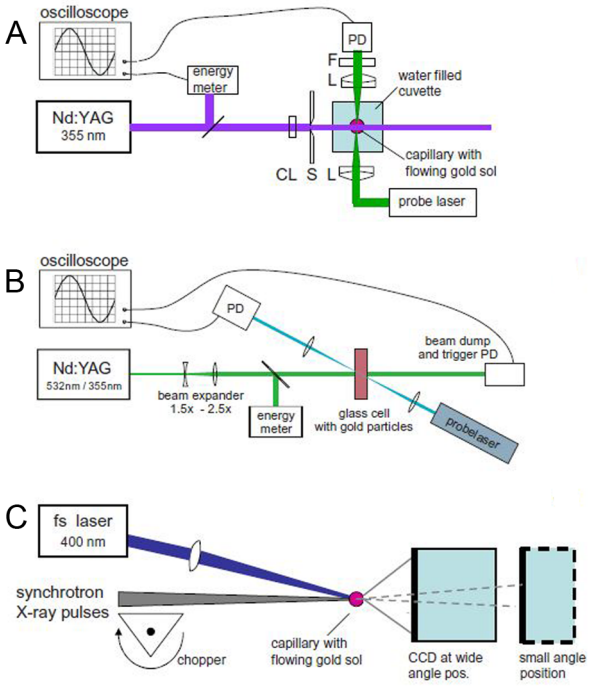

Figure 5.4: Schematic illustration of the three experimental arrangements utilized by Plech et al. Reproduced from [68], with the permission of IOP Publishing

Kotaidis et al. fitted the measured bubble volumes to a numerical integration of the Rayleigh-Plesset Equation 2.63, to obtain the initial radius and vapor pressure $R_0 = 7.5\,\mathrm{nm}$ and $p_0 = 0.3\,\mathrm{GPa}$, respectively [66]. $R_b(t=0) = 4.5\,\mathrm{nm}$ and $dR_b(t=0)/dt = 90\,\mathrm{m\,s^{-1}}$ were required boundary conditions in order to solve the Rayleigh-Plesset equation. They chose a polytropic exponent suggests for an adiabatic bubble expansion. Figure 5.5 shows the determined bubble radii for distinct time points in comparison to the calculated radius-time curves.

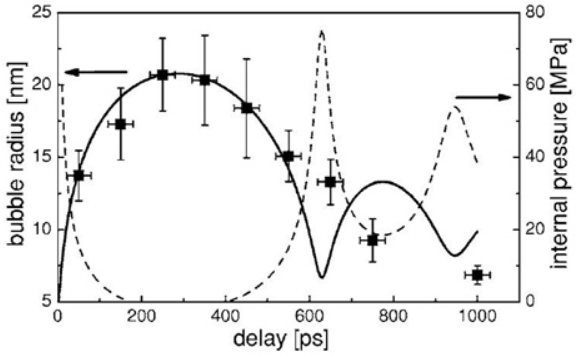

Figure 5.5: Bubble radii measured at distinct time delays and the calculated radius-time (solid line) and pressure-time (dashed line) curves as predicted from the Rayleigh-Plesset equation for gold nanoparticles of 9 nm irradiated with 100 fs pulses at a wavelength of 400 nm, fluence was not quantified explicitly ("at the highest laser power with the largest bubbles accessible"). Reproduced from [66], with the permission of AIP Publishing..

At the threshold for bubble formation they assumed, that explosive boiling occurs as soon as a water layer around the nanoparticle reaches a temperature of 85 % of the critical temperature T_c[67]. Besides measuring shape and size of vapor bubbles, SAXS provided a measure, though of limited precision, for the density of the vapor [66]. A maximum vapor density of 10 % of the surrounding liquid density was observed. For gold nanoparticles with diameter of 9 nm a bubble formation threshold fluence of $29\,\mathrm{mJ\,cm^{-2}}$ was determined. Above threshold, increase of bubble

size almost linearly with the applied fluence was observed. For irradiation with 100 mJ cm^{-2} a maximum bubble radius of approximately 20 nm was detected. For gold nanoparticles with diameters of 39 nm the bubble formation started around 10 mJ cm^{-2} and the maximum measured bubble radius was around 100 nm for irradiation with 100 mJ cm^{-2} [67]. Figure 5.6 shows the maximum bubble radius Kotaidis et al. measured for gold nanoparticles with diameters 9 nm and 39 nm irradiated with 100 fs pulses at a wavelength of 400 nm. The arrows indicate the fluence thresholds for bubble formation. For increasing radius nanoparticles exhibit a decreasing surface to volume ratio, whereas at a given fluence the liquid phase around larger nanoparticles will reach higher temperature. Thus, for larger nanoparticles a lower fluence is expected for bubble nucleation.

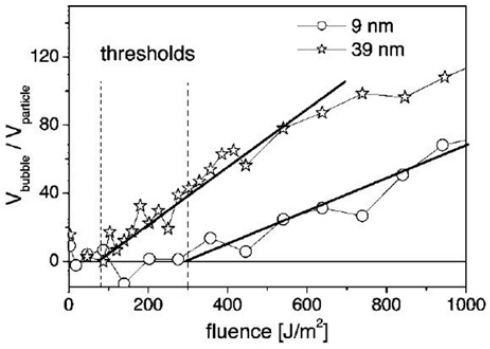

Figure 5.6: Ratio of bubble volume to particle volume against the laser fluence measured for gold nanoparticles of 9 nm and 39 nm diameter. The particles were irradiated with 100 fs pulses at a wavelength of 400 nm, bubble measurement at the maximum bubble radius (650 ps for 39 nm AuNP, 300 ps for 9 nm AuNP). Dashed vertical lines indicate the threshold. Reproduced from [67], with the permission of AIP Publishing.

SAXS measurements were done in samples containing particles with mean sizes from 9 nm to 110 nm diameter in aqueous solution with size dispersion of 12 % for the smaller, through 15 % for the larger particles [67]. Even though errors are introduced by size distribution of the particles within the sample and their possible asymmetry as well as the applied fluence, Kotaidis et al. showed, that a simple model approach can describe the dynamics of nanobubbles around nanoparticles in fair agreement with experimental data.

Besides the SAXS method, the group of Plech utilized time resolved optical spectroscopy in order to characterize the nonlinear thermal behavior of pulsed laser irradiated gold nanoparticles. Siems et al. reported results for pump probe laser experiments for nanosecond excitation ($\tau_l = 10$ ns, $\lambda_l = 532$ nm) of gold nanoparticle in water [68]. The optical pump-probe method provides only an indirect measure for the bubble nucleation temperature of the particle and the adjacent liquid. Siems et al. calculated the temperature in and around the nanoparticles with Equations 2.37 to 2.45. They determined bubble threshold fluence for nanosecond pulsed irradiated gold nanoparticles with diameters of 18 nm, 30 nm, 40 nm and 60 nm, and showed that also for nanosecond pulsed irradiation the threshold temperature corresponds quite well to 0.85 T_c. Only for nanoparticles with diameters around 18 nm a decreased fluence threshold was determined strongly deviating from the conditions of a spinodal decomposition driven process. Siems et al. supposed two reasons. First, as the the amount of gold was kept constant in the investigated samples, the particle number density was highest for the smallest particles. Thus, they speculated clustering could have lowered the bubble formation threshold. Second, the melting point for small particles is lower, and thus, early surface melting may also contribute to a plasmon bleaching, which can be subsequently interpreted as bubble formation.

However, in contrast to Lapotko et al. they demonstrated a quite well correspondence of a measured and an analytically determined bubble formation threshold for gold nanoparticles with diameters ranging from 30 nm to 100 nm [67, 68].

Vapor bubble generation around gold nanoparticles

Kitz et al. studied the vapor bubble generation around gold nanoparticles and its application to damaging cells with help of a microscopic setup [16], comparable to Neumann et al. In order to detect gold nanoparticles with diameters around 90 nm, which were spin coated onto a quartz glass object slide and covered by pure water, they implemented darkfield contrast in an epi-illumination setup with a NA 1.2 immersion objective. A frequency tripled Nd:YAG laser with 5 ns pulse duration was utilized to pump an optical parametric oscillator (OPO). Thus, the bubble formation threshold dependency on radiant exposure was investigated in irradiation experiments with five different wavelengths in the range between 498 nm and 780 nm. For the irradiation wavelength of 532 nm the bubble life time was measured for different radiant exposures and correlated with the bubble radius with help of the Rayleigh Equation 2.67. A confocally aligned HeNe laser allowed for measurement of the bubble life times by detection of the scattered light in transmission with help of a avalanche photo diode (APD). Flash photography with help of a dye laser with a pulse duration of 700 ps was used to image bubbles at a tunable delay after irradiation. Figure 5.7 shows the experimental setup used by Kitz et al [16].

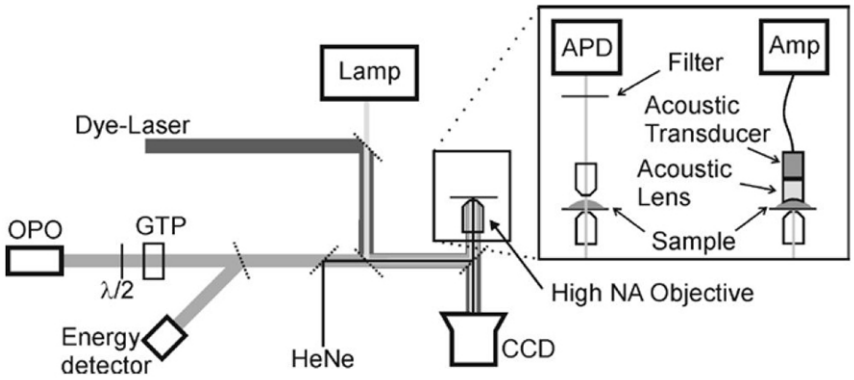

Figure 5.7: Experimental setup used by Kitz et al to study the bubble formation threshold and maximum bubble expansion around gold nanoparticles irradiated with 5 ns laser pulses. Reproduced from [16], with the permission of OSA Publishing

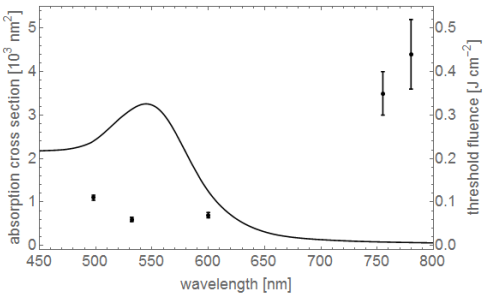

Figure 5.8: Absorption spectrum of 90 nm diameter gold nanoparticle in water. Corresponding nucleation thresholds for excitation wavelengths 498 nm, 532 nm, 600 nm, 750 nm and 780 nm measured by Kitz et al. reflect the absorption of the nanoparticle quite well.

Kitz et al. observed for irradiation with wavelength around the plasmon absorption band of the gold nanoparticles the lowest threshold fluence, while for irradiation in the near infrared (NIR) wavelength range a fluence up to 7 times higher was required in order to nucleate vapor bubbles. For irradiation with 532 nm a bubble formation threshold of $(60 \pm 4)\,\mathrm{mJ\,cm^{-2}}$ was reported. Figure 5.8 shows the absorption spectrum of a gold nanoparticle with 90 nm diameter in water,

calculated by Mie theory (Equation 2.10 to 2.12) and the experimentally determined cavitation thresholds [16].

Besides threshold fluence Kitz et al. determined the maximum bubble radius assuming, that also the detected bubble oscillations were symmetric in time, i. e. expansion τ_{ex} equals collapse duration τ_c. Thus, the equation of bubble collapse duration (Equation 2.67) was used to determine the maximum radius $R_{b,max}$ under the condition, that the measured life time correlates by

$$\tau_{osc} = \tau_{ex} + \tau_c = 2\tau_c. \tag{5.4}$$

Correlation with the simultaneously imaged vapor bubbles revealed, that a collapse time based on the Rayleigh-Plesset model leads to overestimated maximum bubble radius by approximately 20 %, which Kitz et al. accounted to the nanoparticles being in contact to a rigid interface the glass object slide. Additionally, an uncertainty in the determination of the maximum bubble radius by imaging was caused by a jitter of the timing of the illumination laser used for short time photography.

Mechanism of femtosecond laser interaction with gold nanoparticles

Boulais and Meunier et al. studied the generation of cavitation bubbles around plasmonic nanoparticles using ultrashort laser pulses. They found, that for femtosecond pulse besides heating a plasma-mediated mechanism exists for bubble formation [113]. In the vicinity of the nanoparticle plasma collisions and relaxation lead to emission of a pressure wave and further to bubble formation.

From their experimental data Meunier et al. proposed a mechanism to generate cavitation bubbles using an off-resonance wavelength irradiation of gold nanoparticles with fs-pulses. In contrast to pulsed irradiation at the absorption of the nanoparticle plasmon a fragmentation caused by the strong temperature increase can be avoided. Pulse durations of femtoseconds are required in order to create a plasma in the plasmon enhanced nearfield of the nanoparticle. Nanocavitation is then induced by the recombination of the plasma generating a rapid temperature and pressure increase [114, 162]. As a result of the energy transfer being much faster (1 - 3 ps) than thermal diffusion, the liquid-vapor phase transition may occur under isochoric condition yielding in high initial bubble pressures.

Boulais et al. found for gold nanoparticles with 100 nm diameter in water under off-resonant irradiation with 200 mJ cm^{-2} at 800 nm and 45 fs pulse duration a bubble formed with a diameter of around 1.2 µm. Linear absorption of energy in the AuNP contributed only 10 % of the total energy absorption, while 90 % was absorbed by the plasma, which was formed near the particle. Cavitation without particle fragmentation was observed [114].

Boulais et al. provide an excellent review of their work and further compare cavitation due to plasma formation to the thermally induced cavitation around gold nanoparticles [102].

Bubble formation on laser irradiated gold nanoparticles

Ho-Young Kwak et al. studied the liquid vapor phase transition in the thermal boundary layer on the surface of a nanoparticle heated by ultrashort pulsed laser irradiation. In order to determine bubble nucleation they estimated the pressure increase responsible for growth of the initial vapor layer to an expanding bubble with the help of a model based on molecular interactions. The resulting temperature, pressure and initial velocity provided boundary conditions for calculation of the bubble wall motion by solving the Keller-Miksis differential equations [156].

Kwak et al. concluded that the initially vaporized volume and the large expansion velocity were crucial for bubble formation. The initially vaporized volume was defined by the initial radius, which was estimated by $R_0 \simeq 1.9 \cdot R_p$.

This is in contrast to the investigations of Pitsillides et al. [5], who determined temperature decreases in the surrounding liquid to $1/e$ of the surface temperature at a distance of one particle radius. Kwak et al. proposed, that (overheated) liquid water with a temperature above the boiling point participates in the evaporation process. Therefore, they estimated in the case of a gold nanoparticle with 9 nm diameter reaching a temperature of 1000 K a participating liquid layer exhibiting a diameter of 17 nm and an average temperature of 630 K. The molecular

dynamics simulations predicted an initial vapor pressure and bubble wall velocity of 83.09 MPa and 1000 m s^{-1}, respectively, and reaching a maximum bubble radius of 22.5 nm [156].

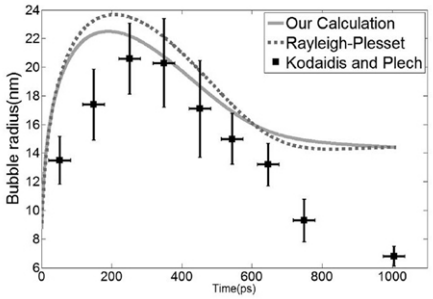

Figure 5.9: Measured (squares, data by [66]) and calculated bubble radius as a function of time formed around a 9 nm AuNP. For calculation an initial radius of 8.5 nm, pressure of 83.09 MPa, temperature of 575 K, initial expansion velocity of 1036 m/s were assumed. Reproduced from [156], with the permission of ASME Publishing.

Their calculations (cf. Figure 5.9) of the change in time of a bubble radius generated around a gold nanoparticle with a diameter of 9 nm showed consistency with the experimental results reported by Kotaidis et al. [66].

5.2.4 Summary of relevant studies

Most of the investigations on laser induced vapor bubble formation around gold nanoparticles concentrated on the measurements of physical parameters such as the bubble formation thresholds and maximum bubble radii for different boundary conditions. Special setups were utilized to measure the oscillation time of the induced cavitation bubble by detection of the forward scattering of a tightly focused probe laser beam (Kotaidis), while other groups imaged the bubble at discrete times with the help of fast time flash photography (Neumann, Lapotko and Kitz). The temporal modulation of the scattering signal correlates with the bubble oscillation time and allows calculations of bubble formation threshold and the maximum bubble radius, provided the relation of the oscillation time to bubble size is known.

Neumann et al. and Kitz et al. conducted experiments on single gold nanoparticles, which were immobilized on a glass slides, Kotaidis et al. and Lapotko et al. conducted experiments on colloid ensembles in aqueous solution. They adjusted the nanoparticle concentration to allow for measurements of a single particle event in the focal volume of the irradiating laser beams.

Groups of Pustovalov, Egerev, Brujan, Merabia (cf. Chapter 2.4) and Kwak numerically investigated temperature increase in AuNP and subsequent bubble formation and dynamics. Their models were verified partly by comparison with experimental data published by Plech and co-workers, who utilized the experimentally elaborate SAXS method for measurements at a solution containing gold nanoparticle ensembles. Besides the bubble nucleation threshold they were able to determine the bubble radius at a distinct time delay of the SAXS measurement to the laser pulse. An insight into the bubble dynamics was gained by sequencing the bubble radii measured at discrete times and comparison with a solution of the Rayleigh-Plesset differential equations.

5.3 Experimental methods

5.3.1 Preparation of gold nanoparticles

All experiments were carried out on gold nanoparticles in aqueous solution. Spherical nanoparticles with diameters of 30 nm, 50 nm and 80 nm were purchased from BBI Solutions (British Biocell International, United Kingdom). Due to the production process size and shape of the nanoparticles vary. With the help of UV-Vis spectroscopy, dynamic light scattering (DLS), transmission and scanning electron microscopy (TEM and REM respectively) the gold nanoparticles were characterized before preparing for experiments.

The results of absorption spectra measurements conducted at spherical nanoparticles are shown in Figure 5.10. Spectra calculated by Mie theory for particles with diameters of 30 nm, 50 nm and 80 nm showed blue shift compared to the used AuNP, which were specified as (30 ± 4) nm, (50 ± 6) nm and (80 ± 8) nm, respectively. The results of corresponding DLS measurements conducted at these particles are shown in Figure 5.11. Fitting a Gaussian distribution function to the data the mean AuNP radius and the corresponding standard deviation of each colloid solution was determined. Mean hydrodynamic diameter of (18 ± 6) nm, (56 ± 4) nm and (82 ± 16) nm were measured.

SEM (Zeiss, DSM 940 scanning electron microscope) reveal deviations of the AuNP from spherical shape. Chrystal facets, cylindrical and also triangular shapes were observed in different samples of spherical nanoparticles (cf. Figure 5.12).

The measured size deviation of more than 10 % of the AuNP diameter for the colloid solutions motivates a measurement of particle size by spectral analysis of scattered light for each individual particle before the pulsed irradiation and measurement of cavitation bubble dynamic. Besides particle size also detection of non-spherical particles, which were excluded from the experiments, is provided by the evaluation of the scattering spectra.

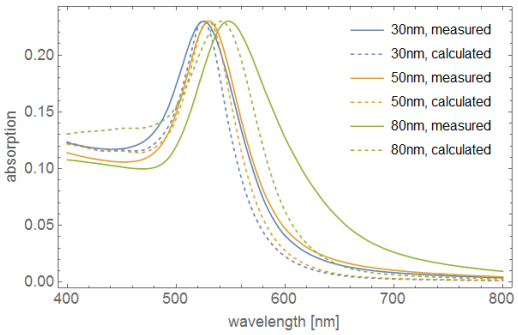

Figure 5.10: UV-VIS absorption spectra of the 30 nm, 50 nm and 80 nm gold nanoparticle suspensions as delivered by the manufacturer (solid lines) differ from spectra calculated with the Mie theory for particles with the average diameter (dashed lines). Deviation is largest for 80 nm particles. The size distribution within each sample leads to deviation of the absorption from spectra calculated with help of the Mie theory.

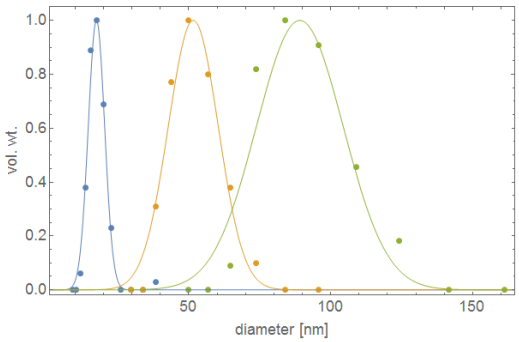

Figure 5.11: DLS measurements (PSS Nicomp 380 ZLS Zeta Potential / Particle Sizer, Particle Sizing Systems, USA) of the 50 nm (blue) and 80 nm (yellow) gold nanoparticles as delivered by the manufacturer.

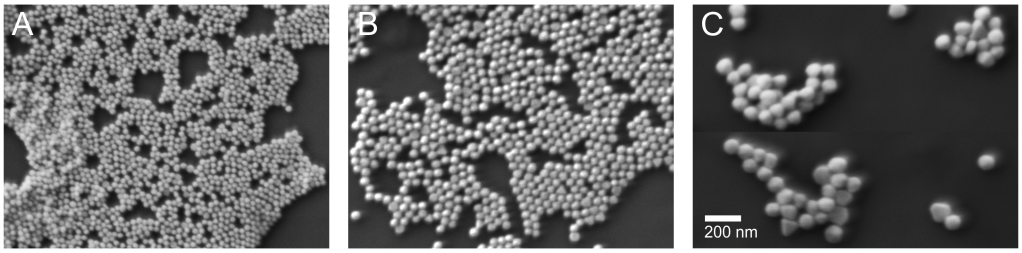

Figure 5.12: Scanning electron microscopic images of (A) 30 nm , (B) 50 nm and (C) 80 nm gold nanoparticles. The images were acquired at the same magnification of 50,000.

In preparation of the experiments the solution of AuNP was placed in a chamber on a glass object slide. Spherical nanoparticles with a diameter of up to 100 nm remained in solution without aggregating due to stabilization by citrate.

For the measurements on single gold nanoparticles, an aqueous suspension was first placed in special chambers (Gene Frames, Nr. AB-0576, Thermo Fisher Scientific, Waltham, MA USA) on glass slides. The chambers were closed with 170 μm coverslips. Immobilization of the nanoparticle was required for the measurement of the scattering spectrum, the irradiation and the detection of the cavitation bubble. For immobilization of the nanoparticles, the slides were silanized by bathing in a 3-aminopropyltriethoxysilane (APES) solution, whose excess was removed by repeated rinsing. After this treatment the slightly negatively charged gold nanoparticles tend to bind electrostatically to the positively charged glass surface. Figure 5.13 shows a slide with two chambers containing nanoparticle samples.

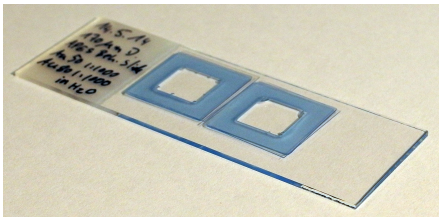

Figure 5.13: Glass slide with two chambers containing nanoparticle samples in aqueous solution used for the measurements.

5.3.2 Optical setups

Experiments were carried out with two optical setups. The first one, a flash photography setup developed by Vogel and co-workers [151, 152], was used for fast image acquisition of cavitation bubbles nucleated by optical breakdown in medium. It was utilized in this work in order to validate the bubble interferometry and to study the interference in the scattered light that can be measured for bubbles generated in free medium and on a rigid glass surface. Images on the laser beam axis (front view) and from the side onto the focus were acquired at different time points during the bubble oscillation. Bubble shape was visualized and the maximum expansion radius was correlated with the measured expansion time.

In the second set up a darkfield microscope was combined with spectrally resolved scattered light detection with the time resolved detection of the backscattering of coherent light. This setup allows the investigation of bubble formation around the nanoparticles.

Flash photography setup

Centerpiece of the experimental setup shown in Figure 5.14 is a water cuvette, which holds three microscope objectives and a long distance (LD) condenser in position, that allows spatially precise focusing of the laser beams to induce and detect cavitation bubbles as well as the imaging setup. An infinity corrected immersion objective (type HPX APO UV Vis IR, 40 x / 0.8, Leica, Wetzlar, Germany) with a nominal NA 0.8, which was reduced to an effective NA 0.58

by use of an iris, was used to focus the continuous-wave laser (type Obis, single frequency, 561 nm, PN 152755, Coherent, Santa Clara, USA) and a pulsed laser (type PNV-001525-140, 355 nm, 560 ps, Teem Photonics, Grenoble, France) collinearly and confocally in the cuvette. The back scattered light of the cw laser was collected with help of the same microscope objective. Transmitted cw laser light passed the LD-condenser on the opposite side of the cuvette. For both, backscattered light detection bubble interferometry and the transmitted light detection, an amplified PIN photodiode with 200 MHz bandwidth (photoreceiver type HCA-S-200M-SI, Femto, Berlin, Germany) was utilized.

In order to image bubbles on the beam axis from backward direction a Köhler illumination was established with a 18 ns pulsed plasma flash lamp (Nanolite KL-L, High-Speed Photosysteme, Wedel, Germany) and the long distance condenser (Leica, NA 0.55). Before passing the condenser a part of the light was directed by a dielectric beam splitter and mirrors into the microscope objective (type HCX APO L U-V-I, 10x/NA 0.3, Leica, Wetzlar, Germany) to illuminate the bubble under 90°. Images of the bubble were acquired in the backwards and 90° view with the digital cameras Canon EOS 5D and Nikon D5100, respectively. Part of the light from the flash lamp was picked up by a photodiode and displayed on the oscilloscope together with the interference in the backscattered light in order to measure the time delay between the photograph and the bubble generation.

A combination of a $\lambda/2$ plate and a thin film polarizator (TFP) allowed continuous adjustment of the pulse energy by which the plasma was formed to generate cavitation bubbles. Pulse energy was measured by guiding a certain fraction of the light after the TFP to a detector (PD10PJ, Ophir). The energy measured here was calibrated with a second energy detector (PD10, Ophir) placed behind the water filled cuvette instead of the LD condenser. The energy calibration measurements were conducted before the experiments.

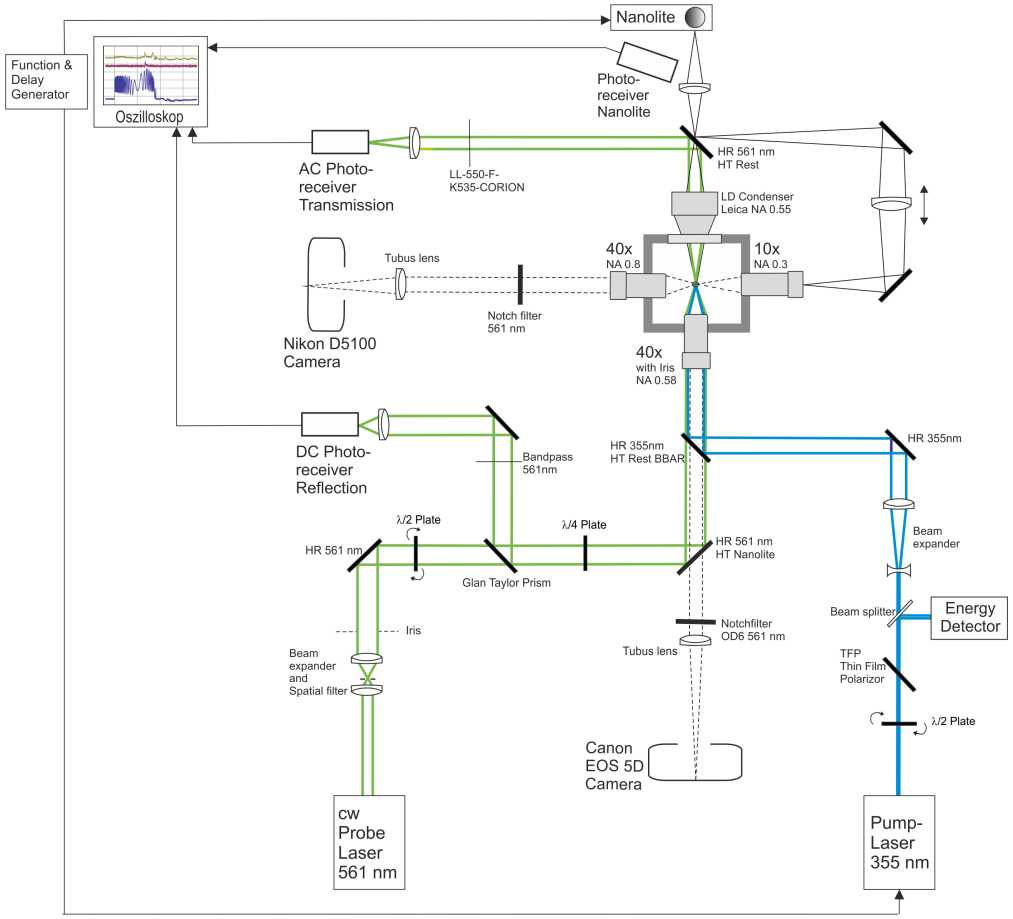

Figure 5.14: Experimental arrangement for imaging of laser induced cavitation bubbles by flash photography. Synchronously bubble dynamics was measured by backscattered light detection. The original setup was developed by Vogel and co-workers [151].

Setup for single particle measurements

The optical arrangements used for darkfield microscopic spectroscopy and investigation of cavitation bubbles around gold nanoparticles are shown in Figure 5.15. In order to detect single gold nanoparticles and to measure their scattering spectra a darkfield microscope was used. Essential components of the setup were a white light source (high-pressure Xenon arc discharge lamp, 5121 Auto LP, Richard Wolf, Knittlingen, Germany), an infinity corrected microscope objective of high numerical aperture (Zeiss, LD Plan Neofluar 40x/0.6 corr) and a sensitive scientific electron multiplying charge-coupled device (EMCCD) camera (Andor, iXON X3 897D, Belfast, Northern Ireland).

For darkfield microscopy the sample had to be illuminated with light that was not collected by the objective. Therefore, the condenser had a larger NA than the objective and a darkfield aperture had to block light, that would propagate into the objective. The condenser had an illumination numerical aperture of $0.8 \leq \mathrm{NA} \leq 0.95$. Hence, for imaging objectives with numerical apertures below NA 0.8 could be used. For imaging the particles a long distance microscope objective (Zeiss, LD Plan Neofluar 40x/0.6 corr) was utilized . The objective had a transmission of above 80 % in range between 400 nm and 800 nm and above 40 % for wavelengths up to 1100 nm. Nanoparticles with diameters down to 50 nm could be detected in the dark field images. A grating allowed not only to image of the particles but also their scattering spectra. The exact layout is described in Chapter 5.3.3.

Two different pulsed lasers, CryLas Type FDSS532 (passively Q-switched, frequency doubled Nd:YAG laser, 532 nm, $\tau_L = 800$ ps full width at half maximum) and Continuum Type SureLite I (actively Q-switched, frequency doubled Nd:YAG laser, 532 nm, $\tau_L = 4$ ns FWHM) were used for

excitation of the nanoparticles. A 30 mW continuous-wave (cw) single longitudinal mode laser (CrystaLaser, CRL-DL640-035-S) emitting at 640 nm was coupled confocally to the pulsed laser into the microscope objective. A beam splitter cube aligned in the optical path of the cw-laser guided the light backscattered from the cavitation bubble to an amplified PIN photodiode with 200 MHz bandwidth (Femto, HCA-S-200M-SI, DC-coupled). Perfectly confocally adjustment between pump and probe laser was sought to get a good signal-to-noise ratio (SNR) of the detected interference signals.

The experimental routine consisted of searching of a particle, positioning of the particle in the center of the laser beam and measurement of the cavitation bubble. The scattered light spectra were measured at the same position before and after irradiating the particle.

In order to measure scattered light in transmission a combined bright-/darkfield (BF/DF) microscope objective (Zeiss, LD EC Epiplan Neofluar 100x/NA 0.75) was incorporated in the illumination path instead of the darkfield condenser. Thereby darkfield illumination for particle detection and scattered light spectroscopy as well as the bubble measurement by transmitted light detection were possible without changing the alignment of the setup during the experiment. Transmitted light was detected with an amplified PIN photodiode with 1.4 GHz bandwidth (Femto, HSA-X-S, AC-coupled). The signals of both detectors were acquired with a 1 GHz oscilloscope (Tektronix, DPO 4000). The 200 MHz receiver had 20 V/mA transimpedance gain resulting in a sensitivity of 11 V/mW at 800 nm (8.4 V/mW at 640 nm), whereas the sensitivity of the 1.4 GHz receiver was 2.5 V/mW at 760 nm (2 V/mW at 640 nm).

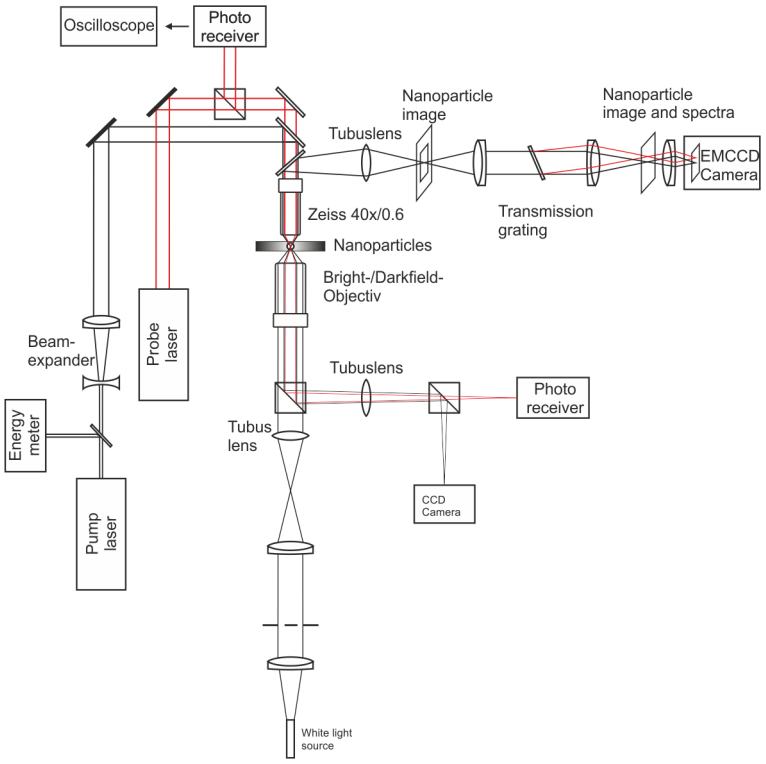

Figure 5.15: Setup for the detection of cavitation bubbles around gold nanoparticles. Darkfield microscopy was combined with a scattering light spectroscopy and time-resolved backscattering detection. A bright-/darkfield microscope objective in the illumination path allows for darkfield illumination and detection of scattered probe laser light in transmitted by the sample.

5.3.3 The scattered light spectroscopy under darkfield microscopy

The optical setup for combined darkfield microscope and scattered light spectroscopy is shown in more detail in Figure 5.16. Light from an intermediate image (image 1) formed by the objective and tube lens was collimated by L_2 through a holographic transmission grating. By L_3 an image is formed at image 2, which contained the darkfield contrast image of the nanoparticles (zero order of the grating) and the spectral information of the AuNP (first diffraction order),

respectively. By means of a lens (L_4) image 2 was recorded by the EMCCD camera (Andor iXON X3 897D, Andor, Belfast, Northern Ireland).

A slit placed in the plane of image 1. The slit width was adjustable perpendicular to the diffraction direction of the grating. Thus, overlapping spectra nearby AuNPs could be masked.

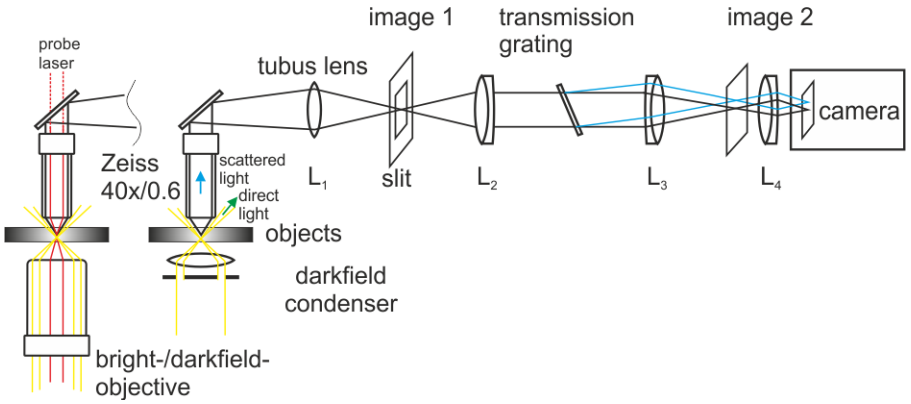

Figure 5.16: Darkfield microscopy setup with integrated scattered light spectroscopy. Experiments were conducted with the darkfield condensor and a combined bright-/darkfield microscope objective in the illumination path.

In order to measure the spectra of the light scattered by the nanoparticles a holographic transmission grating with 300 lines/nm and a blaze angle of 17.5° was used.

Optical layout was based on the grating equation

$$\sin(\Theta_i) + \sin(\Theta_m) = \frac{m \cdot \lambda}{g},$$

in which m denotes the diffraction order, g the grating constant (unit mm/line) and Θ_i and Θ_m the angle between the normal vector of the grating and the incident and diffracted light respectively. In combination with the resolution of the grating $\lambda/\Delta\lambda = m \cdot N$ with the number of irradiated lines N and the dispersion $d\alpha/d\lambda \approx \Delta\alpha/\Delta\lambda = n/(g \cdot \sin(\Theta))$ (n refractive index) the required grating constant was determined in order to cover a spectral range between 0 nm and 1000 nm. An image of the nanoparticle in the 0^{th} diffraction order as well as the spectrum in the 1^{st} order were recorded. For normal incidence to the grating the diffraction angle and the resulting NA behind the grating were determined by

$$\Theta_m = \arcsin\left(\frac{m \cdot \lambda}{g}\right) = \arcsin\left(\frac{1000\,nm}{g}\right)$$

$$NA = n \cdot \sin\left(\frac{\Theta_m}{2}\right)$$

An object field of 100 µm x 100 µm and a dispersion of 5 nm/pixel, which corresponds to 120 pixel for a spectrum between 400 nm and 1000 nm, could be recorded with the EMCCD camera. The required resolution of the grating needed $600\,nm/5\,nm = 120\,lines$ to be irradiated. The optical lenses in the setup Figure 5.16 were a tubus lens with $f_1 = 164.5\,mm$, a lens (projector objective) with $f_2 = 90\,mm$ and $f-number = 2.5$, a (photography) objective with $f_3 = 50\,mm$, $f - number = 1.2$ as well as a (photography) objective with $f_4 = 50\,mm$, $f - number = 1.8$.

The use of a combined bright-/darkfield microscope objective (Zeiss, LD EC Epiplan-Neofluar 100x/0.75 HD DIC) for illumination allowed also detection of transmitted light. The objective contains a light path for illumination in the sheathing of the objective, which is aligned coaxially to the central imaging beam path. Both paths are confocally aligned. Usually the objective is operated in the epi-illumination mode in order to inspect surfaces. Here, the outer beam path was utilized for illumination of the sample, while laser light for the transmission measurements was detected in the central beam path.

Spectral resolution and calibration

In order to characterize the effective magnification and resolution of the two-stage imaging setup a resolution test chart (positive USAF, test chart, Edmund Optics, Karlsruhe, Germany) was used (Figure 5.17 A and B). The line pattern of group 6 and 7 of the test chart were imaged in the transmitted light and in the darkfield contrast. The first two elements of group 6 were well resolved and separated from each other, from group 7 the lines of element 4 (181 $lines/mm$, 2.76 µm/line) were resolved. With the test chart and the detected image on the EMCCD chip an effective magnification of around 8 was determined.

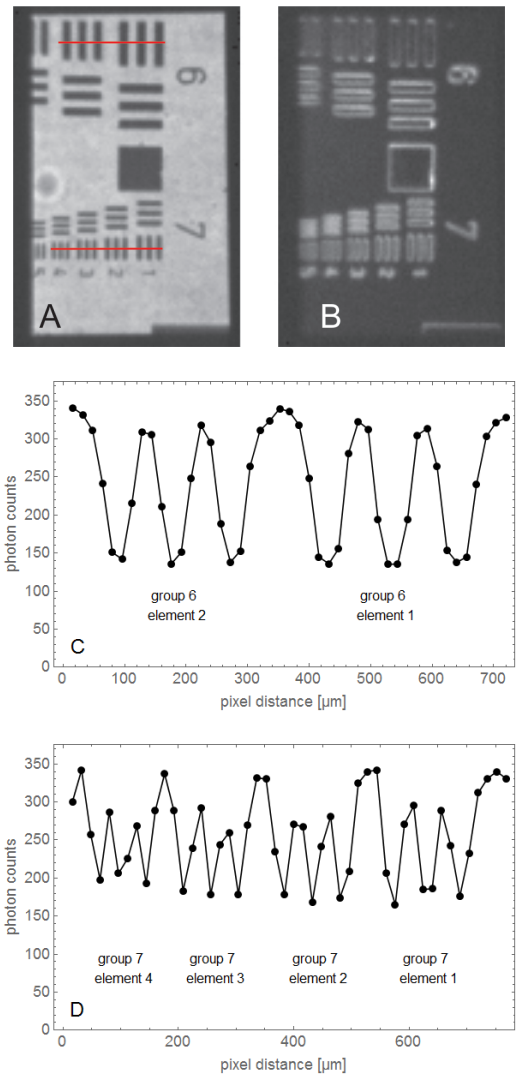

Figure 5.17: USAF resolution test chart imaged by the microscope setup in transmitted light (A) and darkfield contrast (B). Along the red lines in (A) the photon counts for group 6 and group 7 are shown in (C) and (D) respectively.

The spectral calibration was performed with help of a calibration standard light source with known emission spectrum. The white light source used for illumination was replaced by a low pressure mercury lamp (Lot Oriel, type Hg (Ar), model no. 6035). A slit placed in the image plane behind the tubus lens simulated a point source same intensity distribution as the detected nanoparticle. Thus, the reference was measured with the same spectral resolution as the nanoparticle spectrum.

To the measured line spectrum of the Hg (Ar) lamp a quadratic function was fitted, which was used for calibration:

$$\lambda\,(pix) = m_2 \cdot x^2 + m_1 \cdot x - m_0 \cdot x_0. \tag{5.5}$$

x denotes the pixel number and x_0 the pixel of the 0th diffraction order. Parameters m_1, m_2, m_0 were determined from pairs of measured line positions and the corresponding wavelengths of the mercury lamp spectrum (Figure 5.18). From the calibration function, spectral dispersion between pixel 160 (400 nm) and pixel 85 (702 nm) was determined to vary linearly between 4.1 nm/pixel and 3.9 nm/pixel respectively.

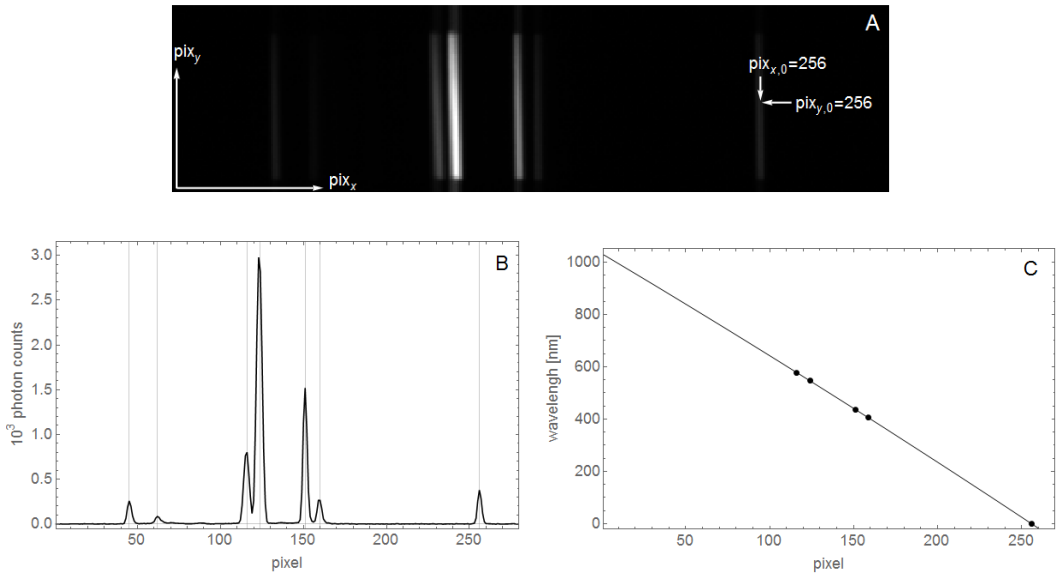

Figure 5.18: Measurements of calibration lamp spectrum (A). Detected photon counts along pixel row $pix_y = 256$ (B). The calibration function was fitted for the calibration wavelength as well as the origin of the spectrum for $O = (x_{x,0},\, \lambda = 0)$ (C).

Effect of the AuNP immobilization on detection and temperature increase

For reproducible measurements of scattered light spectra and bubble formation immobilization of nanoparticles was required. Here spontaneous binding to the surface of a glass object slide was used. When the particle is captured for example with the help of an optical trap, bubble formation around AuNP in free medium can be measured. Optical trapping of a nanoparticle was established with cw lasers [163, 164] and also with a supercontinuum laser [165, 166, 167]. For optical trapping of gold nanoparticles typically infrared wavelengths, which are significantly longer than the particle resonance wavelength, are used [163, 168]. The duration for which an AuNP can be captured and the stiffness of the trap, which determines the stability of the particle spatial position, depend on the laser power. Depending on the size of the metal particles and the numerical aperture of the used microscope objective, higher powers of the order of 100 milliwatts and more are required [163, 166, 168]. However, optical trapping can lead to significant heating of the captured gold nanoparticle [169] and thus of the surrounding medium. This consequently effects the measurement of the nanoparticle scattering spectrum and also the formation of a vapor bubble around the nanoparticle.

In contrast to the complex method of optical trapping the electrostatic binding to a silanated glass slide is technically simple and provides immobilization without effecting the initial temperature of a AuNP. Nevertheless, for the calculation of the scattering spectrum the change in refractive index of the surrounding due to the glass slide has to be considered. Mie theory cannot directly account for a supporting substrate. In order to determine AuNP size the measured scattering spectrum was compared to the plasmon resonance spectrum calculated with Mie theory and an effective refractive index [82].

Further, impact of the the supporting glass slide on thermal behavior of the nanoparticle was considered negligible. Setoura et al. found that temperature increase of a cw laser irradiated nanoparticle generally depends on both, the surrounding medium and the supporting substrate [170]. Experiments and simulations were carried out with AuNP heated up to 600 K while located on a glass with a refractive index of n = 1.52 and thermal conductivity of 1.0 $W\,m^{-1}\,K^{-1}$,

which is in the range of the water thermal conductivity of 0.6 $W\,m^{-1}\,K^{-1}$ [170]. Their simulation results show only minimal deviation from the radial symmetric temperature distribution due to the glass substrate. The exact extend of the deviation was not quantified. Thus, for further analysis and discussion of the results obtained for bubble interferometry it will be assumed that the glass substrate exhibits negligible cooling effect compared to a particle in free medium.

Detection and size measurement of gold nanoparticles

By light scattering spectroscopy, the size of the irradiated particle was determined before pulsed laser irradiation. In order to determine the particle size the measured scattering spectrum of a detected gold nanoparticle was related to a reference spectrum of the white light source used for illumination. This white light reference spectrum was measured in the same manner as the line spectrum used for the spectral calibration. Figure 5.19 shows images of a reference and a gold nanoparticle as well as the scattering spectrum determined by dividing the particle spectrum by the reference spectrum. Noise in the ranges below 480 nm and above 780 nm is due to the bandwidth of the light source as well as the lower diffraction efficiency of the transmission grating. The particle size was determined calculating the scattering spectrum and varying the particle parameter radius in the calculated Mie scattering spectrum (equations 2.8to 2.10) until the calculated curve fitted best to the measurement. For the calculation the supporting glass object slide was considered (equation 2.32) with a weighting factor of $g = 0.7$.

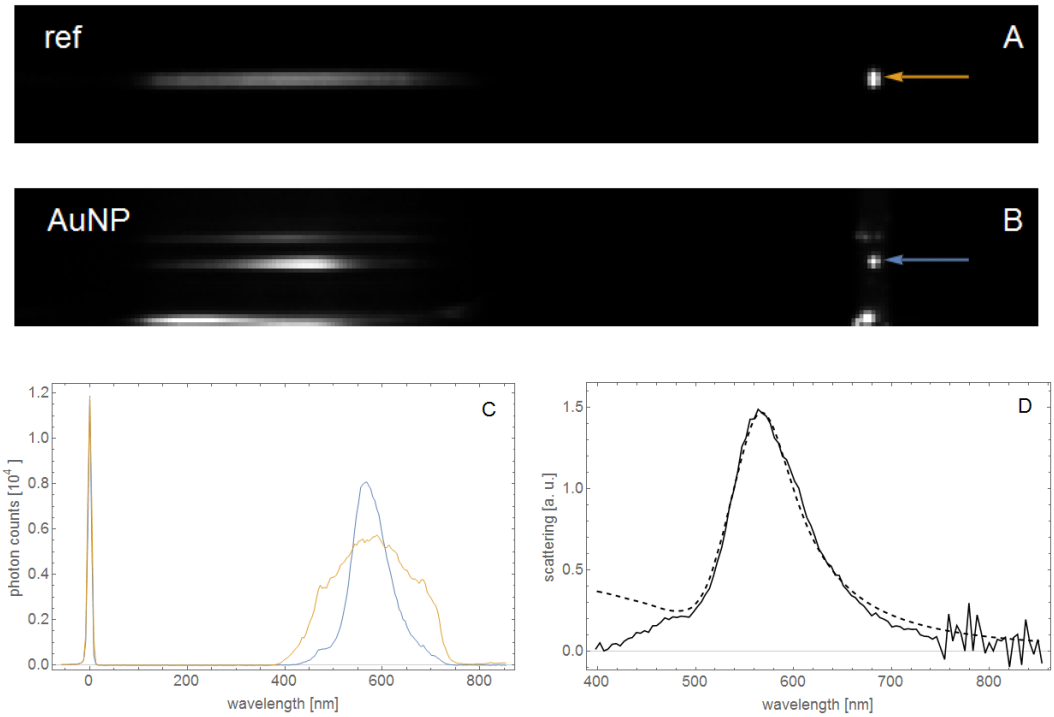

Figure 5.19: Acquired images of a reference (A) and a 40 nm gold nanoparticle (B) were used to extract the scattering spectra were extracted (C). Dividing the nanoparticle spectrum (blue) by the reference spectrum (yellow) results in the particle scattering spectrum (solid line, D). Calculated Mie scattering spectrum (dashed line) for an AuNP with a radius of 40 nm fits best the characteristic spectrum.

For each irradiation experiment the nanoparticle size was determined by this spectral analysis. Figures 5.20 and 5.21 show the spectra and images of six and four bright objects, respectively, indicated by arrows in the darkfield image. Two suspensions of gold nanoparticles with a nominal diameter of 50 nm and 80 nm (manufacturer datasheet) were filled in the measuring chambers. Imaged objects (Figure 5.20 A-F and Figure 5.21 A-D) were spectrally analyzed. Calculated Mie scattering spectra were fitted to the measured spectra by varying the nanoparticle radius. Four (Figure 5.20 B, C, D, F) and three (Figure 5.21 A, B, D) objects were identified gold nanopar-

ticles, while three objects exhibited scattering spectra without plasmonic band (Figure 5.20 A, E and Figure 5.21 C). For the sample with nominal 50 nm AuNPs (Figure 5.20) the calculated spectra in (B, D) correspond to particles with diameters of 50 nm, calculated spectra (C, F) correspond to particles with a diameter of 66 nm and 74 nm, respectively. For the sample with nominal 80 nm AuNPs (Figure 5.21) the calculated spectra in (B, D) correspond to particles with diameters of 80 nm, calculated spectrum (A) corresponds to a 100 nm particle. The spectra measured for (Figure 5.20 A, E and Figure 5.21 C) exhibit increased scattering above 600 nm. This could be explained by aggregation of several particles.

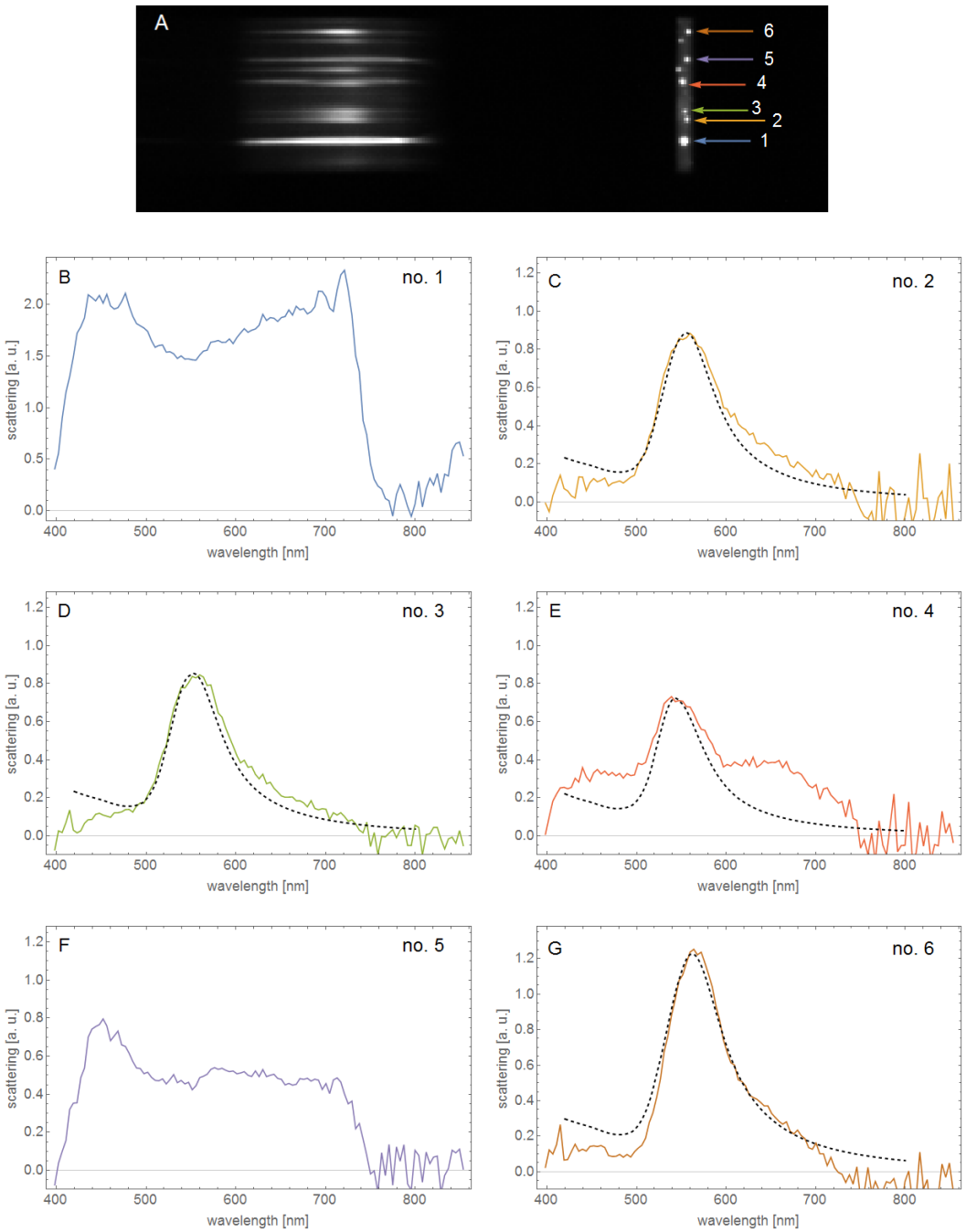

Figure 5.20: (A) Darkfield microscopy (darkfield condenser in illumination setup) of a sample of gold nanoparticles with a nominal diameter of 50 nm. Scattering Spectra (B-F) measured for objects (1-6). Objects (2, 3, 4, 6) were identified gold nanoparticles, while (1, 5) exhibit scattering spectra of non-metallic particles. Calculated spectra (2, 4) correspond to scattering of 50 nm nanoparticles, calculated spectra (3, 6) correspond to scattering of a 66 nm and a 74 nm nanoparticles, respectively.

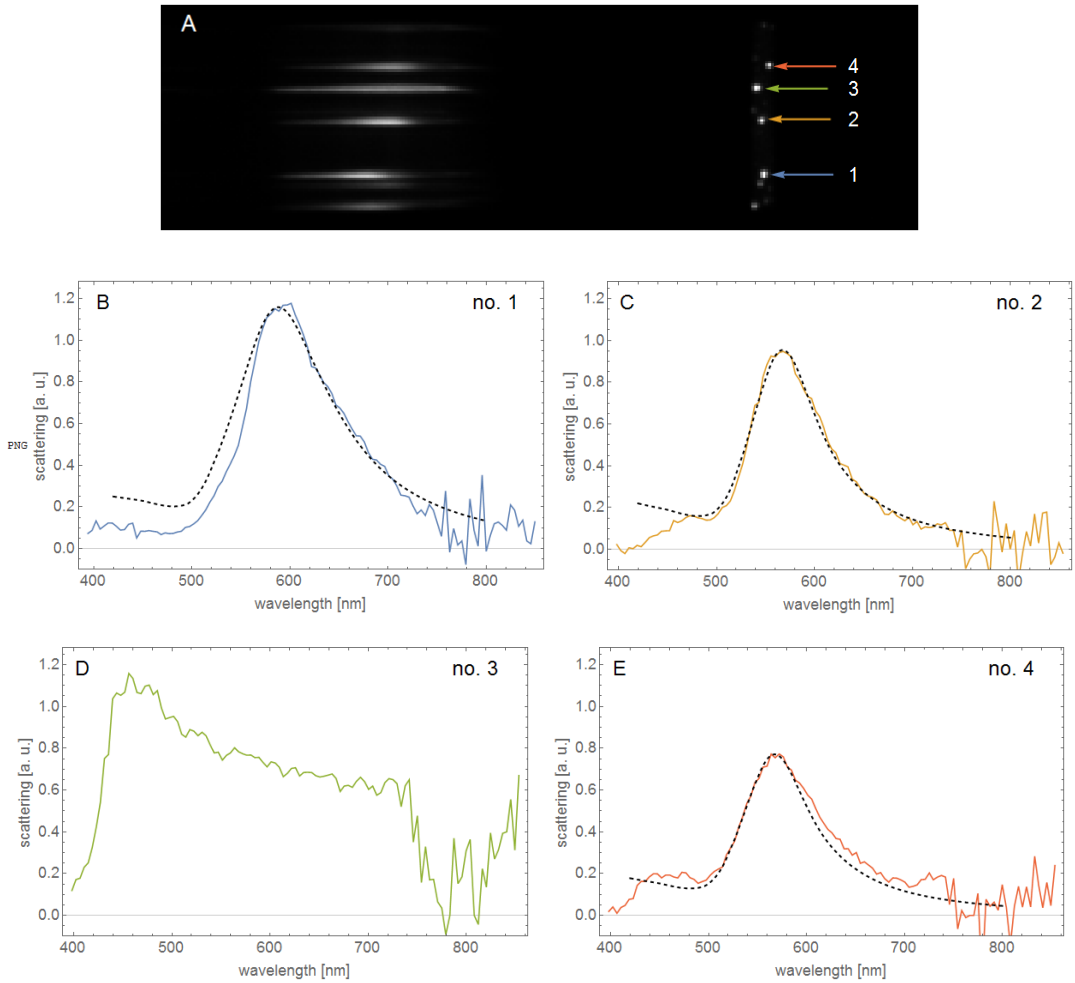

Figure 5.21: (A) Darkfield microscopy (darkfield condenser in illumination setup) of a sample of gold nanoparticles with a nominal diameter of 80 nm. Scattering Spectra (B-E) measured for objects (1-4). Objects (1, 2, 4) were identified gold nanoparticles while (3) exhibits scattering spectra of a non-metallic particle. Calculated spectra (2, 4) correspond to scattering of 80 nm nanoparticles, calculated spectrum (1) corresponds to scattering of a 100 nm nanoparticle.

The darkfield microscopy allows for identification and positioning of the nanoparticles in the laser beam. The measured scattering spectra provide information on the size of the detected nanoparticles, which is a fundamental parameter for energy deposition, the bubble nucleation and the subsequent development of the bubble wall motion.

Resolution of scattered light spectroscopy

Position and the size of gold nanoparticle were detected by darkfield imaging and detection of the scattering spectra of the nanoparticles.

More than the optical resolution the established spectral resolution is of importance for the accuracy by which the size of a detected AuNP can be determined.

A spectral sampling of 4 nm / pixel was obtained (cf. Chapter 5.3.3). Mie theory predicts for the scattering spectra of 50 nm and 80 nm sized AuNP, that deviating ±1 nm from the nominal radius results in a peak wavelength shift of ±1 nm and ±2 nm respectively (Figure 5.22). In the experimental setup a deviation in nanoparticle radius by approximately ±2 nm can be resolved for the AuNP investigated here.

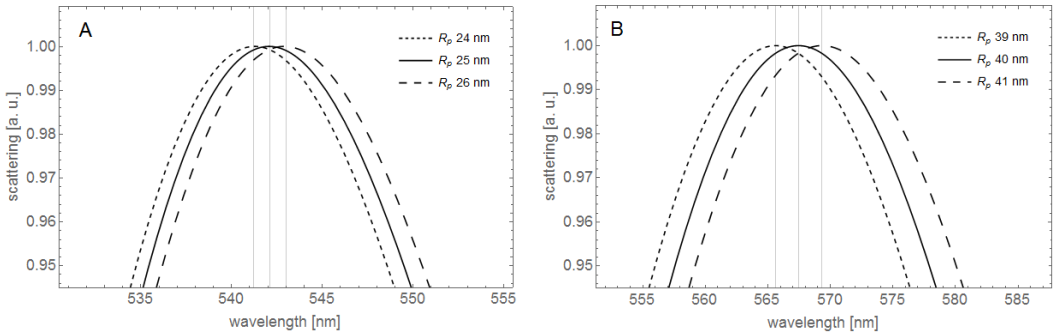

Figure 5.22: Spectra calculated for 50 nm and 80 nm sized AuNP. Mie theory predicts for deviating ±1 nm off the nominal radius a peak wavelength shift of ±1 nm and ±2 nm respectively in the scattering spectra.

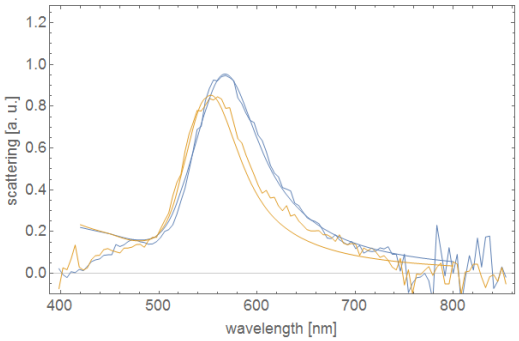

Figure 5.23: Measured scattering spectra (solid lines) for 50 nm (yellow lines) and 80 nm (blue lines). Mie scattering spectra (dashed lines) were calculated for 50 nm and 80 nm and weighting the refractive index by weighting factor g = 0.7 (cf. Equation 2.32, [82]).

5.3.4 Generation of vapor bubbles around gold nanoparticles

Temporal laser pulse shape

For the bubble formation on the AuNPs two different Q-switched lasers emitting pulses of 800 ps and 4 ns duration were used. Besides in pulse duration, the lasers differ in temporal profiles of the pulses. The passively Q-switched laser (CryLas, Type FDSS532) emitted smooth pulses which temporal profile can be considered Gaussian shaped, while the actively Q-switched laser (Continuum, Type SureLite I) emitted a strongly modulated pulse pattern (Figure 5.24).

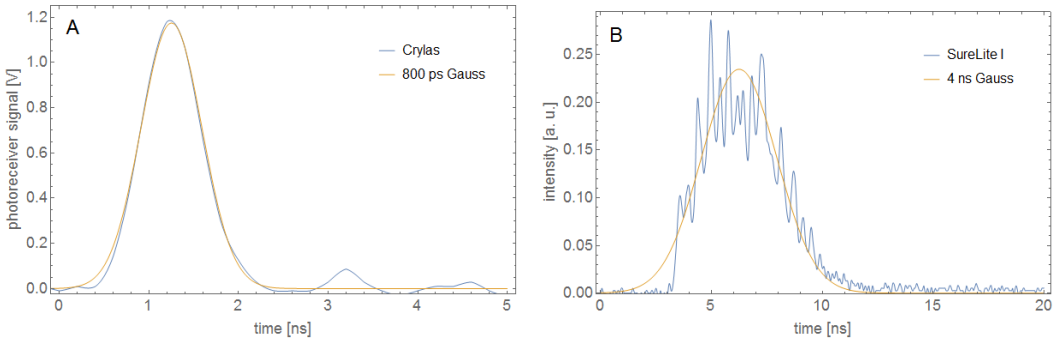

Figure 5.24: Measured laser pulses (blue lines) of the passively Q-switched CryLas laser (A) and the actively Q-switched Continuum laser (B). A Gaussian fit to pulse shape (yellow lines) reveals pulse lengths of 800 ps (A) and 4 ns (B).

Figure 5.25 shows a measured laser pulse of the SureLite I and the calculated temperature in-

crease inside a 50 nm and an 80 nm sized AuNP. The temperature increase follows the irradiation pulse over time, which is given by the convolution of the instantaneous thermal AuNP response with the pulse shape of the irradiation. The temperature modulations are the less prominent the larger the particles are. This is due to the increasing thermal capacity. For 30 nm and larger particles only a minimal effect of the pulse modulation on the bubble formation is expected.

Compared to a Gaussian shape the pulses of the SureLite I laser exhibit a stronger slope of the intensity at the onset, which subsequently lead to a stronger heating rate. The deviation from a Gaussian pulse shape has an influence on the bubble formation. In particular the evaporation time point can be reached during this onset phase of the irradiation pulse. In this case, deposited energy will be smaller than compared to the Gaussian pulse used in the calculations. The extent to which the steeper rising edge of the laser pulse has an effect on the temperature increase can only be determined in comparative experiments. For this, the utilized laser would have to be seeded, which could not be done in the context of the work.

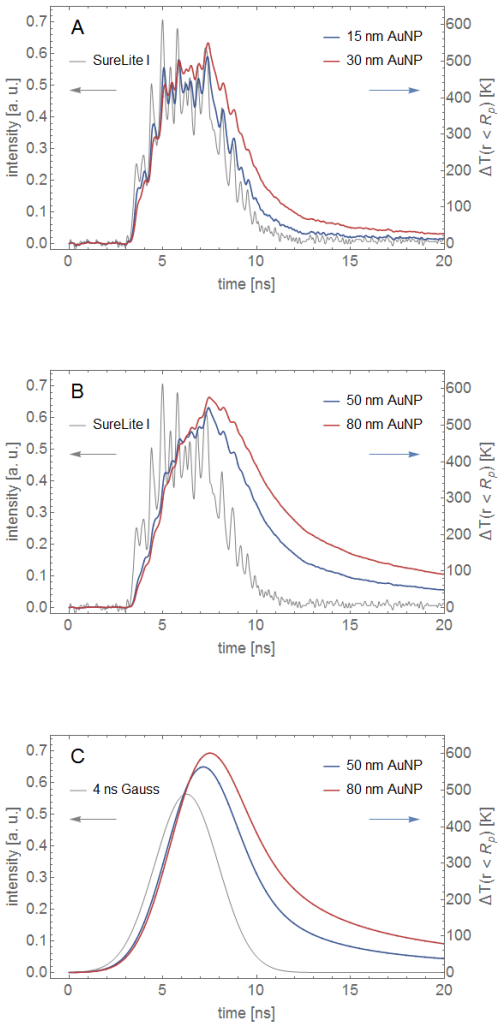

Figure 5.25: (A) Typical laser pulse of the Surelite I and the calculated temperature increase inside a 50 nm and an 80 nm sized AuNP for radiant exposure with 10 mJ cm^{-2}. (B) Temperature increase inside a 15 nm and a 30 nm sized AuNP irradiated with radiant exposure of 50 mJ cm^{-2} and 20 mJ cm^{-2}. Laser pulses of the Surelite I are strongly modulated. The larger the size of the AuNP the smoother is the temperature increase inside the AuNP. (C) For comparison a Gaussian pulse of 4 ns duration (FWHM) and calculated temperature increase inside a 50 nm and an 80 nm sized AuNP is shown for radiant exposure with 10 mJ cm^{-2}.

Energy reference and irradiation spot size

To prepare an irradiation experiment radiant exposure was determined in the sample. The energy of an applied pulse was measured with the help of a calibrated reference energy meter located at the site of the excitation laser (cf. Figure 5.15). The focus shape was measured by imaging with help of the BF/DF objective in transmission geometry. Figure 5.26 (A) shows the Airy pattern of the laser beam in the sample plane. This pattern was generated due to the coupling of the collimated laser beam with a spatially Gaussian intensity profile into the microscope objective. Figure 5.26 (B) shows the intensity profile of the irradiation beam (solid red line) and a fit of the center peak by a Gaussian function (dashed black line). Only pulse energy in the center peak is incident on the particle. Its part from total incident energy is calculated by dividing the spatial integral over the Gaussian function with the spatial integral over the measured pulse function. In result, only 3 to 4% of the irradiation was located in the center peak, which exhibits a full width at half maximum intensity at a radius of around 250 nm.

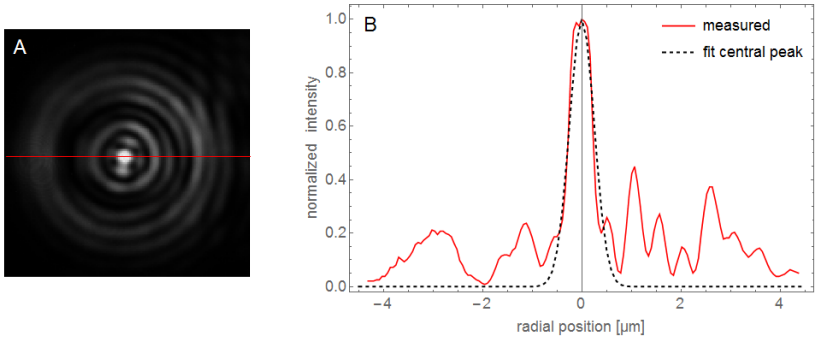

Figure 5.26: (A) Image of the excitation laser beam (CryLas, Type FDSS532) in the sample plane detected with a CCD camera in transmission. (B) Peak normalized intensity distribution (solid, red line) measured along the red line shown in (A). The center peak was fitted with a Gaussian distribution function.

5.3.5 Bubble detection by transmitted light measurement

Cavitation bubbles generated around an AuNP were detected by changes of the transmitted light. Already a small variation of the refractive index within the focus can scatter light off the probe laser beam and lead to a measurable signal loss in transmission. A cavitation bubble caused a rapid signal decrease, which is related to sidewards and backwards scattering at bubble wall. Figure 5.27 shows the signal of a bubble oscillation induced by 800 ps pulsed irradiation with 535 mJ cm^{-2} at a wavelength of 532 nm around a gold nanoparticle with 80 nm diameter. The transmission changes symmetrically. Local minima were observed shortly after the onset of the bubble expansion and close to the bubble collapse. After half of the oscillation time t_{osc} a local maximum is usually observed. The measure of the bubble oscillation time t_{osc} can be used to determine the maximum bubble radius $R_{b,max}$ with the help of equation 2.67.

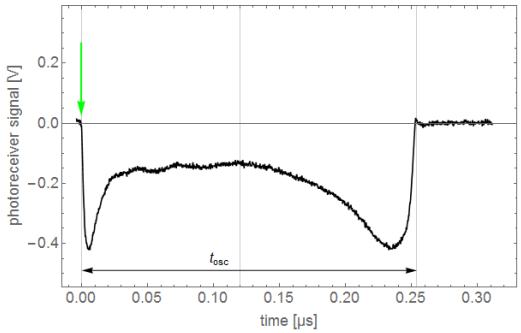

Figure 5.27: Transmission signal measured during a cavitation bubble generation around a gold nanoparticle with 80 nm diameter, which was irradiated with 800 ps pulsed irradiation and 535 mJ cm^{-2} at a wavelength of 532 nm. Onset of the laser pulse marked by the green arrow. The oscillation time t_{osc} was 254 ns.

5.3.6 Bubble detection by measurement of backscattered light

The intensity of light backscattered by the cavitation bubble is modulated. In addition to the bubble oscillation time the bubble wall velocity can be determined from the modulation frequency. Following the backscattering signal of cavitation bubbles in free water and the corresponding signal analysis for determining the bubble wall velocity will be introduced. Afterwards, the measurement of cavitation bubbles formed on a rigid surface will be shown.

Signal analysis for cavitation bubbles in free medium

The bubble interferometry utilizes the backscattered probe light from a laser focus, which is positioned in the center of the bubble. The interference modulation of the components reflected at the front and rear side of the oscillating bubble is evaluated. The method offers single-shot detection of a laser induced bubble oscillation. Coherent laser light, backscattered at the anterior and rear bubble walls is superimposed in the photoreceiver and generates a modulated signal for a varying bubble radius. Figure 5.28 shows the bubble interferometry signal of a cavitation bubble in free water.

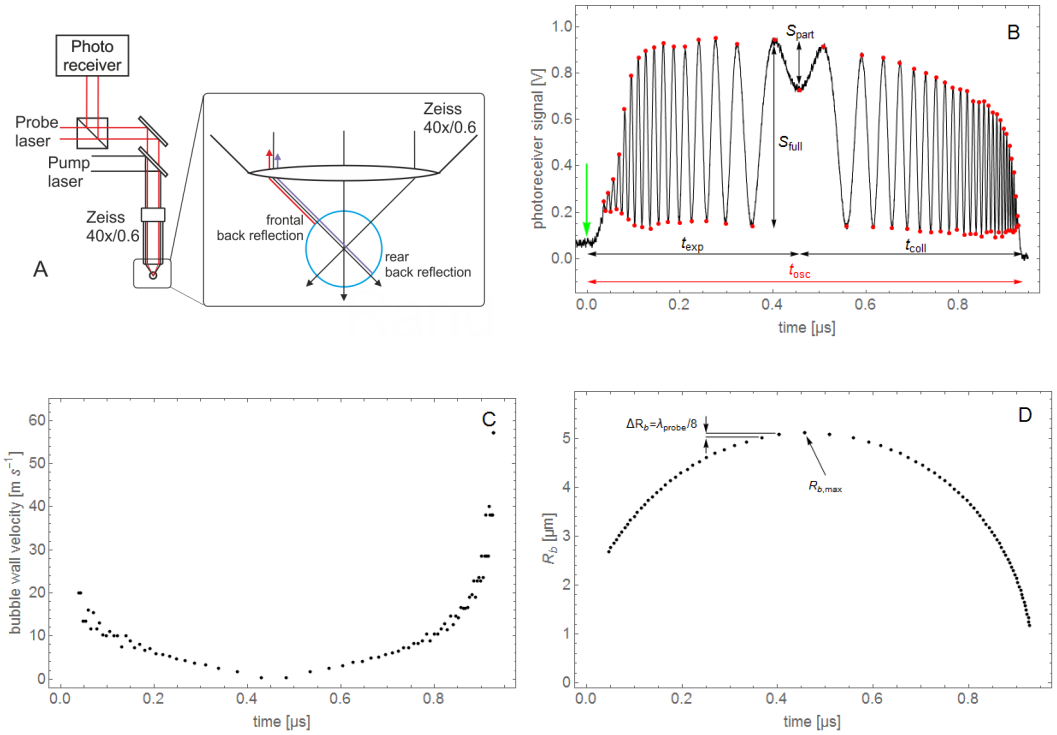

Figure 5.28: A) Schematic drawing of the experimental arrangement for the detection of bubble formation and interferometric measurement of the temporal evolution of bubble size. B) An interference signal of a free cavitation bubble generated by a focused laser pulse in water. C) The bubble wall velocity is directly calculated from the interferometry signal by Equation 5.8 and Equation 5.9. The diameter of the bubble wall corresponds to $\lambda_{probe}/4$ for a modulation fringe of the interferometry signal. D) Bubble radius time curve was determined by starting at the maximum bubble radius counting each fringe.

Photoreceiver signal duration and amplitude measured for the backscattered light strongly depends on the bubble size. During bubble formation and initial growth the signal amplitude increases, while the bubble cavity contains dense vapor. With further bubble growth the proceeding phase transition forms a bubble wall and an oscillating interference pattern appears in the potoreceiver signal. This is due to superposition of light that backscatters from the rear bubble wall with light backscattered from the frontal bubble wall. The bubble oscillation with duration t_{osc} refers to an expansion phase and a subsequent collapse phase with durations t_{exp} and t_{col} respectively (see Figure 5.28 B).

While the bubble oscillates with varying bubble wall velocity the interference pattern varies in frequency. The detected signal depends on the phase difference between the backscattered waves from the front and rear bubble wall. A photoreceiver detects the intensity of the two interfering waves, which can be written in terms of the intensities and phase difference of the individual waves.

$$I(t) = I_1(t) + I_2(t) + 2\sqrt{I_1(t) \cdot I_2(t)} \cos[\triangle\varphi(t))] \quad (5.6)$$

$$\triangle\varphi(t) = \varphi_1(t) - \varphi_2(t) \quad (5.7)$$

The time dependence is controlled by the time varying distance $s(t)$ between the front and backside bubble wall. Thus, phase difference $\triangle\varphi$ of the backscattered waves is related to $s(t)$. Assuming a spherically expandion $s(t)$ corresponds to the bubble diameter $D_b = 2 \cdot R_b$.

$$\triangle\varphi = \frac{2\pi}{\lambda}\triangle s(t) = \frac{2\pi}{\lambda} \cdot 2R_b(t) \quad (5.8)$$

The bubble wall velocity u is then calculated from the local frequency υ of the detected inter-

ference modulation.

$$u(t) \quad = \quad \frac{dR_b\,(t)}{dt} = \frac{\lambda}{8\pi} \cdot \frac{\partial \varphi}{\partial t} = \frac{\lambda}{4} \cdot \nu(t) \tag{5.9}$$

Thus, the bubble wall velocity dR_b/dt is directly measured from the local frequency of the backscattered signal depicted in Figure 5.28 (B). A high precision of the velocity measurement is obtained since the evaluation of maxima and minima of the interference signal provides a data point whenever R_b changes by $\lambda/8$. For $\lambda = \lambda_{probe} = 640\,\text{nm}$, this corresponds to a step size of 80 nm between data points.

With the maximum bubble radius calculated from the oscillation time, the radius time evolution can be calculated (5.28 D). For the measured bubble expansion time t_{exp} a maximum bubble radius was calculated with help of equation 2.67. The precision of the absolute values of R_b depends on the accuracy of the $R_{b,max}$ calibration. In most cases the maximum bubble radius is reached for a non-integer number of $\lambda_{probe}/8$, whereas the last fringe exhibits not the full amplitude S_{full}. The traveled distance here can be estimated empirically by weighting $\lambda_{probe}/8$ with a partial fringe amplitude S_{part}/S_{full}.

As an example, interferometry signals of cavitation bubbles in free medium generated by optical breakdown are shown in Figure 5.29. The threshold at which a bubble signal was measured in the configured experiment was 1.89 µJ. With increasing pulse energy the bubble oscillation time t_{osc} and the bubble radius grew.

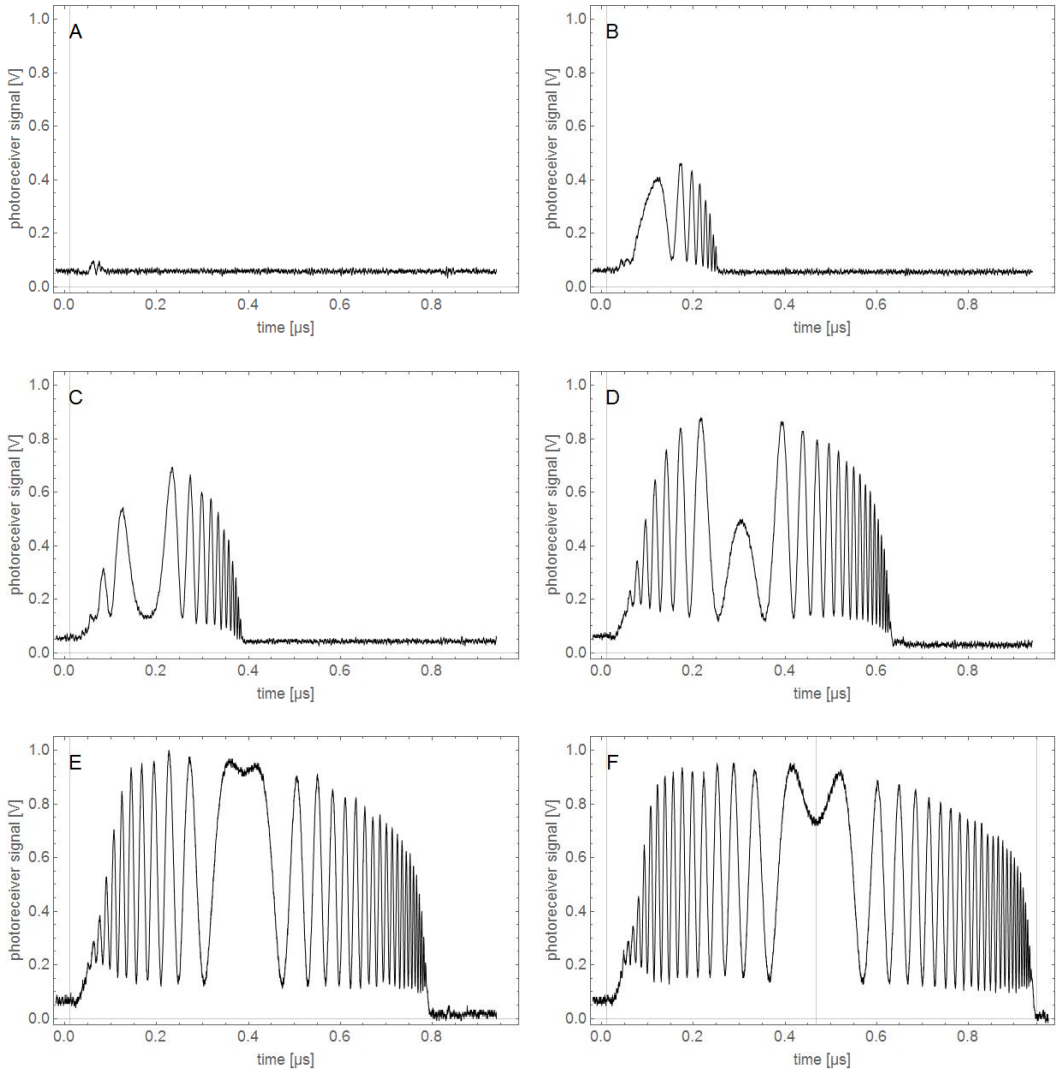

Figure 5.29: Time-dependent photoreceiver signal of the backscattered signal. For free cavitation bubbles in water signals were produced by optical breakdown with pulse energies of 1.89 µJ (A), 2.20 µJ (B), 2.64 µJ (C), 2.86 µJ (D), 3.29 µJ (E) and 3.29 µJ (F).

The interferometric measurement has a large dynamic range and the maximum detectable radius is limited by the imaging geometry. The minimum bubble radius, which can be detected, depends on probe laser wavelength, the numerical aperture of the utilized microscope objective and the photoreceiver sensitivity. More precisely, the probe laser wavelength determines the modulation frequency of the interference and numerical aperture determines the detected intensity of backscattered light, which together with the photoreceiver sensitivity effects the signal to noise ratio of the detected signal.

Figure 5.31 (A) shows the sketch of a bubble with radius R_{b1} much smaller than the beam waist and a larger bubble with radius R_{b2}. For the case of R_{b1} illumination can be assumed parallel, while for larger bubbles when R_{b2} approaches the radius of the spherical wave fronts of the cw laser beam, illumination can be considered parallel and calculation of backscattering on axis approximates the detected interference. Figure 5.31 (A, B) shows the back scattering intensity (cf. equation 2.25 to 2.27) expected for bubbles with different radii on the optical axis and when collected by a numerical aperture of NA = 0.6 . The first intensity maximum detected during a bubble measurement (Figure 5.29) results from the interference between front and rear bubble wall reflections and corresponds to $R_b = \lambda_{probe}/4$, which is a fundamental lower limit of the dynamic range accessible by fringe evaluation. For spherical bubbles with $R_b < \lambda_{probe}/10$ Mie scattering can be approximated by Rayleigh scattering. Intensity of backscattered light is proportional to R_b^6. Thus, back scattering intensity decreases strongly with the bubble radius. For larger radius with $R_b > \lambda$, Mie scattering intensity approaches a R_b^2 proportionality and pronounced interference fringes occur. In this range, the focused probe beam strikes the bubble walls from a perpendicular direction, if the bubble radius is larger than the Rayleigh range z_R of the beam waist. Incident light is reflected back exactly perpendicular and interference fringes will be observed as expected for a bubble radius larger than z_R. However, in the range of $\lambda_{probe}/10 < R_b < \lambda_{probe}/4$ a transition from Rayleigh scattering $\left(\propto R_b^6\right)$ to Mie scattering $\left(\propto R_b^2\right)$ occurs. In this range the relation of scattering and bubble size can be calculated in principle for a known refractive index of the bubble content. Scattered light intensity depends on bubble radius and also on refractive index of the bubble content (cf. Equation 2.14 to 2.27). However, the refractive index decreases during the phase change and the bubble expansion from n = 1.333 of liquid water at room temperature to approximately n = 1.0 of a gas filled bubble. Because the evolution of the refractive index is unknown, also the bubble size cannot be determined directly from the amplitude of the backscattered or the transmitted light.

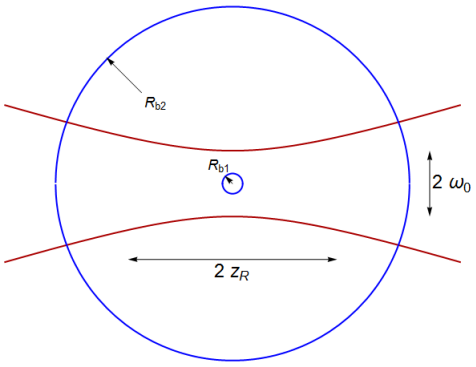

Figure 5.30: Cavitation bubbles of two different sizes within the focus of the probe laser with beam waist ω_0 and Rayleigh range z_R. For small bubbles with $R_b < \omega_0$ the probe laser light wave fronts can be considered plane and for large bubbles with $R_b > z_R$ the spherical wave fronts of the probe laser light here the same radius as the expanding bubble.

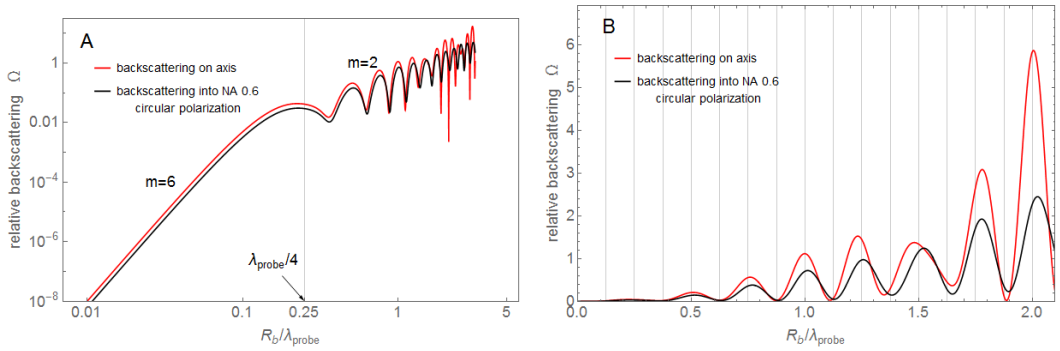

Figure 5.31: (A and B) Dependence of back scattering intensity on normalized bubble radius detected with the microscope objective under a NA = 0.6 (black lines) and for direct backscattering (red line). Calculations were performed for $\lambda = 640\,\mathrm{nm}$.. Small bubbles with $R_b < \lambda_{probe}/10$ show Rayleigh scattering characteristic with a slope of m = 6 in the logarithmic plot (A) and for larger bubble Mie scattering with a slope of m = 2. Back scattered light intensity calculated for detection with numerical aperture NA 0.6 shows small deviation from detection on the optical axis (B).

Limitations of sensitivity are given by spectral sensitivity, noise and bandwidth of the photodetector. A low spectral sensitivity of a detector and noise can be compensated by using a more powerful probe laser beam, whereby focal heating from the cw probe laser sets an upper limit. A high bubble wall velocity corresponds to fast modulation of the interference signal detected by the photoreceiver. Fringes can be fully resolved as long as the time distance between a fringe minimum and the subsequent maximum is larger than the detector rise time t_r or the combined rise time $t_{comb} = \sqrt{t^2_{photodetector} + t^2_{oscilloscope}}$ of the detection system composed of photodetector and oscilloscope [171]. The rise time is linked to the bandwidth BW [171], given by

$$t_r \cong \frac{0.35}{BW}.$$

Thus, for a given probe laser wavelength and detection bandwidth the maximum bubble wall velocity, which can be detected is limited approximately to

$$v_{b,limit} = \frac{\lambda_{probe}}{8}\frac{BW}{0.35}.$$

For example, detection with $\lambda_{probe} = 640\,\mathrm{nm}$ and use of a detection bandwidth of 200 MHz allows for recording of a maximum bubble wall motion $v_{b,limit} = 45\,\mathrm{m{\cdot}}s^{-1}$.

A gold nanoparticle located in the center of the oscillating vapor bubble affects the backscattering signal only at the lower limit of the detection system dynamic range. Figure 5.32 shows the calculated back scattering intensity (cf. Equation 2.14 to 2.27) when the backscattered light of $\lambda_{probe} = 640\,\mathrm{nm}$ is collected within a numerical aperture of NA = 0.6. Also with gold nanoparticles the first intensity maximum accessible by fringe evaluation corresponds to $R_b = \lambda_{probe}/4$.

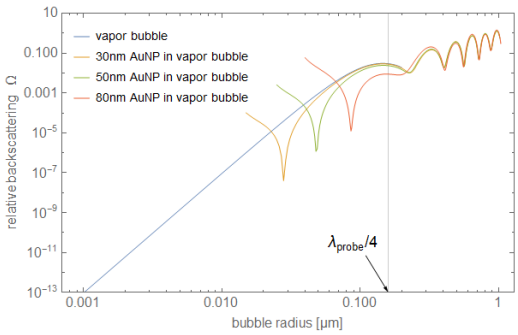

Figure 5.32: Backscattering of circular polarized light with a wavelength of 640nm at a vapor bubble without particle (blue) and at a vapor bubble surrounding a 30 nm, 50 nm and an 80 nm sized AuNP. Detection with a microscope objective of NA 0.6 was simulated.

Measurement and imaging of cavitation bubbles at a rigid surface

Vogel and co-workers analyzed the backscattered light signals measured on free cavitation bubbles in numerous experiments. They used flash photography during the bubble oscillation and synchronous detection of transmitted probe laser light to verify the modeling of bubble size evolution [108, 151]. Also for investigation of cavitation bubbles with different distances in front of interfaces they used flash photography [172, 173]. Backscattering light evaluation on bubbles at a rigid surface was not investigated, so far.

In the experimental work of this thesis the combination of both, the bubble interferometry and the flash photography of plasma generated cavitation bubbles on a rigid surface was used the first time. The experiment contained three parts: First, the threshold of bubble nucleation in free water was determined. Second, a glass slide was positioned with help of a x-y-z-stage in the water-filled cuvette and brought close to the laser foci. The reflection and transmission signals as well as images around maximum bubble expansion were detected for different distances to the glass surface. Third, the threshold of bubble nucleation on the glass surface was determined. Bubbles were detected for a specific energy above threshold in order to reproduce bubble oscillations of equal durations. Imaging at different times during the oscillations shows the evolution of the hemispherical bubble.

In order to analyze the bubble interaction with a rigid interface independently from bubble size a dimensionless parameter γ was defined, which is the ratio of the distance bubble center to surface to the maximum bubble radius [172]. For a γ at least up to 2.6 a rigid interface can affect the bubble oscillation [125]. In particular, the collapse phase is sensitive to disturbances of the surrounding. Near a rigid boundary surface the inflow of the liquid during the collapse is hindered by the rigid interface and deformation of the bubble wall can occur. For $\gamma < 1$ the bubble is disturbed already during the expansion phase.

The threshold of bubble formation in free water was found for a pulse energy of around 168 nJ. Up to a pulse energy of 450 nJ bubble oscillation time increased continuously and for pulse energy above 450 nJ a stronger increase of oscillation time was observed. The threshold of bubble formation on the glass surface was found for a pulse energy of around 35 nJ and bubble oscillation time increased continuously up to 105 nJ. For a pulse energy above 105 nJ the bubble oscillation time increased more strongly. The measurements of bubbles in free medium exhibited good reproducibility, while the bubbles on the glass surface exhibited larger size variation when generated by equal pulse energies.

Figure 5.33 shows side view images of cavitation bubbles imaged at time points approximately at maximum bubble expansion. The bubbles were generated at distances of approximately 60 µm ($\gamma \approx 12$) (A) and 5 µm ($\gamma \approx 1$) (B) to the rigid surface of the glass slide. The glass surface was brought in from the left hand side, the irradiation beam is coming from the right hand side. Due to a slight tilt of the glass side a mirror image of the bubble was detected. The corresponding interferometry signals (blue) as well as the illumination pulse (yellow), that indicates the moment of image exposure during the bubble oscillation, are shown in Figure 5.33. For bubbles close to the surface a beat frequency in the interference pattern can be observed in the backscattering signal during the expansion phase. Backscattered waves from the near glass

surface caused additional frequencies by interference with backscattered components from the bubble front- and backside.

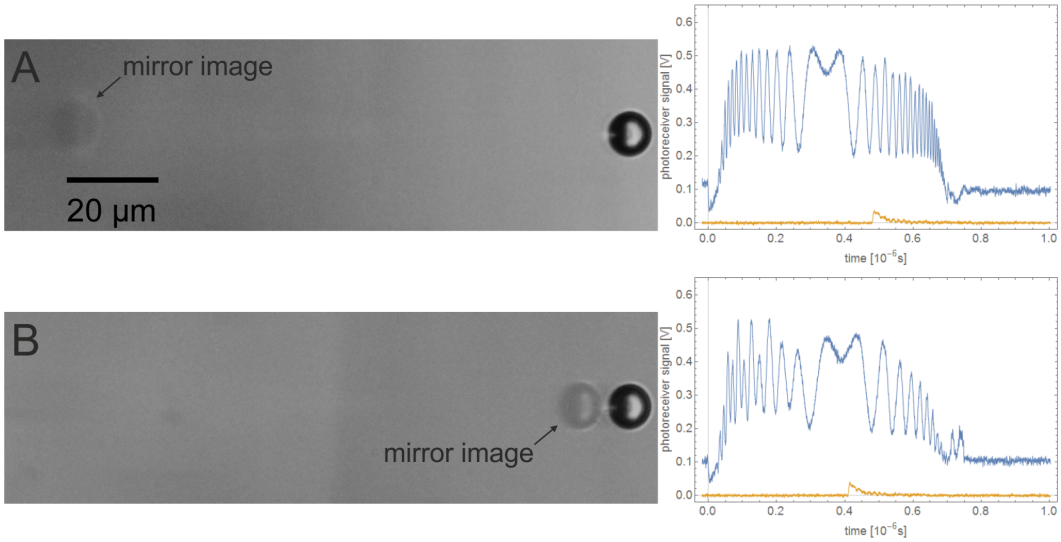

Figure 5.33: Cavitation bubbles with maximum radius $R_{b,max}$ of 5 µm generated by a laser pulse energy of 424 nJ (A) and 414 nJ (B). bubbles were generated at a distance between the focus and the glass surface of 60 µm ($\gamma \approx 12$) (A) and 5 µm ($\gamma \approx 1$) (B).

Figure 5.34 shows side and front view images and the back reflection signals of cavitation bubbles formed on the glass surface for $\gamma = 0$ at irradiation with 36.1 nJ. Images of the bubble were taken during the onset of their expansion (A) and at the end of their collapse phase (B).

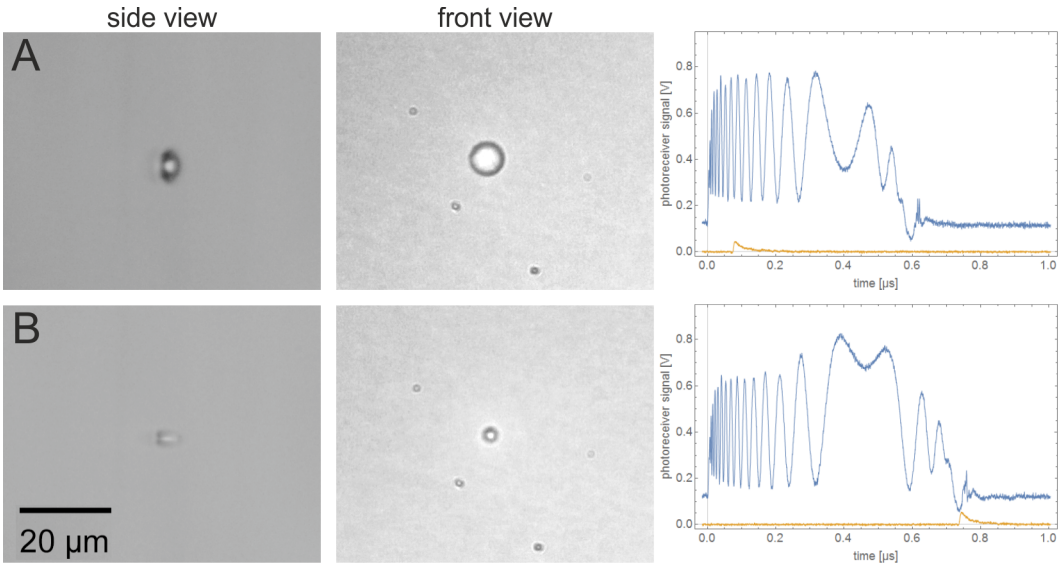

Figure 5.34: Cavitation bubbles formed on the glass surface ($\gamma \approx 0$) at a pulse energy of 36.1 nJ (A and B).

In contrast to cavitation bubbles in free medium, the backscattered light at bubbles nucleated on the glass surface shows a strong asymmetry between expansion and collapse phase. Furthermore, observed for $\gamma \approx 1$ the additional frequencies disappeared since the interferometry signal origins only from two defined surfaces, the bubble wall and the glass surface. Thus, the bubble expansion phase exhibits a signal modulation, which corresponds to the bubble wall motion. During the collapse phase, the signal decreases abruptly and fewer signal oscillations occur. Friction between the rigid glass surface and the moving water molecules at the bubble wall

causes a gradient of the collapse velocity along the bubble interface, by what the collapse occurs non-spherically. Figure 5.35 and 5.36 show images and signals acquired during the collapse phases of different bubbles generated on the glass surface. Each bubble has approximately the same bubble oscillation time of 1.5 µs (Figure 5.35) and 1.0 µs (Figure 5.36), respectively. Image (A) of Figure 5.35 was acquired in the expansion phase and illustrates, that the bubble expands hemispherically already before reaching maximum expansion. Subsequent images (B-F) were acquired during the collapse phase. During the final stage of the collapse phase shown in Figure 5.35 (E) a cigar shaped bubble is seen. During the transition from collapse to a rebound bubble a torus shaped vortex can arise. Imaging the bubble after the collapse shows such a vortex (Figure 5.36 C).

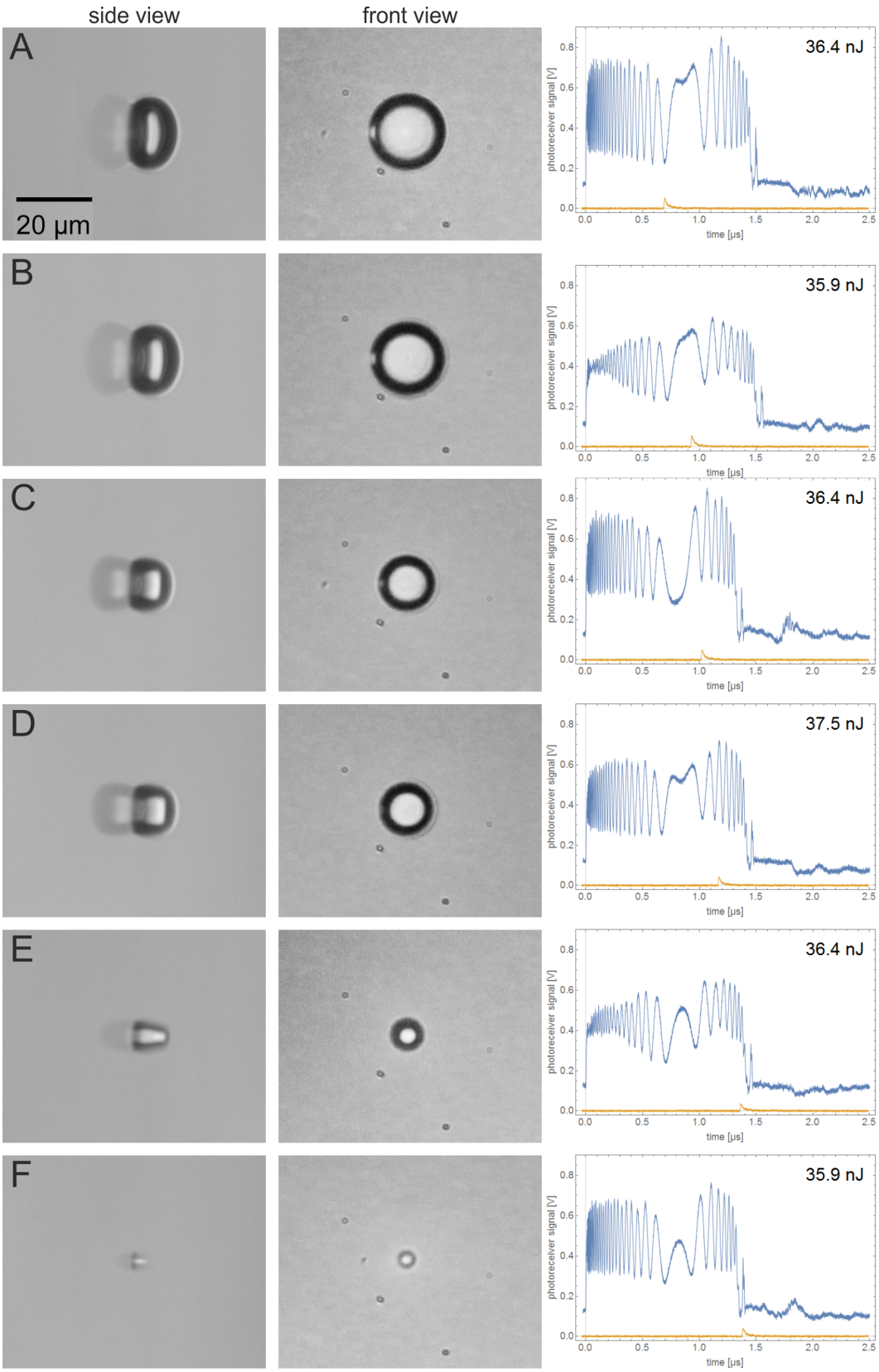

Figure 5.35: Flash photography images and interferometry signals of plasma generated cavitation bubbles formed on a glass surface ($\gamma \approx 0$) at laser pulse energy around 36 nJ.

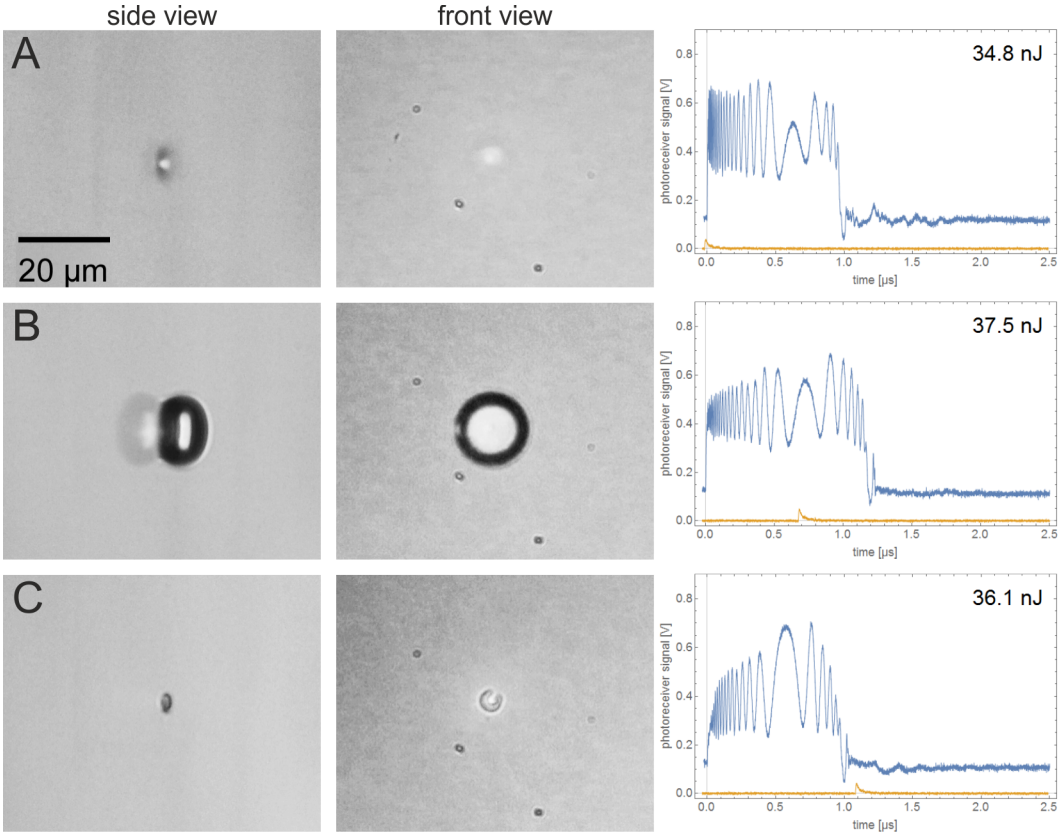

Figure 5.36: Flash photography images and interferometry signals of plasma generated cavitation bubbles formed on a glass surface ($\gamma \approx 0$) at laser pulse energy around 36 nJ. The bubbles expand and collapse within a time of 1 µs (A and C) and 1.2µs (B). The acquisition time point of image (A) corresponds to the onset of bubble expansion. Image (B) shows a maximum bubble expansion and (C) a flat torus after the collapse phase.

Signal analysis of the interferometry on cavitation bubbles at a rigid surface

When a bubble is formed on a rigid surface, the bubble wall moves against the direction of the laser beam, while the surface remains stationary. Thus, in contrast to the free cavitation bubble, exactly half the modulation frequency of the interference signal is to be expected for equal changes of the bubble radius. Figure 5.37 shows schematically the expansion of a bubble nucleated in free medium and on a glass surface in the medium. The underlying images were acquired at an irradiation with 472 nJ and 281 nJ respectively and illustrate the radial symmetry of a free bubble, while the bubble on the glass surface exhibits a hemispherical shape. Close to the glass surface a deviation from hemispherical shape can be observed, which indicates that bubble wall velocity in the center on the laser beam axis is lower than the velocity on the surface lateral to the laser beam axis. However, in the backscattered signal mainly the bubble wall velocity on the laser beam axis was determined due to the detection of backscattered light within a moderate NA of 0.58.

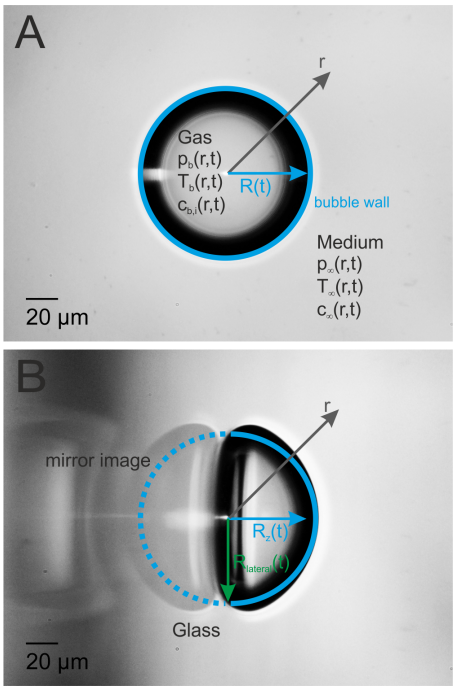

Figure 5.37: Image of (A) a free and (B) surface nucleated bubble for irradiation with 472 nJ (free) and 281 nJ (surface) respectively. The time point of image exposure corresponds to the maximum bubble radius. The bubble generated in free medium oscillates with symmetrical shape, while for the bubble generated on a rigid surface the friction of the surface causes a different velocity on the beam axis $R_z\,(t)$ (blue arrow) than in lateral direction to the beam axis $R_{lateral}\,(t)$ (green arrow). This leads to a deviation from the hemispherical shape.

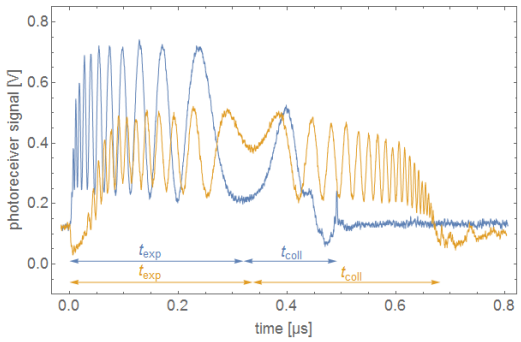

Figure 5.38: Interferometry signals of cavitation bubbles nucleated in free water (yellow) and on a glass surface in water (blue). Arrows indicate the expansion and the collapse phase of each one of bubble oscillation.

In case of a free oscillating cavitation bubble expansion and collapse phase can be determined from the interferometry signal quite well. Apparently, both are separated by an inflection point, which is related to the maximum bubble radius. During bubble expansion the modulation frequency decreases until the maximum radius is reached and starts to increase again, whereby the signal exhibits symmetry around the inflection point. For a cavitation on a surface the inflection point is more difficult to determine, because of the rapid signal decrease during bubble collapse, which effects the signal symmetry.

As an example Figure 5.38 shows the interferometry signals of a free cavitation bubble in free water and on the glass surface. Despite of the different pulse energy of around 425 nJ and 36 nJ focused into the free medium and onto the glass surface respectively, the measured bubbles exhibit approximately the same expansion times. Remarkably to note, the first interference modulation in the signal for a free cavitation bubble (yellow line) occurs around 30 ns after

nucleation, while for the cavitation bubble formed at the glass surface (blue line) the first interference modulation already shows after approximately 5 ns. However, the interferometry signals significantly differ in length and structure during collapse phase as well as in the measured frequency. Assuming that bubble size strongly correlates with expansion time, for both measurements the bubble walls move the same distance to the laser foci (nucleation center) and also the bubble wall velocity is expected to be the same for both during expansion on the beam axis. As shown in Chapter 5.3.6 the velocity dR_b/dt measured for a free bubble corresponds to the distance of $\lambda_{probe}/4$ traveled during the time Δt_{max} between subsequent maxima in the interference signal. In the case of the bubble wall moving away from the stationary glass surface the measured velocity $dR_{b,z}/dt$ corresponds to the distance of $\lambda_{probe}/2$ during Δt_{max}. For the free and the surface nucleated bubble (signals shown in Figure 5.38) the mean velocity over time was calculated and is shown in Figure 5.39. The measured bubbles exhibit a comparable expansion times and approximately the same velocity profile during the expansion.

The volume of the spherical bubble corresponds to approximately twice the volume of the hemispherical bubble formed on the glass surface, while both bubbles exhibit the same expansion dynamics.

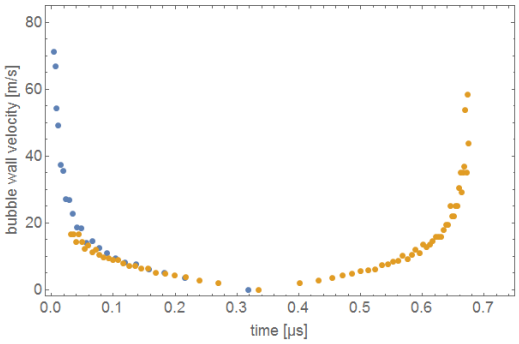

Figure 5.39: The velocity of a bubble in free water (yellow) decreases during the expansion until the maximum radius is reached and increases again during the collapse. The bubble wall velocity of a bubble nucleated on a glass surface can be determined earlier during expansion. Hence higher velocities are measured there. The collapse cannot be followed by backscattered light.

Detection of cavitation bubbles around gold nanoparticles by backscattered light

The interference in coherent backscattered light allows to detect the bubble wall velocity and radius with high temporal resolution. Bubble formation around free spherical nanoparticles should show high sphericity, while non-spherical plasma [107, 108] or nanoparticles and also nearby interfaces can cause distortion in spherical bubble expansion. Plasma generated bubbles on a rigid surface showed during later stage of the collapse bubble shape deviation from sphericity (cf. Figure 5.35), which can be expected for bubble formation near a surface.

An interface such as a cell membrane close to the nucleation site should also have an impact on the bubble formation and oscillation. The expansion to its maximum diameter, which may already deviate from sphericity, is followed by an asymmetrical collapse. Full bubble oscillation time, also referred to as bubble life time, can be precisely determined by scattered light detection in forward direction. Detecting the time point of maximal expansion is inaccurate for a bubble near an interface, since a local signal maximum is not necessarily associated with maximum bubble size. In contrast, backscattered laser light detects the whole bubble dynamics during bubble oscillation in a single-shot experiment very precisely.

For a bubble formed in free medium the expansion phase corresponds to a series of fringes with decreasing frequency, which is related to a decrease of bubble wall velocity, while the collapse goes along with a narrowing of the fringe separation. $R_{b,max}$ is reached at a fringe maximum or minimum between decreasing and increasing fringe frequency. An interface particularly effects the collapse phase of a bubble oscillation and thus the evaluation of the backscattered light signal. For bubble formation around AuNP immobilized on a glass slide the time point, when $R_{b,max}$ is reached can be determined in the same manner from the backscattering signal. An

example is shown in Figure 5.40. However, the location of the turning point, as marked in the illustration by an arrow, becomes difficult to determine for smaller bubbles. As long as a sufficient number of fringes are available for evaluation, a RP-model can be fitted to the bubble expansion.

The backscattered light signal of bubble formation around an AuNP on a rigid surface exhibits an asymmetry of the with $t_{exp} \simeq 0.6 \cdot t_{osc}$ and $t_{col} \simeq 0.4 \cdot t_{osc}$, respectively (cf. Figure 5.40). This ratio could not be verified for bubbles measured at the detection threshold, which were too small to generate interference related detector signal modulation. However, for calculation of bubble collapse some parameters such as the polytropic exponent $\kappa \leq 1.67$ (cf. Equation 2.65), which was used to solve the Rayleigh-Plesset equations for description of the bubble expansion, need to be changed for calculation of the collapse phase. Otherwise the RP-model overestimates the collapse phase. For instance, Figure 5.53 shows the bubble wall velocity- and radius-time curves, for calculations without changing parameters for the collapse phase. The resulting RP-model exhibits full bubble collapse around 0.345 µs, while the measured bubble signal is shorter than 0.3 µs.

Note, that for bubbles with diameter smaller than $\lambda/2$ as formed on AuNP under irradiation near the threshold, the back scattering signal lacks of interference related modulations. The radii of these bubbles were approximated then by the Rayleigh-Plesset equation (cf. Equation 2.67) and considering a correction given by [108], which was obtained by comparison with the maximum bubble radius calculated with the Gilmore model as a function of the bubble oscillation time t_{osc} .

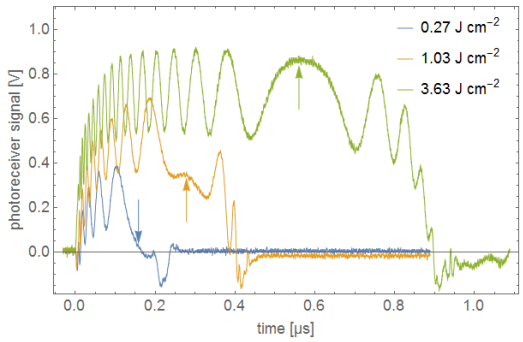

Figure 5.40: Backscattering signals of bubbles around 80 nm AuNP, which were immobilized on a rigid glass surface. The time point of maximum bubble expansion is located between the phase of decreasing and increasing interference frequency, which modulates the backscattered light signals.

Conclusions for the measurements on nanoparticles located on a rigid surface

In conclusion, a rigid surface such as the glass slide supporting the AuNP significantly affects the bubble oscillation dynamics.

1. A bubble nucleated on a rigid surface expands (approximately) hemispherical. During expansion phase one bubble wall moves, while the rigid surface, which contributes with a second reflected beam to the interference pattern, remains stationary in place. The frequency of the interference pattern measured with the photoreceiver is half of the frequency of a free cavitation bubble with the same expansion velocity of the bubble wall.

2. The oscillation of bubbles nucleated on a rigid surface exhibits a strong asymmetry. Their collapse exhibits only fewer interference fringes. For smaller bubbles generated at threshold energy the signal amplitude decreases strongly during the collapse and interference fringes disappear.

3. Synchronously measured signals of back scattered and transmitted probe laser exhibit equal bubble oscillation times. In contrast to the transmission signal a significant asymmetry between the expansion and collapse phase during the bubble oscillation was observed in the backscattered light signals (Figure 5.40).

5.4 Results and discussion

5.4.1 Backscattered light signals at cavitation bubbles around gold nanoparticles

Gold nanoparticles in free medium

A sample of suspension containing nanoparticles with an average diameter of 30 nm was filled into a chamber on a glass object slide and placed under the microscope objective. A pulsed laser irradiation of the detected gold nanoparticle at sufficient radiant exposure induced formation of a vapor bubble. Figure 5.41 shows signals of bubble interferometry, which were measured under irradiation of a detected particle with three sequential pulses of each 0.82 µJ. Usually, the nanoparticles were immobilized on the glass surface to provide reproducible bubble measurements. In this case, however, three irradiation pulses and measurements could be applied on the same particle, which floated freely in the liquid. These measurements were carried out by laser pulses emitted in short time intervals and by fast measurement of the backscattering signals. Imaging was done manually after each bubble measurement.

This experiment demonstrates, that bubble generation and measurement around free gold nanoparticles is in principle possible. However, measurements on the same AuNP with the same irradiation caused different signals. Due to Brownian motion the position of the particle in the focus changes and thus the irradiation of the particle varies for each applied laser pulse. Besides, the permanent motion of the nanoparticles prevented a spectral analysis in order to determine the AuNP size. Spectral shifts due to particle motion within the imaging plane can be compensated by correcting for the particle position. In contrast, spectral shifts related to motion in z-direction off the imaging plane cannot be compensated due to the unknown particle position.

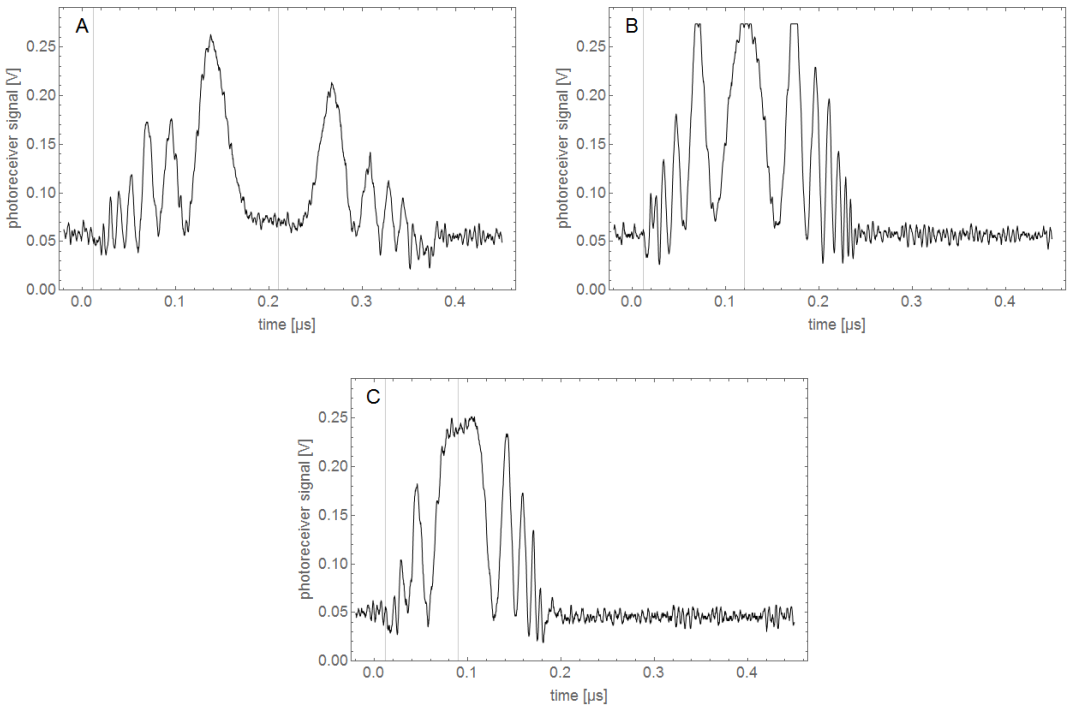

Figure 5.41: Bubble interferometry signals acquired for a free floating gold nanoparticle with nominal 30 nm diameter. The particle was irradiated with 3 subsequent 800 ps pulses of 0.82 µJ at a wavelength of 532 nm.

Gold nanoparticles on a rigid surface

In order to provide reproducibility of the spectral analysis for single-shot measurements of AuNP mediated cavitation an immobilization of the AuNP is required. The nanoparticle spontaneously attached to silanized glass slide (cf. chapter 5.3.1). Pulsed laser irradiation of the gold nanoparticles resulted in hemispherical bubbles with similar signals as measured for plasma

induced cavitation on a glass surface. For an 80 nm AuNP placed on a glass slide Figure 5.42 shows the spectra of scattered light (A-C) and the measured bubble interferometry signal (D) under radiant exposure of 510 mJ cm^{-2} at a pulse duration of 800 ps. During expansion phase of the cavitation the interference related modulation of the signal correlates well with the bubble wall motion. After reaching the maximum bubble radius, the bubble collapses rapidly with no regular interference pattern formed during the collapse phase.

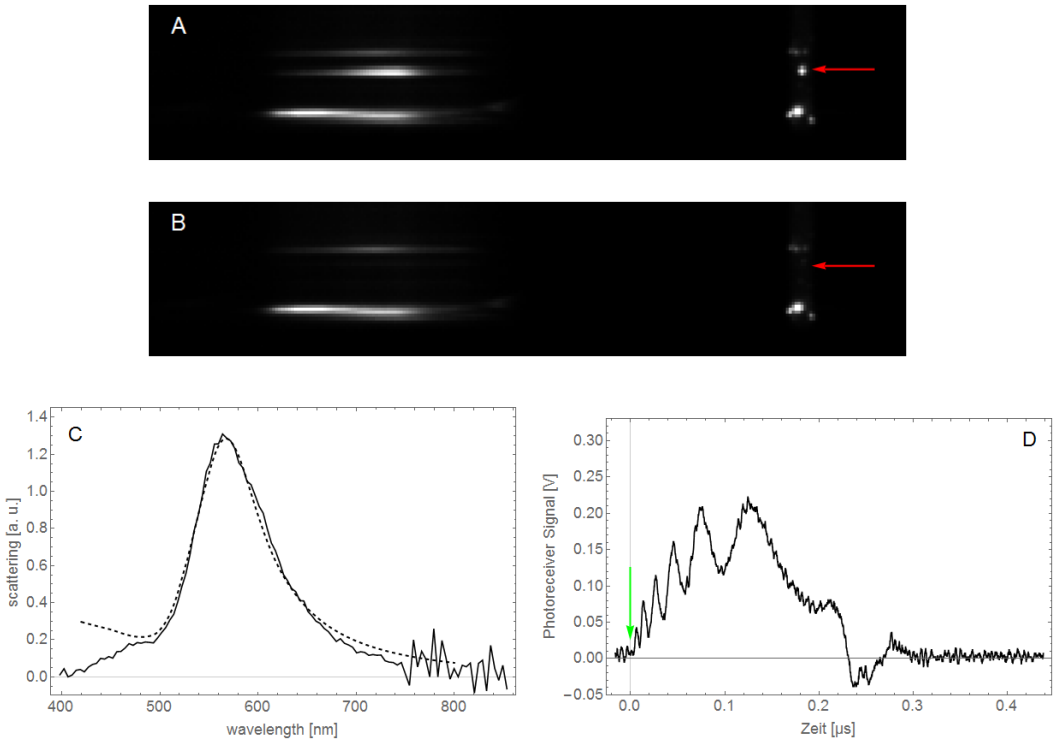

Figure 5.42: A) Darkfield microscopy and scattered light spectroscopy of a gold nanoparticle (red arrow) before irradiation. B) After irradiation the nanoparticle disappeared from the imaging field. C) A scattering spectrum, which was calculated by Mie theory (dotted line) was fitted to the measured spectrum (black line). The best fit nanoparticle radius was 80 nm. D) The bubble interferometry signal was measured during irradiation of the gold nanoparticle with an 800 ps pulse of 510 mJ cm^{-2} at a wavelength of 532 nm. Onset of irradiation is marked by the green arrow.

The origin of interference modulation is the same as the signal measured for a plasma induced cavitation at a rigid surface. The bubble wall velocity can be obtained from the signal modulation in the similar manner as described in Chapter 5.3.6, since after the formation of the bubble wall, the same optical signals are measured irrespective of the generation mechanism of the bubble. Figure 5.43 compares the signals of a cavitation bubble on a glass surface generated by a pulsed laser induced plasma (A) and an AuNP on the glass surface (B) irradiated by a pulsed laser. Both exhibit a similar asymmetry in bubble oscillation. The collapse phase is significantly shortened. Also for the AuNP generated bubbles the duration as well as the expansion rate of the cavitation bubble can be determined as described in Chapter 5.3.6.

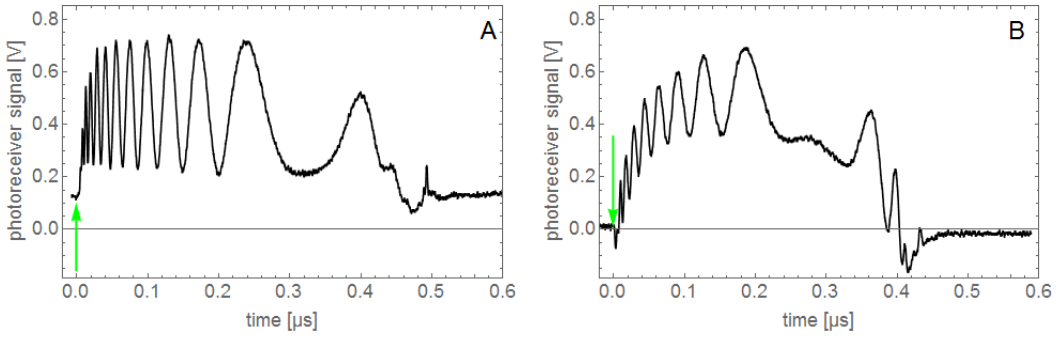

Figure 5.43: Interferometry signals caused by cavitation bubbles induced by a plasma (A) and by a 80 nm AuNP (B) on a glass slide. Irradiation pulse onset marked by the green arrow.

Combined measurements of backscattering and transmission at bubbles

Bubble interferometry and light transmitted by a cavitation bubble, which was generated around an AuNP, were detected with help of the combined bright-/darkfield microscope objective. Figure 5.44 shows the synchronously acquired signals of a cavitation bubble induced by 800 ps pulsed irradiation with 480 mJ cm^{-2} at a wavelength of 532 nm around a gold nanoparticle with a measured diameter of 80 nm diameter. Kitz et al. measured comparable transmission signals for 90 nm AuNP, which were spin-coated onto a glass cover slip and exposed to laser pulses with 5 ns duration [16]. They correlated maximum bubble expansion with the local maximum of the signal due to assumption that at this point the bubble diameter exceeds the probe laser spot, which leads to decrease in diffraction. However, the maximum bubble radius determined from flash photography images taken at this time point was approximately 20 % smaller than the one calculated from the measured bubble oscillation time according to Equation 2.67. From this result, Kitz et al. deduced that bubble oscillation close to a rigid surface is damped compared to one in free liquid and found an explanation to this in investigations on laser generated cavitation bubbles near a solid boundary [172].

In contrast to the findings by Kitz et al. the backscattered light signals showed asymmetric location of the maximum bubble expansion time point (cf. Figure 5.44). The non-spherical collapse was not shown in the transmitted light signal, which leads to underestimation of the bubble expansion time and the maximum bubble size.

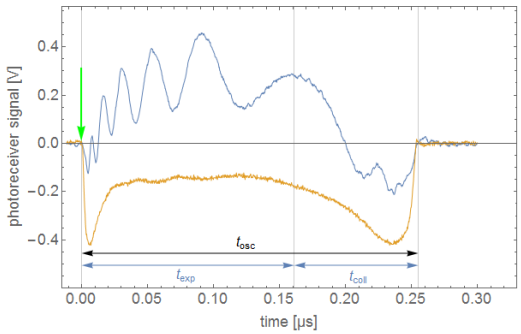

Figure 5.44: Backscattered (blue) and transmitted (yellow) light signals measured at bubble formation around a gold nanoparticle with 80 nm diameter under 800 ps pulsed irradiation with 535 mJ cm^{-2} at a wavelength of 532 nm. Irradiation pulse onset marked by the green arrow. The expansion phase of the bubble oscillation exhibits the interferometric modulation. During the collapse a deformation of the (hemi-)spherical bubble leads to decrease of the backscattered light and thus in loss of signal amplitude.

5.4.2 Bubble detection threshold, bubble expansion time and maximum radius

Expansion times for different radiant exposures were measured for 50 nm and 80 nm AuNP when irradiation with pulse durations of 800 ps and 4 ns respectively was applied (Figure 5.45).

Following the details of bubble formation threshold, an estimation of the nucleation temperature and effects of AuNP size as well as the laser pulse duration on the bubble size will be presented.

In general, an increase in the maximum bubble expansion with the applied irradiation was observed. Figure 5.45 represents the cavitation bubble expansion times on irradiation of 50 nm and 80 nm AuNPs with 800 ps and 4 ns pulses respectively. Maximum bubble radius was calculated with help of Equation 2.67 assuming it correlates with the expansion duration similarly as the collapse duration. For measured expansion times between 15 ns and 330 ns at 80 nm AuNP under 800 ps pulsed irradiation, maximum bubble radii ranged between 164 nm and 3.59 µm (Figure 5.45).

The Equation 2.67 for calculating the maximum bubble diameter was derived from the Rayleigh-Plesset differential equations neglecting surface tension and viscosity of the medium and correlates explicitly the collapse duration with the maximum bubble radius. However, for a free bubble of certain size the expansion and collapse exhibit equal durations, the time to reach maximum diameter can as well be used to calculate maximum bubble diameter. For a hemispherical bubble formed at a rigid surface, this equation delivers only an estimate of the occurring bubble dimensions. Surface tension and viscosity of the surrounding are inhomogeneous due to the rigid surface and thus when being neglected a deviation of predicted from measured maximum hemispherical bubble expansion were expected. In the subsequent Chapter fitting a numerical solution of the Rayleigh-Plesset model (Equation 2.63) to the measured data of the bubble wall velocity will be used to calculate the bubble size more precisely.

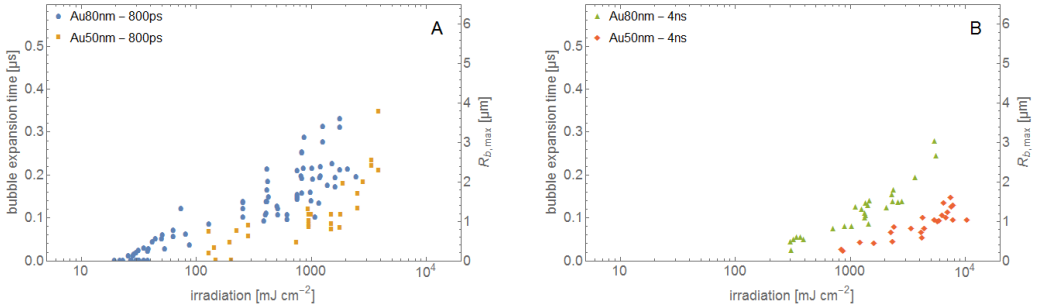

Figure 5.45: The duration of a bubble expansion increases with the applied irradiation. The expansion time was determined from bubble interferometry signals acquired for 50 nm and 80 nm AuNPs under irradiation with 800 ps (A) and 4 ns (B) pulses. Maximum bubble radius $R_{b,max}$ at the right y-axis was calculated from the bubble expansion time by Equation 2.67.

Application of a laser pulse with radiant exposure near the nucleation threshold leads to very small and short lived bubbles (Figure 5.46). The shortest bubble expansion time measured was around 10 ns, which correlates to 106 nm, which is less than $\lambda_{probe}/4 = 160$ nm. At this point it should be mentioned, that Equation 2.67 overestimates the bubble radius of very small bubbles due to neglecting the surface tension and the viscosity of the surrounding medium. This will be discussed in more detail in Chapter 5.4.4.

The bubble velocity could not be determined for bubble oscillation times below 30 ns. One interference related modulation fringe, which is at least required for analysis of the bubble wall motion, generally occurred on signals with durations above 30 ns expansion. Figure 5.46 depicts typical signals recorded for an AuNP with 80nm diameter under pulsed irradiation with 800 ps at the bubble nucleation threshold (A-C) and above (D, E). A nanoscopic bubble formed under irradiation just above nucleation threshold can already result in a good measurable signal change in transmission, while the increase in backscattered intensity causes a barely visible signal (B). For bubbles generated by irradiation well above threshold in both, the backscattering and transmission, a signal change is detected (D-E). The backscattered light signal exhibited interference modulations only for bubble sizes above $\lambda_{probe}/4$ (D). Both, the bubble interferometry as well as the transmission signal exhibited the equal oscillation time t_{osc}.

Bubble formation is initiated by high local temperatures inside gold particles. Partial or com-

plete melting or even vaporization of the gold nanoparticle may result. The scattering spectra measured after irradiation showed changes, which can be related to alterations in shape and size of the AuNP. Figures 5.46 and 5.47 allow to correlate changes of the scattering spectra with the signal of the backscattered and transmitted probe laser light. The disappearance of an irradiated AuNP from the field of view was observed for cavitation considerably above the threshold (D, E). As a result of the bubble collapse the AuNP may be displaced by the occurring fluid flow. Also melting or evaporation could have caused the disappearance. For irradiation near the bubble threshold (A-C), the AuNP remained in place, which allows to determine the possible spectral variation. The resulting nanoparticle sizes of 76 nm (A), 68 nm (B) and 70 nm (C) were determined from the measured spectra after irradiation.

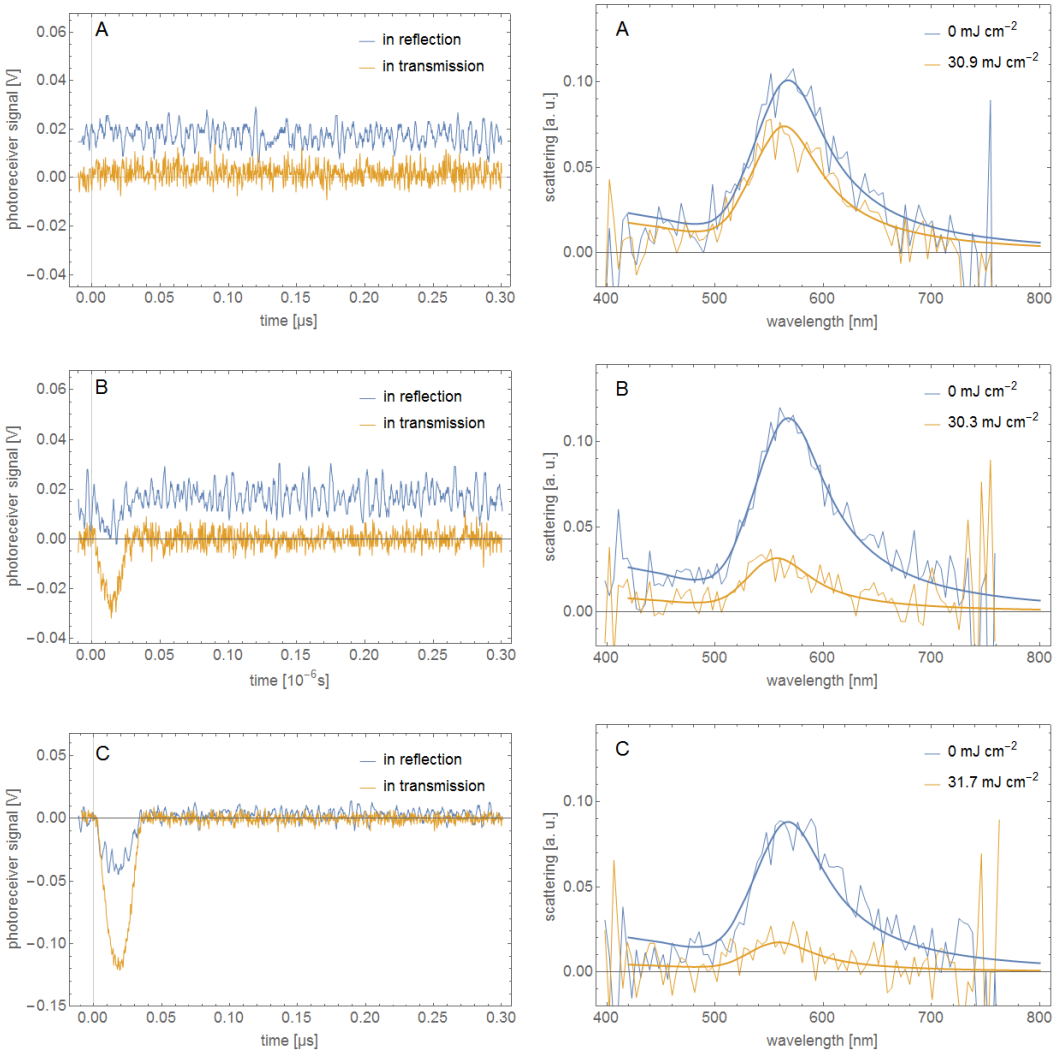

Figure 5.46: Interferometry and transmission signals (left column) and scattering spectra (right column) recorded for AuNPs with 80 nm diameter under pulsed irradiation with 800 ps. Particles were irradiated with radiant exposure around the bubble detection threshold 30.9 mJ cm^{-2} (A), 30.3 mJ cm^{-2} (B), 31.7 mJ cm^{-2} (C). The corresponding scattered light spectra were measured before and after the pulsed irradiation. After irradiation near the bubble formation threshold the AuNP remained in place, while a decrease of the scattering amplitude and a shift of the peak to shorter wavelength was observed.

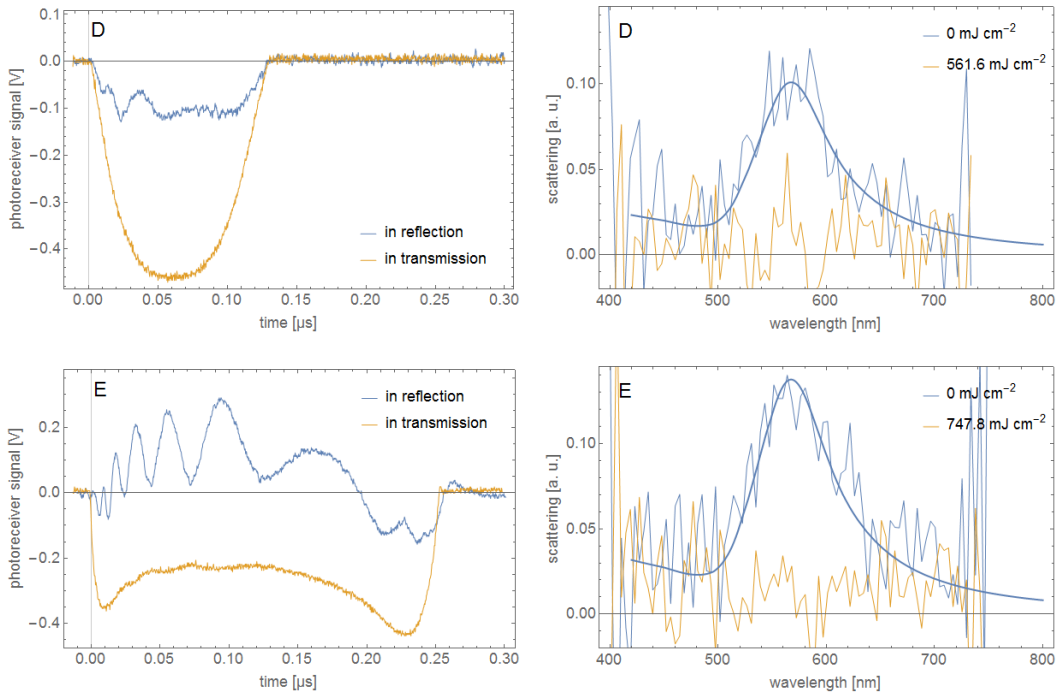

Figure 5.47: Interferometry and transmission signals (left column) and scattering spectra (right column) recorded for AuNPs with 80 nm diameter under pulsed irradiation with 800 ps. Particles were irradiated with radiant exposure was above the bubble detection threshold 561.6 mJ cm^{-2} (D), 747.8 mJ cm^{-2} (E). The corresponding scattered light spectra were measured before and after the pulsed irradiation. After irradiation above the threshold (D, E) the AuNP was dislocated and no scattering was measured at the irradiation location.

Detection threshold of bubble formation

The lower limit of detecting bubble formation around gold nanoparticles was determined experimentally. Starting at pulse energies that lead to a significant bubble signal the irradiation of the single AuNP was decreased always irradiating a new particle until neither by the detector in back reflection nor the detector in transmission direction a bubble related signal could be detected. An exemplary measurement with irradiation around the bubble nucleation threshold of an AuNP with 80 nm diameter is shown in Figure 5.48. The calculated Mie scattering spectrum (solid blue line), which corresponds to an AuNP of 80 nm diameter, exhibits a peak position at 567 nm. After irradiation the measured scattering band shifted to a shorter wavelength, whereas the fitted spectrum (yellow solid line) exhibits a shift to 556 nm. This peak position corresponds to a nanoparticle with a diameter of 66 nm. However, neither bubble interferometry nor the transmission exhibited a cavitation bubble related signal.

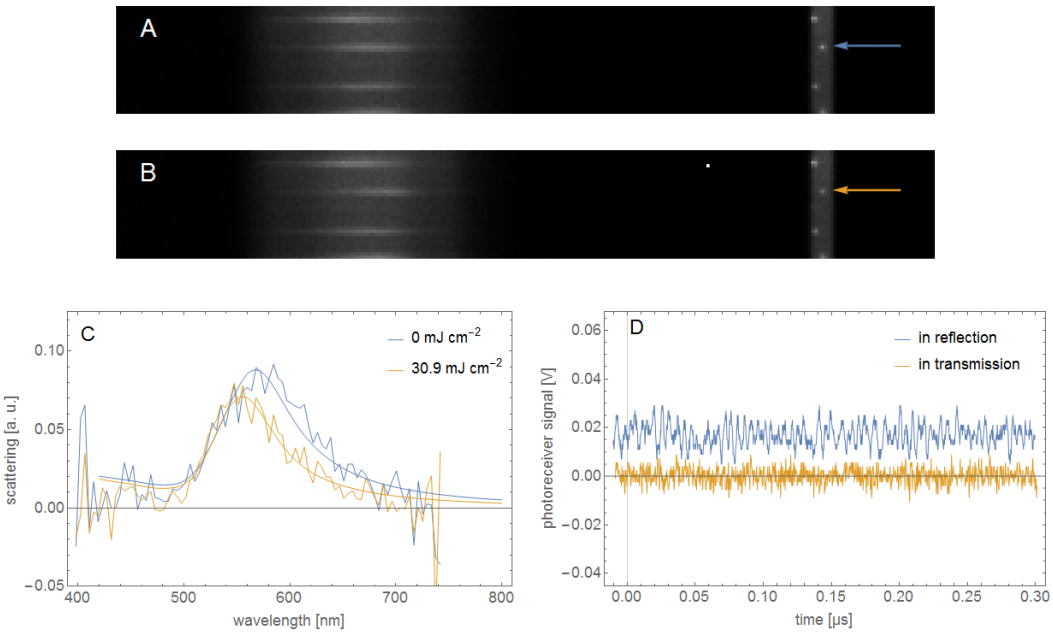

Figure 5.48: Scattered light of an 80 nm AuNP before (A) and after (B) irradiation around the detection threshold of bubble formation with a pulse duration of 800 ps. After irradiation with 30.9 mJ cm^{-2} (yellow), the measured spectra show a decrease in scattering amplitude and a shift of the peak position from 567 nm to 556 nm (C). Spectra calculated by Mie theory for nanoparticles with diameters of 80 nm (blue line) and 66 nm (yellow line) were fitted to the data. No bubble signal was detected by both detectors (D). Offset was added to the reflection signals for representation purpose.

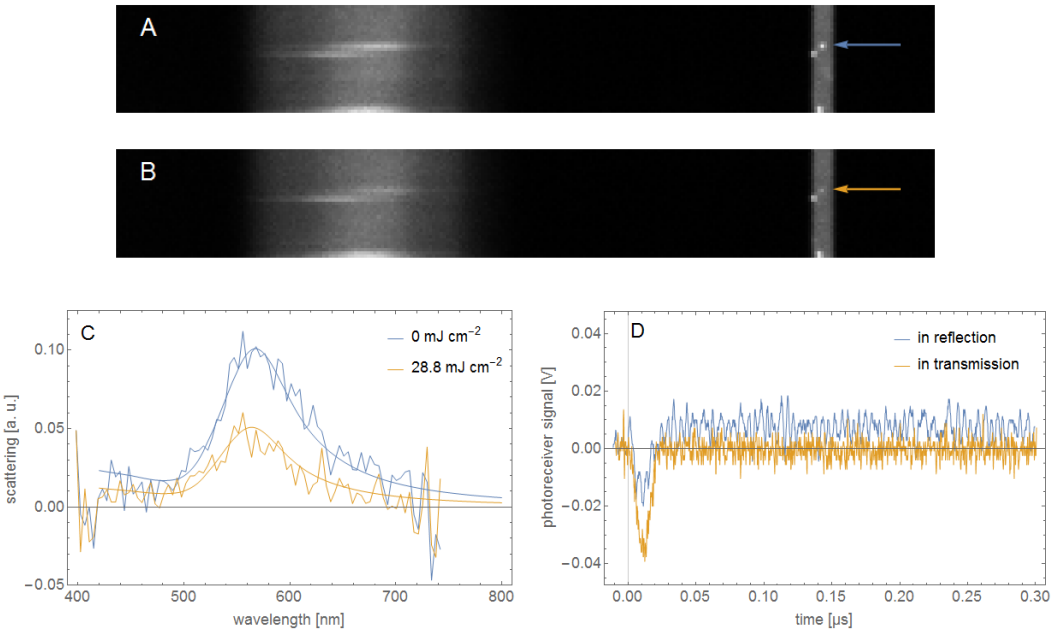

Figure 5.49: Scattered light of an 80 nm AuNP before (A) and after (B) irradiation around the detection threshold of bubble formation with a pulse duration of 800 ps. After irradiation with 28.8 mJ cm^{-2} (yellow) the measured spectra show a decrease in scattering amplitude and a shift of the peak position from 567 nm to 564 nm (C). Spectra calculated by the Mie theory for nanoparticles with diameters of 80 nm (blue line) and 76 nm (yellow line) were fitted to the data. A bubble signal was detected by both detectors (D). An offset was added to the reflection signals for representation purpose.

The probit distribution was applied to the binary values for bubble generated signals (1 = bubble related signal, 0 = no signal) as a function of the applied irradiation. The value of irradiation for which the probability of bubble formation is 50% (also referred to as effective dose $ED50$) is the detection threshold of bubble formation. Further, the probit slope S describes the dispersion of the distributed values similar to a standard deviation in the normal distribution. A slope value of $S \lesssim 1.10$ means, that the irradiation required to form a bubble with a probability of 50% differs by less then $S-1 \lesssim 10\%$ from the irradiation required to form a bubble with a probability of 84% or 16% respectively. Figure 5.50 shows the probability of detecting bubble formation found for the irradiation of AuNP with diameters of 50 nm and 80 nm with the smooth 800 ps pulses. For radiant exposure of 132 mJ cm^{-2} and 34 mJ cm^{-2} the cavitation bubble formation around a 50 nm and 80 nm AuNP, respectively, will be detected with a probability of 50%

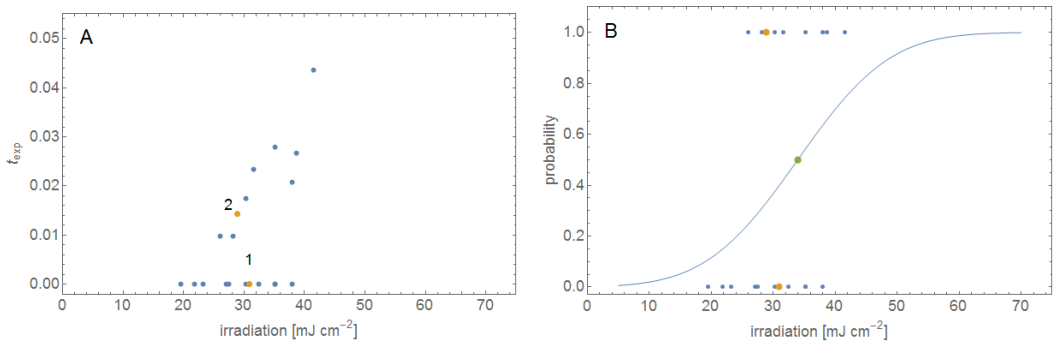

Figure 5.50: A) The measured bubble expansion times for irradiation of 80 nm AuNP near the detection threshold of bubble formation. From these data the detection threshold was determined. Colored data points 1 and 2 correspond to the measurements shown in Figure 5.48 and Figure 5.49 respectively. B) By fitting a probit function (solid lines) to the binary values of bubble occurrence (= 1) and non-occurrence (= 0) an ED50 value for the bubble detection threshold of 34 mJ cm^{-2} was determined.

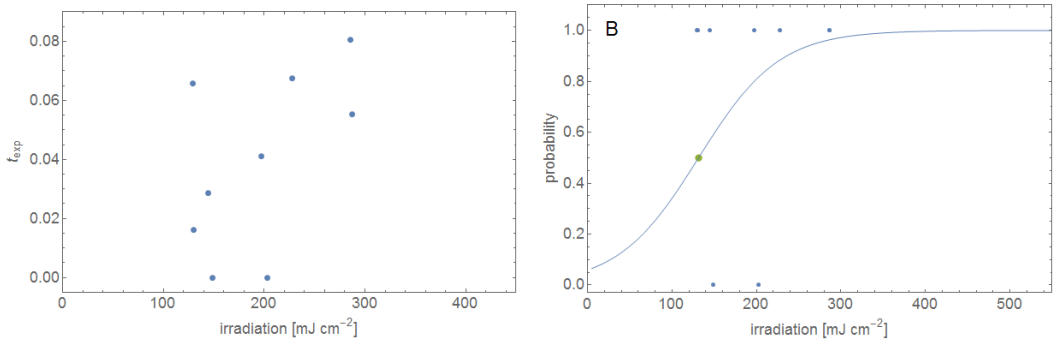

Figure 5.51: A) The measured bubble expansion times for irradiation of 50 nm AuNP around the bubble detection threshold. From these data the detection threshold of bubble formation was determined. B) By fitting a probit function (solid lines) to the binary values of bubble occurrence (= 1) and non-occurrence (= 0) a bubble detection threshold corresponding to the ED50 value of 132 mJ cm^{-2} was determined.

Effect of radiant exposure above detection threshold on the bubble dynamics

Above detection threshold the measured expansion time and thus the maximum bubble expansion radius around an AuNP increased non-linearly with the applied irradiation (cf. Figure 5.45). Bubble wall velocity varies during the whole measurement continuously until the maximum radius is reached. Shortly after onset of the bubble expansion at initial bubble radius R_0 the bubble wall velocity approaches its maximum value and decelerates until reaching maximum expansion $R_{b,max}$. As an example, Figure 5.52 shows the measured wall velocity of bubbles generated around 50 nm sized AuNP when irradiated with 800 ps (A) and 4 ns (E) pulses and for 80 nm sized AuNP (C, G), respectively. The continuous course of the bubble

wall velocity (solid lines) for each measurement represents a solution of the RP-model. Each individual solution was calculated for an initial condition, a combination of R_0 and $p_0$at an appropriate time point t_{vap}, in order to fit the RP-model to the measurement.

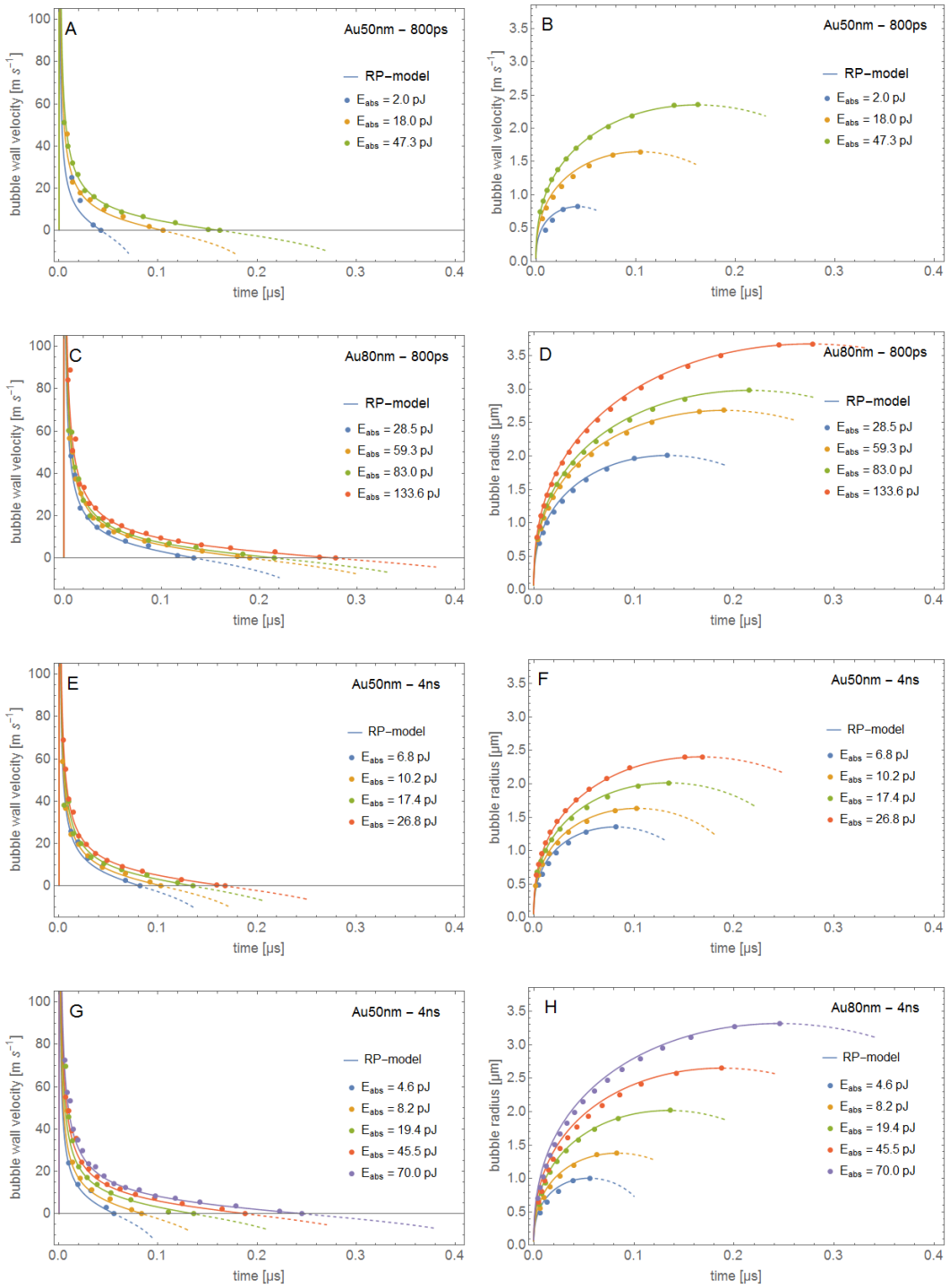

Figure 5.52: (A, C) Measured bubble wall velocity and the calculated radius (B, D) around 50 nm and 80 nm sized AuNP under 800 ps pulsed irradiation. (E, G) Measured bubble wall velocity and the calculated radius (F, H) around 50 nm and 80 nm sized AuNP under 4 ns pulsed irradiation. The solid lines represent solutions of the RP-model for each measurement individually.

5.4.3 Rayleigh-Plesset equation - fitting the measured bubble wall velocity

Interference in the backscattered light signal of the cavitation bubble gives information on the bubble wall velocity, which was fitted to numerical solutions of the Rayleigh-Plesset differential equation for the bubble wall velocity dR_b/dt. The fitting procedure involved spatio-temporal temperature calculation for the gold nanoparticle in water in order to obtain the initial radius R_0 and internal bubble pressure p_0 at a specific time point. This time point was fitted as such that the resulting R_0 and p_0 were the boundary conditions of the solution $dR_b(t)/dt$, which fitted best to the measured bubble wall velocity. Initial velocity $dR_b(t=0)/dt = 0\,m\,s^{-1}$ was assumed. From dR_b/dt the radius function $R_b(t)$ was calculated by integration over time and bubble pressure $p_b(t)$ was determined by equation 2.68.

Estimation of the initial bubble radius and pressure is based on spatio-temporal temperature calculations for the irradiated nanoparticle (cf. Equation 2.42 to 2.44). The location r, where the liquid water reaches the spinodal temperature determines the initial bubble radius R_0. The pressure p_0 of water within the layer in the range $R_p < r < R_0$ is determined with help of the equation of state of water (EOS), which gives the pressure $p_{EOS}(T,\rho)$, a function of temperature and density for water heated up to a temperature of 10^5 K [174]. It is assumed that spinodal decomposition initially results in an isochoric phase transition. Thus, thermal energy is deposited in the surrounding water layer with (nearly) constant density of around $1000\,kg\,m^{-3}$ until phase transition creates a cavity of high pressure. For sufficient initial pressure the cavity of high density vapor expands forming a vapor-liquid interface with radius above R_0. Viscosity $\mu = 10^{-3}\,N\,s\,m^{-2}$ and surface tension $\sigma = 0.072\,N\,m^{-1}$ [175] of the surrounding bulk water under atmospheric pressure $p_\infty = 0.1\,MPa$ were used in the calculations. The vapor temperature dependent isentropic exponent was $\varkappa = 4/3$. These boundary conditions, which assume spinodal decomposition in a thin layer of overheated water being responsible for the cavitation bubble formation on an AuNP surface, were used for all following solutions of the Rayleigh-Plesset equation determined throughout the thesis, unless otherwise stated explicitly.

The initial conditions were obtained by calculating the spatial temperature increase for the specific time point t_{vap} at which the condition

$$T\left(r = R_0, t_{vap}\right) = T_{spin} \tag{5.10}$$

is satisfied. With the help of $p_{EOS}(T,\rho)$ the pressure p_0 was calculated for the mean temperature $\bar{T}_{shell}$ within the water shell surrounding the AuNP in $R_p < r < R_0$ for water with a density of $\rho = 998\,kg\,m^{-3}$:

$$p_0 = p_{EOS}(\bar{T}_{shell}\left(R_p < r < R_0, t_{vap}\right), 998.2\,kg\,m^{-3}) \tag{5.11}$$

t_{vap} was varied until the RP-model obtained from solving Rayleigh-Plesset equation with the corresponding initial radius and pressure fits the measurement. The best representation of the measurement by the RP-model was determined by a minimum of the root mean square (RMS) of measured and calculated bubble wall velocity values.

Figure 5.53 shows the analysis of a measurement on an AuNP with 80 nm diameter irradiated by an 800 ps pulse with $480\,mJ\,cm^{-2}$. In result of the irradiation the bubble reached 0.162 µs after onset of the irradiation pulse a maximum radius. During the collapse phase the bubble wall velocity could not be determined. At the time point t_{vap} of 1270 ps after onset of the irradiation pulse the initial radius of $R_0 = 65.3$ nm and an initial pressure of $p_0 = 5.78$ GPa were determined from the equation of state and the calculated temperature gradient within the liquid layer $R_p < r < 65.3$ nm for the best fit RP-model to the measurement.

From Equation 2.67 (cf. Chapter 5.4.2) a maximum radius of 1.78 µm results from the bubble expansion time of 0.162 µs. However, the use of Equation 2.67 underestimates the maximum bubble radius due to neglecting the surface tension and viscosity of the surrounding water. Fitting the RP-model to the measured bubble wall velocity, a maximum bubble radius of 2.35 µm was found. After reaching the maximal radius, the symmetrical collapse of the vapor bubble, which is predicted by the RP-model, is not seen due to the rigid surface Figure 5.53 shows the RP-model solution (solid lines) and the measured bubble wall velocity over time.

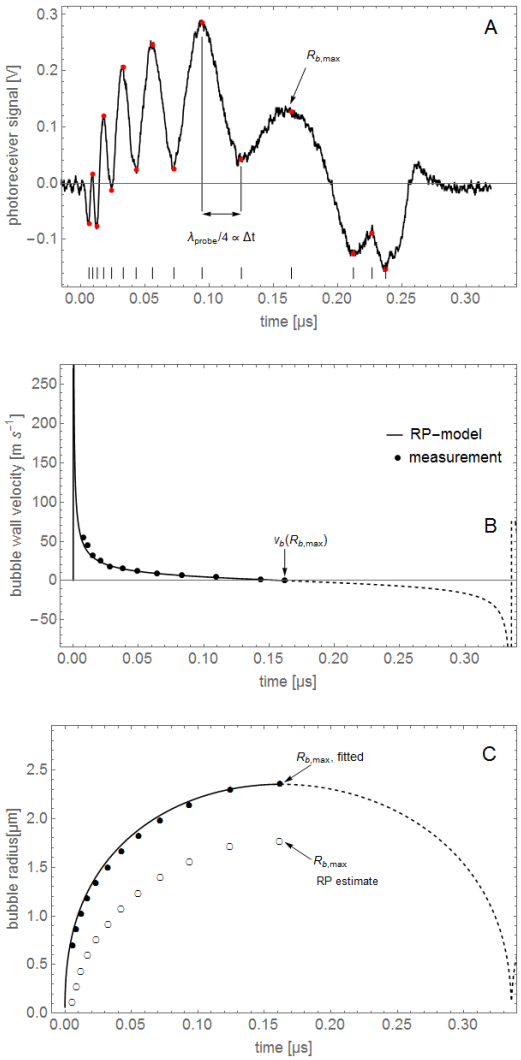

Figure 5.53: A) Backscattered light signal measured at a bubble around an 80 nm sized AuNP under 800 ps pulsed irradiation with 480 mJ cm^{-2}. The red dots highlight the minima and maxima, which were utilized for the estimation of bubble wall motion (B) and the bubble radius (C). The solid lines in (B) and (C) result from the solution of the RP-model fitted to the experimental values (solid circles). Using the measured bubble expansion time to calculate the maximum bubble size according to Equation 2.67 results in a radius time curve of a bubble with smaller maximum radius (empty circles in (C)). Initial radius and pressure of $R_0 = 65.3$ nm and $p_0 = 5.78$ GPa, respectively, delivered best fit of the RP-model to the measurement.

Example of bubble formation

Backscattered light signals measured on bubbles formed around 50 nm sized AuNP showed interference related modulation for irradiation above 500 mJ cm^{-2} (pulse duration 800 ps) and above 1200 mJ cm^{-2} (4 ns). For 80 nm sized AuNP the modulation occurred up on irradiation with 50 mJ cm^{-2} and 300 mJ cm^{-2}, respectively. For each irradiation the corresponding time point of bubble formation was found exhibiting a combination of initial bubble radius R_0 and initial pressure p_0, that can drive the bubble over the measured expansion time. As an example Figure 5.54 shows the evaluation of a backscattering signal measured on a bubble formed around an 80 nm sized AuNP irradiated with a 800 ps pulse of 50.5 mJ cm^{-2}. An initial bubble radius of $R_0 = 53$ nm was found based on the temperature profile calculated at a time point of 1300 ps after irradiation pulse onset at $t = 0$ s. The corresponding initial pressure according to Equation 5.11 was $p0 = 1.9$ GPa.

Increasing irradiation leads to higher temperature increase and higher initial bubble pressures, which drive the bubble was to larger maximum radius. Figure 5.55 shows the analysis of a

signal measured for a bubble around an 80 nm sized AuNP under 800 ps pulsed irradiation with radiant exposure of 1775 mJ cm^{-2}.

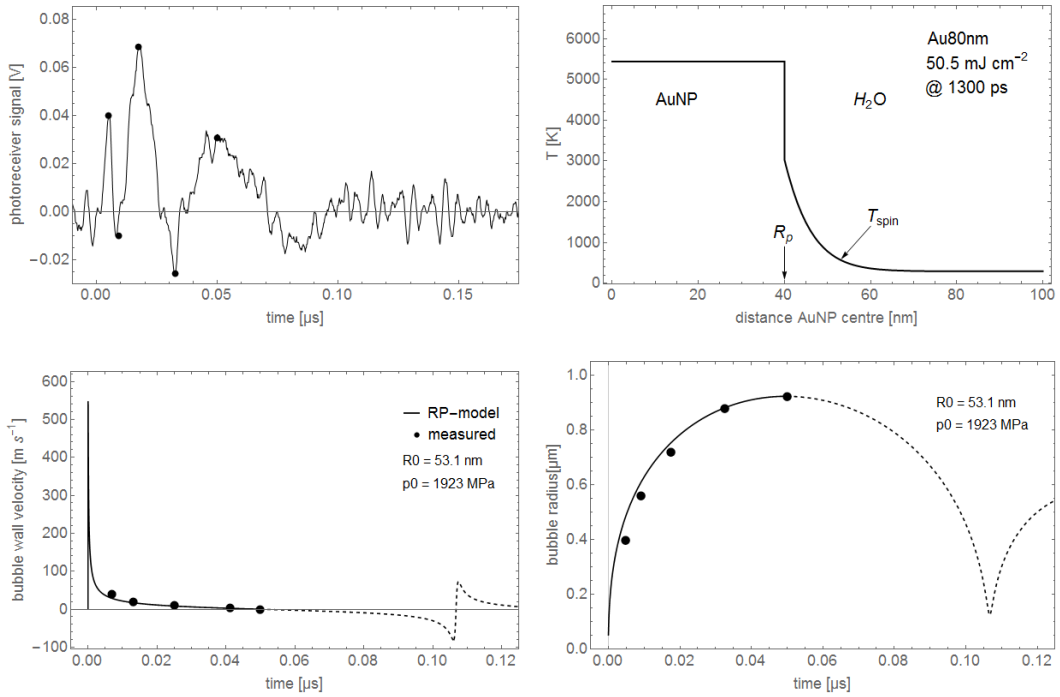

Figure 5.54: Backscattered signal of a bubble formed by an 80 nm sized AuNP under 800 ps pulsed irradiation with 50 mJ cm^{-2}. Based on the temperature profile and the equation of state, which was calculated at a time point of 1300 ps, the initial bubble condition of $R_0 = 53$ nm and $p_0 = 1923$ MPa respectively were obtained. The resulting RP-model fits the measured bubble wall velocity for the expansion phase of the bubble and delivers the maximum bubble expansion.

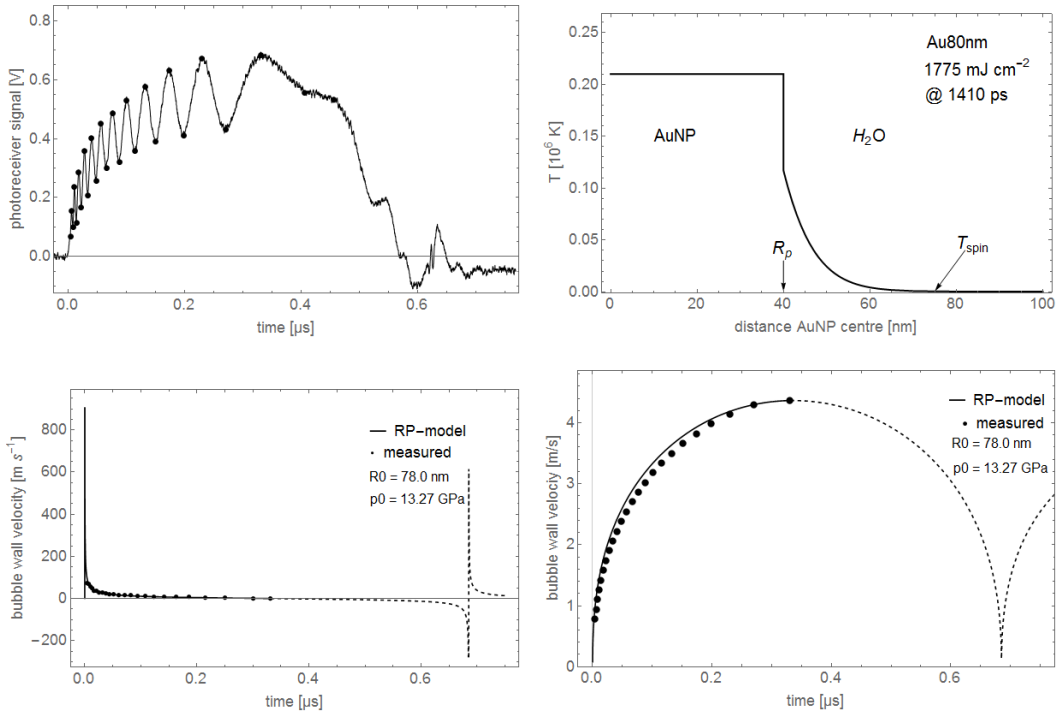

Figure 5.55: Backscattered signal of a bubble formed by an 80 nm sized AuNP under 800 ps pulsed irradiation with 1775 mJ cm^{-2}. Based on the temperature profile and the equation of state calculated at a time point of 1410 ps the initial bubble condition of $R_0 = 78$ nm and $p_0 = 13.27$ GPa respectively was obtained. The resulting RP-model fits the measured bubble wall velocity determined for the expansion phase of the bubble and delivers the maximum bubble expansion.

Estimation of the bubble formation temperature

The physical model for heat conduction and temperature increase described in Chapter 2.2.2 allows to estimate the temperature increase at the experimentally determined bubble formation threshold. For both, 50 nm and 80 nm AuNPs, the thermalization of the particle lattice is completed within a time of at least two orders of magnitude smaller than the pulse duration of 800 ps. Thus, the particle will reach an even temperature profile already during the irradiation pulse. Thermal equilibrium with the surrounding of the 50 nm and 80 nm AuNPs is achieved at 1.12 ns and 2.86 ns after onset of irradiation, respectively (cf. Table 5.1). Thus, a pulse duration of 800 ps complies with thermal confinement conditions, while 4 ns pulses exceed the thermal confinement. For 30 nm AuNP also 800 ps pulses exceed thermal confinement. Further, the pulse durations of 800 ps and 4 ns exceed for nanoparticle with diameters of 80 nm and below the stress confinement. Thermoelastic pressure waves are emitted within less than 25 ps. Table 5.1 contains the relevant nanoparticle properties and the thermal coefficients of gold nanoparticles with diameters D_p of 30 nm, 50 nm and 80 nm.

D_p [nm]	σ_{abs}@532nm $10^{-15} m^2$	σ_{abs}@640nm $10^{-15} m^2$	thermalization of AuNP $\tau_{T,p}$ [ps]	thermalization of surround. $\tau_{T,l}$ [ps]	acoustic confinement $\tau_{ac,p}$ [ps]
30	1.40	0.05	0.5	400	9
50	6.93	0.27	1.3	1120	15
80	18.40	1.61	3.3	2860	25

Table 5.1: Absorption cross sections (cf. equation 2.10 to 2.12) of gold nanoparticles with diameters D_p at the excitation and probing wavelengths. The thermalization times $\tau_{T,p}$ and $\tau_{T,l}$ of the nanoparticle and the surrounding medium respectively were calculated with the help of Equations 2.33 and 2.34. The acoustic confinement time τ_{ac} was determined by Equation 2.53.

Using Mie theory to calculate absorption cross sections and the experimentally determined bubble formation threshold, the temperature increase as function of time and distance r from the nanoparticle center was calculated. Figure 5.56 shows the temperature increase over time within and around a 50 nm and an 80 nm AuNP and as well as the spatial distribution at the time of maximum temperature on the nanoparticle surface under radiant exposures of 132 mJ cm^{-2} and 34 mJ cm^{-2}, respectively. A Gaussian pulse with a duration of 800 ps (full width at half maximum) was assumed. According to the calculations of by equation 2.42 to 2.45, a maximum nanoparticle temperature increase of $2.7{\cdot}10^3$ K and $4.3{\cdot}10^3$ K was determined for the 50 nm and 80 nm AuNP, respectively. The finite interface conductance of 105 MW K^{-1} m^{-2} [67] generates a discontinuity between the temperature increase in the AuNP $\triangle T_p(r = R_p, t)$ and in the water layer adjacent to the nanoparticle surface $\triangle T_l(r = R_p, t)$. Here, a maximum temperature increase of $1.67{\cdot}10^3$ K and $2.9{\cdot}10^3$ K was calculated at 1.7 ns and 1.8 ns, respectively. Thereafter cooling dominates the AuNP, while the surrounding water is heated. The calculated temperature increase would lead to vaporization of the gold nanoparticle, since the boiling temperature of bulk gold is around 3110 K. Figure 5.56 B and D show the spatial temperature distribution, when maximum temperature on the surface is reached (solid line) and for earlier (dashed line) and later (dashed dotted line) time points.

This calculated temperature increase at the experimentally determined threshold irradiation is not consistent with the assumption that an increase of the water at the particle surface to spinodal temperature of around 583 K leads to bubble formation. In order to reach spinodal temperature under isobar conditions temperature has to increase by approximately 290 K from a room temperature of 293 K. The temperature model predicts for 50 nm and 80 nm AuNP irradiated with 800 ps pulses at radiant exposure of 3.16 mJ cm^{-2} and 3.39 mJ cm^{-2}, respectively, to heat the water at the surface of the particles by $\triangle T_l(r = R_p, t) = 290$ K.

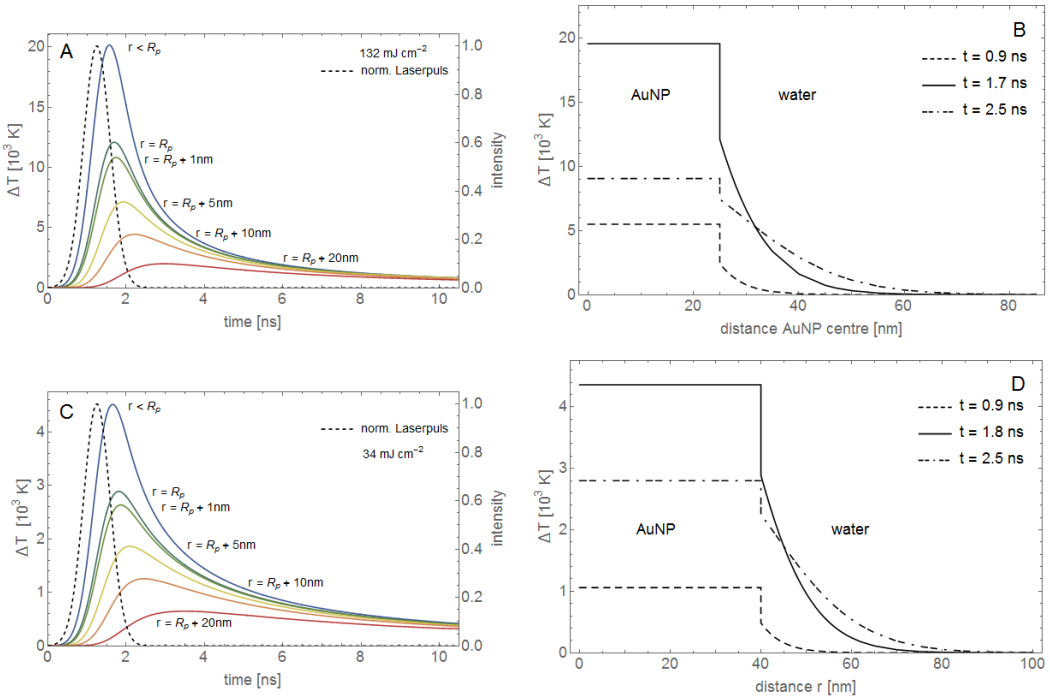

Figure 5.56: Calculated temperature increases for irradiation, which was experimentally determined for bubble formation threshold around 50 nm (A, B) and 80 nm (C, D) AuNP respectively. The corresponding spatial temperature increase was calculated in (B) and (C) for the time point of the maximum temperature increase on the AuNP-water interface (solid line) as well as for an earlier (dashed line) and later time point (dashed dotted line). The finite interface conductivity generates a discontinuity across the AuNP-water interface.

Mean temperature of overheated water at evaporation time point

The short pulsed laser irradiation at a strongly absorbed wavelength cause rapid temperature increase within the AuNP. Inside the particle a homogeneous temperature distribution is established, while heat diffusion across the nanoparticle surface causes a strong spatial temperature gradient $T_l(r,t)$ in the surrounding water. The pressure generated during the phase transition follows this gradient. Bubble formation is assumed to occur due to spinodal decomposition in a thin layer of liquid water on the nanoparticle surface and that only water with temperature above the spinodal point participates in the phase transition. The pressure gradient $p(r,t)$, which developed within the overheated water layer confined by the AuNP surface at R_p and the inertia of the water behind the surface of the initial bubble at r(T = 583 K) drives the bubble expansion. In order to calculate the bubble wall motion by means of fitting a solution of the Rayleigh-Plesset equation to the measurements the initial pressure p_0 was determined as the pressure for a mean temperature $\bar{T}_l$ within the volume of a thin water layer in the range $R_p < r < R_0$ determined by

$$\bar{T}_l = \frac{\oint_{V_p}^{V_0} T\,(r, t = t_{vap})\,dV}{\oint_{V_p}^{V_0} dV}.$$

This way, for each measured bubble wall motion a solution of the Rayleigh-Plesset equation was calculated numerically (cf. Figure 5.52) with the initial condition $R_0 = r\,(T_l = 585\,K)$ and $p_0 = p\left(\bar{T}_l\right)$. The pressure p_0 is calculated from the equation of state from Wagner and Pruß allows for water at a temperature up to 10^5 K [174].

5.4.4 Bubble dynamics around laser irradiated gold nanoparticles

Experimental results show, that pulse duration, radiant exposure and particle size effect the maximum bubble expansion (Figure 5.45). The maximum bubble radius and also the evolution of the bubble wall velocity can serve for an estimation of a possible damage region around the AuNP.

The initial conditions, i. e. the initial radius and the initial internal pressure of the expanding bubble determine the maximum bubble size, but cannot be measured directly. Also, the exact time point of the onset of bubble expansion could not measured experimentally due to insufficient bandwidth of the backscattered light detector. It was limited, since a high sensitivity was needed in order to provide detection of the interference related signal modulation at low backscattering intensity.

Nevertheless, the time point can be estimated by fitting the solution of the Rayleigh-Plesset equation to measurements of bubble wall velocity, while the initial physical conditions can be estimated by temperature calculations and the equation of state for water at high density. Throughout the following parts of this thesis, solution of the Rayleigh-Plesset equation is referred to as RP-model.

Onset of bubble formation at the evaporation time point

Calculation of the spatio-temporal temperature increase and the pressure increase, which is calculated from the temperature, define for a distinct time point the boundary conditions to solve the Rayleigh-Plesset equation, that provides the best fit to the measured bubble wall motion. For a measured bubble signal with interference related modulation, the time point t_{vap} at which the condition of the R_0 - p_0 combination drives the bubble formation can be determined by fitting (cf. Chapter 5.4.3). The evaporation time point t_{vap} limits energy deposition within the AuNP, referred to as $E_{abs,p}$ (Equation 5.12), provided that the explosive evaporation of the water causes instantly thermal and optical isolation of the AuNP. Figure 5.57 shows the bubble formation time t_{vap} for measured backscattering signals on bubbles around 50 nm and 80 nm sized AuNP. Independent from the applied pulse durations of 800 ps and 4 ns, a shorter t_{vap} was determined for the 50 nm than for the 80 nm sized AuNP. With respect to the temporal position of the maximum laser pulse intensity, under 4 ns pulsed irradiation bubble formation occurred during an earlier phase than during an 800 ps pulse. Assuming bubble formation to

cause a thermal as well as an optical isolation of the irradiated AuNP the part of absorbed energy can be determined by

$$E_{abs,p} = \sigma_{abs} \cdot H \int_0^{t_{vap}} f_n(t)\, dt = E_{abs,max} \int_0^{t_{vap}} f_n(t)\, dt, \tag{5.12}$$

with the laser pulse fluence H and the normalized laser pulse function $f_n(t)$,

$$\int_0^{\infty} f_n(t)\, dt = 1 \tag{5.13}$$

$E_{abs,max} = \sigma_{abs} \cdot H$ is absorption corrected radiant exposure and corresponds to the maximum energy, which is absorbed before the bubble forms. It is interestingly to note, the fitted t_{vap} ranges in the order of the particle thermalization time as determined by Equation 2.34. After this time span thermal equilibrium is established between the particle and the surrounding, which means that the amount of energy emitted from the AuNP is equal to the absorbed energy (Table 5.1). The mean evaporation time for 80 nm AuNP was around 1.289 ns under 800 ps pulsed irradiation and 3.655 ns under 4 ns pulsed irradiation, while thermal equilibrium between particle and surrounding is established after 2.86 ns (Table 5.2). Under 800 ps pulsed irradiation bubble formation occurs prior to thermal equilibrium (Table 5.1), while an irradiation with a pulse duration of 4 ns leads to heating times longer than $\tau_{T,l}$, before a bubble is formed. Besides the modeled evaporation time points, Table 5.2 holds the determined irradiation threshold of the detectable bubble formation. Threshold values for 800 ps pulsed irradiation were determined in experiments, while for 4 ns detection threshold was estimated. The pulse to pulse energy variation of the 4 ns pulsed laser prohibited a more precise adjustment of pulse energy near the threshold.

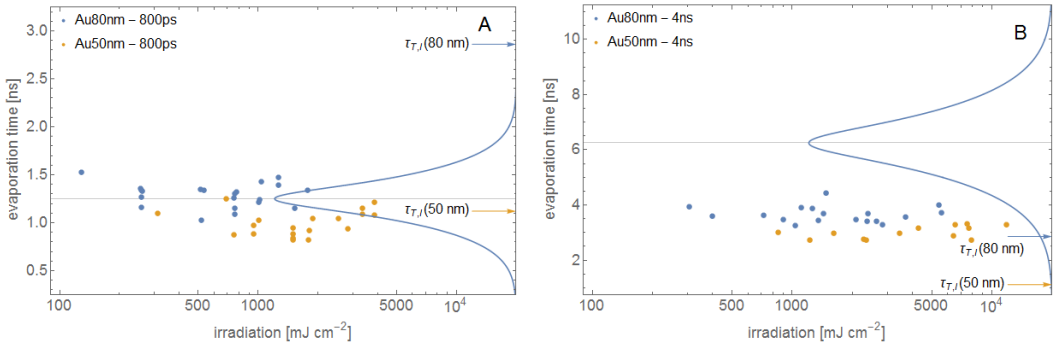

Figure 5.57: The calculated time point of bubble formation t_{vap} on an AuNP occurs during laser irradiation. (A) Under irradiation with an 800 ps pulse the bubble formation occurs on 50 nm and 80 nm sized AuNP around peak intensity. (B) Under 4 ns pulsed irradiation the formation occurs for both AuNP sizes during the irradiation pulse onset.

D_p	H_{thr}[mJ cm^{-2}]		t_{vap}[ns]	
	800 ps	4 ns	800 ps	4 ns
50	132	750	0.995	3.005
80	34	250	1.289	3.655

Table 5.2: The threshold for detectable bubble formation for 800 ps pulses measured and for 4 ns pulses estimated. The mean time point of evaporation was obtained from the fitted RP-models.

5.4.5 Effect of nanoparticle size, laser pulse duration and radiant exposure

Bubble formation and growth are based on the temperature increase of the AuNP with volume V_p. The efficiency of energy transfer across the AuNP-medium interface to heat and evaporate

the adjacent water layer and to provide energy for the subsequent bubble formation determines the maximum bubble expansion.

Analysis of the bubble expansion time dependency on $E_{abs,p}$ (Equation 5.12) shows, that besides the absorption cross section, other particle size related parameters influence bubble formation. The absorption corrected irradiation threshold of bubble formation is for 80 nm sized AuNP smaller than for 50 nm AuNP (Figure 5.58). Besides, for generation of equally sized cavitation bubbles around 50 nm and 80 nm particles, generally a lower radiant exposure was required for the larger particles.

Analysis of the pulse duration impact shows, that with 4 ns pulses a higher radiant exposure was required to form maximum bubble radii equal to 800 ps irradiation pulses. Further, when considering same absorption corrected radiant exposure, larger bubbles were generated with 800 ps pulses than with 4 ns pulses.

The larger gold particles have a lower bubble formation threshold and lead to larger bubbles at the same radiant exposure (Figure 5.58). This behavior can be understood with help of the RP-model, which predicts the dependence of the maximum bubble radius $R_{b,max}$ on the absorption corrected radiant exposure $E_{abs,max}$ according to

$$R_{b,max}(H) = [A \cdot (\sigma_{abs} \cdot H - E_t)]^{1/3} \tag{5.14}$$

$R_{b,max}$ follows a third root of the absorbed energy. Fitting this relation to the experimental data allows to determine the parameters E_t and A, the threshold energy of bubble formation and an inverse pressure, respectively.

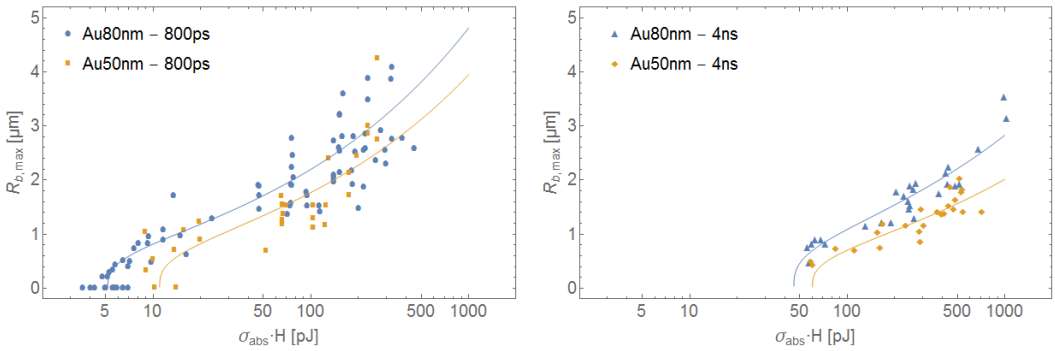

Figure 5.58: Measured bubble radius vs. absorption corrected exposure $\sigma_{abs} \cdot H$ for 50 nm and 80 nm AuNPs under irradiation with 800 ps (A) and 4 ns pulses (B). Solid lines are fits of the expected relation of maximum bubble radius and irradiation according to Equation 5.14.

Variation of the measured bubble expansion time

Bubble expansion time and thus the maximum bubble radius increase with the radiant exposure. The experiments on different particles of the same size irradiated with the same radiant exposure and pulse duration show variation in the measured bubble expansion. Figure 5.59 (A) shows as an example the measured expansion times of bubbles around 80 nm AuNP irradiated with 800 ps pulses. Irradiation with $H = 258 \pm 2\,mJ\,cm^{-2}$ caused bubble formation with $t_{exp} = 125 \pm 16$ ns (yellow points). Higher irradiation with $H = 764 \pm 8\,mJ\,cm^{-2}$ caused even stronger variation of the resulting bubble formation with $t_{exp} = 186 \pm 30$ ns (green points). Figure 5.59 (B) shows the estimated evaporation time depending on the radiant exposure (colored points correspond to the ones in Figure 5.59 (A)) and Figure 5.59 (C) shows the measured bubble expansion time depending on the energy $E_{abs,p}$, which was absorbed by the irradiated particle until time point t_{vap}.

The calculated $E_{abs,p}$ compensates for the particle absorption cross section of particles with 50 nm and 80 nm mean diameter, however, for different bubble measurements at similar irradiation a variation of the evaporation time point occurs. The individual cause of this variation and thus of the variation of partial energy absorption could not be specified. It is presumable that the particle size, which as determined with a precision of ±2 nm, the particle sphericity and

the occurrence of facets have an influence on the bubble formation. In particular, the position in the irradiation laser beam leads to different energy deposition in the particles.

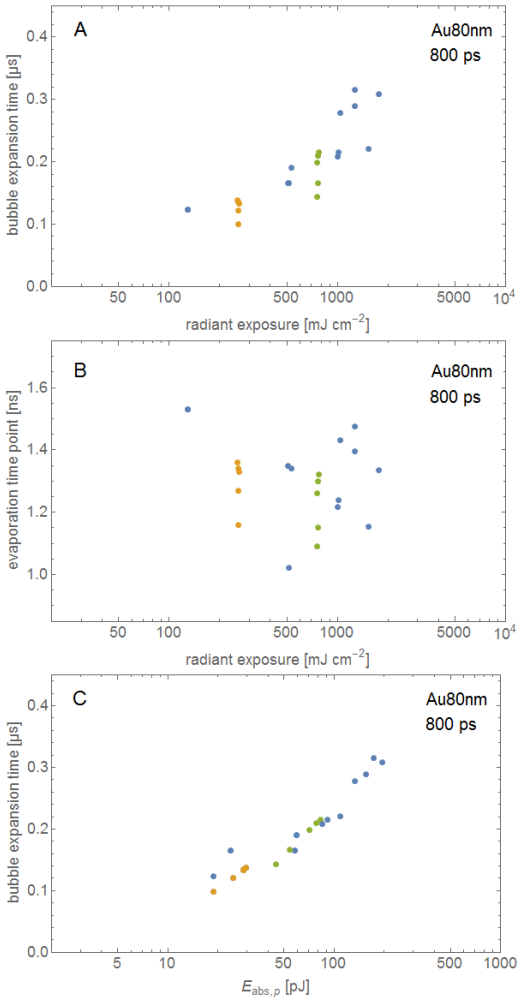

Figure 5.59: (A) Measured expansion times of bubbles formed around 80 nm AuNP for irradiation with 800 ps pulses with different radiant exposure. Evaporation time t_{exp} increases with radiant exposure and also varies for irradiation with different pulses at the same radiant exposure (yellow points $H = 258 \pm 2$ mJ cm^{-2} and $t_{exp} = 125 \pm 16$ ns; green points $H = 764 \pm 8$ mJ cm^{-2} and $t_{exp} = 186 \pm 30$ ns). The data is part of the data set shown in Figure 5.45. (B) Estimated evaporation time points t_{vap} depending on the radiant exposure and (C) t_{exp} depending on partial absorbed laser pulse energy $E_{abs,p}$. Colors in B and C correspond to colors in A.

Effect of the laser pulse duration on bubble formation

Pulsed irradiation with both, 800 ps and 4 ns duration, can induce cavitation bubbles of similar maximum radii around an AuNP of the same size, when irradiance is adjusted. When applying 4 ns pulses a higher radiant exposure is required than for application of 800 ps pulses. Thus, it can be concluded that the interface on which the bubble formation takes place has only a small influence on the bubble expansion. Figure 5.60 shows the measured backscattered light signals on bubbles around 50 nm and 80 nm particles generated by irradiation with a pulse duration of 800 ps (blue) and 4 ns (yellow).

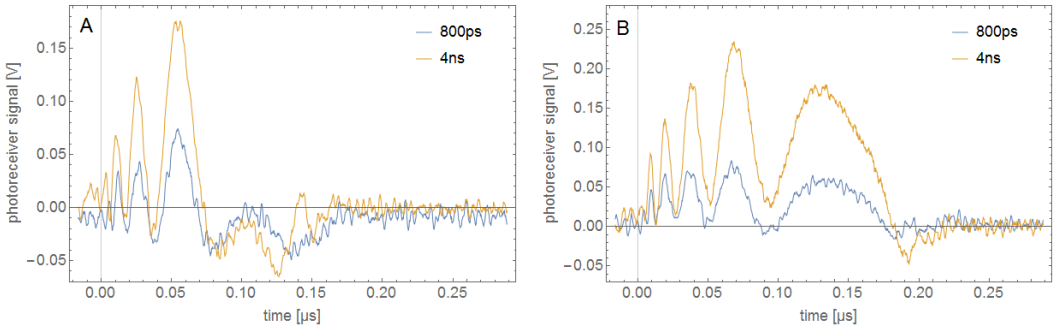

Figure 5.60: (A) Measured bubble interferometry signals of two gold nanoparticles with 50 nm diameter for irradiation with 1.5 J cm^{-2} and 4.3 J cm^{-2} at pulse durations of 800 ps (blue) and 4 ns (yellow) respectively. A bubble radius of around 1.15 µm correlates with the bubble expansion time. (B) The measured bubble interferometry signals of two gold nanoparticles with 80 nm diameter for irradiation with 0.26 J cm^{-2} and 1.43 J cm^{-2} at pulse durations of 800 ps (blue) and 4 ns (yellow) respectively (B).

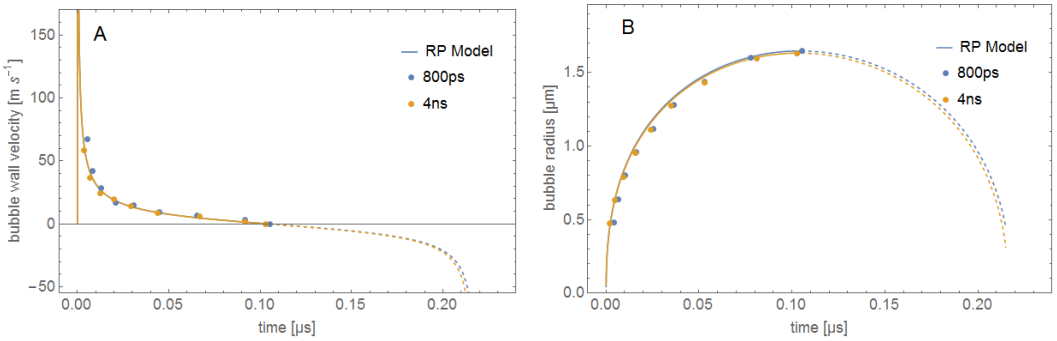

Figure 5.61: The measured and calculated bubble wall velocity (A) and radius (B) for 50 nm AuNP irradiated with 1.506 J cm^{-2} and 4.290 J cm^{-2}at a pulse duration of 800 ps (blue) and 4 ns (yellow) respectively.

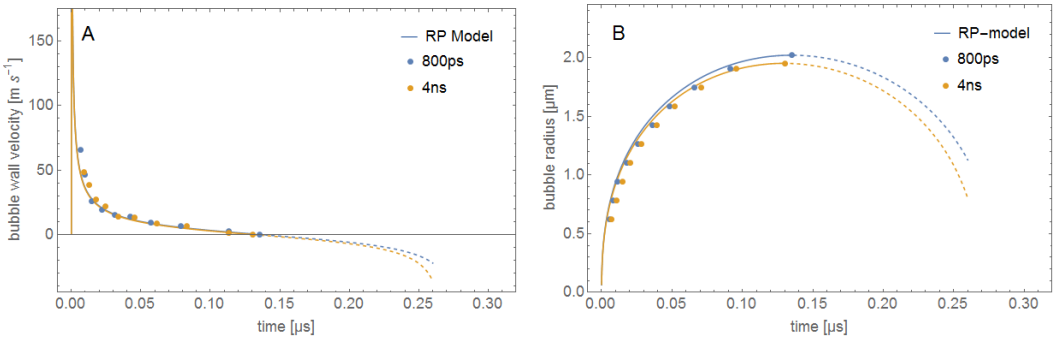

Figure 5.62: The measured and calculated bubble wall velocity (A) and radius (B) for 80 nm AuNP irradiated with 0.258 J cm^{-2} and 1.433 J cm^{-2} at pulse durations of 800 ps (blue) and 4 ns (yellow) respectively.

The measured signals show equal bubble expansion times and the same number of modulations for both, 800 ps and 4 ns irradiation pulses. Thus, similar bubble dynamics by means of velocity time curves and radius time curves are assumed. As an example for a 50 nm sized AuNP Figure 5.61 depicts the RP-model (solid lines) and measured values (dots) of the bubble wall velocity. Also for measurements on 80 nm sized AuNP, similar velocity and radius time courses were found as depicted in Figure 5.62.

However, the solutions of the Rayleigh-Plesset differential equation corresponding to each pulse

duration are based on different initial conditions due to the different temperature profiles at the appropriate time point of evaporation. For these measurements the fitting results for t_{vap}, the corresponding initial conditions and the maximum bubble radius are shown in Table 5.3.

	80 nm		50 nm	
	800 ps	4 ns	800 ps	4 ns
H [mJ cm^{-2}]	258	1433	1506	4290
t_{vap} [ps]	1340	3700	950	3165
$E_{abs,p}$ [pJ]	28.7	17.6	19.7	10.3
p_0 [MPa]	4504	3140	6737	3784
R_0 [nm]	63.8	68.6	46.3	54.4
$R_{b,max}$ [µm]	2.021	1.952	1.647	1.632
$\overline{T_l}$ [K]	3192	2069	5101	3784

Table 5.3: Fitting results for t_{vap} of RP-models solved for bubble formation measurements at 80 nm and 50 nm sized particles shown in Figure 5.60.

5.5 Conclusions

With the help of the dark field microscope, the detection of single spherical gold nanoparticles as well as the generation and measurement of cavitation bubbles were achieved. For the first time, the velocity of the cavitation bubble expansion around nanoparticles was detected in a temporally resolved manner. The principle of the coherent measurement of the backscattering of probe laser light from a vapor bubble allows the determination of their bubble wall velocity from the signal interference pattern once the bubble has reached a size of $\lambda_{probe}/4$. An estimation of the expansion rate below this radius and thus at the onset of the bubble formation is unfortunately not possible by interferometry.

Backscattered and transmitted light of cavitation bubbles around gold nanoparticles was detected synchronously and showed the expected equal bubble oscillation times. In contrast to the measured signal of transmitted light, the backscattered light signal shows the bubble dynamics and further an asymmetry between the expansion and collapse phase. The bubble wall velocity was determined during the expansion phase, while during bubble collapse the detected signal showed no regular interference pattern. In conclusion, a rigid interface only affects the bubble collapse, while the motion to maximum bubble radius is not affected. Thus, determination of the bubble radius based only on transmission measurements would underestimate the actual maximum bubble radius.

Laser pulse duration and the nanoparticle diameter were varied in the investigations. As expected, the development of the nanoparticle temperature and thus the time point of the spontaneous bubble nucleation depends on radiant exposure and is influenced by AuNP size as well as the pulse duration of the irradiation. Both significantly influence the cavitation bubble formation around gold nanoparticles.

For irradiation with 800 ps pulses the longest expansion time was measured for a bubble with 3.76 µm radius formed around an 80 nm AuNP, while a 4 ns laser pulse caused maximum expansion to 3.0 µm. The shortest expansion time measured at bubbles around AuNP with 80 nm and 50 nm diameter on a glass surface under irradiation with a pulse duration of 800 ps were 10 ns and 16 ns, respectively. The corresponding maximum bubble radii were around 110 nm and 175 nm. For 4 ns laser pulses on 50 nm and 80 nm sized particles measured expansion times were not shorter than 23 ns, which correspond to a maximum bubble radius of 250 nm. In conclusion, the lower bubble detection limit ranged around 100 nm radius.

A model based on the temperature calculations was used to determine the physical boundary conditions of initial radius and pressure for the bubble formation around AuNP at a specific evaporation time point after onset of irradiation. This time point was varied until the solution of the Rayleigh-Plesset equation determined for the initial radius and pressure fit the measurement. It was found, that water temperature on the particle surface was increased above critical temperature for irradiation, at which bubble formation was detected.

The temperature increase of the AuNP follows the laser pulse, while the finite conductivity of the AuNP-water interface limits heat diffusion into the surrounding. Thus, spatial temperature

increase shows a discontinuity across the nanoparticle-water interface. After the maximum particle temperature is reached cooling dominates the particle and the temperature discontinuity decreases until it finally disappears. However, for irradiation at bubble detection threshold the formation of a bubble is accompanied by partial or complete melting of the particle. The scattering spectra measured before and after irradiation showed changes, which are related to decreasing particle radius. Further, for higher irradiation, the evaporation of the particles is very likely, because after the laser pulse, the particle could no longer be detected.

6 Discussion

6.1 Measuring cavitation bubbles around gold nanoparticles

Within the experimental part of this investigation, the bubble wall velocity was directly measured on individual gold nanoparticle. In order to identify the nanoparticles and determine their size, a darkfield microscope was setup to measure spectrally resolved light scattered by the nanoparticles. For generation of bubbles around nanoparticles, the microscope was equipped with a pulsed laser. A focused cw laser, which allows the synchronous detection of the forward- and backscattered laser light from the cavitation bubble, was coupled collinear with the pulsed laser beam to measure the bubble size.

Sönnichsen et al. established a microscope with a total internal reflection illumination and an imaging spectrograph in the focal plane behind the microscope exit port in order to detect scattered light spectra of single nanoparticles (SPSS, single particle scattering light spectroscopy)[74].

Several publications describe the measurement of bubble oscillations around gold nanoparticles by detection of intense forward scattering of a tightly focused probe laser beam adjusted collinear to the laser beam used for particle heating [176, 177, 6, 60, 16, 114]. A bubble formed around an AuNP modulates the probe laser intensity detected by an amplified photodiode or a PMT. From the modulation of the scattering signal the bubble oscillation time t_{osc} can be determined. This allows calculating of the maximum bubble radius, provided the relation of $R_{b,max}$ and t_{osc} is known. With the help of this scattering technique single bubbles in water with an oscillation time below 10 ns and a corresponding radius below 200 nm were measured. Since there is no kown relationship between bubble size and signal amplitude of the forward scattered light detection, the temporal evolution of the bubble radius is not accessible.

Besides scattered light measurements, short time flash photography was used in order to determine the maximum bubble radius of cavitation bubbles in free water [108] and around immobilized AuNP [16]. For cavitation bubbles around AuNP floating in water also the bubble wall motion was measured by imaging [178]. The used imaging techniques cover a large spatial and temporal dynamic range but the spatial resolution is limited to about 1 µm, while maximum framing rates of the available cameras limit the temporal resolution. Due to the limited optical resolution, short time flash photography is restricted to the investigation of micrometer-sized bubbles.

Radius time curves of bubbles with maximum diameter of few nanometers generated around gold nanoparticles were only measured by Plech et al. with enormous experimental effort by time-resolved small angle X-ray scattering (SAXS) [66].

The challenge to measure laser-induced bubble dynamics around single gold nanoparticles with high temporal and spatial resolution over a large dynamical range was met by the technique of coherent backscattered light detection presented in this thesis.

In this thesis SPSS to identify particles was combined with generation and detection of cavitation bubbles with two confocal laser beams. In particular,coherent backscattered light detection from a cavitation bubble is used for the AuNP mediated bubble formation here for the first time. The bubble wall motion of a cavitation generated around a particle by a single laser pulse was captured in only one single measurement.

The detection of backscattered light of a tightly focused collinear laser beam allowed to measure the bubble wall velocity $v_b(t)$ from the interference signal detected by the photodetector. A solution of the Rayleigh-Plesset equation was fitted to the measured bubble wall velocity. The initial bubble radius and pressure required to solve the Rayleigh-Plesset (RP) equation were obtained by the temporal and spatial resolved calculation of the temperature distribution within and around the irradiated AuNP. Further, for each measurement the maximum bubble radius was calculated with help of the corresponding solution of the RP equation, which consists of the time dependent functions of bubble wall velocity and bubble radius. The largest range of bubble sizes covered in the experiments was measured for 80 nm sized gold nanoparticles, when irradiated with 800 ps pulses. Here, bubbles with expansion times between 50 ns and 330 ns, which correlate to maximum bubble radii ranging from approximately 0.90 µm to 4.50 µm respectively, were measured. In backscattering signals shorter bubble oscillations from smaller bubbles could not be measured on the background of the signal noise. This lower limit of the dynamic range was given by the intensity of the probe laser as well as the photodetector

sensitivity and noise. Low detector sensitivity can be compensated by using a more powerful probe laser beam. However, heating by the probe laser beam in particular with wavelength in the absorption band of the gold nanoparticles should be avoided. Using a higher NA microscope objective allows to detect more photons and leads to increase in the detected backscattered light signals at higher SNR. Though, a microscope objective with NA higher than the utilized one (cf. Chapter 5.3.2), which provides at the same time the required large working distance, could not be customized.

6.2 Limits of measuring bubble dynamics by backscattered light detection

For cell elimination, when a targeted cell is addressed by a large number of nanoparticles, the knowledge of the individual cavitation dynamics and effects of individual nanoparticles may appear unimportant, since one aims for destruction of the cell. However, specific elimination in cell sorting processes as well as manipulation of cells by means of targeted membrane transfection or release of biologically active substances require high precision in order to retain control of the desired result. The setup of the darkfield microscope in combination with the scattering light spectroscopy and two collinear laser beams coupled into the microscope objective allows to measure cavitation bubbles around individual nanoparticles located on transparent surfaces.

The setup provides optically detection and sizing of nanoparticles, which are positioned in a laser beam in order to measure the laser induced cavitation bubbles by scattered light detection.

6.2.1 Detection threshold of bubble formation

Accuracy of determining the bubble formation threshold depends on the detection of a forming bubble and the measurement of the laser pulse energy. Detection threshold systematically effects the determination of the bubble formation threshold. Reproducibility of the bubble measurements is also effected by particle size variation and laser pulse to pulse stability. The passively Q-switched Nd:YAG laser (CryLas Type FDSS532) emitted smooth pulses of 800 ps duration and a pulse-to-pulse energy variation of around ±1.0 %. The actively Q-switched Nd:YAG laser (Continuum Type SureLite I) emitted strongly spiked pulses of 4 ns duration and a pulse-to-pulse energy variation of around ±5 %. This behavior prohibited to determine the detection threshold empirically by increasing the pulse energy in small steps. Thus, for irradiation with the pulse duration of 4 ns the detection threshold of bubble formation could not be determined as precise as for the 800 ps pulsed irradiation.

Further, each measurement had to be done on a different nanoparticle, because even irradiation below bubble formation could change optical properties of the irradiated particle and thus effect the radiant exposure required to generate a bubble. Partial melting of the irradiated gold nanoparticle may occur already at the bubble formation threshold. The finite thermal interface conductivity between the gold nanoparticle and surrounding medium can lead to particle temperature above 700 K (cf. Figures at which melting or superficial structure alteration can occur [89, 179], while the water exhibits temperature below the spinodal point of around 583 K. Material loss was observed by spectral shift of the absorption peak after irradiation (Figure 5.46 A). Even subthreshold irradiation decreases the particle radius and thus increases the threshold of bubble formation. Therefore, repetitive irradiation around bubble formation threshold is limited to the extend of the induced structure alterations and their effect on nucleation.

Detection threshold at 800 ps pulse duration

Bubble formation related forward scattering signals were detected at 50 nm and 80 nm AuNP under 800 ps pulsed irradiation with radiant exposure around 132 mJ cm^{-2} and 34 mJ cm^{-2}, respectively. At this detection limit of bubble formation a decrease of scattering and a small shift of the peak in the detected spectrum were observed even when no bubble was detected (cf. Figure 5.48). The spectral change indicates substance loss due to melting and evaporation of the nanoparticle.

Shortest oscillation times of around 22 ns were detected at both, 50 nm and 80 nm AuNP, under 800 ps pulsed irradiation with radiant exposure of 165 mJ cm^{-2} and 28.8 mJ cm^{-2}, respectively

(Figure 6.1 C and D). Fitting a RP-model to the bubble wall velocity (cf. Chapter 5.4.4) at the detection threshold was not possible, because the bubble wall velocity could not be measured. The interference related signal modulation was undetectable due to limited sensitivity and bandwidth of the photodetector. Thus, an RP-model was calculated, which exhibits the same expansion time as the measured photodetector signal. Therefore, also the evaporation time point t_{vap} was determined at which the corresponding initial bubble radius and pressure (cf. Chapter 5.4.4) give the best solution of the Rayleigh-Plesset equation.

For 800 ps pulse irradiation the time points of maximum temperature t_{Tmax} are 1.69 ns for 50 nm AuNP (Figure 5.56 A) and 1.81 ns for 80 nm AuNP (Figure 5.56 C) after onset of the irradiation pulse (Equations 2.42 to 2.44), provided that properties of the involved materials remain constant over the temperature increase. However, this is not given for irradiation at the detection threshold, because even before the hypothetical temperature maximum, temperatures higher than the melting point of gold or as the spinodal point of the surrounding water are reached. Thus, at a time point before t_{Tmax} the surrounding water undergoes phase transition, which causes optical and thermal isolation. Further energy deposition at lower absorption efficiency still can cause phase transitions of the gold nanoparticle, which are indicated by the spectral changes after irradiation. For instance the spectral shift and decrease of the scattering band detected after irradiation of an 80 nm AuNP corresponds to a reduction of the nanoparticle diameter from 80 nm to 74 nm shown in Figure 5.49, which corresponds to a volume loss of 21 %.

Figure 6.1 exemplary shows the calculated radial temperature profile at evaporation times $t_{vap} = 780$ ps for 50 nm AuNP irradiated with 165 mJ cm^{-2} and $t_{vap} = 1040$ ps for 80 nm AuNP irradiated with 28.8 mJ cm^{-2}. The calculated bubble radius time curves with expansion times equal to the corresponding bubble measurement (Figure 6.1 C and D) are based on the initial bubble radius and pressure determined from the calculated temperature (Figure 6.1 A and B) as described in Chapter 5.4.3.

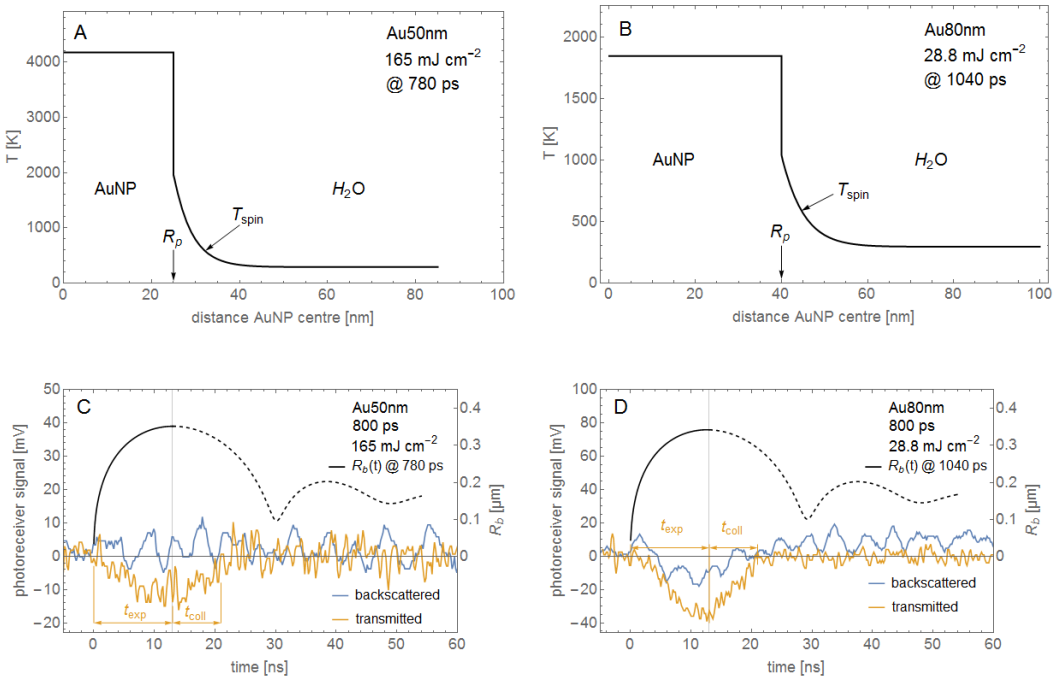

Figure 6.1: Bubble formation at detection limit of cavitation bubbles around 50 nm (A, C) and 80 nm (B, D) AuNP under 800 ps pulsed irradiation. A) Calculated radial temperature profile at 780 ps after onset of the irradiation with 165 mJ cm^{-2}. B) Calculated radial temperature at 1040 ps after onset of irradiation with 28 mJ cm^{-2}. C) Signals of backscattered (blue line) and transmitted (yellow line) light detection at the bubble formed around the 50 nm AuNP. The radius time curve of the bubble was calculated based on the RP-model for mean temperature in the water shell with an outer radius of $R_0 = 32.2$ nm and the corresponding pressure of $p_0 = 1460$ MPa. D) The radius time curve of the bubble around the 80 nm AuNP for an initial bubble temperature in the water shell with an outer radius of $R_0 = 44.6$ nm and $p_0 = 937$ MPa. Note, that modulations in the backscattered light signals are due to detector noise.

Also for the bubble signal measured at the detection threshold an expansion time $t_{exp} \simeq 0.6 \cdot t_{osc}$ (cf. Chapter 5.3.6) was assumed. Thus, collapse phases were systematically overestimated, because solutions to the Rayleigh-Plesset equation are not capable of describing bubble collapse of a hemispherical bubble formed on a rigid surface.

Further, for the detected bubble signals shown in Figure 6.1 C and D a maximum radius of around 350 nm was calculated, which is larger than the fundamental detection limit of $\lambda/4$. Interference related modulation in the backscattering signal was not detected due to insufficient sensitivity. A more powerful probe laser may help to increase the dynamical range, but can also involve much stronger heating of the AuNP. However, optical detection techniques such as the backscattered and the transmitted light detection lack of sensitivity to resolve the bubble oscillation at the physical bubble formation threshold.

Threshold of bubble formation in literature

Data on bubbles formation thresholds around single AuNP are scarce in literature. In some publications the impact of AuNP size and geometry as well as pulse duration on the bubble formation threshold was investigated [66, 67, 68, 6, 60, 65, 16]. Mostly an irradiation wavelength of 532 nm, which was near the plasmon resonance peak, was used. In most of the published data the influence of the temporal pulse profile, for instance the strong spiking of Q-switched lasers, was not discussed. However, for nanoparticle radius above 10 nm only minor effect of spiking in the pulse pattern on the temporal temperature evolution (cf. Figure 5.25) and thus minor effect on bubble formation is expected. Table 6.1 shows published data on the bubble formation threshold for gold nanoparticles of different sizes under short pulsed irradiation. Experiments were conducted on samples containing particle ensembles as well as on single gold nanoparticles.

AuNP [nm]	Sample	λ_l [nm]	τ_l [s]	H_{thr} [mJ cm^{-2}]	Author and group	Year	Ref.
9	multi	400	$100{\cdot}10^{-15}$	29	Kotaidis and Plech	2005	[66]
39	particle	400	$100{\cdot}10^{-15}$	8	Kotaidis & al.	2006	[67]
38	solution	400	$100{\cdot}10^{-15}$	25	Plech & al.	2007	[180]
60		355	$3{\cdot}10^{-9}$	15	Siems & al.	2011	[68]
500	single	527	$12{\cdot}10^{-9}$	106	Neumann,	2005	[6]
			$240{\cdot}10^{-9}$	216	Brinkmann		
			$1.8{\cdot}10^{-6}$	651			
30	considered	532	$0.5{\cdot}10^{-9}$	720	Lapoko	2009	[60]
100	single		$0.5{\cdot}10^{-9}$	380			
30	in sol.		$10{\cdot}10^{-9}$	9360			
100			$10{\cdot}10^{-9}$	9100			
90			$0.5{\cdot}10^{-9}$	360	Lukianova-Hleb	2009	[181]
250			$0.5{\cdot}10^{-9}$	180	& al.		
10			$0.5{\cdot}10^{-9}$	1800	Lukianova-Hleb	2010	[65]
30			$0.5{\cdot}10^{-9}$	230	& al.		
60			$0.5{\cdot}10^{-9}$	115			
80			$0.5{\cdot}10^{-9}$	100			
90			$0.5{\cdot}10^{-9}$	100			
250			$0.5{\cdot}10^{-9}$	130			
90	single,	498	$5{\cdot}10^{-9}$	110	Kitz, Frenz	2011	[16]
	sputtered	532		60			
	on slide	600		70			
		755		350			
		780		440			
50	single,	532	$0.8{\cdot}10^{-9}$	132	this thesis	2018	
80	on slide		$0.8{\cdot}10^{-9}$	34			
50			$4{\cdot}10^{-9}$	750			
80			$4{\cdot}10^{-9}$	250			

Table 6.1: Irradiation threshold H_{thr} for bubble formation at laser irradiated gold nanoparticles with different diameters Ø. Lasers pulse width τ_l ranging between 100 fs and 10 ns and wavelengths λ_l between 400 nm and 780 nm were used.

Kotaidis et al. showed that bubble formation is a threshold process, where explosive boiling or spinodal decomposition occurs as soon as a water layer around the particles reaches 85% of the critical water temperature [66, 67]. Initial melting of a gold nanoparticle was found for particle temperature increase of 529 K [89], which is below the bubble formation threshold [66]. The evaporation temperature of gold nanoparticles is not known. Bulk gold melts and evaporates at temperature increase of around 1063 K and 2830 K, respectively.

In their SAXS measurements at 9 nm sized AuNP under femtosecond pulsed irradiation Kotaidis et al. detected bubbles with maximum radius of around 21 nm. The related bubble oscillation time was approximately 0.65 ps. However, the SAXS method does not prove the occurrence of a well defined gas-liquid interface. Nevertheless, the alteration in the water liquid scattering, which was used to determine pressure transients, indicated occurrence of a vapor phase of the medium. In order to model the measurements with help of the Rayleigh-Plesset differential equation they assumed an equilibrium radius and pressure of $R_0 = 7.2$ nm and $p_0 = 0.3$ GPa. Further, initial radius $R(t = 0) = 4.5$ nm and bubble wall velocity $dR/dt = 90\,m\,s^{-1}$ were assumed.

In comparison to the SAXS method optical measurements allowed to detect single bubbles in free water with an oscillation time $\lesssim 10$ ns and thus a maximum radius < 200 nm [103]. Oscillation times in the range of 9 to 13 ns were also optically measured for bubbles around 90 nm AuNP irradiated with 0.5 ns pulses and radiant exposure around 100 mJ cm^{-2} at a wavelength of 532 nm [65]. In this study, Lukianova-Hleb et al. found, that bubble formation follows a threshold mechanism and bubble oscillation time does not gradually decrease to zero as the pulse radiant exposure is reduced. Their thermal model showed, that irradiation much lower than

the threshold fluence would already increase the surrounding water temperature to the critical point at 647 K. They concluded from threshold experiments on nanoparticles with different sizes and the corresponding temperature calculations, that additional energy was provided to the vapor layer in order to form a bubble. However, their conclusion disagrees with a study, that utilized similar optically techniques [68]. This study showed in experiments with different particle sizes, that radiant exposure of bubble formation threshold corresponds to the calculated fluence causing temperature increase, which leads to spinodal decomposition in the surrounding water layer. For gold nanoparticles with a diameter of 18 nm the bubble formation occurred even at lower radiant exposure than theoretically required.

In conclusion, reported bubble formation thresholds are rather detection limits of the experimental settings. Only the SAXS method provides sensitivity, which can resolve bubble radius generated by irradiation around the threshold fluence of bubble formation.

6.2.2 Bubble expansion above bubble formation threshold

With increasing irradiation of the particles, the time point of bubble formation with respect to the begin of the irradiation changes, since the temperature at which phase transition occurs is reached at an earlier time point. Initial bubble radius and pressure were estimated from the spatial temperature distribution at the evaporation time point t_{vap}, which was calculated from the heat differential equation. The corresponding RP-model describes the oscillation of a bubble instantaneously formed with radius R_0 and high density vapor a pressure p_0.

The expansion phase for a bubble formed around a nanoparticle located on a rigid surface was modeled by solving the Rayleigh-Plesset Equation 2.63. It was assumed, that the rigid interface has only minor effect on the bubble formation. Also viscosity and surface tension are considered being only slightly affected by the interface. This assumption bases on finding only minor deviation from the (hemi-) spherical shape, which were shown in flash photography images of bubbles at the maximum expansion show (Figure 5.37). Solutions of the Rayleigh Plesset equation for calculating formation of a hemispherical bubble at a rigid interface has not been reported so far.

The RP-models were calculated as described in Chapter 5.4.4 to fit the bubble wall velocity measured during the bubble expansion phase. The evaporation time point was determined, in a way that initial bubble radius and pressure calculated from the thermal model gave the best starting conditions for the Rayleigh Plesset calculation of the bubble expansion. Based on the initial pressure p_0 and radius R_0 the expansion to maximum radius was calculated starting at the evaporation time point. After formation of the bubble, transfer of thermal energy to the initial bubble is assumed to be interrupted due to the thermal insulation of the nanoparticle by the vapor bubble. According to numerical analysis by the group of Merabia et al. thermal isolation occurs not necessarily up on formation of the initial bubble [182]. The initial bubble contains overheated vapor of high density. Depending on the vapor density and heat capacity further thermal energy is supplied by diffusion from the nanoparticle surface across the bubble while it expands. Thus, the maximum bubble radius calculated by the corresponding RP-model is a lower limit and larger bubble size should be expected.

Maximum bubble radius

With higher radiant exposure the maximum bubble diameter increases. Figure 6.2 shows maximum bubble radius plotted against the particle absorption cross section corrected radiant exposure $\sigma_{abs} \cdot H$. Backscattered light measurements at bubbles formed around 50 nm and 80 nm sized AuNP under 800 ps pulsed irradiation showed only for signal duration above 0.10 µs interference related modulation. The corresponding RP-model gives maximum bubble expansion of 1.043 µm (50 nm) and 0.970 µm (80 nm AuNP) respectively. Under 4 ns pulsed irradiation for both, 50 nm and 80 nm sized AuNP, modulated backscattering signals were measured for duration above 0.08 µs, which corresponds to a bubble radius of around 640 nm. The sensitivity of the utilized photodetector prohibits detection of smaller bubbles. Further, bubble wall motion higher than a velocity of 45 $m\,s^{-1}$, which occur at the onset of bubble expansion, could not be resolved due to the detector bandwidth.

The absorbed energy within an AuNP increased with irradiation and therefore the bubble driving pressure related to the temperature raised. According to Equation 5.14 bubble size

is related by a 3rd root function to the bubble energy. $R_{b,max}$ shows non-linear increase with absorption cross section corrected exposure. For 800 ps pulsed irradiation a bubble growth from R_0 to $R_{b,max}$ by a factor of 84 and of 98 was be observed for 50 nm and 80 nm sized AuNP respectively. The 4 ns pulsed irradiation led to a growth by a factor of 59 and of 72 for 50 nm and 80 nm sized AuNP respectively. Interestingly to note, the growth from initial to maximum bubble radius increases with AuNP size, while for increasing pulse duration the dependency on the AuNP size becomes weaker.

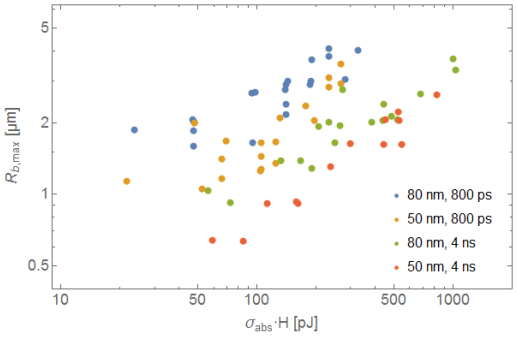

Figure 6.2: Maximum bubble radius around 50 nm and 80 nm AuNP generated by irradiation by 800 ps and 4 ns pulses shown against $\sigma_{abs} \cdot H$.

6.3 Limits of the analytical modeling of bubble formation around gold nanoparticles

Calculation of the optical absorption and scattering cross sections of the gold nanoparticles and the temperature distribution in and around laser irradiated gold nanoparticles plays a major role in the investigations of bubble formation around AuNP. The modeling was based on the Mie theory and an analytical description of heat dissipation. The bubble expansion was subsequently described with help of an extended Rayleigh-Plesset model.

A qualitative model for the bubble formation around gold nanoparticles was developed, which should help to understand the mechanisms of cell elimination and molecular release from AuNP. Besides laser pulse duration and radiant exposure, the AuNP size and the absorption cross section determine initial bubble formation conditions R_0 and p_0. Based on these parameters, a qualitative model of the bubble formation and bubble dynamics was developed. Figure 6.3 illustrates the different parameters and physical models involved in the calculation of the bubble formation around pulsed laser irradiated gold nanoparticles.

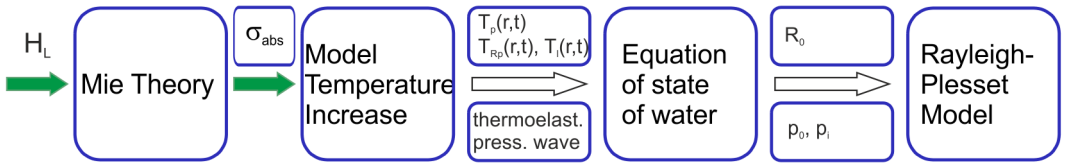

Figure 6.3: Parameters and physical models involved in the calculation of the bubble formation around laser irradiated gold nanoparticles.

Short pulsed laser irradiation with wavelengths around the plasmon resonance peak absorption leads to high temperatures of the nanoparticle lattice. Optical energy is converted by plasmon oscillations within 500 fs to thermalized electrons and further to thermalized phonons on the picosecond time scale (cf. Chapter 2.2.1). Equilibrium heat diffusion with the surrounding water is established within nanoseconds (cf. Table 5.1). The high heating rates allow thermal energy

deposition before particle lattice expands, which is therefore considered isochoric condition. The density of the gold nanoparticle and the surrounding water remain for this time constant. At a certain point explosive evaporation of the surrounding medium follows and a cavitation bubble is formed.

Using the Rayleigh-Plesset differential equation based on the initial bubble radius and pressure, which were estimated by the thermal model for a certain time point bubble growth was calculated (cf. Chapter 5.4.4). Even if the calculated temperature is purely hypothetical and gives values above the melting and evaporation of gold, a RP-model results, that describes the measured bubble dynamics with the least deviations. Due to subsequent bubble wall expansion with a velocity, which can be much higher than $100\,\mathrm{m\,s^{-1}}$, within picoseconds, energy transfer from the nanoparticle into the bubble changes .

6.3.1 Optical properties of gold nanoparticles effecting the temperature increase upon irradiation

When calculating absorption and scattering by the Mie theory the temperature dependent optical properties of the gold nanoparticle were neglected. Figure 6.4 shows absorption spectra of 50 nm and 80 nm sized AuNP, which were calculated with help of the dielectric function for solid gold at temperatures ranging between 283 K and the melting point around 1336 K as well as liquid gold at 1336 K [183]. With increasing temperature the dielectric function of gold varies as such that the absorption decreases. During the melting process optical parameter change discontinuously and absorption approaches the intraband absorption. Accordingly, the absorption cross section at the irradiation wavelength of 532 nm decreases for a temperature increase of gold in the solid phase from 283 K to 1336 K approximately linear by 45 % for a 50 nm and and 22 % for an 80 nm sized AuNP. In liquid state the absorption cross section decreases further to 38 % and 63 % respectively.

When calculating the temperature increase the temperature dependence of optical absorption was not considered. Thus, the calculated temperatures are only an upper limit.

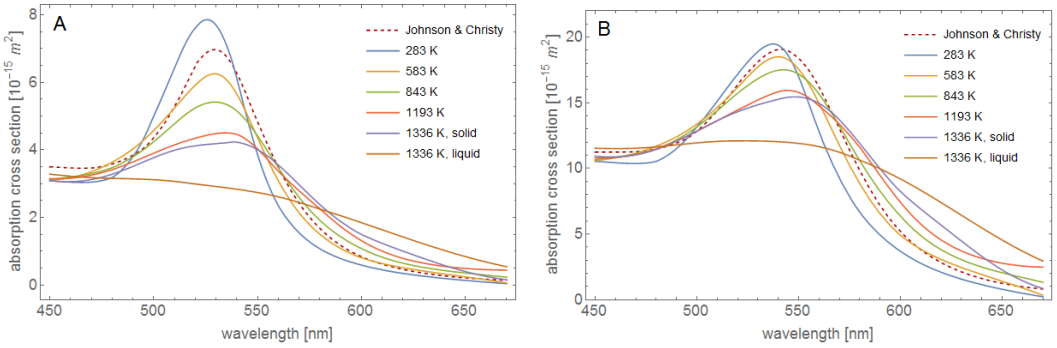

Figure 6.4: Temperature dependent absorption spectra of (A) 50 nm and (B) 80 nm sized gold nanoparticles. The refractive index of gold measured by Johnson and Christy [70] (dashed lines) and measured by Otter for gold at different temperatures [184] (solid lines) was used for the calculations.

The analytical model, which was used in this thesis for calculating temperature diffusion, does not consider temperature dependent change of absorption. However, the error can be estimated as follows. The temperature dependent refractive index, which is given for the specific temperatures 283 K, 583 K, 843 K, 1193 K and 1336 K (liquid gold) [183], was used to calculate absorption of the AuNP $\sigma_{abs}\,(T_p)$. Temporal temperature increase inside a nanoparticle was calculated based on this absorption, which was changed at the five time points when the specific temperatures were reached. Figure 6.5 shows the temperature time response of an 80 nm AuNP for constant refractive index (dashed line) and for temperature dependent refractive index (red line). The estimation shows a reduction of the peak AuNP temperature by around 25 %, when considering the temperature dependent refractive index of (bulk) gold during the heating. At radiant exposure around the bubble formation threshold of $34\,\mathrm{mJ\,cm^{-2}}$ was simulated. For increasing irradiation the difference will be even higher, because at higher heating rates particle

melting occurs earlier during the irradiation and a larger part of the pulse energy is absorbed by the liquid particle, which has the lowest absorption.

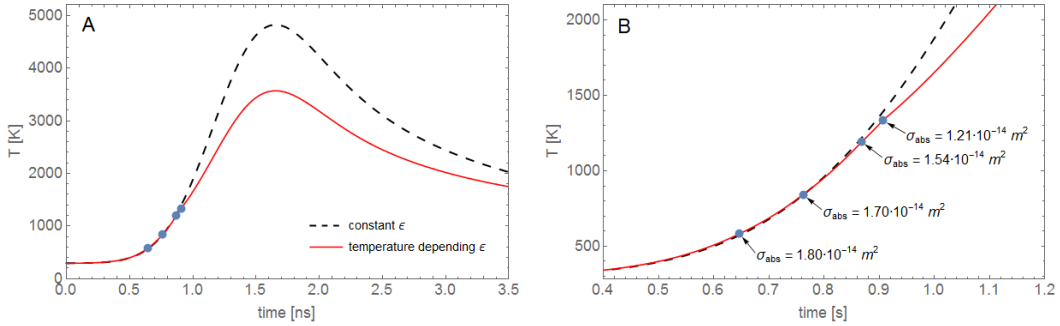

Figure 6.5: A) Temperature increase calculated for a constant absorption cross section of the irradiated AuNP (dashed) and for temperature dependent absorption cross section (red, solid). B) At specific temperature (blue dots, rrow markups) the change of absorption was considered in the temperature calculation. Irradiation of an 80 nm sized AuNP with 34 mJ cm^{-2} at 800 ps pulse duration was assumed.

6.3.2 Modeling temperature increase within and around gold nanoparticles

Besides neglecting the temperature dependence of the optical properties the thermal model itself contains simplifications, that effect the calculated temperature distribution in and around a nanoparticles upon irradiation. The temperature dependency of material properties such as the specific heat capacity as well as the thermal conductivity are neglected. However, this simplification allows to use an analytical solution of the differential equations for heat diffusion. Here, it is interesting to note, that up to 640 K the temperature dependence of the specific heat capacity of the gold nanoparticle and water have only minor impact on the temperature evolution in the nanoparticle and in the surrounding. In the equations the specific heat capacities appear in the ratio $k = \frac{4\pi R^3 \rho_l c_l}{m_p c_p}$, which remains approximately constant. Besides neglecting the temperature dependency of the material properties the thermal modeling has further limitations:

- Formation of vapor bubbles. In the case of water evaporation and bubble formation, heat conduction across the particle surface decreases. If a bubble with low density vapor is formed, the particle is nearly thermally isolated. For a pulse duration above bubble formation time the vapor layer strongly affects the energy deposition in the particle and the particle temperature. For a pulse duration below 10 ps, which is within the thermalization time of the AuNP lattice and at the beginning of heating the surrounding medium, the complete energy is deposed before the cavitation bubble can form. In this case the maximal peak temperature will be reached regardless of the bubble formation. Only the cooling is influenced by the thermal isolation due to the vapor layer. In contrast, for nanosecond pulse the temperature increase of the particle is determined by heat conduction.

- Melting. In case the particle lattice reaches the melting point, phase transition from solid to fluid will take place. The transition requires energy (latent heat of fusion), while temperature remains constant until the process of melting is completed for the whole particle. As a result of melting the thermal and optical properties vary. Rod shaped nanoparticles also change to a more spherical shape due to the surface tension of melted gold and the LSPR absorption shifts to shorter wavelength or even vanishes.

- Evaporation. In case the particle lattice reaches the boiling point, phase transition from liquid gold to vapor will take place. Evaporation requires latent heat and temperature of the liquid gold drop remains constant until the process is completed. After vaporization some material can condensate in the surrounding, while the size of the nanoparticle reduced and the optical properties change [185].

Due to these dynamic physical processes, the temperature distribution in and around the particles can only be calculated with the described model for the water temperature increase on the particle surface below 300 K, where melting and bubble formation does not occur. Calculations for higher temperatures require dynamical adaptations of the optical and thermal parameters, which was impossible in this work.

6.3.3 Latent heat and change of optical properties

Latent heat and change of optical properties leads to reduced peak temperature increase Figure 6.6 shows the impact of latent heat and of a changing refractive index on the evolution of temperature and energy density inside a nanoparticle. Three phases are identified. In the first phase, the temperature increase is calculated for constant refractive index of the nanoparticle and the surrounding water. In the next phase, when the water on the AuNP surface has reached spinodal temperature already during the incident laser pulse, heat diffusion across the particle water interface provides latent heat of evaporation. At the same time melting can occur, if the nanoparticle temperature increased above 800 K [89] and further absorbed energy provides latent heat of melting. During solid-liquid phase change the particle temperature is constant. After complete melting temperature increases again while particle and water density remain constant. At this isochoric condition nanoparticle and surrounding water are overheated until cavitation expands and a cavity of low density vapor forms rapidly.

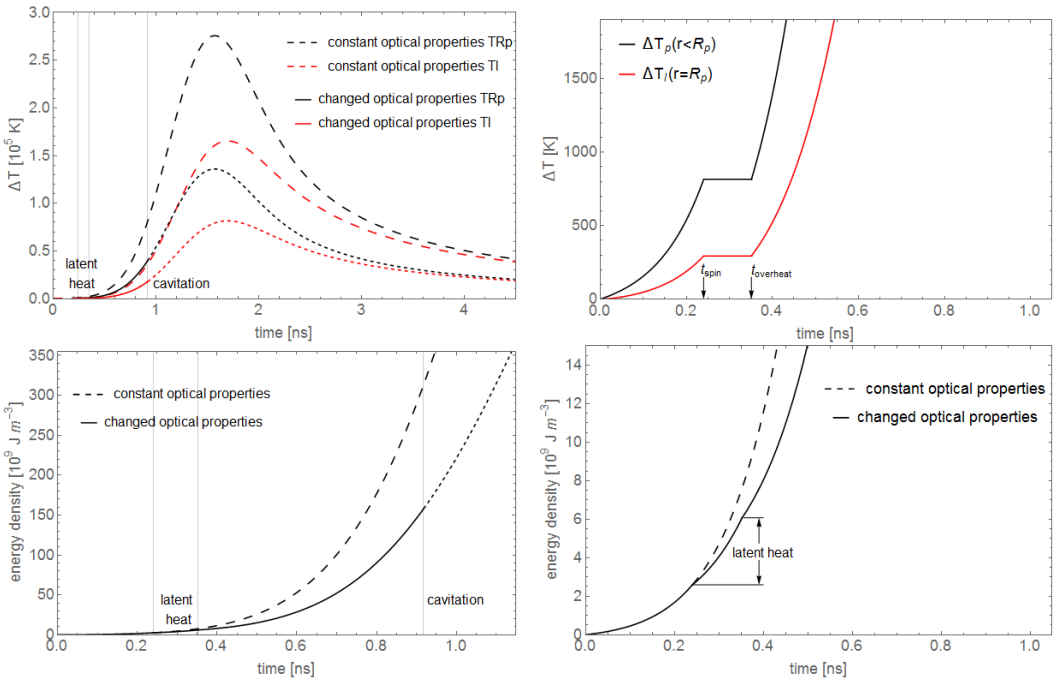

Figure 6.6: (A) Calculated temperature increase inside (black) a 50 nm AuNP and in the water on the particle surface (red). (B) Calculated energy density inside a 50 nm AuNP. For $0 < t < t_{spin}$ heating of the AuNP and heat diffusion into surrounding, the refractive index of water n=1.333 and the refractive index of the AuNP[70] were constant. For $t_{spin} < t < t_{overheat}$ phase changes consume latent heat of melting (AuNP) and evaporation (water), the refractive index of water n_{water}=1.17 [186] and n_p for solid gold at 1063°C [183] were used in the calculations. For $t_{overheat} < t < t_{vap}$ AuNP and water were overheated, the refractive index of water n_{water}=1.17 [186] and n_p for liquid gold at 1063°C [183] were used in the calculations. The calculations correspond to a conducted experiment with 800 ps pulsed irradiation with radiant exposure of 1804 mJ cm^{-2}.

In conclusion, short pulsed laser irradiation outside the thermal confinement leads to complex mechanism of bubble formation and expansion around gold nanoparticle. The spatio-temporal temperature increase and bubble dynamics are described by nonlinear differential equations, which can be solved only with the help of extensive models and experiments. A full numer-

ical description followed by bubble formation, has not been reported so far. For instance, pulsed laser induced heating and evaporation of gold nanoparticles was numerically analyzed by applying a two-temperature model [187] including temperature dependent changes in physical properties, while bubble formation was neglected considering AuNP in water under high pressures [185].

In this thesis, backscattered light detection revealed the bubble dynamics on single AuNPs in one-shot experiments. A solution of the modified Rayleigh-Plesset equation was fitted to the measured bubble wall motion. This solution is based on the initial bubble radius and pressure obtained from spatio-temporal temperature calculations. It was assumed that the entire energy consumed by bubble formation and expansion was deposited in the water by thermal diffusion from the particle. Ballistic heat transfer, which occurs during early phase of bubble growth [182], was neglected.

Under isochoric condition, both, the particle and the surrounding water can reach high temperature accompanied by high pressure. Bubble expansion from the initial radius of a few 10 nm to the measured diameter of a few µm requires a pressure in the 10^{10} Pa range within the thin water layer on the particle surface. This extraordinary high pressure goes along with high temperatures of the water and the particle. Provided, that the pulsed laser irradiation induced a nanoparticle temperature of 3000 K the lattice pressure can rise to almost 20 GPa [188]. Therefore, also the AuNP should evaporate rapidly and contribute to the bubble formation. However, the time point of evaporation of the gold nanoparticle and thus the contribution of gold vapor pressure to the water vapor bubble expansion could not be determined from experiments.

6.4 Bubble formation temperature and mechanism

At bubble formation threshold the temperature increase within a thin layer on the AuNP surface is much higher than expected. As an example, for an 80 nm AuNP the temperature model predicts to reach the critical temperature on the nanoparticle surface ($T_l(r = R_p) = 647\,K$) under irradiation with a 800 ps pulse of around 4.2 mJ cm^{-2}, while in corresponding experiments an eight-fold threshold of bubble detection around 34 mJ cm^{-2} was found. For 50 nm AuNP the discrepancy is even stronger. The model predicts, that the surface reaches critical temperature when irradiated with 3.9 mJ cm^{-2}, while in corresponding experiments a threshold of bubble detection around 132 mJ cm^{-2} was found, which is 34 time higher.

Bubble formation is expected to take place at the spinodal temperature. An explosive evaporation followed by bubble expansion can only occur, if the liquid layer around the nanoparticle with finite thickness is heated above the spinodal temperature and overcomes the inertia of mass of the surrounding liquid. Thus, for higher irradiation also overcritical heating of the liquid within the thin layer surrounding the AuNP occurs, while the locus of spinodal temperature travels a distance from the AuNP surface. Merabia et al. calculated spinodal temperature at a distance between 1 nm and 2 nm from the surface of a 10 nm sized AuNP, when bubble formation occurred in their simulations [110]. These bubbles showed oscillation times between 200 ps and 450 ps and the corresponding maximum bubble radius ranged between 12 nm and 15 nm.

Calculation of the radial temperature distribution with the Equations 2.42 to 2.44 shows, that the spinodal point will be reached at 1.6 nm distance from the surface of a 50 nm AuNP irradiated with an 800 ps pulse and radiant exposure of 3.87 mJ cm^{-2} (Figure 6.7 A). For an 80 nm AuNP the spinodal temperature will be reached at a distance of 1.9 nm from the surface when irradiated with 4.16 mJ cm^{-2} (Figure 6.7 B). At the same time the water on the particle surface reaches the critical temperature. Considering isochoric energy deposition in the nanoparticle and in the liquid shell the mean pressure will rise and cause expansion of a nanobubble, which reaches a diameter of 185 nm for 50 nm particles and 340 nm for 80 nm AuNP. Corresponding bubble wall velocity and radius curves are shown in Figure 6.8. Figures 6.9 and 6.10 show corresponding calculations for both particle sizes under 4 ns pulsed irradiation. For these calculations the Rayleigh-Plesset equation was solved with the locus of the spinodal temperature being the initial bubble radius R_0, while initial pressure was determined by Equation 5.11 from the average temperature between the particle surface and the spinodal point. Details of calculating initial conditions and the bubble radius are given in Chapter 5.4.4.

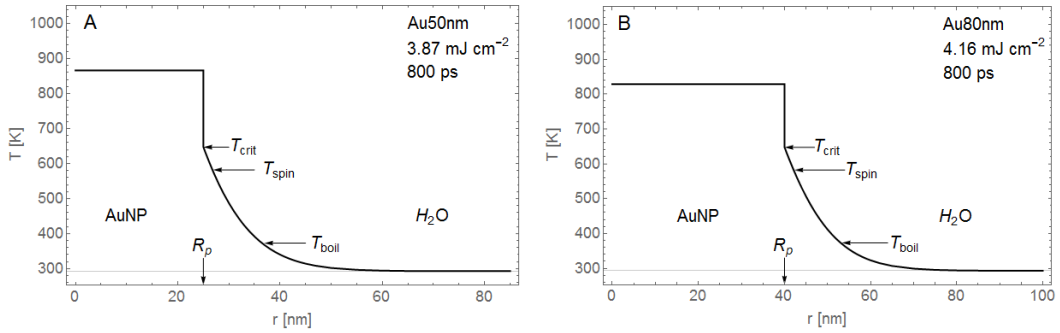

Figure 6.7: Maximum temperature at distance r to the particle center. The temperature on the surface of (A) 50 nm AuNP irradiated with 3.87 mJ cm^{-2} and (B) 80 nm AuNP irradiated with 4.16 mJ cm^{-2} reaches the critical point. Spinodal temperature is reached at a distance of 1.6 nm (A) and 1.9 nm (B)

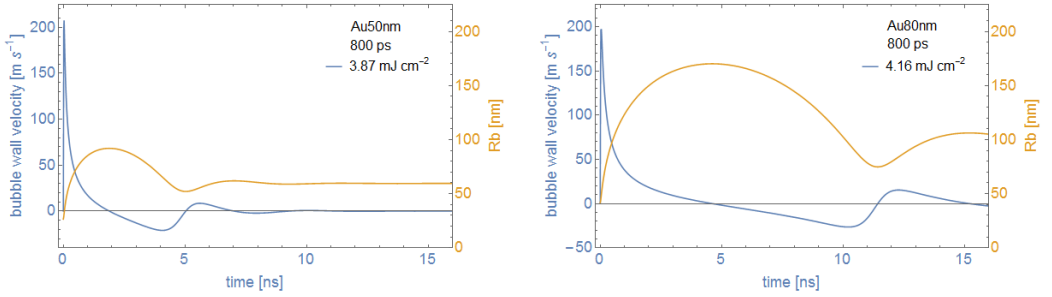

Figure 6.8: Bubble radius and bubble wall velocity around 50 nm and 80 nm sized AuNP under 800 ps pulsed irradiation with radiant exposure of 3.87 mJ cm^{-2} and 4.16 mJ cm^{-2}, respectively. Calculations of the bubble around the 50 nm AuNP are based on the RP-model for $R_0 = 26.6$ nm and $p_0 = 0.608$ GPa considering the conditions obtained at 1.695 ns after irradiation pulse onset corresponding to the time point of maximum nanoparticle temperature. Calculations of the bubble around the 80 nm AuNP are based on the RP-model for $R_0 = 41.9$ nm and $p_0 = 0.611$ GPa considering the conditions obtained at 1.81 ns after irradiation pulse onset.

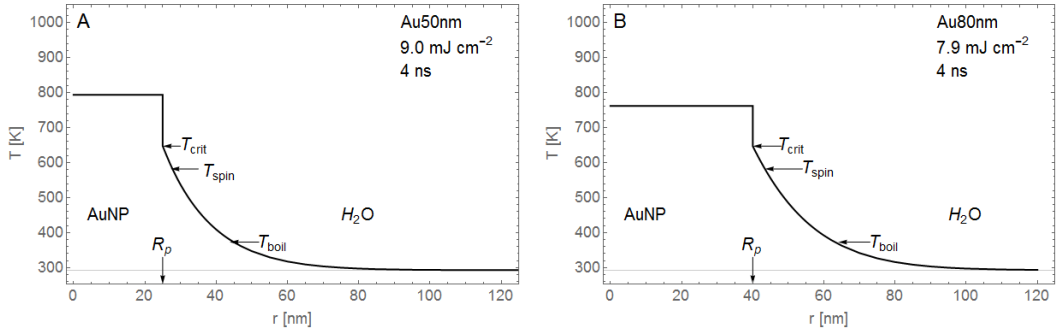

Figure 6.9: Maximum temperature at distance r to the particle center. The temperature on the surface of (A) 80 nm AuNP irradiated with 9.0 mJ cm^{-2} and (B) 80 nm AuNP irradiated with 7.9 mJ cm^{-2} reaches the critical point. Spinodal temperature is reached at a distance of 2.6 nm (A) and 3.2 nm (B)

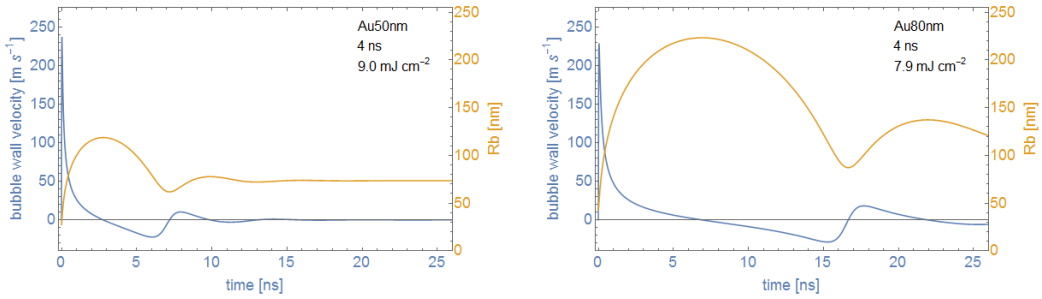

Figure 6.10: Bubble radius and bubble wall velocity around 50 nm and 80 nm sized AuNP under 4 ns pulsed irradiation with radiant exposure of 9.0 mJ cm^{-2} and 7.9 mJ cm^{-2}, respectively. Calculations of the bubble around the 50 nm AuNP are based on the RP-model for $R_0 = 27.6$ nm and $p_0 = 0.601$ GPa considering the conditions obtained at 7.43 ns after irradiation pulse onset corresponding to the time point of maximum nanoparticle temperature. Calculations of the bubble around the 80 nm AuNP are based on the RP-model for $R_0 = 43.2$ nm and $p_0 = 0.605$ GPa considering the conditions obtained at 7.83 ns after irradiation pulse onset.

Calculations of the bubble dynamics with the RP-model show the full oscillation of a spherical bubble. After oscillations a residual bubble remains, which exhibits larger diameter than the initial radius since condensation of water vapor is not accounted for. Hemispheric bubbles form on a rigid surface, for which the validity of the RP-model expansion phase of the bubble was assumed. Measured expansions of both, small bubbles (cf. Figure 5.54) and larger bubbles (cf. Figure 5.55) are represented well by calculated bubble wall velocity and radius time curves. Images of cavitation bubble formation on a rigid surface, which show growth of a bubble exhibiting hemispherical shape (cf. Figure 5.34 A, 5.35 A and Figure 5.37), corroborate this assumption.

However, the RP-model cannot describe the collapse phase and a possible rebound of the bubble wall due to the non-spherical collapse. This was found by imaging bubbles on a glass slide during the collapse (cf. Figure 5.35 D - F), and by comparing the backscattered light signals with the Rayleigh-Plesset model calculations. Measured curves are asymmetric with shorter collapse than expansions phases, while the solution of the Rayleigh-Plesset equation gives a symmetric evolution of the bubble oscillation.

Bubble nucleation occurs in the medium, whereas the increasing pressure within the superheated layer on the AuNP drives the nanobubble. Experimental results in studies by Plech et al. [66, 67, 68] allow a similar interpretation. They showed, that bubble formation corresponds quite well with the calculated fluence required to increase the water temperature on the AuNP surface above the spinodal point.

6.5 Conclusions for the applications of cell elimination

6.5.1 Transfer of laser pulse energy to bubble expansion

When a cavitation bubble forms after irradiating gold nanoparticles with short laser pulses, optical energy is transferred to mechanical energy. In the following discussion the ratio of these energies will be referred to as energy transfer efficiency. The calculations underlie limitations (cf. Chapter 6.3), which lead to overestimation of energy deposition in the particle and the surrounding water. Thus, the estimated values should be considered as upper limit of the efficiency. In total, the laser pulse energy will be transferred only partially to the mechanical bubble energy.

The efficiency of conversion from the laser pulse energy to the mechanical energy of the bubble wall gradually increased with irradiation. The mechanical bubble energy can be estimated by the energy required for the work to expand the initial bubble volume to the maximum expansion, given by Equation 2.66. However, the equation requires a modification due to the experimental condition given by the immobilization of the AuNP on a rigid glass surface, which leads to hemispherical bubble expansion (Figure 6.11 II). A spherical shape was assumed

for the calculation of the temperature distribution, which is the basis for the calculation of the bubble formation around the nanoparticle (Figure 6.11 I). The supporting glass substrate causes negligible alteration in the spherical symmetry of heat diffusion [170].

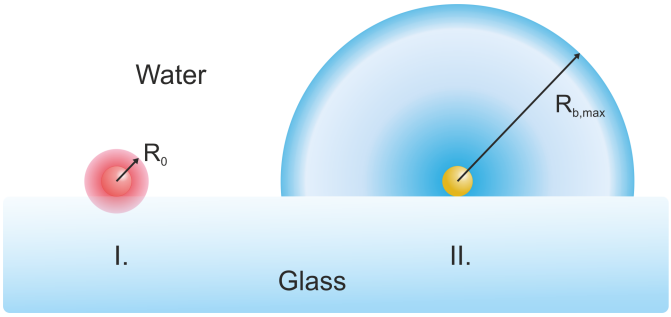

Figure 6.11: Sketch of a bubble at formation with initial radius R_0 (I.) and expanded to $R_{b,max}$ (II.). Calculation of the bubble energy was based on formation of an initial bubble with spherical shape containing high density vapor at high temperature and pressure. During expansion the bubble approaches hemispherical shape, while vapor density and temperature strongly decrease.

Neglecting surface tension and viscosity of the surrounding medium as well as deformation of the rigid surface, potential bubble energy at maximum hemispherical expansion can be estimated by

$$E_{b,h} = \frac{1}{2}\left(V_{b,max} - V_p\right) \cdot \Delta p = \frac{2}{3}\pi R_{b,max}^3 \left(p_\infty - p_v\right). \tag{6.1}$$

Bubble radius and thus the bubble energy increased with irradiation (Figure 6.12). Considering a constant evaporation time point as obtained in calculations for irradiation above 0.2 J cm^{-2} at given pulse duration and AuNP size (cf. Figure 5.57), increasing irradiation will cause higher temperature in the particle and surrounding water. Thus, the accompanying higher pressure drives the formed bubble to larger maximum expansion radius.

In general, non-linear increase of kinetic bubble energy $E_{b,h}$ (Equation 6.1) was found with the increase of the absorption cross section corrected laser pulse energy $\sigma_{abs} \cdot H$ (Figure 6.12). Under 800 ps pulsed irradiation with radiant exposure between 0.2 mJ cm^{-2} and 5 J cm^{-2} the transfer efficiency given by $E_{b,h}/\left(\sigma_{abs} \cdot H\right)$ ranged between 0.4 and 7 %. Under 4 ns pulses with radiant exposure up to 10 J cm^{-2} the transfer efficiency was even lower than 2 %.

For comparison, Neumann et al. found on experiments with 500 nm sized AuNP under 12 ns pulsed irradiation a much lower efficiency, which increased linearly to 0.4% for irradiation with radiant exposure up to 800 mJ cm^{-2}. The lower efficiency was caused by the larger AuNP size. Heat diffusion across the particle boundary scales with the surface size and the lower heating rates of 10^{10} K s^{-1} for pulses with 12 ns duration cannot compensate for the heat loss. In comparison the heating rates achieved with 800 ps and 4 ns pulses ranged between 10^{11} and 10^{15} K s^{-1}.

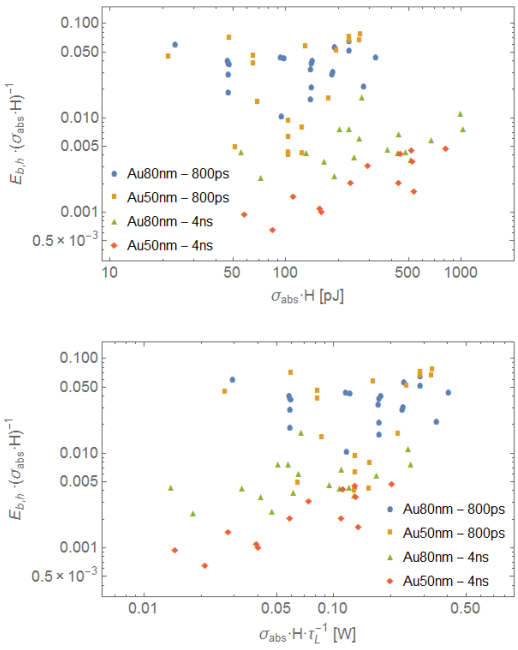

Figure 6.12: Transfer from maximum absorbable energy, given by $\sigma_{abs} \cdot H$, to mechanical bubble energy $E_{b,h}$ depends on the particle size and irradiation parameters.

Transition of energy from irradiation with radiant exposure up to 10 J cm^{-2}finally to the maximum bubble expansion underlies several limitations that lead to an overall efficiency ranging between 0.05 % and 7 %. Most of the supplied laser pulse energy, which was absorbed and generated thermal energy within a particle, is dissipated into the surrounding by thermal diffusion.With increasing particle and water temperature less energy is absorbed due to the decreasing optical absorption cross section. Further energy in the form of latent heat of vaporization is consumed during liquid-vapor phase transition of the water. The solid-liquid phase change of the particle, which is assumed to accompany the bubble formation also consumes energy. Thus, phase changes of the particle and of the water reduce the energy available to bubble expansion. The liquid-vapor phase change of the nanoparticle, which occurs at further increased temperature, could contribute to the pressure of the expanding vapor bubble. However, this has been proposed [59], but not verified and reported so far.

6.5.2 Possible impact on cell elimination and molecular release

The high efficiency by short pulsed laser irradiated AuNP to eliminate and manipulate cells was shown by various groups [4, 5, 15, 9, 154, 137]. However, there are controversial discussions about the mechanism that affects the integrity of cell compartments or the cell membrane. Main parameters which influence the effect on cells are AuNP size, radiant exposure and pulse duration. Also the issue of acting as single particles or as clusters is discussed [153, 154]. Though, dependency of cell elimination on the bubble size or bubble energy were not reported.

In this thesis, an optical setup was used, which allows the detection of single nanoparticles immobilized on surfaces and measurement of cavitation bubble motion over time during a single laser pulse. Particle detection and spectrally resolved measurement of light scattered by the particles had the lower limit of a particle diameter of around 50 nm. In order to detect smaller particles, longer image acquisition times are required due to the decrease of scattering with the particle diameter. Further, the sample preparation must have a higher degree of cleanliness, because light scattered at nano- and microscale objects adds noise to the detected spectral signal and prevents the identification of particles and their size measurement. Higher cleanliness could not be technically provided in this work.

Thus, cell elimination by pulsed laser irradiated 30 nm AuNP (cf. Chapter 3) is discussed based on the modeling, which was developed on the findings obtained in bubble measurements around single 50 nm and 80 nm particles.

No impact on cell elimination at bubble formation threshold on 30 nm AuNP

In general, increasing bubble formation threshold is expected for decreasing particle diameter (cf. Chapter 5.4.5). For irradiation of 30 nm AuNPs with 4 ns pulses a radiant exposure of around 20 mJ cm^{-2} is required in order to overheat a 2 nm layer around the particle, which participates in bubble formation. Figure 6.13 shows the calculated maximum radial temperature and corresponding bubble dynamics.

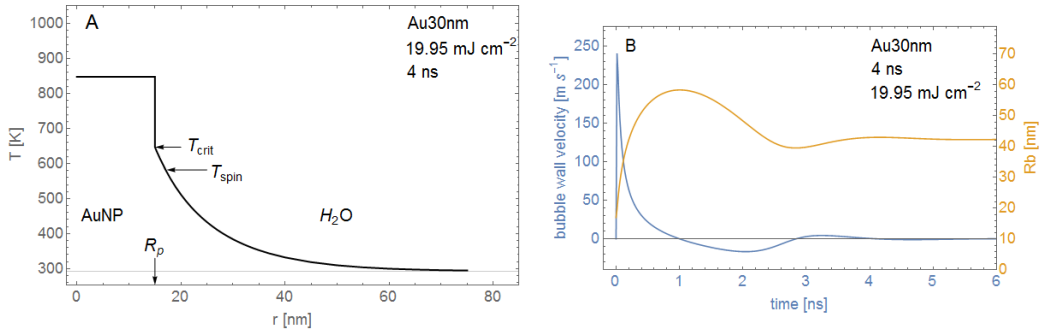

Figure 6.13: (A) Maximum temperature at distance r to the particle center. The temperature on the surface of a 30 nm AuNP irradiated with 19.95 mJ cm^{-2} reaches the critical point. Spinodal temperature is reached at a distance of 2 nm. (B) Calculations of the bubble velocity and radius is based on the RP-model for $R_0 = 17$ nm and $p_0 = 0.596$ GPa. The considered conditions at 7.07 ns after irradiation pulse onset correspond to the time point of maximum nanoparticle temperature.

However, irradiation of cells incubated with 30 nm AuNP conjugates with radiant exposure at the theoretical threshold showed only minor elimination rates, while for irradiation tenfold above threshold was needed to eliminate the cells (cf. Chapter 3.4 Figure 3.8 and Figure 3.10).

Cell damage by laser irradiated nanoparticles

Specific elimination of KARPAS-299 cells with above 95 % efficiency was shown for conjugates with 30 nm AuNP under 4 ns pulsed irradiation. Biocompatibility of the conjugates was shown with non-irradiated cell samples incubated with antibody-functionalized AuNPs, which exhibited a cell viability similar to untreated cell samples. Effective elimination of cells incubated with concentrations between 10^4 and $6{\cdot}10^4$ AuNP conjugates per cell was shown for single pulse irradiation with radiant exposure up to 1 J cm^{-2} (Figure 3.8). However, the results do not show whether the elimination relies on single bubble effects generated on single particles, on single bubbles around neighboring nanoparticles merging to larger bubbles or on formation of larger bubbles around clusters of particles. The observed strong dependency of the elimination on the AuNP conjugate concentration used for incubation favors the latter two.

For cells incubated with 60.000 AuNP conjugates per cell an elimination up to 45 % was found after irradiation with a single pulse of 70 mJ cm^{-2} (cf. 3.8). A cell elimination above 95 % was observed for irradiation with radiant exposure of 870 J cm^{-2}. For incubation with a lower AuNP conjugate concentration (10^4, $2{\cdot}10^4$, $4{\cdot}10^4$ per cell) the elimination rate decreased for the same irradiation.

Approximately 5 % of the antibody labeled AuNP bind to the targeted protein on the cell membranes [189]. Physical and biological reasons for this small yield of bound particles could not be determined. One cause is probably how the antibodies were bound to the nanoparticle surface and the resulting orientation of their binding site, which recognizes the membrane molecules. Incubation with $6{\cdot}10^4$ AuNP conjugates per cell gives up to 3000 specifically bound AuNP. Thus, for homogeneous distribution over the membrane of KARPAS-299 cells with a diameter of around 10 µm the distance between neighboring particles is around 320 nm.

For 50 nm AuNP under 4 ns pulsed irradiation with radiant exposure around 1000 mJ cm^{-2} the measured bubble size was in the range of few hundred nanometers. It is reasonable to assume

that under same irradiation conditions even smaller bubble sizes will be generated around 30 nm AuNP. Though, the bubble size is smaller than the inter particle distance, irradiation with 70 mJ cm^{-2} led to cell elimination between 18 % (10^4 AuNP conjugates per cell) and 45 % ($6{\cdot}10^4$ AuNP conjugates per cell). Thus, small bubbles can cause significant cell elimination, if enough particles are bound to the membrane.

Single vapor bubbles generated around neighboring nanoparticles can merge to larger bubbles that exhibit stronger impact on cell membrane integrity. Overlapping of bubbles around AuNP bound to cell membranes was shown to increase elimination efficiency [153]. Also the efficient elimination of KARPAS-299 cell could be achieved due to merged bubbles.

Further increase of the cell elimination efficiency was shown for nanoparticle clusters that formed on the surface [153] and inside the cytoplasm [154] of targeted cells. Nanoparticle clusters exhibit larger absorption cross sections than each single one of the contained particles. Irradiation with pulses of duration above thermal confinement causes mutual heating of the nanoparticles in the cluster. Thus, in comparison to single nanoparticles larger bubbles can form around clusters due to a higher temperature increase accompanied by higher pressure. For instance, Lapotko et al. found, that inside cells small bubbles with life-times of around 60-70 ns do not cause cell elimination. Formation of nanoparticle clusters lead to lower bubble formation threshold [154].

Cell experiments in this thesis (Chapter 3) showed, that optimal elimination parameters depend on cell type (adherent or suspension cells) and the targeted cell membrane protein. Also for adherent cells a gradual increase of the cell elimination with increasing radiant exposure was found and a maximum efficiency of approximately 70% was achieved. In comparison to the suspension cells incubation with a 5-fold conjugate concentration of 10^6 per targeted OVCAR-3 cell was required. However, as long as no precise information about the location of the gold particles are available, only speculation can be made to explain the higher elimination rates achieved on the KARPAS-299 cells. Reasons could be for example the higher concentration of the targeted receptor on KARPAS-299 and their location in the cell membrane. Further, unspecific endocytotic and also a receptor-mediated uptake via EGFR binding [33] can lead to accumulation of conjugates inside OVCAR-3 cells, which could cause the lower elimination efficiency.

Laser induced molecular release from nanoparticles

Besides cell elimination, nanoparticles also have the potential to selectively modify cell function. Damage and modification at molecular level could be generated by heating of the surrounding of an AuNP [8, 25] or by release of molecules from the particle surface [190, 50]. Impact of cavitation bubbles around AuNP on molecules immobilized on the surface of the particles have been proposed [14]. However, cavitation as responsible mechanism of molecular release has not been reported so far.

It has been shown, that the binding energy of a thiol bond between a Gold nanoparticle and a RNA molecule is around 0.1 eV hence temperatures in excess to 890 °C ($k_b \cdot T = 0.1\,eV$) are required to thermally break this bond [145]. Because melting of the particle occurs at this temperature, non-equilibrium charge transfer of hot carriers from the metal was also proposed as a mechanism to induce bond breakage. Femtosecond laser pulses generate these hot carriers in the nanoparticle lattice, however, under nanosecond pulsed irradiation electrons and atoms of the particle lattice exhibit the same temperature.

The onset of siRNA release from 30 nm AuNP conjugates (16 mJ cm^{-2}, cf. Chapter 4.3.3) correlates with the radiant exposure required for temperature increase to spinodal point on the AuNP surface under ns-pulsed irradiation and thus with possible cavitation bubble onset. The mechanical energy of a bubble with few 10 nm size exceeds the binding energy of the thiol bond many fold, yet the mechanism contributing to release the siRNA molecules is unclear.

In conclusion, the analysis of the experimental data shows, that cavitation bubble formation around gold nanoparticles is involved in the elimination of cells and the release of biomolecules from the particle surface. In contrast to the short pulsed laser irradiation with durations shorter than thermal confinement the physical mechanisms are not yet well understood. In particular, description of the mechanical impact on the cells, which leads to the cell elimination, requires experimental data, which could be obtained by measuring the cavitation bubbles around single

particles located on the cell membrane. This thesis established a microscopic setup, which allows the time-resolved measurement of these bubbles and provided basic knowledge of signal analysis.

7 Summary

This work covers basic biological experiments on cell elimination and molecular release with gold nanoparticles and links to the temperature increase and bubble formation around the particles. To investigate the physical effects and in particular the mechanism of bubble formation, experiments were carried out with single immobilized gold nanoparticles.

Nanoparticle assisted laser inactivation (NALI) is used to purify cell cultures by targeting cells with functionalized AuNPs and short pulsed irradiation with laser wavelength around the nanoparticle peak absorption. Specific functionalization with antibodies provides selectivity, while elimination efficiency depends on the pulse duration and radiant exposure. Using nanosecond laser pulses showed different efficiency for KARPAS-299 cells growing in suspension and adherent OVCAR-3 cells. Spherical AuNP with 30 nm diameter were directly conjugated to IgG monoclonal antibodies targeting the CD30 membrane protein of human KARPAS-299 cells. With 4 ns pulses at 532 nm an elimination efficiency of 99 % was achieved for irradiation with 870 mJ cm^{-2}. With increasing concentrations of antibody-AuNP conjugates the elimination efficiency increased. However, when reaching certain higher concentration also non-specific elimination occurred, which was measured on KARPAS-422 cells in co-culture with the KARPAS-299 cells.

With adherently growing OVCAR-3 cells an elimination efficiency of only 70 % was reached by NALI, even though a 10-fold incubation concentration was used.

Utilizing rod-shaped nanoparticles for NALI with different irradiation wavelengths led to unexpected results. Nanosecond pulsed irradiation at the TSPR wavelength band with 532 nm showed stronger elimination efficiency than irradiation with laser wavelength around 800 nm, even though the LSPR band has a 10 times higher absorption at this wavelength. At both wavelenghts, 532 nm and 800 nm, an elimination efficacy of 99 % can be reached. However, irradiation with the 10-fold higher radiant exposure was required when utilizing the LSPR band at 800 nm. The LSPR band is sensitive to changes in the surrounding and bubble formation during the irradiation pulse reduced the energy absorption of the AuNR by changing the local index of refraction. This bleaching of plasmon resonance absorption strongly reduces possible energy deposition in the particle and thus reduces impact of the formed cavitation bubble on the cell membrane.

Besides cell elimination the molecular release from the nanoparticle surface as principle mechanism to manipulate cells was studied in this thesis. Therefore, conjugates of AuNP functionalized with coumarin dye labeled siRNA, which was covalently bound to nanoparticles, were irradiated with 4 ns pulses at 532 nm. After irradiation, release of siRNA was determined by measuring changes in absorption spectra as well as fluorescence spectra of the coumarin molecule. Due to thiol-bond breakage siRNA was released and measured fluorescence increased with the irradiation, while the AuNP absorption peak shifted to shorter wavelengths. However, for 15 nm and 30 nm AuNP conjugates maximum release of 20 % and 30 % was measured after irradiation with 80 mJ cm^{-2} and 32 mJ cm^{-2}, respectively. Temperature calculations showed that already irradiation at lower radiant exposure leads to melting of the irradiated particle, while the surrounding water reaches temperatures above the spinodal point. Thus, bubble formation around the AuNP conjugates possibly occurred, though siRNA release by the bubble formation could not be directly monitored.

For both, cell elimination and siRNA release, temperature calculations were correlated with and supported the hypothesis of cavitation bubble formation being involved. A bubble formed by explosive evaporation of water near the particle surface is expected to have a strong impact on the cell membrane or a cell compartment. Knowing the extend of damage as a function of the irradiation parameters is an important factor for optimizing the processes for cell depletion and nanoparticle mediated cell manipulation. The question what are the mechanisms of the cell elimination by pulsed laser irradiated AuNP and how the elimination can be optimized motivated investigation of physical effects around single AuNP.

Bubble measurement around laser irradiated gold nanoparticles

To investigate the physical effects darkfield detection and spectral measurement of scattered light from immobilized single AuNP was combined with time resolved scattered light measure-

ment. Bubble formation after short pulsed (800 ps and 4 ns) irradiation was detected with a continuous laser confocal coupled into the microscope co-linear with the irradiation laser beam. Backscattered light detection gives a direct measure of the bubble wall motion and the bubble extension time. Interference in the backscattered light detection by reflections at the bubble wall is used for the first time to characterize bubble formation around gold nanoparticles.

For irradiation at the detection limit backscattered light signals did not show the interference related modulation and bubble size was estimated with help of the measured bubble oscillation time. As shown by the measurements the lower bubble detection limit ranged around 100 nm radius: The shortest expansion time measured at bubbles around AuNP with 80 nm and 50 nm diameter immobilized on a glass surface under irradiation with a pulse duration of 800 ps were 10 ns and 16 ns, respectively. The corresponding maximum bubble radii were around 110 nm and 175 nm. For 4 ns laser pulses expansion times were not shorter than 23 ns, which correspond to a maximum bubble radius of 250 nm.

For irradiation above the detection threshold the bubble wall velocity was directly measured by the backscattered light detection, which was then modeled by solving the Rayleigh-Plesset equation. The starting conditions of initial bubble radius and pressure, were adjusted in order achieve the best fit between the solution of the Rayleigh-Plesset equation and the measured velocity. This also allowed to determine the bubble radius over time. For irradiation with 800 ps pulses and radiant exposure of around 1.8 J cm^{-2} a bubble with 3.75 µm radius formed around an 80 nm AuNP, while a 4 ns laser pulse with the same radiant exposure caused maximum expansion of around 1.35 µm. Maximum bubble radius increased non-linearly up to 3.75 µm for 800 ps pulses and up to 3 µm for 4 ns pulses at radiant exposures up to 10 J cm^{-2}.

Cell elimination by laser irradiated nanoparticles

Generation of pure starting material, for instance pure cell populations is a prerequisite for many investigations using molecular cell analysis techniques such as DNA sequencing or microarray analysis. Also for certain cell therapies such as the of autologous hematopoietic stem cells purification of healthy cells is required prior to transplantation. In particular for this biomedical application high purity of healthy cells is very important, because already a few hundred cells, which were not efficiently eliminated, may lead to recurrence of a tumor disease.

In this thesis it was shown, that elimination of cells by pulsed laser irradiated nanoparticles is very efficient. However, irradiation with 4 ns pulses at the expected bubble formation threshold of 20 mJ cm^{-2} was insufficient for cell elimination with 30 nm AuNP. A tenfold threshold irradiation was needed to achieve an elimination efficiency of more than 50 % and a 30fold threshold irradiation to reach 90 % cell elimination. Thus, the physical mechanism leading to the elimination or manipulation of the cells could not be directly identified.

In order to correlate the experimental results of the measurements on individual 50 nm and 80 nm particles with effects on biological structures, cell elimination experiments should also be carried out with particles of this size. Comparison with the cell elimination efficiency of irradiated 30 nm AuNP should then allow optimizing irradiation range and particle size to achieve sufficient cell culture purification.

However, optical resolution, and spectral sensitivity, did not provide the detection of AuNPs with 30 nm diameters. Further, the backscattered light detection has not yet approached the required sensitivity to detect bubble formation threshold, nevertheless, experiment and calculation suggest, the reaching of the critical point of water is the starting point of the generation of nanobubbles. Biological effects like cell elimination or molecular release need considerably higher temperatures to drive bubbles with sufficient maximum diameters.

Modeling of bubble formation and expansion as well as the calculation of the spatio-temporal temperature increase demonstrate the involvement of more complex mechanisms as could be included in the analytical calculation.

Finally, this work demonstrates a setup and new experimental strategy, to generate experimental data for the development and verification of more detailed modeling of bubble formation around AuNP. Future experiments should aim in particular for clarification of the coupling of the laser pulse energy via the nanoparticle into the bubble. Thus, the sensitivity of backscattered light detection should be increased in order to detect bubbles close to the formation limit.

For instance using a larger numerical aperture for the light detection and a more sensitive photodetector should improve the signal to noise ratio to detect signals from smaller bubbles.

The developed experimental techniques provide the foundations of further investigation on the bubble formation around nanoparticles immobilized on cell membranes. These future studies should contribute to understanding the biological effect of nanocavitation.

References

[1] A. Vogel and V. Venugopalan. Mechanisms of pulsed laser ablation of biological tissues. *Chem Rev*, 103(2):577–644, 2003.

[2] R. Anderson and J. Parrish. Selective photothermolysis: precise microsurgery by selective absorption of pulsed radiation. *Science*, 220(4596):524–527, Apr 1983.

[3] G. Hüttmann and R. Birngruber. On the possibility of high-precision photothermal microeffects andthe measurement of fast thermal denaturation of proteins. *IEEE J Quantum Electron*, 5:954–962, 1999.

[4] G. Hüttmann, B. Radt, J. Serbin, B. I. Lange, and R. Birngruber. High precision cell surgery with nanoparticles. *Med Laser Appl*, 17:9–14, 2002.

[5] C. M. Pitsillides, E. K. Joe, X. Wei, R. R. Anderson, and C. P. Lin. Selective cell targeting with light-absorbing microparticles and nanoparticles. *Biophys J*, 84(6):4023–4032, 2003.

[6] J. Neumann and R. Brinkmann. Boiling nucleation on melanosomes and microbeads transiently heated by nanosecond and microsecond laser pulses. *Journal of biomedical optics*, 10(2):024001–02400112, 2005.

[7] J. Neumann and R. Brinkmann. Nucleation dynamics around single microabsorbers in water heated by nanosecond laser irradiation. *Journal of Applied Physics*, 101:114701, 2007.

[8] Benno Radt. *Inaktivierungvon Proteinen und Zellen durch Laserbestrahlung von Mikropartikeln*. PhD thesis, Ph. D. thesis, University Lu beck, 2002.

[9] Vladimir P. Zharov, Kelly E. Mercer, Elena N. Galitovskaya, and Mark S. Smeltzer. Photothermal nanotherapeutics and nanodiagnostics for selective killing of bacteria targeted with gold nanoparticles. *Biophysical Journal*, 90(2):619–627, Jan 2006.

[10] Cuiping Yao, Xiaochao Qu, Zhenxi Zhang, Gereon Hüttmann, and Ramtin Rahmanzadeh. Influence of laser parameters on nanoparticle-induced membrane permeabilization. *Journal of Biomedical Optics*, 14(5):054034, 2009.

[11] Lauren A Austin, Megan A Mackey, Erik C Dreaden, and Mostafa A El-Sayed. The optical, photothermal, and facile surface chemical properties of gold and silver nanoparticles in biodiagnostics, therapy, and drug delivery. *Archives of toxicology*, 88(7):1391–1417, 2014.

[12] Prashant K Jain, Xiaohua Huang, Ivan H El-Sayed, and Mostafa A El-Sayed. Noble metals on the nanoscale: optical and photothermal properties and some applications in imaging, sensing, biology, and medicine. *Accounts of chemical research*, 41(12):1578–1586, 2008.

[13] G Raschke, S Kowarik, T Franzl, C Sönnichsen, TA Klar, J Feldmann, A Nichtl, and K Kürzinger. Biomolecular recognition based on single gold nanoparticle light scattering. *Nano letters*, 3(7):935–938, 2003.

[14] Marco Bever. *Untersuchung zu den Mechanismen der Proteininaktivierung an laserbestrahlten Goldnanopartikeln*. PhD thesis, University of Lübeck, 2010.

[15] Jörg Neumann and Ralf Brinkmann. Cell disintegration by laser-induced transient microbubbles and its simultaneous monitoring by interferometry. *Journal of Biomedical Optics*, 11(4):041112, 2006.

[16] M Kitz, S Preisser, A Wetterwald, M Jaeger, GN Thalmann, and M Frenz. Vapor bubble generation around gold nano-particles and its application to damaging of cells. *Biomedical optics express*, 2(2):291–304, 2011.

[17] Sara Peeters, Michael Kitz, Stefan Preisser, Antoinette Wetterwald, Barbara Rothen-Rutishauser, George N. Thalmann, Christina Brandenberger, Arthur Bailey, and Martin Frenz. Mechanisms of nanoparticle-mediated photomechanical cell damage. *Biomed. Opt. Express*, 3(3):435, Feb 2012.

[18] Florian Rudnitzki, Marco Bever, Ramtin Rahmanzadeh, Katrin Brieger, Elmar Endl, Jürgen Groll, and Gereon Hüttmann. Bleaching of plasmon-resonance absorption of gold nanorods decreases efficiency of cell destruction. *Journal of biomedical optics*, 17(5):0580031–05800313, 2012.

[19] Florian Levold. *Nano-Photothermolyse: Eine effiziente Methode zur selektiven Elimination von Zellen in vitro mittels Laser aktivierter Nanogoldpartikel*. PhD thesis, Rheinische Friedrich-Wilhelms-Universität Bonn, 2010.

[20] Kiran Bhattacharyya, Benjamin S Goldschmidt, and John A Viator. Detection and capture of breast cancer cells with photoacoustic flow cytometry. *Journal of biomedical optics*, 21(8):087007, 2016.

[21] Dmitry A Nedosekin, Tariq Fahmi, Zeid A Nima, Jacqueline Nolan, Chengzhong Cai, Mustafa Sarimollaoglu, Enkeleda Dervishi, Alexei Basnakian, Alexandru S Biris, and Vladimir P Zharov. Photoacoustic flow cytometry for nanomaterial research. *Photoacoustics*, 6:16–25, 2017.

[22] Stefanie Terstegge, Franziska Winter, Barbara H. Rath, Iris Laufenberg, Claudia Schwarz, Anke Leinhaas, Florian Levold, Andreas Dolf, Simone Haupt, Philipp Koch, and et al. Laser-assisted photoablation of human pluripotent stem cells from differentiating cultures. *Stem Cell Reviews and Reports*, 6(2):260–269, Feb 2010.

[23] G. Hüttmann, J. Serbin, B. Radt, B. I. Lange, and R. Birngruber. Model system for investigating laser-induced subcellular microeffects. volume 4257, pages 398–409. SPIE, 2001.

[24] J. Neumann. *Mikroskopische Untersuchungen zur laserinduzierten Blasenbildung und -dynamik an absorbierenden Mikropartikeln*. Dissertation, Universität Lübeck, 2005.

[25] Ramtin Rahmanzadeh. *Untersuchungen zur Inaktivierung von Zellen und Proteinen mit Hilfe optischer Absorber*. PhD thesis, 2006.

[26] Ravi Shukla, Vipul Bansal, Minakshi Chaudhary, Atanu Basu, Ramesh R Bhonde, and Murali Sastry. Biocompatibility of gold nanoparticles and their endocytotic fate inside the cellular compartment: a microscopic overview. *Langmuir*, 21(23):10644–10654, 2005.

[27] David A. Giljohann, Dwight S. Seferos, Weston L. Daniel, Matthew D. Massich, Pinal C. Patel, and Chad A. Mirkin. Gold nanoparticles for biology and medicine. *Angewandte Chemie International Edition*, 49(19):3280–3294, Apr 2010.

[28] Weiwei Gao, Che-Ming J Hu, Ronnie H Fang, Brian T Luk, Jing Su, and Liangfang Zhang. Surface functionalization of gold nanoparticles with red blood cell membranes. *Advanced Materials*, 25(26):3549–3553, 2013.

[29] Carolina Vericat, Maria Elena Vela, Gastón Corthey, E Pensa, E Cortés, Mariano Hernan Fonticelli, F Ibanez, GE Benitez, P Carro, and Roberto Carlos Salvarezza. Self-assembled monolayers of thiolates on metals: a review article on sulfur-metal chemistry and surface structures. *RSC Advances*, 4(53):27730–27754, 2014.

[30] Cuiping Yao, Ramtin Rahmanzadeh, Elmar Endl, Zhenxi Zhang, Johannes Gerdes, and Gereon Hüttmann. Elevation of plasma membrane permeability by laser irradiation of selectively bound nanoparticles. *Journal of Biomedical Optics*, 10(6):064012, 2005.

[31] Dag Heinemann, Markus Schomaker, Stefan Kalies, MAximilian Schieck, Regina Carlson, Hugo Murua Escobar, Tammo Ripken, Heiko Meyer, and Alexander Heisterkamp. Gold nanoparticle mediated laser transfection for efficient sirna mediated gene knock down. *PLoS ONE*, 8(3), 2013.

[32] Markus Schomaker, Dag Heinemann, Stefan Kalies, Saskia Willenbrock, Siegfried Wagner, Ingo Nolte, Tammo Ripken, Hugo Murua Escobar, Heiko Meyer, and Alexander Heisterkamp. Characterization of nanoparticle mediated laser transfection by femtosecond laser pulses for applications in molecular medicine. *Journal of Nanobiotechnology*, 13(1):10, 2015.

[33] Cuiping Yao, Florian Rudnitzki, Gereon Hüttmann, Zhenxi Zhang, and Ramtin Rahmanzadeh. Important factors for cell-membrane permeabilization by gold nanoparticles activated by nanosecond-laser irradiation. *International Journal of Nanomedicine*, 2017:12:5659–5672, 2017.

[34] R Pepperkok, M Zaneti, R King, D Delia, W Ansorge, L Philipson, and C Schneider. Automatic microinjection system facilitates detection of growth inhibitory mrna. *Proceedings of the National Academy of Sciences of the United States of America*, 85:6748–6752, 1988.

[35] D J Stephens and R Pepperkok. The many ways to cross the plasma membrane. *PNAS*, 98(8):4295–4298, 2001.

[36] S D Patil, D G Rhodes, and D J Burgess. Dna-based therapeutics and dna delivery systems: A comprehensive review. *The AAPS Journal*, 7(1):61–77, 2005.

[37] Sijia Wang, Gereon Hüttmann, Thomas Scholzen, Zhenxi Zhang, Alfred Vogel, Tayyaba Hasan, and Ramtin Rahmanzadeh. A light-controlled switch after dual targeting of proliferating tumor cells via the membrane receptor egfr and the nuclear protein ki-67. *Scientific reports*, 6:27032, 2016.

[38] Eberhard Neumann, M Schaefer-Ridder, Y Wang, and PhH Hofschneider. Gene transfer into mouse lyoma cells by electroporation in high electric fields. *The EMBO journal*, 1(7):841–845, 1982.

[39] Tai-Kin Wong and Eberhard Neumann. Electric field mediated gene transfer. *Biochemical and biophysical research communications*, 107(2):584–587, 1982.

[40] Dan Luo and W Mark Saltzman. Synthetic dna delivery systems. *Nature biotechnology*, 18(1):33, 2000.

[41] Steven E Raper, Marc Yudkoff, Narendra Chirmule, Guang-Ping Gao, Fred Nunes, Ziv J Haskal, Emma E Furth, Kathleen J Propert, Michael B Robinson, Susan Magosin, et al. A pilot study of in vivo liver-directed gene transfer with an adenoviral vector in partial ornithine transcarbamylase deficiency. *Human gene therapy*, 13(1):163–175, 2002.

[42] Neeltje A Kootstra and Inder M Verma. Gene therapy with viral vectors. *Annual review of pharmacology and toxicology*, 43(1):413–439, 2003.

[43] Susie Eustis and Mostafa A El-Sayed. Why gold nanoparticles are more precious than pretty gold: noble metal surface plasmon resonance and its enhancement of the radiative and nonradiative properties of nanocrystals of different shapes. *Chemical society reviews*, 35(3):209–217, 2006.

[44] G. Mie. Beiträge zur optik trüber medien, speziell kolloidaler metallösungen. *Annalen der Physik*, 330:377–445, 1908.

[45] Paul Mulvaney. Surface plasmon spectroscopy of nanosized metal particles. *Langmuir*, 12(3):788–800, 1996.

[46] Jacob D. Gibson, Khanal Bishnu P., and Eugene R. Zubarev. Paclitaxel-functionalized gold nanoparticles. *Journal of the American Chemical Society*, 129:11653–11661, 2007.

[47] Nathaniel L. Rosi, David A. Giljohann, Shad Thaxton, Abigail K. R. Lytton-Jean, Min Su Han, and Chad A. Mirkin. Oligonucleotide-modified gold nanoparticles for intracellular gene regulation. *Science*, 312:1027–1030, 2006.

[48] L. Poon, W. Zandberg, D. Hsiao, Z. Erno, D. Sen, B. D. Gates, and N. R. Branda. Photothermal release of single-stranded dna from the surface of gold nanoparticles through controlled denaturating and au-s bond breaking. *ACS Nano*, 4(11):6395–6403, 2010.

[49] Adela C Bonoiu, Supriya D Mahajan, Hong Ding, Indrajit Roy, Ken-Tye Yong, Rajiv Kumar, Rui Hu, Earl J Bergey, Stanley a Schwartz, and Paras N Prasad. Nanotechnology approach for drug addiction therapy: gene silencing using delivery of gold nanorod-siRNA nanoplex in dopaminergic neurons. *Proceedings of the National Academy of Sciences of the United States of America*, 106(14):5546–50, apr 2009.

[50] D. A. Giljohann, D. S. Seferos, A. E. Prigodich, P. C. Patel, and C. A. Mirkin. Gene regulation with polyvalent sirna-nanoparticle conjugates. *Journal of the American Chemical Society*, 131(6):2072–2073, 2009.

[51] Ryan Huschka, Oara Neumann, Aoune Barhoumi, and Naomi J Halas. Visualizing light-triggered release of molecules inside living cells. *Nano Letters*, pages 4117–4122, 2010.

[52] Andy Wijaya, Stefan B. Schaffer, Ivan G. Pallares, and Kimberly Hamad-Schifferli. Selective release of multiple DNA oligonucleotides from gold nanorods. *ACS Nano*, 3(1):80–86, Jan 2009.

[53] L. J. Scherer and J. J. Rossi. Approaches for the sequence-specific knockdown of mrna. *Nature Biotechology*, 21(12):1457–1465, 2003.

[54] Ryan Huschka, Aoune Barhoumi, Qing Liu, Jack A. Roth, Lin Ji, and Naomi J. Halas. Gene silencing by gold nanoshell-mediated delivery and laser-triggered release of antisense oligonucleotide and sirna. *ACS Nano*, 6(9):7681–7691, Sep 2012.

[55] Charles P Lin and Michael W Kelly. Cavitation and acoustic emission around laser-heated microparticles. *Applied Physics Letters*, 72(22):2800–2802, 1998.

[56] S. Link, C. Burda, B. Nikoobakht, and M. A. El-Sayed. Laser-induced shape changes of colloidal gold nanorods using femtosecond and nanosecond laser pulses. *J. Phys. Chem. B*, 104(26):6152–6163, Jul 2000.

[57] A. Plech, V. Kotaidis, M. Lorenc, and M. Wulff. Thermal dynamics in laser excited metal nanoparticles. *Chem Phys Lett*, 401:565–569, 2005.

[58] R. R. Letfullin, C. Joenathan, T. F. George, and V. P Zharov. Laser-induced explosion of gold nanoparticles: potential role for nanophotothermolysis of cancer. *Nanomed*, 1(4):473–480, Dec 2006.

[59] V.K. Pustovalov, A.S. Smetannikov, and V.P. Zharov. Photothermal and accompanied phenomena of selective nanophotothermolysis with gold nanoparticles and laser pulses. *Laser Physics Letters*, 5(11):775–792, Nov 2008.

[60] Dmitri Lapotko. Optical excitation and detection of vapor bubbles around plasmonic nanoparticles. *Optics Express*, 17(4):2538–2556, 2009.

[61] Dmitri Lapotko. Pulsed photothermal heating of the media during bubble generation around gold nanoparticles. *International Journal of Heat and Mass Transfer*, 52(5):1540–1543, 2009.

[62] Florian Rudnizki. Modelling of optical properties and temperature distribution in and around gold nanorods. Master's thesis, University of Lübeck, 2008.

[63] Carsten Sönnichsen, Björn M Reinhard, Jan Liphardt, and A Paul Alivisatos. A molecular ruler based on plasmon coupling of single gold and silver nanoparticles. *Nature biotechnology*, 23(6):741–745, 2005.

[64] Andrea Csaki, Thomas Schneider, Janina Wirth, Norbert Jahr, Andrea Steinbrück, Ondrej Stranik, Frank Garwe, Robert Müller, and Wolfgang Fritzsche. Molecular plasmonics: light meets molecules at the nanoscale. *Philosophical Transactions of the Royal Society of London A: Mathematical, Physical and Engineering Sciences*, 369(1950):3483–3496, 2011.

[65] Ekaterina Lukianova-Hleb, Ying Hu, Loredana Latterini, Luigi Tarpani, Seunghyun Lee, Rebekah A Drezek, Jason H Hafner, and Dmitri O Lapotko. Plasmonic nanobubbles as transient vapor nanobubbles generated around plasmonic nanoparticles. *ACS nano*, 4(4):2109–2123, 2010.

[66] V. Kotaidis and A. Plech. Cavitation dynamics on the nanoscale. *Appl Phys Lett*, 87(21):213102, 2005.

[67] V. Kotaidis, C. Dahmen, G. von Plessen, F. Springer, and A. Plech. Excitation of nanoscale vapor bubbles at the surface of gold nanoparticles in water. *The Journal of Chemical Physics*, 124:184702, 2006.

[68] A Siems, SAL Weber, J Boneberg, and A Plech. Thermodynamics of nanosecond nanobubble formation at laser-excited metal nanoparticles. *New Journal of Physics*, 13(4):043018, 2011.

[69] U. Kreibig and M. Vollmer. *Optical Properties of Metal Clusters*. Number 25 in Springer Series in Materials Science. Springer-Verlag, Berlin, 1995.

[70] P. B. Johnson and R. W. Christy. Optical constants of the noble metals. *Phys Rev B*, 6(12):4370–4379, 1972.

[71] John David Jackson. *Classical Electrodynamics*. John Wiley & Sons, 1962.

[72] Craig F Bohren and Donald R Huffman. *Absorption and scattering of light by small particles*. John Wiley & Sons, 1983.

[73] H. C. van de Hulst. *Light Scattering by Small Particles*. Structure of Matter Series. Dover Publications Inc., New York, 1981.

[74] Carsten Sönnichsen. *Plasmons in metal nanostructures*. PhD thesis, LMU, 2001.

[75] J Sinzig, U Radtke, M Quinten, and U Kreibig. Binary clusters: homogeneous alloys and nucleus-shell structures. *Zeitschrift für Physik D Atoms, Molecules and Clusters*, 26(1):242–245, 1993.

[76] J Sinzig and M Quinten. Scattering and absorption by spherical multilayer particles. *Applied Physics A: Solids and Surfaces*, 58(2):157–162, 1994.

[77] Jorge Pérez-Juste, Isabel Pastoriza-Santos, Luis M. Liz-Marzán, and Paul Mulvaney. Gold nanorods: Synthesis, characterization and applications. *Coordination Chemistry Reviews*, 249(17-18):1870–1901, Sep 2005.

[78] Viktor K. Pustovalov. Theoretical study of heating of spherical nanoparticle in media by short laser pulses. *Chemical Physics*, 308(1-2):103–108, Jan 2005.

[79] E. Stefan Kooij and Bene Poelsema. Shape and size effects in the optical properties of metallic nanorods. *Physical Chemistry Chemical Physics*, 8(28):3349, 2006.

[80] Thomas Wriedt. A review of elastic light scattering theories. *Particle & Particle Systems Characterization*, 15(2):67–74, Apr 1998.

[81] Stuart W. Prescott and Paul Mulvaney. Gold nanorod extinction spectra. *Journal of Applied Physics*, 99(12):123504, Jun 2006.

[82] A Curry, G Nusz, A Chilkoti, and Adam Wax. Substrate effect on refractive index dependence of plasmon resonance for individual silver nanoparticles observed using darkfield micro-spectroscopy. *Optics express*, 13(7):2668–2677, 2005.

[83] C Sönnichsen, T Franzl, T Wilk, Gero von Plessen, J Feldmann, OV Wilson, and Paul Mulvaney. Drastic reduction of plasmon damping in gold nanorods. *Physical review letters*, 88(7):077402, 2002.

[84] S Link, C Burda, Zhong Lin Wang, and Mostafa A El-Sayed. Electron dynamics in gold and gold–silver alloy nanoparticles: The influence of a nonequilibrium electron distribution and the size dependence of the electron–phonon relaxation. *The Journal of chemical physics*, 111(3):1255–1264, 1999.

[85] M. Perner. *Optische Untersuchung der Elektronen- und Gitterdynamik in Edelmetall-Nanopartikeln*. Dissertation, 1999.

[86] Stephan Link and Mostafa A. El-Sayed. Shape and size dependence of radiative, non-radiative and photothermal properties of gold nanocrystals. *International Reviews in Physical Chemistry*, 19(3):409–453, 2000.

[87] C-K Sun, F Vallée, LH Acioli, EP Ippen, and JG Fujimoto. Femtosecond-tunable measurement of electron thermalization in gold. *Physical Review B*, 50(20):15337, 1994.

[88] Orla M Wilson, Xiaoyuan Hu, David G Cahill, and Paul V Braun. Colloidal metal particles as probes of nanoscale thermal transport in fluids. *Physical Review B*, 66(22):224301, 2002.

[89] A. Plech, V. Kotaidis, V. Grésillon, C. Dahmen, and G. von Plessen. Laser-induced heating and melting of gold nanoparticles studied by time-resolved x-ray scattering. *Physical Review B*, 70(19):195423, 2004.

[90] H. S. Carslaw and J. C. Jaeger. *Conduction of Heat in Solids*. Oxford University Press, 2. edition edition, 1959.

[91] Lihong V Wang and Hsin-i Wu. *Biomedical optics: principles and imaging*. Number 978-0-471-74304-0. John Wiley & Sons, 2007.

[92] Walter Benenson, John W Harris, Horst Stöcker, and Holger Lutz. *Handbook of physics*. Number 978-0-387-95269-7. Springer Science & Business Media, 2002.

[93] M. I. Khan and Gerald J. Diebold. The photoacoustic effect generated by an isotropic solid sphere. *Ultrasonics*, 33(4):265–269, 1995.

[94] Yanni Cao and Gerald J. Diebold. Effects of heat conduction and viscosity on photoacoustic waves from droplets. *Optical Engineering*, 36(2):417–422, 1997.

[95] S. Glod, D. Poulikakos, Z. Zhao, and G. Yadigaroglu. An investigation of microscale explosive vaporization of water on an ultrathin pt wire. *Int J Heat Mass Trans*, 45(2):367–379, 2002.

[96] M. M. Martynyuk. Phase explosion of a metastable fluid. *Combustion, Explosion, and Shock Waves*, 13(2):178–191, 1977.

[97] L. D. Landau and E. M. Lifshitz. *Statistical physics, part I*, volume 5 of Course of Theoretical Physics. Pergamon Press Ltd., Oxford, third edition edition, 1980.

[98] Herbert B. Callen. *Thermodynamics and an Introduction to Thermostatistics*. John Wiley and Sons, 2nd edition edition, 1985.

[99] C. E. Brennen. *Cavitation and Bubble Dynamics*. Oxford University Press, New York, 1995.

[100] Antonio Miotello and Roger Kelly. Laser-induced phase explosion: new physical problems when a condensed phase approaches the thermodynamic critical temperature. *Applied Physics A: Materials Science & Processing*, 69(7):S67–S73, 1999.

[101] Milton Blander and Joseph L. Katz. Bubble nucleation in liquids. *AIChE Journal*, 21(5):833–848, 1975.

[102] E. Boulais, R. Lachaine, A. Hatef, and M. Meunier. Plasmonics for pulsed-laser cell nanosurgery: Fundamentals and applications. *Journal of Photochemistry and Photobiology C: Photochemistry Reviews*, 17:26–49, Dec 2013.

[103] A Vogel, J Noack, G Hüttman, and G Paltauf. Mechanisms of femtosecond laser nanosurgery of cells and tissues. *Applied Physics B*, 81(8):1015–1047, 2005.

[104] Milton S Plesset and Andrea Prosperetti. Bubble dynamics and cavitation. *Annual Review of Fluid Mechanics*, 9(1):145–185, 1977.

[105] W. Lauterborn. *Cavitation and Inhomogenities in Underwater Acoustics*. Springer-Verlag, Berlin, 1980.

[106] Werner Lauterborn and Alfred Vogel. Modern optical techniques in fluid mechanics. *Annual Review Fluid Mechanics*, 16:223–244, 1984.

[107] A. Vogel, S. Busch, and U. Parlitz. Shock wave emission and cavitation bubble generation by picosecond and nanosecond optical breakdown in water. *The Journal of the Acoustical Society of America*, 100(1):148–165, Jul 1996.

[108] Alfred Vogel, Norbert Linz, Sebastian Freidank, and Günther Paltauf. Femtosecond-laser-induced nanocavitation in water: implications for optical breakdown threshold and cell surgery. *Physical review letters*, 100(3):038102, 2008.

[109] Jörg Neumann and Ralf Brinkmann. Self-limited growth of laser-induced vapor bubbles around single microabsorbers. *Applied Physics Letters*, 93(3):033901, 2008.

[110] Julien Lombard, Thierry Biben, and Samy Merabia. Kinetics of nanobubble generation around overheated nanoparticles. *Physical review letters*, 112(10):105701, 2014.

[111] Julien Lombard, Thierry Biben, and Samy Merabia. Nanobubbles around plasmonic nanoparticles: Thermodynamic analysis. *Physical Review E*, 91(4):043007, 2015.

[112] Julien Lombard, Thierry Biben, and Samy Merabia. Threshold for vapor nanobubble generation around plasmonic nanoparticles. *The Journal of Physical Chemistry C*, 2017.

[113] E. Boulais, R. Lachaine, and M. Meunier. Basic mechanisms of the femtosecond laser interaction with a plasmonic nanostructure in water. *Frontiers in Ultrafast Optics: Biomedical, Scientific, and Industrial Applications XI*, Feb 2011.

[114] Étienne Boulais, Rémi Lachaine, and Michel Meunier. Plasma mediated off-resonance plasmonic enhanced ultrafast laser-induced nanocavitation. *Nano Lett.*, 12(9):4763–4769, Sep 2012.

[115] Sergey Egerev, Sergey Ermilov, Oleg Ovchinnikov, Andrey Fokin, Dmitry Guzatov, Vasily Klimov, Andrey Kanavin, and Alexander Oraevsky. Acoustic signals generated by laser-irradiated metal nanoparticles. *Applied optics*, 48(7):C38–C45, 2009.

[116] Emil-Alexandru Brujan. Numerical investigation on the dynamics of cavitation nanobubbles. *Microfluidics and nanofluidics*, 11(5):511–517, 2011.

[117] Emil-Alexandru Brujan. Behaviour of plasmonic nanoparticle-generated cavitation bubbles. *Romanian Journal of Technical Science Applied Mechanics*, 2013.

[118] Robert H. Cole. *Underwater explosions*. Princeton University press, 1948.

[119] J. W. Rayleigh. On the pressure developed in a liquid during the collapse of a spherical cavity. *Phil Mag*, 34:94–98, 1917.

[120] Shigeo Fujikawa and Teruaki Akamatsu. Effects of the non-equilibrium condensation of vapour on the pressure wave produced by the collapse of a bubble in a liquid. *Journal of Fluid Mechanics*, 97(03):481–512, 1980.

[121] Ritva Löfstedt, Bradley P Barber, and Seth J Putterman. Toward a hydrodynamic theory of sonoluminescence. *Physics of Fluids A: Fluid Dynamics (1989-1993)*, 5(11):2911–2928, 1993.

[122] Detlef Lohse and Sascha Hilgenfeldt. Inert gas accumulation in sonoluminescing bubbles. *The Journal of chemical physics*, 107(17):6986–6997, 1997.

[123] Sascha Hilgenfeldt, Michael P Brenner, Siegfried Grossmann, and Detlef Lohse. Analysis of rayleigh-plesset dynamics for sonoluminescing bubbles. *Journal of fluid mechanics*, 365:171–204, 1998.

[124] I Akhatov, O Lindau, A Topolnikov, R Mettin, N Vakhitova, and W Lauterborn. Collapse and rebound of a laser-induced cavitation bubble. *Physics of Fluids (1994-present)*, 13(10):2805–2819, 2001.

[125] Werner Lauterborn and Thomas Kurz. Physics of bubble oscillations. *Reports on progress in physics*, 73(10):106501, 2010.

[126] R. I. Nigmatulin. Fundamentals of the mechanics of heterogeneous media. *Moscow Izdatel Nauka*, 1978.

[127] V.K. Pustovalov. Thermal processes under the action of laser radiation pulse on absorbing granules in heterogeneous biotissues. *International Journal of Heat and Mass Transfer*, 36(2):391–399, Jan 1993.

[128] Akira Onuki. Dynamic van der waals theory. *Physical Review E*, 75(3):036304, 2007.

[129] Leonard A Herzenberg, David Parks, Bita Sahaf, Omar Perez, Mario Roederer, and LEONORE A HERzENbERG. The history and future of the fluorescence activated cell sorter and flow cytometry: a view from stanford. *Clinical chemistry*, 48(10):1819–1827, 2002.

[130] Stefan Miltenyi, Werner Müller, Walter Weichel, and Andreas Radbruch. High gradient magnetic cell separation with macs. *Cytometry Part A*, 11(2):231–238, 1990.

[131] Marcos de Lima and Elizabeth J Shpall. Ex-vivo purging of hematopoietic progenitor cells. *Current hematology reports*, 3(4):257–264, 2004.

[132] Monika Stich, Stefan Thalhammer, Renate Burgemeister, Gabriele Friedemann, Susanne Ehnle, Carsten Lüthy, and Karin Schütze. Live cell catapulting and recultivation. *Pathology-Research and Practice*, 199(6):405–409, 2003.

[133] Verena Horneffer, Norbert Linz, and Alfred Vogel. Principles of laser-induced separation and transport of living cells. *Journal of biomedical optics*, 12(5):054016–054016, 2007.

[134] Alfred Vogel, Verena Horneffer, Kathrin Lorenz, Norbert Linz, Gereon Hüttmann, and Andreas Gebert. Principles of laser microdissection and catapulting of histologic specimens and live cells. *Methods in cell biology*, 82:153–205, 2007.

[135] K Schütze, Yilmaz Niyaz, M Stich, and A Buchstaller. Noncontact laser microdissection and catapulting for pure sample capture. *Methods in cell biology*, 82:647–673, 2007.

[136] Manfred R Koller, Elie G Hanania, Janine Stevens, Timothy M Eisfeld, Glenn C Sasaki, Annabeth Fieck, and Bernhard Ø Palsson. High-throughput laser-mediated in situ cell purification with high purity and yield. *Cytometry Part A*, 61(2):153–161, 2004.

[137] Xiaohua Huang, Prashant K Jain, Ivan H El-Sayed, and Mostafa A El-Sayed. Plasmonic photothermal therapy (pptt) using gold nanoparticles. *Lasers in medical science*, 23(3):217, 2007.

[138] Ekaterina Y Hleb, Jason H Hafner, Jeffrey N Myers, Ehab Y Hanna, Betty C Rostro, Sergey A Zhdanok, and Dmitri O Lapotko. Lantcet: elimination of solid tumor cells with photothermal bubbles generated around clusters of gold nanoparticles. *Nanomedicine*, 3(5):647–667, 2008.

[139] C Sönnichsen, S Geier, NE Hecker, G Von Plessen, J Feldmann, H Ditlbacher, B Lamprecht, JR Krenn, FR Aussenegg, V ZH Chan, et al. Spectroscopy of single metallic nanoparticles using total internal reflection microscopy. *Applied Physics Letters*, 77(19):2949–2951, 2000.

[140] J Sabine Becker, Miroslav Zoriy, Andreas Matusch, Bei Wu, Dagmar Salber, Christoph Palm, and J Susanne Becker. Bioimaging of metals by laser ablation inductively coupled plasma mass spectrometry (la-icp-ms). *Mass spectrometry reviews*, 29(1):156–175, 2010.

[141] Irene Ament, Janak Prasad, Andreas Henkel, Sebastian Schmachtel, and Carsten Sönnichsen. Single unlabeled protein detection on individual plasmonic nanoparticles. *Nano Letters*, pages 1092–1095, 2012.

[142] A Plech, S Grésillon, G Von Plessen, K Scheidt, and G Naylor. Structural kinetics of laser-excited metal nanoparticles supported on a surface. *Chemical physics*, 299(2):183–191, 2004.

[143] Hironobu Takahashi, Takuro Niidome, Ayuko Nariai, Yasuro Niidome, and Sunao Yamada. Photothermal reshaping of gold nanorods prevents further cell death. *Nanotechnology*, 17(17):4431, 2006.

[144] Prashant K Jain, Wei Qian, and Mostafa A El-Sayed. Ultrafast cooling of photoexcited electrons in gold nanoparticle- thiolated dna conjugates involves the dissociation of the gold- thiol bond. *Journal of the American Chemical Society*, 128(7):2426–2433, 2006.

[145] Amanda M. Goodman, Nathaniel J. Hogan, Samuel Gottheim, Carrie Li, Susan E. Clare, and Naomi J. Halas. Understanding resonant light-triggered dna release from plasmonic nanoparticles. *ACS Nano*, 11(1):171–179, Jan 2017.

[146] Feng Li, Hongquan Zhang, Brittany Dever, Xing-fang Li, and X Chris Le. Thermal stability of dna functionalized gold nanoparticles. *Bioconjugate Chemistry*, 24:1790–1797, 2013.

[147] Anton Plech, Vassilios Kotaidis, Maciej Lorenc, and Johannes Boneberg. Femtosecond laser near-field ablation from gold nanoparticles. *Nature Physics*, 2(1):44, 2006.

[148] Daniel Werner, Akihiro Furube, Toshihiro Okamoto, and Shuichi Hashimoto. Femtosecond laser-induced size reduction of aqueous gold nanoparticles: In situ and pump- probe spectroscopy investigations revealing coulomb explosion. *The Journal of Physical Chemistry C*, 115(17):8503–8512, 2011.

[149] Aoune Barhoumi, Ryan Huschka, Rizia Bardhan, Mark W Knight, and Naomi J Halas. Light-induced release of dna from plasmon-resonant nanoparticles: towards light-controlled gene therapy. *Chemical Physics Letters*, 482(4):171–179, 2009.

[150] Benno Radt, Jesper Serbin, Bjoern I Lange, Reginald Birngruber, and Gereon Huettmann. Laser-generated micro-and nanoeffects: inactivation of proteins coupled to gold nanoparticles with nano-and picosecond pulses. In *Laser-Tissue Interactions, Therapeutic Applications, and Photodynamic Therapy*, volume 4433, pages 16–25. International Society for Optics and Photonics, 2001.

[151] Alexandra Grün. Interferometric and photographic investigations of bubble dynamics in laser-induced corneal dissection for refractive surgery. Bachelor thesis, Institute of Biomedical Optics, University of Lübeck, 2014.

[152] Norbert Linz, Sebastian Freidank, Xiaoxuan Liang, and Alfred Vogel. Experimental and theoretical investigations of the mechanisms of free-electron-mediated modification of biomolecules in nonlinear microscopy. Technical Report Grant FA9550-15-1-0326, Institute of Biomedical Optics, 2016.

[153] VP Zharov, RR Letfullin, and EN Galitovskaya. Microbubbles-overlapping mode for laser killing of cancer cells with absorbing nanoparticle clusters. *Journal of Physics D: Applied Physics*, 38(15):2571, 2005.

[154] Dmitri O Lapotko, Ekaterina Lukianova, and Alexander A Oraevsky. Selective laser nanothermolysis of human leukemia cells with microbubbles generated around clusters of gold nanoparticles. *Lasers in surgery and medicine*, 38(6):631–642, 2006.

[155] V. K. Pustovalov. Theoretical study of the heating of solid ellipsoidal nanoparticle in media by short laser pulses. *Laser Physics Letters*, 2(8):401–406, 2005.

[156] Ho-Young Kwak, Jaekyoon Oh, Yungpil Yoo, and Shahid Mahmood. Bubble formation on the surface of laser-irradiated nanosized particles. *Journal of Heat Transfer*, 136(8):081501, Apr 2014.

[157] S. E. Lee, D. Y. Sasaki, T. D. Perroud, D. Yoo, K. D. Patel, and L. P. Lee. Biologically functional cationic phospholipid-gold nanoplasmonic carriers of rna. *Journal of the American Chemical Society*, 131(39):14066–14074, 2009.

[158] H. Goldenberg and C. J. Tranter. Heat flow in an infinite medium heated by a sphere. *Br J Appl Phys*, 3:296–298, 1952.

[159] Maria Holmberg, Anders Kühle, Jørgen Garnæs, Knud A Mørch, and Anja Boisen. Nanobubble trouble on gold surfaces. *Langmuir*, 19(25):10510–10513, 2003.

[160] YY Hsu. On the size range of active nucleation cavities on a heating surface. *Journal of Heat Transfer*, 84(3):207–213, 1962.

[161] Ekaterina Y Lukianova-Hleb, Alexey N Volkov, and Dmitri O Lapotko. Laser pulse duration is critical for the generation of plasmonic nanobubbles. *Langmuir*, 30(25):7425–7434, 2014. A readers concerns related to figures in this article is under investigation.

[162] Rémi Lachaine, Étienne Boulais, and Michel Meunier. From thermo- to plasma-mediated ultrafast laser-induced plasmonic nanobubbles. *ACS Photonics*, 1(4):331–336, Apr 2014.

[163] Poul Martin Hansen, Vikram Kjøller Bhatia, Niels Harrit, and Lene Oddershede. Expanding the optical trapping range of gold nanoparticles. *Nano letters*, 5(10):1937–1942, 2005.

[164] Poul M Bendix, Liselotte Jauffred, Kamilla Norregaard, and Lene B Oddershede. Optical trapping of nanoparticles and quantum dots. *IEEE journal of selected topics in quantum electronics*, 20(3):15–26, 2014.

[165] Peng Li, Kebin Shi, and Zhiwen Liu. Manipulation and spectroscopy of a single particle by use of white-light optical tweezers. *Optics letters*, 30(2):156–158, 2005.

[166] Maria Dienerowitz, Michael Mazilu, and Kishan Dholakia. Optical manipulation of nanoparticles: a review. *Journal of Nanophotonics*, 2(1):021875–021875, 2008.

[167] Maria Dienerowitz. *Plasmonic effects upon Optical Trapping of metal nanoparticles*. PhD thesis, University of St Andrews, 2010.

[168] Lana Bosanac, Thomas Aabo, Poul M Bendix, and Lene B Oddershede. Efficient optical trapping and visualization of silver nanoparticles. *Nano letters*, 8(5):1486–1491, 2008.

[169] Yeonee Seol, Amanda E Carpenter, and Thomas T Perkins. Gold nanoparticles: enhanced optical trapping and sensitivity coupled with significant heating. *Optics letters*, 31(16):2429–2431, 2006.

[170] Kenji Setoura, Yudai Okada, Daniel Werner, and Shuichi Hashimoto. Observation of nanoscale cooling effects by substrates and the surrounding media for single gold nanoparticles under cw-laser illumination. *Acs Nano*, 7(9):7874–7885, 2013.

[171] Bob Orwiler. *Verticle Amplifier Circuits*. Tektronix, Inc., 1969.

[172] A. Vogel, W. Lauterborn, and R. Timm. Optical and acoustic investigations of the dynamics of laser-produced cavitation bubbles near a solid boundary. *Journal of Fluid Mechanics*, 206:299–338, 1989.

[173] Emil-Alexandru Brujan, Kester Nahen, Peter Schmidt, and Alfred Vogel. Dynamics of laser-induced cavitation bubbles near an elastic boundary. *Journal of Fluid Mechanics*, 433:251–281, 2001.

[174] W. Wagner and A. Pruß. The iapws formulation 1995 for the thermodynamic properties of ordinary water substance for general and scientic use. *J Phys Chem Ref Data*, 31(2):387–535, 2002.

[175] D. R. Lide, editor. *CRC Handbook of Chemistry and Physics*. CRC Press, 76. auflage edition, 2005.

[176] Vladimir Zharov and Dmitri Lapotko. Photothermal sensing of nanoscale targets. *Review of scientific instruments*, 74(1):785–788, 2003.

[177] Vladimir P Zharov, Valentin Galitovsky, and Mark Viegas. Photothermal detection of local thermal effects during selective nanophotothermolysis. *Applied Physics Letters*, 83(24):4897–4899, 2003.

[178] Christos Boutopoulos, Ali Hatef, Matthieu Fortin-Deschênes, and Michel Meunier. Dynamic imaging of a single gold nanoparticle in liquid irradiated by off-resonance femtosecond laser. *Nanoscale*, 7(27):11758–11765, 2015.

[179] Anton Plech, Roland Cerna, Vassilios Kotaidis, Florian Hudert, Albrecht Bartels, and Thomas Dekorsy. A surface phase transition of supported gold nanoparticles. *Nano Letters*, 7(4):1026–1031, Apr 2007.

[180] Anton Plech, Vassilios Kotaidis, Konstantin Istomin, and Michael Wulff. Small-angle pump-probe studies of photoexcited nanoparticles. *Journal of SynchrotronRadiation*, 14:288–296, 2007.

[181] Ekaterina Y Lukianova-Hleb and Dmitri O Lapotko. Influence of transient environmental photothermal effects on optical scattering by gold nanoparticles. *Nano letters*, 9(5):2160–2166, 2009.

[182] Julien Lombard, Thierry Biben, and Samy Merabia. Ballistic heat transport in laser generated nano-bubbles. *Nanoscale*, 8(31):14870–14876, 2016.

[183] M. Otter. Optische konstanten massiver metalle. *Z Physik A*, 161(2):163–178, 1961.

[184] M Otter. Temperaturabhängigkeit der optischen konstanten massiver metalle. *Zeitschrift für Physik A Hadrons and Nuclei*, 161(5):539–549, 1961.

[185] Michael Strasser, Kenji Setoura, Uwe Langbein, and Shuichi Hashimoto. Computational modeling of pulsed laser-induced heating and evaporation of gold nanoparticles. *The Journal of Physical Chemistry C*, 118(44):25748–25755, 2014.

[186] P Schiebener, Johannes Straub, JMH Levelt Sengers, and JS Gallagher. Refractive index of water and steam as function of wavelength, temperature and density. *Journal of physical and chemical reference data*, 19(3):677–717, 1990.

[187] Alexey N Volkov, Carlos Sevilla, and Leonid V Zhigilei. Numerical modeling of short pulse laser interaction with au nanoparticle surrounded by water. *Applied Surface Science*, 253(15):6394–6399, 2007.

[188] Masanori Matsui. High temperature and high pressure equation of state of gold. In *Journal of Physics: Conference Series*, volume 215, page 012197. IOP Publishing, 2010.

[189] Elmar Endl. Final report laser activated nanoparticle directed cell elimination and modulation. Report of a research project found by the federal ministry of education and research, University of Bonn, Institute of Molecular Medicine, 2017.

[190] S. E. Lee, G. L. Liu, F. Kim, and L. P. Lee. Remote optical switch for localized and selective control of gene interference. *Nano Letters*, 9(2):562–570., 2009.

Acknowledgments

At this point, I would like to thank the people who contributed to this good feeling and the success of this work.
My thanks go first of all to Gereon Hüttmann, my doctoral supervisor, who took me into his workgroup. He introduced me to the extremely exciting field of plasmonic nanoparticles and gave me the opportunity to do this work and the doctorate. I thank Gereon for his enthusiasm and his outstanding theoretical support, that made great contributions to this work. On the one hand, it left me a lot of space for my work and, on the other hand, kept me on the right track. By involving me in the work on proposals for the project funds as well as attending conferences, he has promoted my own development.
I thank Alfred Vogel and Reginald Birngruber for advice and interest in my work. Your openness and ideas have always supported me. In particular, I thank Alfred for the discussions on the physics of cavitation bubbles as well as the development of the detection technique, which forms a cornerstone of this work. Here, I also thank Ralf Brinkmann, director of the Medical Laser Center Lübeck, for his support and many pragmatic advice.
Questions about optical constructions and adjustment often led me to the door or into the laboratory of Norbert Linz and Sebastian Freidank. Therefore, many thanks go to these to collegues for their contribution in experimental approaches and procedures as well as discussions. Without these two, the experimental implementation would not be so successful and I would have learned only half as many tricks for adjusting optical setups. Basti's and Norberts vocal performances were unique.
I would like to express my gratitudes to Ramtin Rahmanzadeh, who shared an office with me the last years, for many discussions, scientific and not so scientific ones. As a biologist, Ramtin always had a different view of my experiments, which helped me a lot getting new ideas and solutions. Astrid Link, from Ramtin's group, should be also mentioned here, who helped me with the care of cell cultures and other work in the cell lab.
Furthermore, I would like to thank all colleagues of the Institute for Biomedical Optics and the Medical Laser Center Lübeck for their support and the comfortable and productive working atmosphere. I would like to mention my companions Jens Horstmann and Alex Baade, thanks to many hours of conversation during and after work with beer or soda.
I thank my parents and my sister and my friends for their support. You had so much forbearance and understanding, especially in the last 2 years.

SONJA
To put this in front of all last but not least, my heartfelt and deepest thanks go to Sonja for standing by me throughout these times. You kept me aware and afloat amid the jostling waves. I look forward to our life.

This work was supported by grants from the Federal Ministry of Education and Research, Project Number 13N11832 (LAND-CEM). Thank you.